UNIVERSITÀ DI SIENA 1240

Department of Physical Sciences, Earth and Environment
**PhD in Experimental Physics**
XXXVII Cycle
Coordinator: Prof. Alessandro Cerri

# The Field Cages of the new Time Projection Chambers (TPCs) for the T2K Upgraded Near Detector: production, characterization, electric field performance and advanced track reconstruction

Disciplinary Scientific Sector: FIS/01

*A thesis submitted in partial fulfillment of the requirements for the degree of Doctor of Philosophy*

*PhD Student*
**Matteo Feltre**
University of Siena
Via Roma 56

*Supervisor*
**Prof. Gianmaria Collazuol**
University of Padova

*Co-Supervisor*
**Prof. Pier Simone Marrocchesi**
University of Siena

A. Y. 2023/2024

# Abstract

T2K (Tokai to Kamioka) is a long-baseline neutrino experiment based in Japan, designed to measure neutrino oscillation parameters, including $\theta_{13}$, $\delta_{CP}$, $\theta_{23}$, and $\Delta m^2_{32}$. These parameters are determined by studying electron neutrino appearance probabilities and muon neutrino survival probabilities. In recent years, T2K has undergone significant upgrades to its beam-line and the magnetized Near Detector (ND280) to increase the neutrino flux and reduce systematic uncertainties. These improvements are critical not only for T2K but also for the next generation of neutrino oscillation experiments, as the beam-line and ND280 will play a key role in the long-baseline program of Hyper-Kamiokande, expected to be completed in 2027.

A key component of the ND280 upgrade is the installation of two High-Angle Time Projection Chambers (HA-TPCs), designed to identify charged particles at large angles relative to the beam direction. Both HA-TPCs were successfully installed at J-PARC by May 2024. This thesis focuses on three main aspects of the HA-TPCs: (i) the design, production, and performance evaluation of field cages, (ii) the study of their electric field properties, and (iii) the development of a novel machine learning-based track reconstruction algorithm.

The HA-TPCs feature a gaseous active volume enclosed in a field cage constructed from lightweight composite materials, offering an optimal balance of mechanical and electrical properties while minimizing radiation length and dead volume. The readout is based on innovative Resistive Micromegas sensors, which include a resistive layer for charge spreading to enhance spatial resolution and protect the electronics from sparks. This technology has been extensively tested through test beams and cosmic ray data-taking campaigns at CERN and later at J-PARC. Following installation at J-PARC in late 2023 and early 2024, the HA-TPCs underwent a commissioning phase with cosmic rays and, subsequently, with a neutrino beam.

Field cages serve multiple functions: (i) providing mechanical support to the detector, (ii) shaping the electric field, and (iii) containing the gas mixture while preventing contamination. The cage walls are made from composite materials with low atomic numbers and minimal material budget to reduce particle interactions and scattering. Precise design, prototyping, and rigorous validation were essential to meet the stringent geometrical tolerances and electrical insulation requirements.

This thesis presents my contributions to the development, characterization, and commissioning of the HA-TPCs, with a focus on the effects of electric fields on track projections and the development of advanced reconstruction techniques. My work is divided into three main parts:

1. **Field Cage Production and Validation** I conducted detailed studies of the electrical and mechanical properties of the HA-TPC field cages, addressing a major issue encountered during the production of the first full-scale prototype (FC0). Measurements revealed nonlinear current-voltage behavior, suggesting the presence of parasitic conductive paths in the field cage walls. Through electrical characterization, mathematical modeling, and design improvements, I identified and resolved the issue. I also supervised the production process, established quality assessment protocols, and contributed to the assembly and commissioning of the HA-TPCs at CERN and J-PARC.

2. **Electric Field Characterization** I investigated the uniformity of the electric drift field, which is critical for accurate track reconstruction. Deviations from ideal conditions can introduce systematic distortions in particle trajectories. Using finite element method (FEM)

simulations and cosmic ray data, I identified distortions in the electric field near the cathode region. These distortions were corrected using a 3D electric field map derived from the FEM simulation, significantly improving track reconstruction accuracy.

3. **Novel Track Reconstruction Algorithm** I developed a machine learning-based track reconstruction method for the HA-TPCs. The algorithm uses the amplitude and full width at half maximum (FWHM) of pad response signals to determine the parameters of a local linear approximation of the track trajectory. While the current method excels in momentum reconstruction, preliminary comparisons with the novel method indicate promising improvements in spatial resolution, particularly for diagonal tracks. The method offers significant potential for further optimization, including refining input features and enhancing the machine learning model.

In conclusion, this thesis demonstrates the successful development, characterization, and commissioning of the HA-TPCs, highlighting their critical role in the ND280 upgrade and the broader T2K and Hyper-Kamiokande programs. The work presented here advances the understanding of electric field effects in TPCs and introduces innovative reconstruction techniques, paving the way for future improvements in neutrino detection and measurement.

# Contents


**1 Neutrinos in the Standard Model** **1**
- 1.1 Neutrinos history . . . 2
  - 1.1.1 Parity violation in weak processes . . . 4
- 1.2 Neutrinos in the Standard Model . . . 6
  - 1.2.1 Neutrino masses . . . 11
- 1.3 Neutrino Oscillations . . . 12
  - 1.3.1 Neutrino oscillations in vacuum . . . 12
  - 1.3.2 Two neutrino mixing . . . 14
  - 1.3.3 Mass ordering . . . 15
  - 1.3.4 Charge-Parity (CP) violation in neutrino oscillation . . . 16
  - 1.3.5 Neutrino oscillations in matter . . . 17
- 1.4 Overview on neutrino oscillation experiments . . . 19
- 1.5 Accelerator neutrinos . . . 27
- 1.6 The role of Near Detectors in Long Baseline Neutrino Oscillation (LBNO) Experiments 29
- 1.7 State of the art, open questions and next steps in neutrino oscillation physics . . . 31
  - 1.7.1 Next generation of neutrino oscillation experiments . . . 33

**2 The T2K Experiment** **35**
- 2.1 Neutrino Beam . . . 37
  - 2.1.1 The neutrino beamline . . . 37
- 2.2 The Near Detector Complex . . . 39
  - 2.2.1 INGRID . . . 39
  - 2.2.2 ND280 . . . 40
  - 2.2.3 The far detector: Super-Kamiokande . . . 45
- 2.3 Latest T2K Oscillation results . . . 48
- 2.4 T2K Phase II . . . 51
  - 2.4.1 ND280 Upgrade . . . 51
- 2.5 Beyond T2K . . . 55
  - 2.5.1 Hyper-Kamiokande . . . 55

**3 HA-TPCs** **58**
- 3.1 Particle detection with gaseous detectors . . . 58
- 3.2 Drift of electrons in gases . . . 60
- 3.3 Time Projection Chambers . . . 63
- 3.4 The High Angle Time Projection Chambers (HA-TPCs) . . . 64
  - 3.4.1 HA-TPC structure . . . 65
  - 3.4.2 Resistive Bulk MicroMegas Modules . . . 66

3.4.3 Electronics . . . 68
3.4.4 Gas system . . . 69
3.4.5 Gas Monitoring Chambers (GMCs) . . . 69
3.5 Assembly and installation of HA-TPCs . . . 69
3.6 Reconstruction in HA-TPCs . . . 70
3.6.1 Spatial reconstruction . . . 73
3.6.2 Estimation of Energy Loss per unit of Length (dE/dx) . . . 76
3.7 Simulation of HA-TPCs . . . 78
3.8 Test beams for HA-TPC prototypes . . . 79

**4 Field cage of HA-TPC** **84**
4.1 Field cage Structure . . . 85
4.2 Field cage production . . . 88
4.2.1 Resin resistivity . . . 92
4.2.2 Assessment of layers resistivity . . . 95
4.2.3 Strip foil resistance . . . 99
4.2.4 Laminated Kapton . . . 100
4.3 Cathode . . . 105
4.4 Field cages assembly . . . 105
4.5 Field cage validation . . . 107
4.5.1 Metrology . . . 108
4.6 Validation of mechanical properties . . . 111
4.6.1 Load test . . . 111
4.6.2 Walls deformation due to gas pressure . . . 113
4.7 Electric properties of the field cages . . . 115
4.8 Summary . . . 116

**5 Characterization of Field Cage response** **118**
5.1 Validation of High Voltage response . . . 119
5.1.1 Possible sources . . . 120
5.2 Measurement on FC0 voltage divider . . . 121
5.3 Model . . . 122
5.4 Local measurements of voltage divider resistors . . . 124
5.5 Estimation of Twaron Resistivity . . . 128
5.5.1 Twaron properties . . . 129
5.5.2 Twaron surface Resistivity . . . 131
5.6 Test of "Vertical" Conduction Mechanism . . . 134
5.6.1 Methods . . . 134
5.6.2 Kapton Volumetric Resistivity . . . 134
5.6.3 Measurements on strip foils . . . 135
5.7 Fit of the model to Kapton and Twaron resistivity estimation . . . 137
5.8 Continuous modelization of field cage . . . 138
5.9 Continuous solution for K and T homogeneous . . . 139
5.10 Model application to field cage . . . 142
5.10.1 Resistance per single cell . . . 145
5.11 Field cage modelization for K and T inhomogeneous . . . 146
5.12 Refurbishment of FC0 . . . 147

5.13 Summary . . . 151

**6 Electric field in HA-TPCs** **153**
6.1 Brief Introduction to Electrostatics . . . 154
6.2 Electric Field Distortions and Track Reconstruction in the HA-TPC . . . 155
6.3 Space charge effects in the HA-TPCs . . . 156
6.4 Electric field model for HA-TPCs . . . 160
6.4.1 Electric field model for early HA-TPC design . . . 160
6.4.2 Electric field model for the real field cage . . . 160
6.4.3 Electric field simulation . . . 163
6.4.4 Electric field map implementation in ND280 Software . . . 167
6.5 Effect of electric field map on drift of a point-like charge . . . 170
6.6 Application of electric field map to Cosmic Rays . . . 170
6.7 Impact of electric field inhomogeneity on timing . . . 172
6.7.1 Effects on a point-like charge . . . 175
6.8 Future investigation of electric field with FC0 . . . 175
6.9 Impact of electric field map correction with magnetic field . . . 177
6.10 Summary . . . 180

**7 Track reconstruction with Multi-Layer Perceptron** **181**
7.1 Outline of the Method . . . 181
7.1.1 Clustering . . . 182
7.1.2 Input parameters to ML algorithm . . . 183
7.1.3 ML algorithm output parameters processing and track fitting . . . 185
7.2 The Multi Layer Perceptron (MLP) . . . 185
7.3 Overfitting and Underfitting . . . 189
7.4 Generation of training and test datasets . . . 191
7.5 Training of the Neural Network for horizontal clustering . . . 191
7.6 Network performance evaluation . . . 192
7.7 Spatial reconstruction performance on Montecarlo simulated data . . . 194
7.8 Momentum resolution performance on simulation . . . 198
7.9 Preliminary Insights into the New Reconstruction of Real Tracks from Neutrino Beam Data . . . 198
7.10 Summary . . . 200

# Chapter 1

# Neutrinos in the Standard Model

The Standard Model (SM) of particle physics is the most successful theory regarding the understanding of our universe. It describes three of the fundamental interactions: electric, weak and strong, while the gravitational interaction is beyond the current formulation. Furthermore, the SM classifies all the known elementary particles discovered since the early part of $20^{\text{th}}$ century, summarized in figure 1.1.

Particles are divided into two macro-categories, fermions and bosons, according to their spin value,

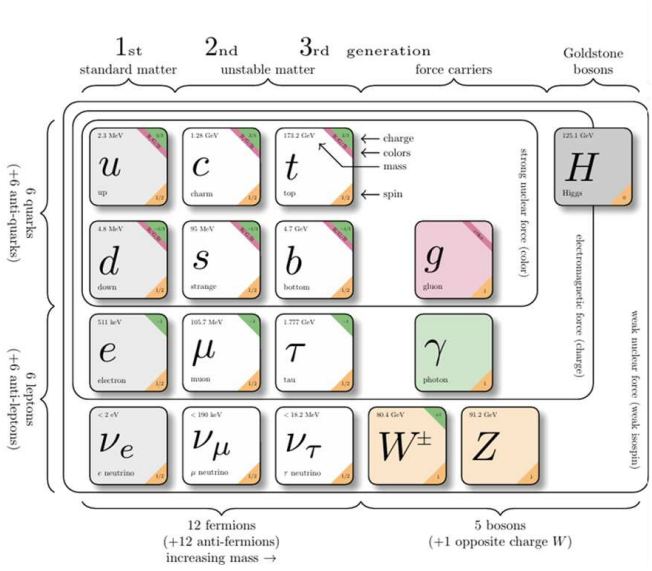


Figure 1.1: The picture summarizes the fundamental particles, grouped according to their properties. Each particle is presented along with its electric charge, color charge and mass. In particular, the mass scale for massive particles span up to 12 orders of magnitude, from the top quark to the very light neutrinos. Adapted from [1].

which can assume respectively half or integer values. Fermions are the basic components of matter: (i) six quarks and (ii) six leptons belong to this category. In addition, each fermion has its own antiparticle, which for charged particles has electric charge of opposite sign. Bosons are the mediators of the fundamental interactions: (i) photon for the electric force, (ii) W and Z for weak force, (iii) gluon for strong force, while the scalar Higgs boson H provides mass to the particles.

Even if the SM theory is supported by a large number of experimental evidence, there are still

open questions that need to be addressed. One of the open puzzles is the neutrino mass. In the SM, neutrinos are predicted to be massless particles, while several experiments proved wrong this assumption thanks to the discovery of neutrino oscillation phenomenon, described in detail in the next section.

## 1.1 Neutrinos history

As anticipated in figure 1.1, neutrinos are neutral fermions and belong to the lepton category, so they are influenced by the action of weak force but do not take part in strong interactions. Furthermore, neutrinos are proved to be massive particles, so they are also subjected to the gravitational force. Neutrinos are renowned for their *elusiveness*, since they interact much less than other particles and for this reason they were discovered about 26 years after their conceptualization.

### Neutrino discovery

Neutrino existence was proposed by W. Pauli in 1930 in his famous letter addressed to the participants of a nuclear conference in Tübingen as a possible explanation of the spectrum of the $\beta$-decay of a nucleus[2]. At the time, a nucleus was considered a bound state of protons and electrons. Considering a nucleus X of mass number A and atomic number Z, a $\beta-$decay was thought to be a process in which an electron is emitted in the nuclear transition according to

$$^{\mathrm{A}}_{\mathrm{Z}}X \rightarrow ^{\mathrm{A}}_{\mathrm{Z+1}}Y + e^{-}. \tag{1.1}$$

Due to energy conservation, the outgoing electron energy is found as

$$E_e = \frac{M_X^2 - M_Y^2 + M_e^2}{2M_X} \tag{1.2}$$

in which the electron energy $E_e$ is expected to be a fixed value. Experimental evidence proved this prediction to be wrong, in fact Chadwick observed that its spectrum was continuous with $E_e$ as endpoint[3]. Therefore, assuming the validity of the energy-momentum conservation, Pauli proposed as a possible solution that the $\beta$-decay was a three body reaction, in which part of the energy is carried away from the system by another particle, that escapes unnoticed. The particle should be neutral to satisfy the charge conservation, with spin $\frac{1}{2}$ in order to conserve angular momentum.
In 1932, Chadwick discovered a particle with no electric charge and with a mass similar to the one of the proton, named neutron[4], and as a consequence Fermi proposed to call the Pauli's particle *neutrino* due to its supposed small mass. At that point, nuclei were considered bound states of protons and neutrons, so the mechanism behind the neutrino and electron emission was still unclear. In 1934, Fermi introduced the first step towards the modern weak interaction in analogy with quantum electrodynamics[5]. He explained the $\beta-$decay as the electron-proton scattering, with the assumption that the electron-neutrino pair is produced in the quantum transition of a neutron in a proton. Fermi assumed that the Hamiltonian was the scalar product of vector $\bar{p}(x)\gamma_\alpha n(x)$ and vector $\bar{e}(x)\gamma^\alpha \nu(x)$:

$$\mathscr{H}^\beta = G_F \bar{p}(x)\gamma_\alpha n(x)\bar{e}(x)\gamma^\alpha \nu(x) + \text{h.c.}, \tag{1.3}$$

in which the constant $G_F$ has been introduced and $\gamma$ are the Dirac matrices. The Hamiltonian represents the interaction of four fermion fields, as a result the Fermi's constant $G_F \propto M^{-2}$, where

M is the mass in natural units. Nowadays, the $\beta-$decay is known to be mediated by the W boson, while the Fermi theory is considered the low energy limit of such process.

### Neutrinos detection

Bethe and Peierls computed the dimensional connection between the lifetime of a $\beta$-decay and the cross section of its inverse[6], which resulted in a limit of $\sigma < 10^{-44}\text{cm}^2$: a penetrating power of 1000 light years in matter![2] Therefore, since neutrinos are *elusive*, a good idea to detect them is to find a very strong source. Physicists Clyde Cowan and Fred Reines performed an experiment in close proximity to the Savannah River nuclear reactor, in which a large flux of antineutrinos is expected to be generated[7]. In fact, during nuclear fission many neutrons are created, which decay emitting electron antineutrinos:

$$n \to p^+ + e^- + \bar{\nu}_e \tag{1.4}$$

The experimental apparatus consisted in a container filled with 200 L of water and $CaCl_3$ in order to exploit the inverse reaction:

$$p + \bar{\nu}_e \to n + e^+ \tag{1.5}$$

with the creation of a neutron and a positron. This reaction is endothermic, so the missing energy has to be carried in the system by an incoming neutrino. The energy required has to be grater than 1.8 MeV in the center of mass reference system, since

$$\Delta E = \Delta m c^2 = \left[(m_\nu + m_p) - (m_n + m_e)\right] c^2 \simeq -1.8\text{MeV} \tag{1.6}$$

The positron in water annihilates with an electron after forming a binary system called positronium, which emits mainly two photons at energy of 0.511 MeV. The neutron is absorbed by Cadmium, which reaches an excited state and successively emits a photon. Therefore, the signal fingerprint consists of two photons with same energy in coincidence and one delayed photon at much larger energy. What made the experiment possible was the employment of an innovative medium which can be (i) scalable, (ii) assembled in large volumes and (iii) purified from radioactive contaminants: liquid scintillators. The expected signal rate was estimated to be 2 counts per hour, with a much smaller background[8], therefore leading to the discovery of electron antineutrinos. Reines (Cowan passed away) was awarded the Nobel Prize of Physics in 1995.
The idea of a neutrino beam from an *in flight* decay of pions is attributed to Markov. Successively, Fakirov calculated the expected neutrino flux starting from protons collisions on a target producing many particles, including pions. Charged pions are then decaying into:

$$\pi^- \to \mu^- + \bar{\nu} \text{ or } \pi^+ \to \mu^+ + \nu \tag{1.7}$$

In 1962 Lederman, Schwartz and Steinberger produced the first neutrino beam from accelerated protons directed to a fixed target at BNL, introducing the idea of a neutrino beam still used in accelerator neutrino experiments. Thanks to their contribution to neutrino physics, they were awarded the Nobel Prize in 1988. The first proposal for testing the hypothesis of $\nu_\mu = \nu_e$ was made by Pontecorvo in 1959[9]. Indipendently, Schwartz proposed to produce neutrinos from decay in flight of the high-energy pions[10] produced from proton interactions on a target. Preliminary calculations showed that an interaction rate on a 10 t detector on the order of one event per hour was feasible, a result similar to that of Fakirov[2]. The performed experiment consisted in a 15 GeV proton beam directed by magnets into a Berillium target. Secondary particles mainly produced forward were aimed at a detector. Hadrons and muons were absorbed by a 13.5 m Fe shield plus

a paraffin shield for neutrons. The massive detector (10 t) was used for neutrino target and was required to give a $(\pi/\mu)$ and $(\pi/e)$ discrimination. Using a spark chamber, 34 $\mu$ candidates were observed, but no $e$. Hence, the neutrino produced with the muon in the pion decay does not produce electrons [11].
In 1975, the discovery of the third lepton family[12] at Stanford Linear Accelerator Complex hinted to the presence of the third flavor of neutrino, named tau neutrino. Eventually, its discovery was announced by DONUT collaboration in 2000[13], more than 20 years later. The tau neutrinos were produced in the decay of $D_s$ mesons into $\tau$ and $\nu_\tau$ and the consequent decay of $\tau$ to $\nu_\tau$.
A strong evidence on the total number of neutrino families was found at Large Electron-Positron Collider thanks to a measurement of $Z^0$ boson decay[14]. $Z^0$ boson decays to visible and invisible particles including neutrinos, therefore the number of neutrino families directly changes the $Z^0$ boson invisible width decay

$$\Gamma_{inv} = \Gamma_Z - (\Gamma_{had} + \Gamma_{ee} + \Gamma_{\mu\mu} + \Gamma_{\tau\tau}) \tag{1.8}$$

The branching ratio to invisible particles is derived by constraining the sum of the hadronic, leptonic and invisible branching fraction to unity and a summary is reported in figure 1.2. The result on $\Gamma_{inv}$ is compared to SM expectations. Assuming only SM particle as $Z^0$ decay products, $\Gamma_{inv}$ determines the number of light neutrino species $N_\nu$ by using the relation

$$R^0_{inv} = \frac{\Gamma_{inv}}{\Gamma_{ll}} = N_\nu \left(\frac{\Gamma_{\nu\bar{\nu}}}{\Gamma_{ll}}\right)_{SM} \tag{1.9}$$

from which an estimation of $N_\nu = 2.9840 \pm 0.0082$ is obtained, $2\sigma$ away from the integer value 3. This result fixes the number of fermion families with light neutrinos to the observed three.

### 1.1.1 Parity violation in weak processes

In the first part of $20^{th}$ century, parity symmetry was considered a law valid for all interactions. This symmetry states that a process is invariant for a particle under inversion of space coordinates. In 1957, Wu[15] and Lederman[16] published experimental evidence of parity violation, which was a huge milestone towards the description of weak interactions.
The experiment led by Wu aimed to the study of $\beta-$decay of polarized Cobalt nuclei, according to

$$^{60}\text{Co} \rightarrow ^{60}\text{Ni}^* + e^- + \bar{\nu}_e. \tag{1.10}$$

The nuclear spin of Cobalt nuclei was aligned thanks to a Magnetic field and an asymmetry in the direction of the emitted electrons was observed. Once the direction of the Magnetic field was reversed, the electrons were found to be emitted more likely in a direction opposed with respect to the nuclear spin as summarized in figure 1.3. The correlation of nuclear momenta and electron spin is explained by angular momentum conservation. The spin of $^{60}$Co is J=5, the spin of $^{60}$Ni$^*$ is J=4, therefore $J_z$ of the electron and antineutrino system has to be 1. This relation holds only if $\bar{\nu}_e$ is right-handed and $e^-$ is left-handed. The presence of only $\bar{\nu}_{e,R}$ and $e^-_L$ and the absence of their mirror image states is a violation of parity symmetry.

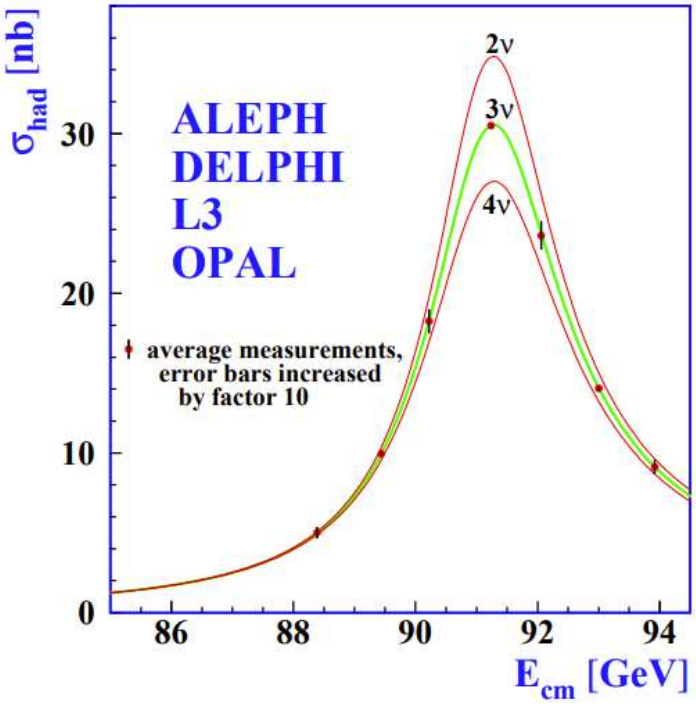


Figure 1.2: Measurements of the hadron production cross-section around the Z resonance and the predicted curves in the case of 2, 3 or 4 neutrino species with SM couplings and negligible mass. SM couplings and negligible mass[14].

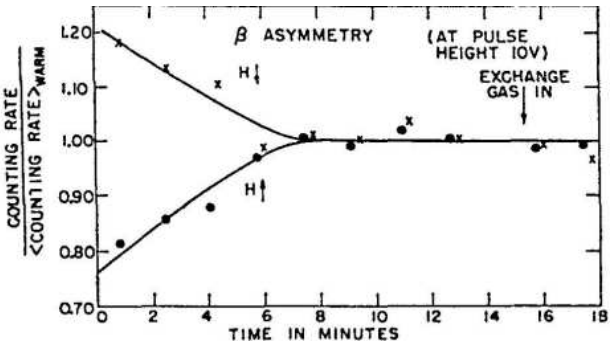


Figure 1.3: The plot shows the electrons emission directions for the two different verses of Magnetic fields. The asymmetry is due to P violation. Graphs from [15].

## 1.2 Neutrinos in the Standard Model

The Standard Model[17] describes the strong, electromagnetic and weak interactions of elementary particles in quantum field theory. It is a gauge theory based on the local symmetry group $SU(3)_C\times$ $SU(2)_L\times$ $U(1)_Y$, where C, L and Y denote color, left-handed chirality and weak hypercharge. For the $SU(3)_C$ groups there are 8 generators $T_a = \frac{\lambda_a}{2}$ in which $\lambda_a$ are the Gell-Mann matrices, corresponding to 8 massless gauge bosons, associated with gluons. $SU(2)_L$ has 3 gauge bosons, the massive $Z^0$ and $W^{\pm}$, while the massless photon $\gamma$ is associated with $U(1)_Y$.
The description of neutrino interactions in the Standard Model Lagrangian is contained in the electroweak part, which considers only the $SU(2)_L \times U(1)_Y$ symmetry group of SM.
Symmetry group $SU(2)_L$ is called *weak isospin*, while the term L refers to the fact that the element of the group acts in a non trivial way only on the left-handed chiral component of the fermion fields. Given a generic spinor field $\psi$, it is always possible to split it into its chiral right-handed and left-handed components $\psi = \psi_R + \psi_L$ with

$$\psi_R = \frac{1+\gamma^5}{2}\psi,\ \psi_L = \frac{1+\gamma^5}{2}\psi. \tag{1.11}$$

$\gamma^5$ is introduced as a product of Dirac $\gamma$ matrices $\gamma^5 = i\gamma^0\gamma^1\gamma^2\gamma^3$[1].

The symmetry group $U(1)_Y$ is called *hypercharge*. It is generated by I operator, linked to $I_3$ and charge operator Q by the Gell-Mann-Nishijima relation

$$Q = I_3 + \frac{Y}{2} \tag{1.12}$$

which implies the unification of weak and electromagnetic interaction[18].
In order to have local gauge invariance, 3 vector gauge boson fields $A_a^\mu$ (a=1,2,3) associated with 3 generators $I_a$ of the group $SU(2)_L$ and 1 vector gauge boson field $B^\mu$ associated with the generator Y of the group $U(1)_Y$ have to be introduced. In the lagrangian, the covariant derivative $D_\mu$ is introduced as

$$D_\mu = \partial_\mu + ig\underline{A}_\mu \cdot \underline{I} + ig' B_\mu \frac{Y}{2} \tag{1.13}$$

where $\underline{A}_\mu = (A_1^\mu, A_2^\mu, A_3^\mu)$, $\underline{I} = (I_1, I_2, I_3)$ and $\underline{A}_\mu \cdot \underline{I}$ is their scalar product. Equation 1.13 contains two independent coupling constants $g$ and $g'$ associated with groups $SU(2)_L$ and $U(1)_Y$.
Considering the whole $SU(2)_L \times U(1)_{(Y)}$ gauge symmetry, left-handed chiral components of the fermion fields are grouped into weak isospin doublets, for example for the first generation:

$$L_L = \begin{pmatrix} \nu_{eL} \\ e_L \end{pmatrix},\ Q_L = \begin{pmatrix} u_L \\ d_L \end{pmatrix}$$

[1] In Dirac representation, $\gamma^0 = \begin{pmatrix} 1 & 0 & 0 & 0 \\ 0 & 1 & 0 & 0 \\ 0 & 0 & -1 & 0 \\ 0 & 0 & 0 & -1 \end{pmatrix}, \gamma^1 = \begin{pmatrix} 0 & 0 & 0 & 1 \\ 0 & 0 & 1 & 0 \\ 0 & -1 & 0 & 0 \\ -1 & 0 & 0 & 0 \end{pmatrix}, \gamma^2 = \begin{pmatrix} 0 & 0 & 0 & -i \\ 0 & 0 & i & 0 \\ 0 & i & 0 & 0 \\ -i & 0 & 0 & 0 \end{pmatrix}, \gamma^3 = \begin{pmatrix} 0 & 0 & 1 & 0 \\ 0 & 0 & 0 & -1 \\ -1 & 0 & 0 & 0 \\ 0 & 1 & 0 & 0 \end{pmatrix}$. It follows that $\gamma^5 = \begin{pmatrix} 0 & 0 & 1 & 0 \\ 0 & 0 & 0 & 1 \\ 1 & 0 & 0 & 0 \\ 0 & 1 & 0 & 0 \end{pmatrix}$

and from the representation choice it follows that the generators of $\mathrm{SU}(2)_L$ are $I_a = \frac{\tau_a}{2}$ [2]:

$$\underline{\mathrm{I}} L_L = \frac{\tau}{2} L_L \; \underline{\mathrm{I}} Q_L = \frac{\tau}{2} Q_L \tag{1.14}$$

while for $\mathrm{U}(1)_Y$, according to Gell-Mann-Nishijima relation1.12:

$$Y L_L = -L_L \; Y Q_L = \frac{1}{3} Q_L \tag{1.15}$$

meaning that the hypercharge of left-handed lepton and quarks doublets is respectively equal to $Y = -1$ and $Y = \frac{1}{3}$.
The right-handed components of charged leptons and quarks are singlets under the weak isospin group of transformations, such that:

$$\underline{\mathrm{I}} f_R = 0 \tag{1.16}$$

while for $\mathrm{U}(1)_Y$:

$$Y e_R = -2 e_R \; Y u_R = \frac{4}{3} u_R \; Y d_R = -\frac{2}{3} d_R \tag{1.17}$$

and according to Gell-Mann-Nishijima relation the hypercharge of $e_R$,$u_R$ and $d_R$ is $Y = -2, \frac{4}{3}, -\frac{2}{3}$.
For neutrinos fields, in the Standard Model it is assumed that they have only left-handed components since there is no evidence of right-handed ones.
The elements of $g$ of the group of local $\mathrm{SU}(2)_\mathrm{L} \times \mathrm{U}(1)_{(\mathrm{Y})}$ transformations are parametrized with a set of 3+1 parameters $(\underline{\theta}(x), \eta(x))$ which depends on space-time x, with unitary representation of $g(\underline{\theta}(x), \eta(x))$ on the vector space of fields

$$U(\underline{\theta}(x), \eta(x)) = e^{i\underline{\theta}(x)\cdot\underline{\mathrm{I}} + i\eta(x)\frac{Y}{2}} = U(\underline{\theta}(x)) U(\eta(x)) \tag{1.18}$$

where we have defined:

$$U(\underline{\theta}(x)) = e^{i\underline{\theta}(x)\cdot\underline{\mathrm{I}}} \; U(\eta(x)) = e^{i\eta(x)\frac{Y}{2}} \tag{1.19}$$

The transformation of left-handed fermions doublet under $g(\underline{\theta}(x), \eta(x))$ is:

$$L_L \to L'_L = U(\underline{\theta}(x), \eta(x)) L_L = U^l_L(\underline{\theta}(x), \eta(x)) L_L \tag{1.20}$$

$$Q_L \to Q'_L = U(\underline{\theta}(x), \eta(x)) Q_L = U^q_L(\underline{\theta}(x), \eta(x)) Q_L \tag{1.21}$$

in which

$$U^l_L(\underline{\theta}(x), \eta(x)) = e^{\frac{1}{2}\underline{\theta}(x)\cdot\underline{\tau} - \frac{1}{2}\eta(x)}$$

$$U^q_L(\underline{\theta}(x), \eta(x)) = e^{\frac{1}{2}\underline{\theta}(x)\cdot\underline{\tau} + \frac{1}{6}\eta(x)}$$

For the right-handed components of fermion fields, the application of the same transformation gives as a result:

$$f_R \to f'_R = U(\underline{\theta}(x), \eta(x)) f_R = U^f_R(\eta(x)) f_R \tag{1.22}$$

[2] The Pauli matrices $\tau_a$ are: $\tau_1 = \begin{pmatrix} 0 & 1 \\ 1 & 0 \end{pmatrix}$, $\tau_2 = \begin{pmatrix} 0 & -i \\ i & 0 \end{pmatrix}$ and $\tau_3 = \begin{pmatrix} 1 & 0 \\ 0 & -1 \end{pmatrix}$

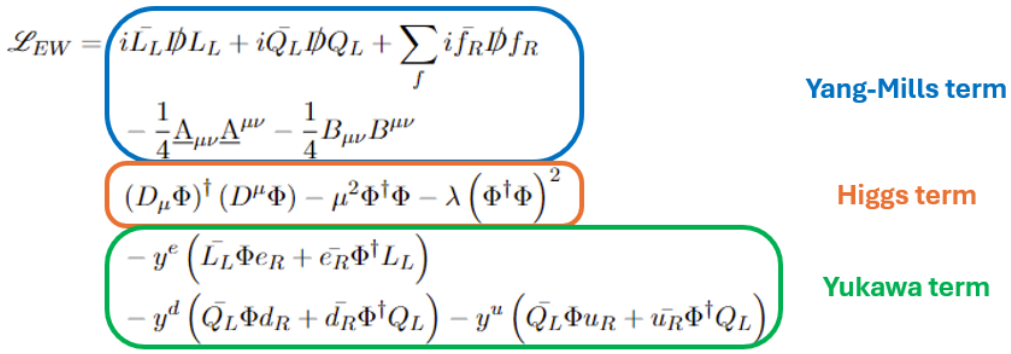


Figure 1.4: Electroweak Lagrangian density for one generation of fermions, in which the terms are arranged by interaction.

where as anticipated:

$$U_R^e(\eta(x)) = e^{-i\eta(x)}$$
$$U_R^u(\eta(x)) = e^{\frac{2}{3}i\eta(x)}$$
$$U_R^d(\eta(x)) = e^{-\frac{1}{3}i\eta(x)}$$

For the first generation of fermions, the electroweak Lagrangian terms are expressed by the equation in figure 1.4, in which (i) the second line contain kinetic terms and self-coupling gauge bosons; (ii) the third line refers to Higgs field, while (iii) third and fourth lines contain the Yukawa couplings that generate lepton masses.

### The Higgs mechanism

In the SM, the masses of the gauge bosons and of the fermions are generated through the Higgs mechanism[19], implemented by the Higgs doublet

$$\Phi(x) = \begin{pmatrix} \phi^\dagger(x) \\ \phi^0(x) \end{pmatrix} \tag{1.23}$$

where $\phi^\dagger(x)$ is a charged complex scalar field and $\phi^0(x)$ is a neutral complex scalar field. The transformation of the Higgs doublet under an element of $g(\underline{\theta}, \eta(x))$ of the gauge group $\mathrm{SU}(2)_L \times \mathrm{U}(1)_Y$ is

$$\Phi \to \Phi' = U(\underline{\theta}(x), \eta(x)) = e^{\frac{1}{2}\underline{\theta}\cdot\underline{\tau} + \frac{1}{2}\eta(x)}\Phi \tag{1.24}$$

The Higgs part of the Lagrangian is given by

$$\mathscr{L}_{Higgs} = (D_\mu\Phi)^\dagger (D^\mu\Phi) - \mu^2\Phi^\dagger\Phi - \lambda\left(\Phi^\dagger\Phi\right)^2 \tag{1.25}$$

which is invariant under a gauge transformation $g(\underline{\theta}(x), \eta(x))$. Equation 1.25 contains a quartic term for Higgs self-coupling with coefficient $\lambda$, that has to be positive in order to have a potential

$$V(\Phi) = \mu^2\Phi^\dagger\Phi + \lambda\left(\Phi^\dagger\Phi\right)^2 \tag{1.26}$$

bounded from below. On the contrary, the squared mass-like coefficient $\mu^2$ is assumed to be negative in order to realize the spontaneous symmetry breaking:

$$SU(2)_L \times U(1)_Y \to U(1)_Q \tag{1.27}$$

where $\mathrm{U}(1)_Q$ is the gauge symmetry group of the electromagnetic interaction associated with the conservation of the electric charge. Defining the new parameter $v$ as

$$v := \sqrt{-\frac{\mu^2}{\lambda}} \tag{1.28}$$

and neglecting the constant term $\frac{v^4}{4}$, the Higgs potential can be rewritten as

$$V(\Phi) = \lambda \left( \Phi^\dagger \Phi - \frac{v^2}{2} \right)^2 \tag{1.29}$$

with a minimum value given by the relation

$$\Phi^\dagger \Phi = \frac{v^2}{2} \tag{1.30}$$

In quantum field theory, the minimum of the potential corresponds to the vacuum, which is the lowest energy state. In vacuum, fermions and vector scalar bosons that carry a nonzero spin must have a zero value in order to preserve the invariance of Nature under spatial rotation. Furthermore, charged scalar fields must have also zero value in vacuum, which is electrically neutral. The requirement does not extend to neutral scalar fields that are not electrically charged, which can present a value different from zero. This value is called *vacuum expectation value* (VEV) $\langle \Phi \rangle$, which for Higgs fields is obtained from 1.30 and has a solution

$$\langle \Phi \rangle = \frac{1}{\sqrt{2}} \begin{pmatrix} 0 \\ v \end{pmatrix} \tag{1.31}$$

that spontaneously breaks the symmetry $\mathrm{SU}(2)_L \times \mathrm{U}(1)_Y$:

$$I_1\langle \Phi \rangle \neq 0,\ I_2\langle \Phi \rangle \neq 0,\ I_3\langle \Phi \rangle \neq 0,\ Y\langle \Phi \rangle \neq 0 \tag{1.32}$$

but

$$Q\langle \Phi \rangle = \left( I_3 + \frac{Y}{2} \right) = \frac{1}{\sqrt{2}} \begin{pmatrix} 1 & 0 \\ 0 & 0 \end{pmatrix} \begin{pmatrix} 0 \\ v \end{pmatrix} = 0 \tag{1.33}$$

Therefore, the vacuum is invariant under gauge transformations belonging to the group $\mathrm{U}(1)_Q$ of the type $e^{i\theta Q}\langle \Phi \rangle = \langle \Phi \rangle$. This invariance guarantees the existence of a massless gauge boson associated with $\mathrm{U}(1)_Q$, which is the photon. The symmetry is broken by the vacuum and consequently by the physical states which are obtained by excitations of the fields above vacuum.

**Towards fermion masses**

In the Standard Model, the mass of fermions arises as a result of the Higgs mechanism through the presence of Yukawa couplings of the fermion fields with Higgs doublet[18].
A fermion mass term has to involve a coupling of a left-handed and right-handed fields. Hence, in the SM neutrinos are massless because their fields do not have a right-handed component. Considering

charged leptons, the products $\bar{L'_{\alpha L}}\ell'_{\beta R}$, with $\alpha, \beta = e, \mu, \tau$ are isospin doublets with hypercharge Y=-1. The Higgs doublet has hypercharge Y=+1, therefore the Higgs-lepton Yukawa Lagrangian

$$\mathscr{L}_{H,L} = -\sum_{\alpha,\beta=e,\mu,\tau} Y'^{\ell}_{\alpha\beta}\bar{L'_{\alpha L}}\Phi\ell'_{\beta R} + \text{h.c.} \tag{1.34}$$

is invariant under the transformation $g(\underline{\theta}(x), \eta(x)) \in \mathrm{SU(2)}_L \times \mathrm{U(1)}_Y$. The matrix $Y'^{e}$ of Yukawa couplings is a complex 3x3 matrix. Introducing the *unitary gauge* in which the physical states of theory appear explicitly, the Higgs doublet can be expressed as

$$\Phi(x) = \frac{1}{\sqrt{2}}\begin{pmatrix} 0 \\ v + H(x) \end{pmatrix} \tag{1.35}$$

in which $H(x)$ is a real scalar field and describes the physical Higgs boson and the density Lagrangian 1.34 becomes

$$\mathscr{L}_{H,L} = -\left(\frac{v+H}{\sqrt{2}}\right)\sum_{\alpha,\beta=e,\mu,\tau} Y'^{\ell}_{\alpha\beta}\ell'_{\alpha L}\bar{\ell'}_{\beta R} + \text{h.c.} \tag{1.36}$$

The term proportional to $v$ is a mass term for charged fermions, while the term proportional to the Higgs boson field $H$ represents a trilinear coupling between the charged leptons and the Higgs boson.
In order to find lepton fields with definite masses, it is necessary to diagonalize the matrix $Y'^{e}$. By defining the arrays of charged lepton fields, the Higgs-lepton Yukawa density Lagrangian becomes

$$\mathscr{L}_{H,L} = -\left(\frac{v+H}{\sqrt{2}}\right)\bar{\ell'_L}Y'^{\ell}\ell'_R + \text{h.c.} \tag{1.37}$$

in which the matrix $Y'^{\ell}$ can be diagonalized into the matrix $Y^{\ell}$ through the biunitarity transformation $V^{\ell\dagger}_{L}Y'^{\ell}V^{\ell}_{R} = Y^{\ell}$. Consequently, the diagonalization leads to

$$\mathscr{L}_{H,L} = -\sum_{\alpha=e,\mu,\tau}\frac{y^{\ell}_{\alpha}v}{\sqrt{2}}\bar{\ell}_{\alpha}\ell_{\alpha} - \sum_{\alpha=e,\mu,\tau}\frac{y^{\ell}_{\alpha}}{\sqrt{2}}\bar{\ell}_{\alpha}\ell_{\alpha}H \tag{1.38}$$

in which $\ell_\alpha$ are the fields of the charged leptons with definite masses. The first term of the right-hand side is the mass term for charged leptons, defined as

$$m_\alpha = \frac{y^{\ell}_{\alpha}v}{\sqrt{2}} \tag{1.39}$$

In the SM, parameters $y^{\ell}_{\alpha}$ are not predicted, so the charged lepton masses have to be measured. From the second term on the equation, it derives that the trilinear coupling between charged leptons and the Higgs boson are proportional to the charged lepton masses as expressed in

$$-\sum_{\alpha=e,\mu,\tau}\frac{m_\alpha}{v}\bar{\ell}_{\alpha}\ell_{\alpha}H. \tag{1.40}$$

In SM, neutrinos cannot couple to the Higgs boson since there is no $\nu_R$ term, therefore in SM are predicted to be massless. However, experimental results proved the phenomenon of neutrino oscillation, which is an indirect way to demonstrate that neutrinos do have mass and an extension of the SM is required.

### 1.2.1 Neutrino masses

The introduction of neutrino masses in the SM has been one of the most important topics in high energy physics. In this paragraph, two cases are presented depending on the nature of neutrinos, which might be Dirac or Majorana particles.

#### Dirac masses

The simplest extension of the SM to include non-zero neutrino masses is to introduce right-handed neutrinos singlets of $\mathrm{SU}(2)_L \times \mathrm{U}(1)_Y$, in order to obtain a coupling with the Higgs boson as for the other particles. Right-handed neutrinos are singlets, neutral fields and from Gell-Mann-Nishijima relation it derives that they have hypercharge Y=0. Therefore, they are not sensitive to any of the SM forces and referred to *sterile neutrinos* and they interact only through gravitation. It is important to notice that the number of sterile neutrinos is not constrained by theory and the introduction of three right-handed neutrinos is not the minimal extension to the SM, for example the presence of only one right-handed neutrino field cannot be excluded.
In a similar way with respect to charged leptons, it is possible to derive a mass term for neutrinos thanks to the spontaneous symmetry breaking and a coupling to the Higgs field, extending the Higgs-Yukawa interaction to the expression:

$$\mathscr{L}_{H,L} = -\sum_{\alpha=e,\mu,\tau} \frac{y_\alpha^\ell v}{\sqrt{2}} \bar{\ell_\alpha} \ell_\alpha - \sum_{\alpha=e,\mu,\tau} \frac{y_\alpha^\ell}{\sqrt{2}} \bar{\ell_\alpha} \ell_\alpha H - \sum_{k=1}^{3} \frac{y_k^\nu v}{\sqrt{2}} \bar{\nu_k} \nu_k - \sum_{k=1}^{3} \frac{y_k^\nu}{\sqrt{2}} \bar{\nu_k} \nu_k H \tag{1.41}$$

in which neutrino masses are proportional to vacuum expectation value and eigenvalues of Yukawa matrix as for charged leptons

$$m_k = \frac{h_k^\nu}{\sqrt{2}} \tag{1.42}$$

with coupling to Higgs boson analogous to 1.40. As a conclusion, neutrino masses are obtained using the same mechanism for charged leptons and quarks, however neutrinos are several orders of magnitude lighter than other particles.

#### Majorana masses

A second way to introduce neutrino masses is to consider neutrinos as Majorana particles, by imposing the Majorana condition

$$\psi = \psi^C := C\bar{\psi}^T \tag{1.43}$$

where C is the charge conjugate operator, in which the right and left handed components of the spinor field are not independent[20]. In other words, if a neutrino is a Majorana particle, it has to be its own antiparticle. This statement means that only neutral fermions can be described by a Majorana field since charged particles and antiparticles have charge with opposed sign. Among the elementary particles in the SM, only neutrinos can be Majorana particles.
In order to find a Majorana mass term using $\nu_L$ alone, it is necessary to find a right-handed function of $\nu_L$ which transforms as $\nu_L$ under Lorentz transformation and can be substituted in place of $\nu_R$ in the Dirac mass term of neutrino field

$$\mathscr{L}_{mass}^D = -m\nu\bar{\nu} = -m\bar{\nu_R}\nu_L + \text{h.c.} \tag{1.44}$$

which is given by the charge conjugated field $\nu_L^C = C\bar{\nu_L}^T$, since it can be proved that it transform as $\nu_L$ under Lorentz transformation and $\nu_L^C$ is right-handed. The Majorana mass term can be expressed as

$$\mathscr{L}_{mass}^{M} = -\frac{1}{2} m \bar{\nu_L^C} \nu_L + \text{h.c.} \tag{1.45}$$

Dirac and Majorana descriptions of neutrinos acquire different phenomenological consequences only if neutrino are massive particles, therefore in practice a way to distinguish between Dirac or Majorana neutrinos is to measure an observable related to neutrino masses. This mass effect cannot be of kinematical origin, since this term is equal for the two hypotheses.

## 1.3 Neutrino Oscillations

Neutrino oscillations are a quantum mechanical phenomenon in which a neutrino created with a specific flavor, defined by the associated emitted lepton, is found at a later time as a neutrino with a different flavor. Neutrino oscillations are historically the first evidence of neutrino mass and lepton number violation. In this section, an overview of neutrino oscillations in vacuum and trough matter is presented.

### 1.3.1 Neutrino oscillations in vacuum

Neutrino oscillations were proposed by Pontecorvo as neutrino-antineutrino oscillations[21], in analogy with the $K^0 \rightarrow \bar{K}^0$ oscillations. At the time only $\nu_e$ were known, but since the discovery of $\nu_\mu$ in 1962, Maki, Nakagawa and Saki[22] proposed a model in which the oscillation between *active* neutrino flavors was present. Since neutrinos are proven to be massive, the flavor and the mass eigenstates do not coincide in analogy with the quark sector. In the standard theory of neutrino oscillations[23], the flavor states $|\nu_\alpha\rangle$ are superpositions of mass eigenstates $|\nu_k\rangle$:

$$|\nu_\alpha\rangle = \sum_{k=1}^{3} U_{\alpha k}^{*} |\nu_k\rangle \tag{1.46}$$

where $U_{\alpha k}^{*}$ are terms of the unitary mixing matrix. The neutrino massive states are eigenstates of the Hamiltonian

$$\mathscr{H}|\nu_k\rangle = E_k|\nu_k\rangle \tag{1.47}$$

with energy eigenvalues

$$E_k = \sqrt{\vec{p}^2 + m_k^2}. \tag{1.48}$$

Ths Schrödinger equation is

$$i\frac{d}{dt}|\nu_k(t)\rangle = \mathscr{H}|\nu_k(t)\rangle \tag{1.49}$$

meaning that massive neutrinos evolve in time as plane waves according to

$$|\nu_k(t)\rangle = e^{-iE_k t}|\nu_k\rangle. \tag{1.50}$$

In the case of a neutrino created with a specific flavor $\alpha$ at time t=0, it is possible to derive its time evolution $|\nu_\alpha(t)\rangle$ as

$$|\nu_\alpha(t)\rangle = \sum_k U_{\alpha k}^{*} e^{-iE_k t}|\nu_k\rangle. \tag{1.51}$$

Now, considering the unitarity of the matrix U, from $U^\dagger U = \mathbb{I} \iff \sum_\alpha U^*_{\alpha k} U_{\alpha j} = \delta_{jk}$ it follows that

$$|\nu_k\rangle = \sum_\alpha U_{\alpha k} |\nu_\alpha\rangle \tag{1.52}$$

and eventually

$$|\nu_\alpha(t)\rangle = \sum_{\beta=e,\mu,\tau} \left( \sum_k U^*_{\alpha k} e^{-iE_k t} U_{\beta k} \right) |\nu_\beta\rangle. \tag{1.53}$$

After the creation of a neutrino of flavor $\alpha$ at time t=0, $|\nu_\alpha(t)\rangle$ is a superposition of different states if the mixing matrix U is not diagonal. From equation 1.53, it is possible to compute the probability of finding the neutrino in a different flavor $\beta$ after a time interval t. The transisition probability is defines as

$$P_{\nu_\alpha \to \nu_\beta}(t) = |A_{\nu_\alpha \to \nu_\beta}|^2 = \sum_{k,j} U^*_{\alpha k} U_{\beta k} U_{\alpha j} U^*_{\beta j} e^{-i(E_k - E_j)t}. \tag{1.54}$$

In the case of ultra-relativistic neutrinos, the energy can be approximated as

$$E_k \simeq E + \frac{m_k^2}{2E}, \tag{1.55}$$

therefore the exponential term in 1.60 can be approximated, giving as a result

$$P_{\nu_\alpha \to \nu_\beta}(t) = \sum_{k,j} U^*_{\alpha k} U_{\beta k} U_{\alpha j} U^*_{\beta j} \exp\left( -i \frac{\Delta m^2_{kj}}{2E} t \right). \tag{1.56}$$

The transition probability depends on the ratio between the difference of the square of neutrino mass eigenvalues over the energy of the neutrino. In neutrino experiments, the detector is located at a distance L from a neutrino source. Since ultra-relativistic neutrinos travel almost at the speed of light, it is possible to approximate t=L/c that in natural units give the relation

$$P_{\nu_\alpha \to \nu_\beta}(L, E) = \sum_{k,j} U^*_{\alpha k} U_{\beta k} U_{\alpha j} U^*_{\beta j} \exp\left( -i \Delta m^2_{kj} \frac{L}{2E} \right). \tag{1.57}$$

For neutrino oscillation experiments, expression 1.57 shows that the distance from the source needs to be carefully chosen, depending on the neutrino energy E. In the case of man-made neutrinos, also the neutrino energy can be chosen in order to modify the phase of the exponential

$$\phi_{kj} = -\frac{\Delta m^2_{kj} L}{2E}, \tag{1.58}$$

which depends also on the physical constant $\Delta m^2_{kj}$. Hence, equation 1.57 means that neutrino oscillation experiment are able to probe the term of the mixing matrix U and $\Delta m^2_{kj}$, which is a proof that neutrino are massive, but it is not possible to measure directly the values of neutrino masses. It might be useful to rewrite relation 1.57 by separating the real and imaginary part of the mixing matrix U, so the expression for oscillation probability becomes

$$P_{\nu_\alpha \to \nu_\beta}(L, E) = \delta_{\alpha\beta} - 4 \sum_{k>j} \mathscr{R}\left[ U^*_{\alpha k} U_{\beta k} U_{\alpha j} U^*_{\beta j} \right] \sin^2\left( \frac{\Delta m^2_{kj} L}{4E} \right) + \sum_{k>j} \mathscr{I}\left[ U^*_{\alpha k} U_{\beta k} U_{\alpha j} U^*_{\beta j} \right] \sin\left( \frac{\Delta m^2_{kj} L}{2E} \right). \tag{1.59}$$

As a convention, the oscillation probabilities in which $\beta \neq \alpha$ are different are called *transition probabilities*, while if $\beta = \alpha$ they are called *survival probabilities*.
For antineutrinos, the coefficients of the massive neutrinos components of flavor antineutrinos are related to the corresponding coefficients of the massive neutrino components of flavor neutrinos by complex conjugation. By deriving the oscillation probabilities analogously to the neutrino case, the expression is given by

$$P_{\bar{\nu_\alpha}\to\bar{\nu_\beta}}(L,E) = \delta_{\alpha\beta} - 4\sum_{k>j} \mathscr{R}\left[U^*_{\alpha k}U_{\beta k}U_{\alpha j}U^*_{\beta j}\right]\sin^2\left(\frac{\Delta m^2_{kj}L}{4E}\right) - \sum_{k>j}\mathscr{I}\left[U^*_{\alpha k}U_{\beta k}U_{\alpha j}U^*_{\beta j}\right]\sin\left(\frac{\Delta m^2_{kj}L}{2E}\right) \tag{1.60}$$

which differs from 1.59 by the sign of the term containing the imaginary part of the quartic product $U^*_{\alpha k}U_{\beta k}U_{\alpha j}U^*_{\beta j}$.

### 1.3.2 Two neutrino mixing

As described in previous sections 3 family of neutrinos are known, however most of neutrino oscillation experiments are not sensitive to the effects of three-neutrino mixing. Therefore, a two flavor neutrino mixing is a sensible effective model to describe experimental data and it is simpler to understand.
Considering the first two families $\nu_e$ and $\nu_\mu$, the two flavor neutrino states are linear superpositions of the two massive neutrinos $\nu_1$ and $\nu_2$ with coefficients given by a 2x2 unitary mixing matrix U:

$$\begin{pmatrix} \cos\theta & \sin\theta \\ -\sin\theta & \cos\theta \end{pmatrix} \tag{1.61}$$

in which a mixing angle $\theta \in \left[0, \frac{\pi}{2}\right]$ is defined. In a two flavor case, there is only one difference of squared masses $\Delta m^2 = m_2^2 - m_1^2$, in which $m_1$ is chosen to be the lightest as convention, in order to obtain $\Delta m^2 > 0$.
Formulas for survival and transition probabilities are derived from a simplified version of equations 1.60. For transition probability ($\alpha \neq \beta$)

$$P_{\nu_\alpha\to\nu_\beta}(L,E) = \sin^2 2\theta \sin^2\left(\frac{\Delta m^2 L}{4E}\right) \tag{1.62}$$

while the survival probability

$$P_{\nu_\alpha\to\nu_\alpha}(L,E) = 1 - P_{\nu_\alpha\to\nu_\beta}(L,E) = 1 - \sin^2 2\theta \sin^2\left(\frac{\Delta m^2 L}{4E}\right). \tag{1.63}$$

Since in both equations 1.62 and 1.63 the dependence on angle $\theta$ is expressed as a function of $\sin^2 2\theta$, there is symmetry under exchange of $\theta$ with $\frac{\pi}{2} - \theta$, which are both allowed in the domain given for $\theta$. The two possibilities correspond to two different mixing conditions: (i) if $\theta < \frac{\pi}{4}$, then $\nu_e$ is composed more of $\nu_1$ than $\nu_2$, otherwise for (ii) $\theta > \frac{\pi}{4}$ $\nu_e$ is composed more of $\nu_2$.
A useful way to write 1.58 in practical cases for neutrino oscillation experiments from reactors or accelerators, where $E_\nu$ is in the range of MeV to few GeV, is

$$\phi = 1.27\frac{\Delta m^2\left[eV^2\right] L\,[km]}{E\,[GeV]}. \tag{1.64}$$

Defining the oscillation length as

$$L_{osc} = 2.47 \frac{E\,[GeV]}{\Delta m^2\,[eV^2]} km, \tag{1.65}$$

that ranges from few hundreds of meters up to thousand kilometers of accelerator neutrinos experiments. If the baseline L is much shorter than $L_{osc}$, the transition probability 1.62 is very small, while for L much larger than $L_{osc}$ the transition probability changes very quickly.

**Generalization to three flavors mixing**

When three neutrino flavors are considered, the mixing matrix becomes a 3x3 unitary matrix. An arbitrary NxN matrix has $2N^2$ independent elements, while a unitarity NxN matrix depends on $N^2$ real parameters. They can be divided into (i) $\frac{N(N-1)}{2}$ mixing angles and (ii) $\frac{N(N+1)}{2}$ phases. For N=3, the total number of parameters is given by 3 mixing angles and 6 phases. However, not every phase is a physical observable, because the only physical effect of the mixing matrix occurs through its presence in the weak charged current. Hence, the total number of phases that can be eliminated is 2N-1= 5 for N=3, which derives from the fact that a rephasing of fields leaves the lepton charged current invariant. As a summary, the total number of physical parameters for a 3 flavor mixing matrix is

$$\begin{cases} \frac{N(N-1)}{2} = 3 \text{ mixing angles} \\ \frac{N(N+1)}{2} - (2N-1) = 1 \text{ physical phase.} \end{cases} \tag{1.66}$$

Neutrino oscillations are described by the Pontecorvo-Maki-Nakagawa-Sakata matrix (PMNS) which can be parametrized as

$$U = \begin{pmatrix} 1 & 0 & 0 \\ 0 & c_{23} & s_{23} \\ 0 & -s_{23} & c_{23} \end{pmatrix} \begin{pmatrix} c_{13} & 0 & s_{13}e^{-i\delta_{CP}} \\ 0 & 1 & 0 \\ -s_{13}e^{i\delta_{CP}} & 0 & c_{13} \end{pmatrix} \begin{pmatrix} c_{12} & s_{12} & 0 \\ -s_{12} & c_{12} & 0 \\ 0 & 0 & 1 \end{pmatrix} \tag{1.67}$$

in which the abbreviations $c_{jk} = \cos\theta_{jk}$ and $s_{jk} = \sin\theta_{jk}$ have been introduced. In 1.67, $\theta_{12}$, $\theta_{13}$ and $\theta_{23}$ are the mixing angles and without loss of generality they can be taken in the in the first quadrant $\theta_{jk} \in \left[0, \frac{\pi}{2}\right]$, while $\delta_{CP}$ is the phase related to charge-parity violations and it can assume any value in the domain $[0, 2\pi]$. The given description of the neutrino mixing assumes that neutrinos are Dirac particles, however as already discussed they could be Majorana particles. If neutrinos are Majorana particles, the PMNS matrix is parametrized by three mixing angles and three phases according to

$$U = U_{Dirac} P_{Majorana} \tag{1.68}$$

where

$$P_{Majorana} = \begin{pmatrix} e^{i\alpha_1} & 0 & 0 \\ 0 & e^{i\alpha_2} & 0 \\ 0 & 0 & 1 \end{pmatrix}. \tag{1.69}$$

Oscillation probabilities do not depend on these two additional phases, so oscillation experiments cannot provide information on the nature of neutrinos.

### 1.3.3 Mass ordering

In equation 1.59, the difference of squared masses for the three neutrinos mass eigenstates. PMNS mixing matrix relates the neutrino mass eigenstates $k = 1, 2, 3$ to the flavor eigenstates $\alpha = e, \mu, \tau$,

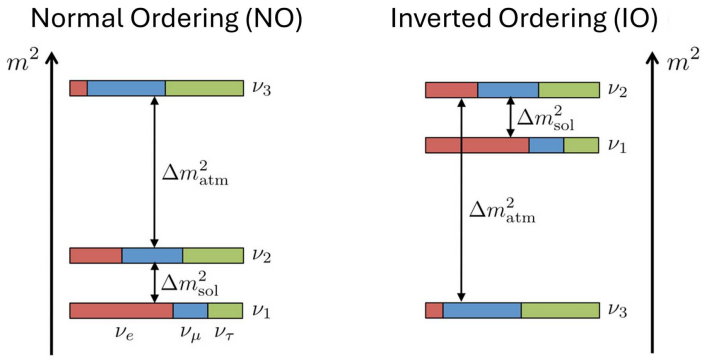


Figure 1.5: Neutrinos mass eigenstates and their composition in neutrino flavor eigenstates (red $\nu_e$, blue $\nu_\mu$, green $\nu_\tau$) for normal (NO) and inverted ordering (IO).

according to

$$|\nu_\alpha\rangle = \sum_{k=1}^{3} U_{\alpha k}|\nu_k\rangle. \tag{1.70}$$

Since there are three eigenstates, three squared mass differences might be defined: $\Delta m^2_{21}$, $\Delta m^2_{31}$, $\Delta m^2_{32}$, however only two of them are independent since $\Delta m^2_{21} + \Delta m^2_{31} + \Delta m^2_{32} = 0$. Experimental results, which will be presented later, proved the $\Delta m^2_{atm}$ related to atmospheric neutrino oscillations is much larger than $\Delta m^2_{sol}$ related to solar neutrino oscillations $\Delta m^2_{atm} \gg \Delta m^2_{sol}$. Solar neutrinos allow us to fix the sign of $\Delta m^2_{21}$ (i.e., the 1-2 mass hierarchy). The sign determines the resonance channel (neutrino or antineutrino) and the mixing in matter[24]. Therefore, the open question regards the determination of the mass eigenstate 3, where two options are possible: (i) $m_3 \gg m_1$ or the opposite (ii) $m_3 \ll m_1$. A visual representation of the mass ordering scheme is reported in figure 1.5.

### 1.3.4 Charge-Parity (CP) violation in neutrino oscillation

The PMNS matrix shows a dependence on the $\delta_{CP}$ parameter, which is called *charge-parity violating phase* since it might affect the neutrino and antineutrino oscillations in a different way. The charge conjugation parity (CP) symmetry states that the laws of Physics should be the same if a phenomenon applied to a given particle is the same if the particle is exchanged with its own antiparticle and its spatial coordinates are inverted. Since $\delta_{CP}$ appears only as a complex parameter, it can be probed only by measurements sensitive to that part of the PMNS matrix. In equation 1.60, in the case of a disappearance channel then $\alpha = \beta$, as a result $\mathscr{I}\left[U^*_{\alpha k}U_{\beta k}U_{\alpha j}U^*_{\beta j}\right] = 0$. Hence, CP symmetry can be investigated only through an appearance channel. From equation 1.60 applied to the case of $\bar{\nu_\alpha} \to \bar{\nu_\beta}$, the corresponding transition probability is obtained by substituting U with U$^*$. In this case, the term containing the imaginary part changes its sign and the the quantity $\Delta P_{\alpha\beta} := P(\nu_\alpha - \nu_\beta) - P(\bar{\nu_\alpha} - \bar{\nu_\beta})$ is given by

$$\Delta P_{\alpha\beta} = \pm 16 J \sin\left(\frac{\Delta m^2_{21} L}{4E}\right) \sin\left(\frac{\Delta m^2_{31} L}{4E}\right) \sin\left(\frac{\Delta m^2_{32} L}{4E}\right) \tag{1.71}$$

where $J$ is the Jarkslog invariant[25]

$$J = c_{12}s_{12}c_{23}s_{23}c_{13}^2 s_{13}\sin\delta_{CP} \tag{1.72}$$

which contains the dependence of $\Delta P_{\alpha\beta}$ from the *charge-parity violating phase*. A violation of CP in the leptonic sector of SM can be observed only if all the PMNS mixing angles and mass splitting are different from 0 and also $\delta_{CP} \neq \{0, \pi\}$.

### 1.3.5 Neutrino oscillations in matter

Neutrinos traveling through matter can interact with particles present along their path, with the possibility to modify their propagation. Neutrinos can interact through weak Charged Current (CC) or Neutral Current (NC) interactions. A NC interaction has the same amplitude for all neutrino flavors and cannot be observed on flavor oscillations since it will change an immeasurable phase in all neutrino states. On the other hand, a CC interaction involves only $\nu_e$, since atoms are made of electrons and do not contain any other lepton. In this way, the oscillation probability differs from the vacuum case and it is known as Mikheyev-Smirnov-Wolfenstein (MSW) effect[26][27].
For an electron neutrino propagating in an homogeneous and isotropic gas of unpolarized electrons, the evolution of the system is described by the Schrödinger equation as in 1.49 with the difference that the hamiltonian is composed by a kinetic energy part $H_0$ and a matter potential V

$$i\frac{d}{dt}|\nu(t)\rangle = \mathscr{H}|\nu(t)\rangle,\ \mathscr{H} = \mathscr{H} + V \tag{1.73}$$

The potential V can be divided into two contributions depending on CC or NC interactions. The potential due to CC interactions is given by the relation $V_{CC} = \pm\sqrt{2}G_F n_e$, in which $n_e$ is the number density of electrons in the medium, while the sign of the potential is related to the neutrino or antineutrino case. The potential due to NC interactions is equal for every neutrino flavor and it is $V_{NC} = -\frac{\sqrt{2}}{2}n_n$, where $n_n$ is the neutron number density.

#### Two flavor mixing

Considering the two flavor basis in which $\alpha = e, \mu$, the effective Hamiltonian assume the form

$$\mathscr{H}_M = \frac{\Delta m^2}{4E}\begin{pmatrix} -\cos 2\theta_V & \sin 2\theta_V \\ \sin 2\theta_V & \cos 2\theta_V \end{pmatrix} + V_{CC}\begin{pmatrix} 1 & 0 \\ 0 & 0 \end{pmatrix}. \tag{1.74}$$

When neutrinos propagate in matter, the probability of an incoherent inelastic scattering is very small. For example, the characteristic cross section for $\nu$-proton scattering is of the order [28] of

$$\sigma_{\nu p}(E) \simeq \frac{G_F^2 s}{\pi} \simeq 10^{-43}\mathrm{cm}^2\left(\frac{E}{\mathrm{MeV}}\right)^2, \tag{1.75}$$

where $G_F$ is the Fermi constant and $s$ is the square of the center of mass energy of the collision. In a dense medium, like the core of our Sun, neutrinos are much more likely to interact coherently. The characteristic value of potential at Earth core is $V_{CC} \simeq 10^{-13}$eV, while at the solar core is equal to $V_{CC} \simeq 10^{-12}$eV. In addition, the density of the medium may change along neutrino paths, changing the conditions of the system.
In a two flavor framework, the local eigenvalues of H are $\frac{\mu_i(x)^2}{2E}$, in which $\mu_i(x)$ are the instantaneous

effective neutrino masses given by

$$\mu_{1,2}^2 = \frac{m_1^2 + m_2^2}{2} + E\left[V_\alpha + V_\beta\right] \mp \frac{1}{2}\sqrt{\left[\Delta m^2 \cos 2\theta - A\right]^2 + \left[\Delta m^2 \sin 2\theta\right]^2}, \tag{1.76}$$

in which the local mixing angle $\theta_V$ is equal to

$$\tan 2\theta_V = \frac{\Delta m^2 \sin 2\theta}{\Delta m^2 \cos 2\theta - A} \tag{1.77}$$

where $\theta$ is the mixing angle in vacuum and the relation $A = 2E\left(V_\alpha - V_\beta\right)$ has been introduced. The sign of A depends on the composition of the medium and on the flavour composition of the neutrino state considered. For a given sign of A, the mixing angle could be larger or smaller than in vacuum if $\theta$ is in the first or second octant. The degeneracy found for $\theta = \frac{\pi}{4}$ in vacuum is broken by the matter potential for neutrino propagating in a medium. From equation 1.77, a special case is obtained when A is close to $\Delta m^2 \cos 2\theta$, that is called *resonant condition* $A_R = \Delta m^2 \cos 2\theta$.
If neutrinos are created in a region where the potential satisfies the condition $A_0 > A_R$, then $sgn\left(\cos 2\theta_{m,0}\right) = -sgn\left(\cos 2\theta\right)$. Hence, the flavor component of the mass eigenstates is inverted with respect to the vacuum case. Asymptotically, if $A_0 \gg A_R$ then $\theta_{0,m} \to \frac{\pi}{2}$. This means that if in vacuum the lightest (heaviest) mass eigenstate has a larger projection of $\alpha$ ($\beta$) flavor eigenstate, then in a medium in which $A > A_R$ holds the opposite is expected. In a region in which the medium density is changing monotonically, there is a point in which $A = A_R$ and the dominant flavor component of a mass eigenstate changes. If the density changes slow enough, the instantaneous mass eigenstates $\nu_i^m$ can be considered as energy eigenstates and they do not mix in the evolution and this is called *adiabatic* transition approximation.

### The Mikheyev-Smirnov-Wolfenstein Effect for solar neutrinos

The two neutrinos oscillation in matter is useful to describe what happens when neutrinos are created in the Sun. The nuclear reactions at play in the Sun produce only electron neutrinos. Inside the Sun, let's consider the propagation in the two neutrinos case $\nu_e$ and $\nu_X$, in which $\nu_X$ is a general superposition of $\nu_\mu$ and $\nu_\tau$ since in matter there is no preference for any of the two flavors and they are involved equally in NC interactions.
The density of solar matter is monotonically decreasing as a function of the distance $R$ from the centre. For $R < 0.9R_\odot$ the following approximation for density holds:

$$n_e(R) = n_e(0)e^{-\frac{R}{r_0}} \tag{1.78}$$

in which $r_0 = \frac{R_\odot}{10.54} = 6.6 \times 10^7$ m. With the characteristic matter density of the Sun and considering the typical energy of solar neutrinos, the requirement $A_R = \Delta m^2 \cos 2\theta$ is fulfilled if $\frac{\Delta m^2}{E} \gg L_{Sun-Earth}$, meaning that the matter effect is negligible

$$P_{ee}\left(\Delta m^2 \cos 2\theta \gg A_0\right) = 1 - \frac{1}{2}\sin^2 2\theta > \frac{1}{2} \tag{1.79}$$

If the relevant matter potential at production is only slightly below the resonant value, i.e. $A_R \simeq \Delta m^2 \cos 2\theta$, then neutrinos do not cross the resonance point but the matter effect is strong enough

to modify the oscillations as in

$$P_{ee}\left(\Delta m^2 \cos 2\theta \geq A_0\right) = \frac{1}{2}\left(1 + \cos 2\theta_{m,0} \cos 2\theta\right) \tag{1.80}$$

in which $P_{ee}$ is still larger than $\frac{1}{2}$. In the last case, in which $A_R = \Delta m^2 \cos 2\theta < A_0$, neutrinos can cross a resonance while moving towards the outer region of the Sun. As presented earlier, if $\nu_e$ is composed mainly by $\nu_1$ in vacuum, then at the production point $\nu_e$ is a combination of $\nu_1^m$ and $\nu_2^m$ with larger $\nu_2^m$ component. Furthermore, if the density at the production point is such that $A_R A_0$ then $\theta_{m,0} = \frac{\pi}{2} \implies \cos 2\theta_{m,0} = -1$ and $\nu_e$ is composed only by $\nu_2^m$. In this case, on the Earth the survival probability for electron neutrinos is given by

$$P_{ee}\left(\Delta m^2 \cos 2\theta < A_0\right) = \frac{1}{2}\left(1 + \cos 2\theta_{m,0} \cos 2\theta\right) = \sin^2\theta, \tag{1.81}$$

therefore $P_{ee}$ may assume values smaller than $\frac{1}{2}$. This phenomenon is called Mikheyev-Smirnov-Wolfestein (MSW) effect.

## 1.4 Overview on neutrino oscillation experiments

Neutrino oscillations have been studied by several experiments using different technologies and neutrino sources. Due to neutrinos small cross section as shown in equation 1.75, a powerful source and a large detector are needed. Experiments are classified according to the source of neutrinos, for example: (i) the Sun, (ii) the atmosphere, or man-made from (iii) accelerators and (iv) nuclear reactors. A fundamental requirement to the study of neutrino oscillations is a good modelization of the neutrino source.

**Solar neutrinos**

In the $20^{th}$ century, a model for the energy production in the Sun was under development, leading to the so-called Standard Solar Model (SSM), a term coined by Bahcall and collaborators[29][30]. In the Sun, the main energy generator is the fusion of Hydrogen to Helium, the so called *pp chain*:

$$\begin{aligned} &{}^1\mathrm{H} + {}^1\mathrm{H} \rightarrow {}^2\mathrm{H} + e^+ + \nu_e \\ &{}^2\mathrm{H} + {}^1\mathrm{H} \rightarrow {}^3\mathrm{He} + \gamma \\ &{}^3\mathrm{He} + {}^3\mathrm{He} \rightarrow {}^4\mathrm{He} + {}^1\mathrm{H} + {}^1\mathrm{H}. \end{aligned}$$

The whole process leads to the fusion of four protons into a $^4$He nucleus, which contains also a weak process, where an $\nu_e$ is produced. The energy released in such process is equal to $Q = 4m_p - m_{^4He} - 2m_e \simeq 26$ MeV. The largest part of the energy is radiated through photons, while a small fraction is carried by neutrinos $\langle E_{2\nu}\rangle = 0.59$ MeV, which escape from the centre of the Sun without any absorption. The synthesis of other heavier nuclei is possible in other cycles (e.g. CNO) and in these case the electron neutrinos are produced at different energies, as reported in figure 1.7. Pontecorvo realized that since neutrinos have a very small cross section, they can be used as a probe to inspect the interior of our star. Therefore, in 1960s the quest for solar neutrinos started. The Homestake experiment located in South Dakota and led by Davis was focused on the search of this kind of neutrinos, named *solar neutrinos*. The detector was based on the chlorine-argon reaction suggested by Pontecorvo

$$^{37}\mathrm{Cl} + \nu_e \rightarrow e^- + {}^{37}\mathrm{Ar} \tag{1.82}$$

which is sensitive in the energy region in which neutrinos produced by $^8$B are dominant. The nucleus $^{37}$Ar is unstable, the rate of its decay provides the measure of the incoming solar neutrino flux. The amount of $^{37}$Ar created was about 1 atom every 2 days, while the Ar atoms were extracted every couple of months. In 1968, the first published results indicate an observed flux much lower than the theoretical expectation[31]. In 1998, the final results obtained by Homestake experiment[32], the average value of solar neutrino rate is

$$2.56 \pm 0.16 \text{ (stat)} \pm 0.16 \text{ (sys) SNU}, \tag{1.83}$$

about a third of the theoretically predicted value of $8.5 \pm 0.9$SNU[33], in which a Solar Neutrino Unit is 1 reaction per $10^{36}$ target atoms per second. The discrepancy was known as solar neutrino problem.

In the following decades, the solar problem was confirmed by experiments based on different technologies: (i) Gallium based GALLEX (and its successor GNO) and SAGE, (ii) water-based Kamiokande and SNO. Gallium-based experiment were expected to contribute to the solution of the solar problem due to their lower energy threshold that allows to detect neutrinos from pp chain. Water-based and radio-chemical experiments present different energy threshold for neutrino detections, since: (i) in water, neutrinos are detected through the elastic scattering on nuclei, (ii) for radio-chemicals the threshold depends on the required energy for the inverse $\beta-$decay. In Gallium, they exploited the reaction $\nu_e + ^{71}\text{Ga} \rightarrow e^- + ^{71}\text{Ge}$ which has an energy threshold of 233 keV and can be used for detecting neutrinos from pp chain. SAGE experiment in Baksan used 50 t of liquid metallic Gallium as a target, while the GALLEX experiment at LNGS used 101 t of $GaCl_3$ corresponding to 30.3 t of Ga. The measured capture rate was $69.3 \pm 4.3 \pm 3.6$ SNU for GALLEX/GNO[34] and $65.4^{+3.1+2.6}_{-3.0-2.8}$ for SAGE[35], about half of the SSM prediction $127.9^{+8.1}_{-8.2}$ SNU[33].

Kamiokande experiment was a 3000 t water-based Cherenkov detector located in Kamioka mine. Its successor Super-Kamiokande started its data taking campaign in 1996 and is still operating. It is based on a 50 kt pure water as target with the addition of Gadolinium in 2020. The two experiments are able to detect solar neutrinos thanks to the electron-neutrino elastic scattering $\nu_x + e^- \rightarrow \nu_x + e^-$, allowed both by NC interaction for every neutrino flavor and by CC interactions for electron neutrinos only. Differently from radiochemical experiments, Kamiokande and Super-Kamiokande are able to detect in real time neutrinos interaction and are able to reconstruct the incoming neutrino direction from the outgoing lepton one. The results from Kamiokande[38] confirmed by Super-Kamiokande[39] were about half of the expected values from SSM. By measuring the direction of the electron hit by the neutrino in the elastic scattering, SK also established that neutrinos were coming from the Sun (the first neutrino telescope)[2].

At that point, the presence of a neutrino solar problem was established. However, it could still depend on a flaw in the solar model or on the *anomalous* behavior of neutrinos. Indeed, the flux of high energy neutrinos were very sensitive to the model parameter, such as the core temperature. In 1995, GALLEX[40] already reached a sufficient precision for excluding the *solar solution* of the problem. Neutrinos observed by the experiment derived from three different contributions: (i) pp-chain, (ii) Boron and (iii) Beryllium reactions. The sum of the first contribution estimation from solar luminosity and the second one from SK measurements were already larger than the total rate from GALLEX. No budget was left for Beryllium neutrinos, however they must have been present since Beryllium is a parent of Boron.

A *nuclear solution* to the problem could have still existed: SSM required as input nuclear cross section at very low energies in the so-called Gamow peak. The values of cross section in such energy

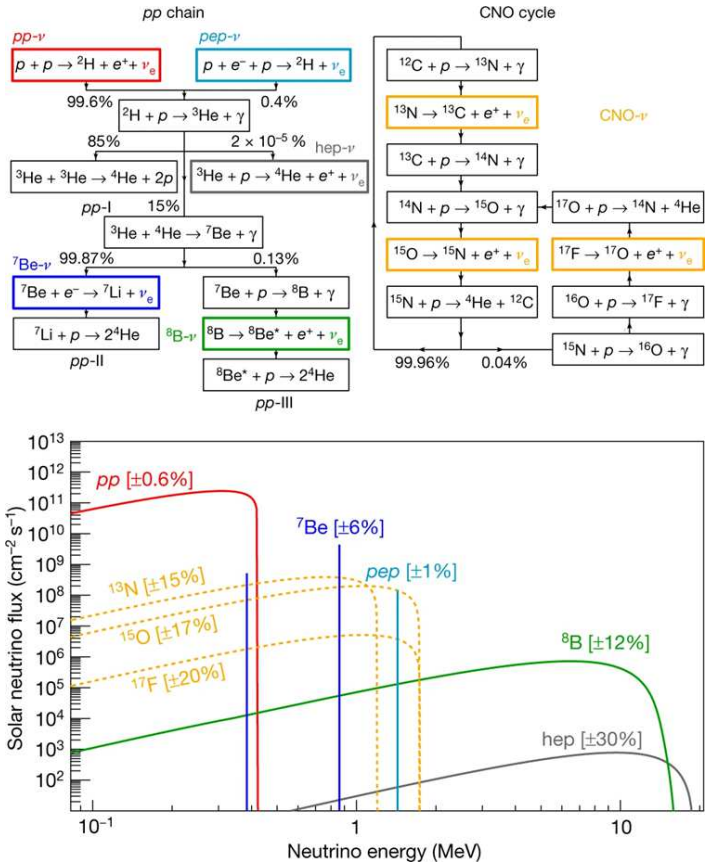


Figure 1.6: Schematic view of the pp and CNO nuclear fusion sequences. The solarneutrino energy spectrum is obtained from http://www.sns.ias.edu/ jnb/, using the updated fluxes taken from [36]. The flux (vertical scale) is given in units of $\mathrm{cm}^{-2}\mathrm{s}^{-1}\mathrm{MeV}^{-1}$ for continuum sources and in $\mathrm{cm}^{-2}\mathrm{s}^{\mathrm{fl1}}$ for monoenergetic sources. Picture from [37].

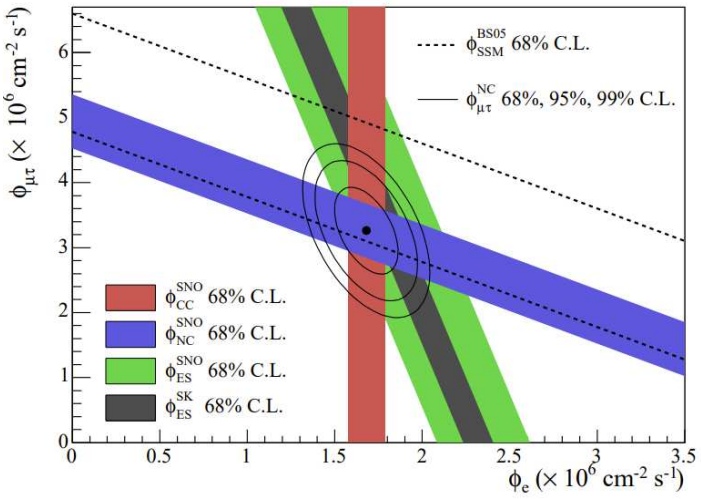


Figure 1.7: Flux of $\nu + \tau$ neutrinos versus flux of electron neutrinos. CC, NC and ES flux measurements are indicated by the filled bands. The total $^8$B solar neutrino flux predicted by the Standard Solar Model[30] is shown as dashed lines, and that measured with the NC channel is shown as the solid band parallel to the model prediction. The narrow band parallel to the SNO ES result correponds to the Super-Kamiokande result in [43]. The intercepts of these bands with the axes represent the $\pm 1\sigma$ uncertainties. The non-zero value of $\phi_{\mu\tau}$ provides strong evidence for neutrino flavor transformation. The point represents $\phi_e$ from the CC flux and $\phi_{\mu\tau}$ from the NC-CC difference with 68%, 95%, and 99% C.L. contours included. Picture from [42].

range was not directly measured, but extrapolated from higher energy measurements. The presence of resonances in this low energy region would not have been considered by such extrapolations. To clarify the issue, a Low energy accelerator facility, the Laboratory for Underground Nuclear Astrophysics (LUNA), was built at LNGS and no resonance was observed[41]. Therefore, since 1998 the neutrino solar problem was attributed to an unexpected neutrino behavior.
The neutrino solar problem was solved thanks to Sudbury Neutrino Observatory (SNO) experiment in Canada, which used 1000 t of heavy water $D_2O$ as a target. Thanks to the presence of deuteron, SNO observed neutrinos produced in the $^8$B stage of CNO cycle through three different reactions at the same time:

$$\nu_e + ^2\mathrm{H} \rightarrow p + p + e^- (CC) \tag{1.84}$$

$$\nu_x + ^2\mathrm{H} \rightarrow p + n + \nu_x (NC) \tag{1.85}$$

$$\nu_x + e^- \rightarrow \nu_x + e^- (ES) \tag{1.86}$$

Charged current interaction 1.84 is sensitive only to the flux of $\Phi(\nu_e)$. Neutral current interaction 1.85 is equally sensitive to every neutrino flavour and therefore they measure the total neutrino flux $\Phi(\nu_e) + \Phi(\nu_\mu) + \Phi(\nu_\tau)$. The electron scattering interaction 1.86 is possible for all neutrino flavours, but it is about 6 times more probable for $\nu_e$ with respect to $\nu_\mu$ and $\nu_\tau$. The first results in 2001 combined with Super-Kamiokande proved directly the presence of a non-$\nu_e$ component in the solar neutrino flux and the measured flux of all the neutrino flavors measured by SNO[42] agrees, within the about 10% uncertainties, with the SSM predictions.
Together with reactor neutrino experiment KamLAND, the solution of solar neutrino problem was found to be the MSW adiabatic flavour transition due to matter in the Sun.
The different components of the solar neutrino spectrum were measured by Borexino experiment at

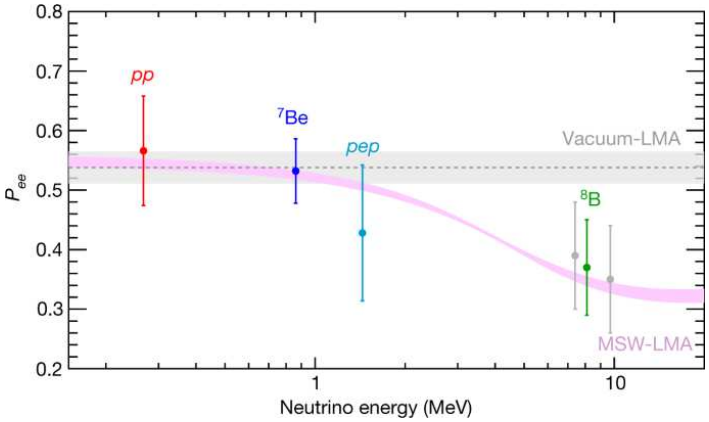


Figure 1.8: The pink band is the $\pm 1\sigma$ prediction of MSW-LMA with oscillation parameters determined from [48]. The grey band is the vacuum-LMA case with oscillation parameters determined from [49][50]. Data points represent the Borexino results for pp (red), $^7$Be (blue), pep (cyan) and $^8$B (green for the HER range, and grey for the separate HER-I and HER-II sub-ranges), assuming HZ-SSM. $^8$B and pp data points are set at the mean energy of neutrinos that produce scattered electrons above the detection threshold. The error bars include experimental and theoretical uncertainties. Picture from [37].

LNGS[44][37][45][46][47]. The experiment was based on a 300 t ultra-pure liquid scintillator target with a energy threshold of 0.19 MeV. The experiment was able to measure the survival probability of solar $\nu_e$ as a function of energy reported in figure 1.8, which helped in the study of MSW effect. The energy of an incoming neutrino was reconstructed by measuring the light emission in the scintillator of the outgoing electron. The results were consistent with the hypothesis of MSM-Large Mixing Angle solution of solar neutrino problem.

### Atmospheric neutrinos problem

A second addition to neutrino puzzle came from the measurement of the rate of neutrinos produced in the atmosphere by the interaction of cosmic rays. Cosmic rays are mainly protons, with a small percentage of heavy nuclei, and present a broad energy distribution. In the interactions with atmospheric nuclei, cosmic rays produce showers. A large amount of these particles are charged pions which decay into muons, which in turn decay into electrons and producing muon and electrons neutrinos called *atmospheric neutrinos*, according to the reactions:

$$\pi^{\pm} \rightarrow \mu^{\pm} + \nu_{\mu}(\bar{\nu_{\mu}})$$
$$\mu^{\pm} \rightarrow e^{\pm} + \bar{\nu_{\mu}}(\nu_{\mu}) + \nu_e(\bar{\nu_e}).$$

For less energetic muons (E $\leq$ 1 GeV) that are allowed to decay before reaching the Earth surface, the ratio of $\nu_{\mu}/\nu_e$ was expected to be close to 2, while at higher energy the ratio is expected to be larger since some muons are not expected to decay before reaching the surface. Atmospheric neutrinos have energies in the hundreds of MeV to few GeV range, where their differential cross sections for CC interactions with nucleons is strongly forward peaked. Therefore, large detectors initially built for the discovery of proton decay were suitable for the real time detection of atmospheric neutrinos. In such experiments, cosmic rays events were studied as a component background of nucleon decay. In addition, the experiments were able to reconstruct the original direction of

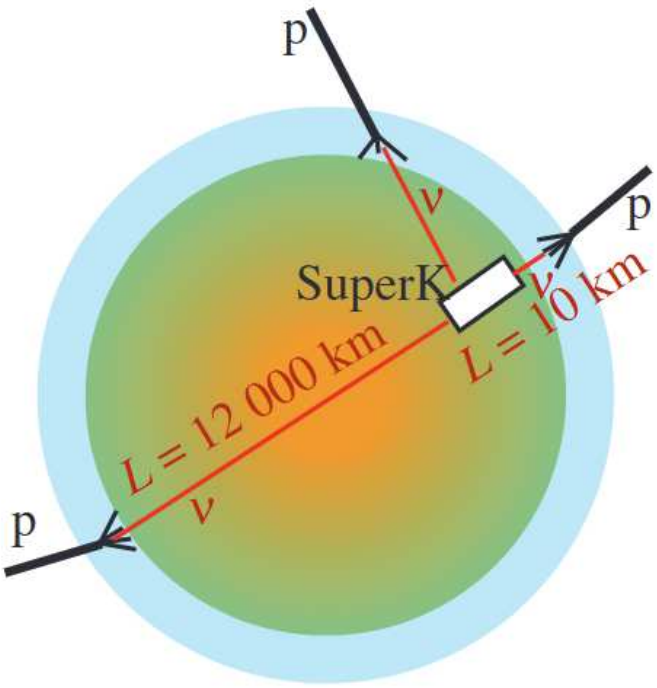


Figure 1.9: Correlation between direction and path length of neutrinos. Picture from [2].

the incoming neutrino. Among these experiments, water-based Kamiokande[51] and IBM[52] found experimental evidence that in this energy region the number of $\nu_e$ and $\nu_\mu$ was similar. On the other hand, experiments NUSEX[53] and Frejus[54] based on fine grained calorimeters were sensitive to higher energy neutrinos and did not find any deficit. This discrepancy between theory and experimental data was called *atmospheric neutrino anomaly*.
A decisive evidence supporting neutrino oscillation was presented by Super-Kamiokande Collaboration in 1998[55]. Super-Kamiokande experiment, still operating, is able to discriminate Cherenkov signals generated by electrons and muons. Electrons generate a *fuzzier* ring due to multiple scattering and showering in water, while for muons the ring is sharper; however SK cannot distinguish between a lepton and its antiparticle. Additionally, it can reconstruct the direction of the interacting neutrinos, expressed in term of angle $\theta$ with respect to the zenith. Depending on $\theta$, the distance traveled by a neutrino might range from 10 km to 10000 km as shown in figure 1.9. In less than 2 years, the Collaboration proved that the flux of $\nu_\mu + \bar{\nu}_\mu$ coming from the opposite side of the Earth (up-going) was smaller than the ones arriving from above the detector (down-going) as reported in figure 1.10, even if the flux of neutrinos was expected to be isotropic. Defining the asymmetry between up-going $-1 \leq \cos\theta \leq -0.2$ (U) and down-going $0.2 \leq \cos\theta \leq 1$ (D) neutrinos as $A = \frac{U-D}{U+D}$, the results for high energy muon neutrinos ($E_{vis} > 1.33$ GeV) indicated that $A = -0.296 \pm 0.048 \pm 0.001$ was more than $6\sigma$ away from 0. In figure 1.10, it is shown that the flux of electron neutrinos has very little dependence on the zenith angle, while muon neutrinos fluxes are significantly different. In the oscillation hypothesis, electron neutrinos travel through Earth without changing their flavor. On the contrary, downgoing muon neutrinos travel for approximately few tens of kilometers, while upgoing muon neutrinos travel for thousands of kilometers oscillating into tau neutrinos since electron neutrino flux is unchanged. Super-Kamiokande results were later on confirmed by experiments MACRO[56] and Soudan2[57] and by experiments based on accelerator

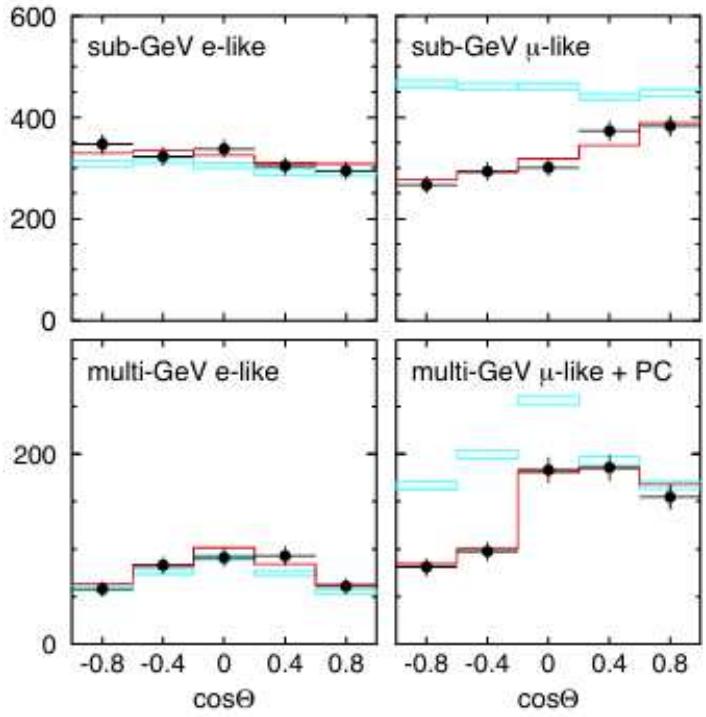


Figure 1.10: Distribution of e-like and $\mu$-like events in Super-Kamiokande as a function of zenith angle. The top two figures refer to events with neutrino energy below 1.33 GeV, while the bottom two represent the case above that energy. Cyan boxes show the expected result in the case of no oscillation, while full drawn lines are the best fit to data in the oscillation hypothesis. Picture from [28], in which it was provided by Super-Kamiokande collaboration.

neutrinos.
A direct proof of $\nu_\mu - \nu_\tau$ oscillation and therefore $\nu_\tau$ appearance signal was searched in atmospheric neutrinos data. However due to high energy threshold given by tau mass and the short lifespan of $\tau$, its observation proved to be challenging. Super-Kamiokande reported evidence of $\nu_\tau$ apperance with a $4.6\sigma$ significance[58]. The observation of $\nu_\tau$ appearance was proved by OPERA experiment located in Gran Sasso which exploited neutrinos from an accelerator located af CERN[59]. Recently, $\nu_\tau$ appearance was reported also by IceCube experiment[60].

**Reactor anti-neutrinos**

Fission reactors are a powerful source of electron anti-neutrinos produced in the $\beta-$decay of neutron rich nuclei. The power of reactors is due to the fission of four isotopes: $^{235}$U, $^{138}$U ($\sim 8\%$), $^{239}$Pu ($\sim 30\%$) , $^{241}$Pu ($\sim 6\%$). On average, each fission produces an energy of 200 MeV with a release of six electron anti-neutrinos. The total number of electron neutrinos is estimated to be $\sim 2 \times 10^{20}$ $s^{-1}$ per $GW_{th}$ of thermal power. Modern fission power plants are equipped with several reactors of around 3 $GW_{th}$ each. Neutrino emission is isotropic, therefore the flux decrease quadratically with the distance, which has to be tuned according to 1.60. The energy of neutrinos emitted in reactors is in the MeV range, requiring a short baseline of few hundreds of meters. Due to their low energy, they are not able to produce $\mu$ or $\tau$ in their interaction with the target, therefore only $\bar{\nu}_e$ disappearance channel can be investigated. In addition, signal from NC interactions of $\bar{\nu}_\mu$ or $\bar{\nu}_\tau$ is too faint to be distinguished from background. Reactor anti-neutrinos experiments are heavily depending on the possibility to modelize and simulate the electron antineutrinos flux characteristics: (i) spectrum, (ii) intensity and (iii) stability in time.
Electron anti-neutrinos are studied thanks to the inverse $\beta-$ decay reaction $\bar{\nu}_e + p \rightarrow e^+ + n$. The energy of the prompt signal from $e^+$ $E_p$ is related to the anti-neutrino energy according to the relation $E_p \sim E_\nu + 0.8$ MeV. The background is suppressed thanks to the delayed coincidence given by $\gamma$ emission from neutron capture on nucleus after thermalization. Usually, a target of liquid scintillator rich in H is used for the inverse $\beta-$decay. Sometimes, in order to increase the neutron detection efficiency, the scintillator is loaded with Gadolinium because of a larger cross section for neutrons and a larger amount of energy emitted: $\sim$8 MeV in Gadolinium compared to 2.2 MeV on Hydrogen target.
In 2002, the first evidence of oscillation of reactor neutrinos was found by KamLAND experiment in Japan. KamLAND consists of a 1 kt liquid scintillator target which receives neutrino from 16 different fission power plants with an average distance of $L_0 \sim$180 km, ranging from 80 km to 800 km. In agreement with the MSW-LMA solution to solar neutrino problem, KamLAND provided an estimation of $\bar{\nu}_e$ disappearance at 99.95% confidence level, since the ratio of measured events with respect to the expected one in no oscillation hypothesis is $0.611 \pm 0.085 \pm 0.041$[61]. The combination of KamLAND and solar neutrino experiments identified the MSW-LMA solution to the solar neutrino problem with a confidence level $> 5\sigma$. In addition, KamLAND experiment measured the survival probability of electron anti-neutrino as a function of the ratio of the effective baseline $L_0$ and their energy reported in figure 1.11, in which a oscillatory behaviour is visible[62].

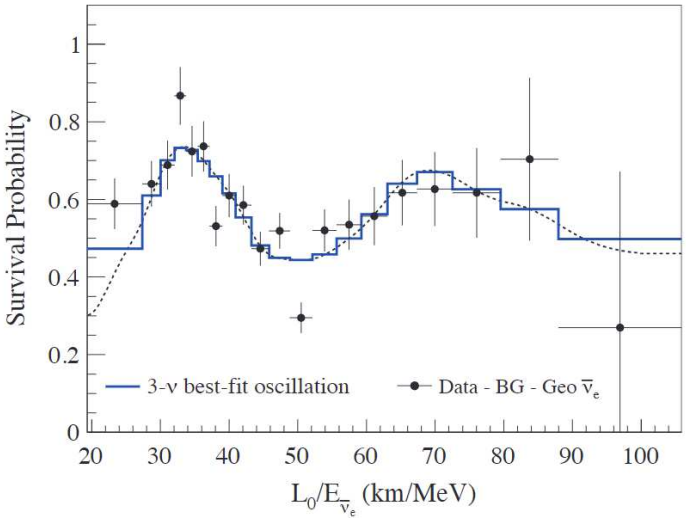


Figure 1.11: Survival probability of $\bar{\nu}_e$ as a function of the ratio $\frac{L_0}{E_{\bar{\nu}_e}}$. The blue histogram is the best $3\nu$ fit from the three-flavor unbinned maximum likelihood with KamLAND data. Picture from [50].

In addition, reactor neutrinos experiments provided important results in the estimation of mixing angle $\theta_{13}$, which requires a much smaller baseline L$\sim$ 1 km in order to be sensitive to $\Delta m^2_{32} \sim 10^{-3}$ eV$^2$ and $\theta_{13}$. Experiments Daya Bay (China), RENO (Korea) and Double Chooz (France) were built with a similar design based on a Gadolinium-doped liquid scintillator target. Daya Bay employs eight detectors to measure anti-neutrino disappearance by three power plants. RENO operates with two detectors placed 290 meters and 1.4 km from the source. Double Chooz also uses two detectors located at 400 m and 1.05 km from the source. The three experiments published their first data in 2012. Daya Bay provided a significance of $5.2\sigma$ for a non-zero value of $\theta_{13}$[63], while RENO showed a significance of $4.9\sigma$[64]. This result enables the search for $\delta_{CP}$ through oscillation experiments, since the Jarkslog invariant 1.72 is not nullified by the mixing angles.

## 1.5 Accelerator neutrinos

High intensity neutrino beams present many advantages with respect to other neutrino sources, such as a high level of control of neutrino flavor at source, flux and energy which are crucial in order to measure with high precision the oscillation parameters.
Accelerator neutrino beams are mostly composed by $\nu_\mu$ produced in the decay of multi-GeV pions. Due to their production on Earth surface, accelerator neutrinos experiments are sensitive only to the energy range in which the oscillation length is within the Earth diameter. Due to the value of $\Delta m^2_{32}$, oscillations are visible for GeV neutrinos if L$\simeq \mathcal{O}$(500 km). Such long baseline is an unfortunate condition, since neutrinos cannot be directly focused by magnets and the transverse size of the flux at the far detector becomes much larger than the detector itself, with the number of neutrinos crossing the detector decreasing as $\propto$ L$^{-2}$. There is a second category of accelerator neutrino experiments named *short baseline*, that studies the possibility of a neutrino oscillations in the $\sim 1$ eV$^2$ scale that necessities a baseline of the order of $\sim 1$ km.
Conventional neutrino beams are created by accelerating protons towards a target, for example made of graphite or beryllium. The interactions produce $\pi$ and K mesons that decay into neutrinos. Since $\pi$ are the most abundant secondary particles, neutrino beams are mainly composed by $\nu_\mu$.

A direct focusing of neutrino beam is not possible, but the charged particles produced in protons interactions can be focused through magnetic devices named horns. In addition, by selecting the polarity of the Magnetic field, it is possible to select positive or negative charged particles, leading to a beam of neutrinos or anti-neutrinos. The study of the interactions between accelerated protons on target is fundamental to understand the neutrino beam composition and energy. Produced neutrinos present a broad energy spectrum, therefore in order to select neutrinos of relevant energy the detectors could be built *off-axis* with respect to beam center. This method is used by T2K and NO$\nu$A experiments.
An additional characteristic of accelerator-based neutrino experiments is the presence of two detectors: (i) a far detector used to study the flux of the oscillated neutrino beam and (ii) a near detector where oscillations are still negligible used to reduce the systematic uncertainties from neutrino flux and neutrino-nucleus interaction. The two detectors might use the same technology (e.g. NO$\nu$A) or different one (e.g. T2K). A crucial topic for the success of accelerator-based neutrino experiments is the understanding of neutrino-nucleus interactions.
Since the very first accelerator-based neutrino experiment in 1962 by Lederman et al., many *long-baseline* and *short-baseline* were built. The first one built in the *long-baseline* category was K2K in 1999, that used 12 GeV protons from KEK facility to Super-Kamiokande with a baseline of 250 km. The near detector complex 300 m away from the production target counted on a 1 kt water Cherenkov detector and a set of fine-grained detectors. K2K results confirmed the $\nu_\mu$ disappearance seen by Super-Kamiokande[65]. Successively, other experiments were built exploiting different detection techniques. One of them is MINOS experiment, which used protons at the energy of 120 GeV and a baseline of 735 km from Fermilab to Soudan mine. MINOS near and far detectors were based on iron-scintillator tracking calorimeters with the use of a toroidal Magnetic field.
The OPERA experiment used a neutrino beam with mean energy of 17 GeV from CNGS neutrino beamline at CERN to LNGS with a baseline of 730 km. The experiment was looking for a direct proof of $\nu_\tau$ appearance using the detection of CC interactions of $\nu_\tau$ with a $\tau$ in the final state. The detector was using an emulsion/lead sandwich target. The experiment detected 10 $\nu_\tau$ candidates over an expected background of 2.0$\pm$0.4, confirming the $\nu_\mu \rightarrow \nu_\tau$ oscillations with a significance of 6.1$\sigma$. After the confirmation of neutrino oscillations, the second generation of accelerator-based neutrino experiments was dedicated to the study of electron neutrino appearance channel and muon neutrino disappearance channel in order to find open questions like (i) mass ordering, (ii) CP violation and (iii) $\theta_{23}$ octant determination. Two experiments belonging in this category are NO$\nu$A[66] and T2K[67].
NO$\nu$A uses the muon neutrino beam produced by the Main Injector of Fermilab (NuMI) with a mean neutrino energy of about 2 GeV. The near and far detectors use the same technology based on liquid scintillator contained in PVC cells that are 6.6 cm $\times$ 3.9 cm in cross section. The near detector is place 1 km away from the production target and its dimension is 3.8 m $\times$ 3.8 m $\times$ 12.8 m for a mass of 290 t followed by a muon range stack. The far detector is 810 km away and is much larger with a volume of 15 m $\times$ 15 m $\times$ 60 m for a mass of 14 kt. NO$\nu$A was designed to search for non-null values of $\theta_{13}$ and the atmospheric parameters $\Delta m^2_{32}$ and $\theta_{23}$. The particularly long baseline plays an important role in the use of matter effect for the determination of mass hierarchy, in fact for long baseline experiments the oscillation probability 1.60 can be approximated according

to

$$P_{\nu_\mu\to\nu_e,(\bar{\nu}_\mu\to\bar{\nu}_e)} \approx 4\sin^2\theta_{13}\sin^2\theta_{23}\frac{\sin^2\Delta(1-A)}{(1-A)^2}$$
$$+8\alpha J_{\mathrm{CP}}^{\max}\cos\left(\Delta\pm\delta_{\mathrm{CP}}\right)\frac{\sin\Delta A}{A}\frac{\sin\Delta(1-A)}{1-A} \quad (1.87)$$
$$+\alpha^2\sin^2 2\theta_{12}\cos^2\theta_{23}\frac{\sin^2 A\Delta}{A^2}$$

in which $\alpha = \frac{\Delta m^2_{21}}{\Delta m^2_{31}}$, $\Delta_{31} = \frac{\Delta m^2_{31} L}{4E}$,

$$A = \frac{2VE}{\Delta m^2_{31}}, \quad (1.88)$$

$$\Delta = \frac{\Delta m^2_{31} L}{4E_\nu} \quad (1.89)$$

and the leading term depends on $\theta_{13}$.
The probability for $\bar{\nu}_\mu \to \bar{\nu}_e$ changes due to $\delta_{CP}$ and A, allowing to look at the same time for CP violation and mass ordering if the effect of the two phenomena on $P(\nu_\mu \to \nu_e)$ and $P(\bar{\nu}_\mu \to \bar{\nu}_e)$ can be decoupled. Matter effect enhances the electron neutrino appearance in case of normal hierarchy (NO) and suppresses it for inverted hierarchy (IO).
The T2K experiment, which will be presented in detail in the next chapter, uses a 30 GeV accelerated proton beam at J-PARC facility to create a $\nu_\mu$ beam. The experiment uses the *off-axis* technique to select a spectrum for neutrinos peaked at 600 MeV. The near detector is located 280 m away from the production source and uses a magnet for charge identification, while the far detector is the water-based Super-Kamiokande 295 km away. In 2011, T2K published its first results by observing an indication of $\nu_\mu \to \nu_e$ appearance with a significance of $2.5\sigma$. The results were confirmed in 2014 with a statistical significance larger than $7\sigma$[68]. In the latest oscillation results published in 2023, T2K measured the neutrino oscillation parameters $\Delta m_{32}$, $\sin^2\theta_{13}$, $\sin^2\theta_{23}$, $\delta_{CP}$ and Jarlskog invariant using the statistics at the far detector equivalent to $3.6 \times 10^{21}$ protons on target (POT)[69] as presented more in detail in the next chapter.
T2K, NO$\nu$A and MINOS+ results are summarized in figure 1.12 along with results from reactor experiments. Among all the experiments, there is a general agreement with T2K providing the strongest constraints on both parameters.

## 1.6 The role of Near Detectors in Long Baseline Neutrino Oscillation (LBNO) Experiments

The impact of Near Detectors (ND) in Neutrino Oscillation experiments is a fundamental topic, described already before the estimation of oscillation parameter angle $\theta_{13}$ as reported in [71]. More recently, focusing on sources related to T2K and Hyper-Kamiokande experiments, the role of a ND is discussed in [72] and [73].

Near detectors are mainly built to: (i) measure the beam flux at the near detector site, which is used to predict the neutrino beam flux at the far detector; (ii) monitor the neutrino beam stability; (iii) measure neutrino cross section and (iv) develop new technology for future neutrino experiments.

The observed rate of neutrino events at ND as a function of the reconstructed neutrino energy

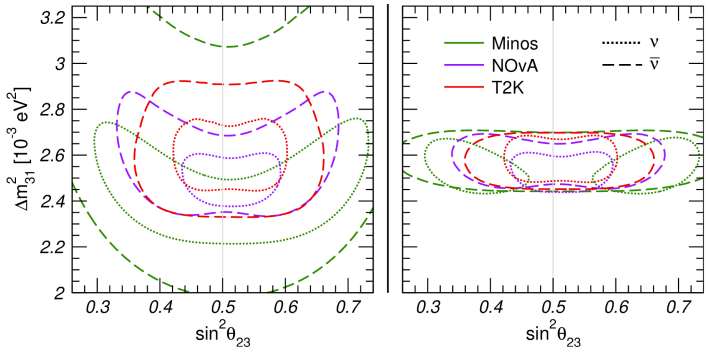


Figure 1.12: Comparison of $2\sigma$ allowed region for T2K (red), NOvA (purple) and MINOS (green) disappearance data assuming Normal Ordering for $\Delta m^2_{32}$ and $\theta_{13}$. The dotted (dashed) lines correspond to neutrino (antineutrino) data. In the left panels a prior on $\theta_{13}$ has been imposed to account for reactor bounds, while in the right panels LBL and reactor data are consistently combined together. In all panels solar and KamLAND data are included to constrain $\Delta m^2_{21}$ and $\theta_{12}$. Picture adapted from [70].

$E'_\nu$ is expressed as

$$N_{ND}(E'_\nu) = \int \Psi_{ND}(E_\nu) \times \sigma(E_\nu) \times \varepsilon_{ND}(E_\nu) \times f_{ND}(E'_\nu, E_\nu) dE_\nu, \tag{1.90}$$

where the following terms are introduced: the neutrino beam flux $\Psi_{ND}(E_\nu)$, the neutrino cross section $\sigma(E_\nu)$, the detection efficiency $\varepsilon_{ND}(E_\nu)$ and the energy response function $f_{ND}(E'_\nu, E_\nu)$ that $E'_\nu$ is measured for as a function of the true neutrino energy $E_\nu$. A similar expression might be used for the far detector, with the fundamental difference due to the introduction of the probability of neutrino oscillation, which depends on $E_\nu$ and on the oscillation parameters:

$$N_{FD}(E'_\nu) = \int P(E_\nu, \theta, \Delta m^2) \times \Psi_{FD}(E_\nu) \times \sigma(E_\nu) \times \varepsilon_{FD}(E_\nu) \times f_{FD}(E'_\nu, E_\nu) dE_\nu. \tag{1.91}$$

Hence, to estimate the oscillation parameters from data, one must model the neutrino (i) flux, (ii) cross-section and (iii) detection efficiency with sufficient precision. The neutrino flux is estimated by hadron production experiments, like NA61/SHINE for T2K. Regarding the total neutrino cross section, near detectors should be capable of measuring the signal and background processes relevant for neutrino oscillation measurements. In fact, neutrino interactions include several channels, which for the design of the experiments might pose as signal or background.
In T2K, the reconstructed neutrino energy is obtained from the lepton kinematics, while the reconstruction efficiencies depend on the hadronic final state as well. Hence, the detector design should be able to sufficiently constrain the modeling of the dependence of lepton kinematics on neutrino energy over the relevant neutrino energy range.
The other two quantities $\varepsilon(E_\nu)$ and $f(E'_\nu, E_\nu)$ depends on the detector design, which should maximize the cancellation of systematic uncertainties when extrapolating from measured event rates in the near detector to predict the event rate at the far detector. In fact, for LBNO experiments, the estimation of neutrino oscillation parameters is based on the observed ratio between far detector $N_{FD}$ and near detector $N_{ND}$. Considering this point of view, a similar detection technology between FD and ND would be optimal, a strategy adopted by NO$\nu$A experiment. However, different technologies for near and far detector might be used if the ND might provide decisive additional

information: in T2K, the FD is a water-based Cherenkov detector, while the ND is magnetized and it provides high tracking performances at the cost of introducing discrepancies between FD and ND systematic uncertainties. The Near and Far detectors of T2K will be described in detail in the next chapter. The next generation of LBNO experiments Hyper-K and DUNE are expected to include more than one ND, in order to exploit the advantages of having a similar design between ND and FD and having a magnetized ND.
As a conclusion, Near Detectors provide crucial information required to reduce the systematic uncertainties at the Far Detector. In particular, near detectors assume a primary importance when such systematical errors are not be negligible with respect to statistical ones, as it would be expected in the next generation of long baseline neutrino experiments where larger active volumes and more powerful beams are expected.

## 1.7 State of the art, open questions and next steps in neutrino oscillation physics

The oscillation neutrinos experiments aim to the estimation of the four mixing parameters $\theta_{12}$, $\theta_{13}$, $\theta_{23}$, $\delta_{CP}$ and the mass splittings $\Delta m^2_{21}$, $\Delta m^2_{31}$ or $\Delta m^2_{32}$ depending on the mass ordering. The best fit results are summarized in the table 1.1. Parameters $\Delta m^2_{21}$ and $\theta_{12}$ are usually called *solar parameters*, since they are estimated by solar neutrinos experiments, but they can also be constrained by reactor experiments. $\Delta m^2_{32}$ and $\theta_{32}$ are known as *atmospheric parameters*, since they are studied by atmospheric neutrinos experiments. $\theta_{13}$ is referred to as *reactor* mixing angle. This nomenclature is also reported in figure 1.5.

In the last decades neutrino physics achieved huge milestones in the discovery of neutrino oscillations and the MSW effect. However some questions still do not have an answer.

- **CP violating phase $\delta_{CP}$:** The phase $\delta_{CP}$ is the only unknown parameter in the PMNS matrix, excluding the Majorana phases. The measurement of $\delta_{CP}$ is the target of the current accelerator neutrinos experiments like T2K and NO$\nu$A, by looking at the possible differences in $\nu_\mu \to \nu_e$ and $\bar{\nu}_\mu \to \bar{\nu}_e$ appearance channels. The updated estimations on $\delta_{CP}$ search are summarized in table 1.1.

- **Neutrino Mass Ordering:** At the moment, we are not able to order the neutrino mass eigenstates from the lightest to the heaviest. In particular, the neutrino mass ordering problem can be summarized in the question $m_1 \sim m_2 < m_3$ for Normal Ordering or $m_1 \sim m_2 > m_3$ for Inverted Ordering, as shown in figure 1.5. This question can be studied by looking at the matter effect in accelerator neutrinos experiments as seen in equation 1.87. The next generation of neutrino experiments will address also this topic.

- **Neutrino mass scales:** Neutrino oscillations experiment can investigate only $\Delta m^2_{ij} = m^2_i - m^2_j$, but they cannot probe the absolute value of each neutrino mass eigenstate. From $\Delta m^2_{ij}$ only a lower bound can be imposed, since $|m_i| \geq \sqrt{m^2_{ij}}$, while there is no upper bound from this kind of experiments. Other kind of experiments can provide this information, for example from the $\beta-$decay spectrum, called *kinematic constraint*. KATRIN experiment did not find any indication for $m_{\nu_e} \neq 0$ yet, but it has provided the most recent result for an upper limit equal to $m^{eff}_{\nu_e} < 0.45$ eV at 90% C.L. [74].

| | Normal | Ordering (**best fit**) | Inverted | Ordering ($\Delta\chi^2 = 9.1$) |
|---|---|---|---|---|
| **Parameter** | **Best fit$\pm 1\sigma$** | **3$\sigma$ range** | **Best fit$\pm 1\sigma$** | **3$\sigma$ range** |
| $\sin^2\theta_{12}/10^{-1}$ | $3.07^{+0.12}_{-0.11}$ | 2.71→3.69 | $3.07^{+0.12}_{-0.11}$ | 2.71→3.69 |
| $\theta_{12}/^\circ$ | $33.67^{+0.73}_{-0.71}$ | 31.61→35.94 | $33.67^{+0.73}_{-0.71}$ | 31.61→35.94 |
| $\sin^2\theta_{23}/10^{-1}$ | $4.54^{+0.19}_{-0.16}$ | 4.11→6.06 | $5.68^{+0.16}_{-0.21}$ | 4.12→6.11 |
| $\theta_{23}/^\circ$ | $42.3^{+1.1}_{-0.9}$ | 39.9 →51.4 | $48.9^{+0.9}_{-1.2}$ | 39.9 →51.4 |
| $\sin^2\theta_{13}/10^{-2}$ | $2.224^{+0.056}_{-0.057}$ | 2.047-2.397 | $2.222^{+0.069}_{-0.057}$ | 2.049-2.420 |
| $\theta_{13}/^\circ$ | $8.58^{+0.11}_{-0.11}$ | 8.23→8.91 | $8.57^{+0.13}_{-0.11}$ | 8.23→8.95 |
| $\delta_{CP}/^\circ$ | $232^{+39}_{-25}$ | 128→359 | $273^{+24}_{-26}$ | 195→342 |
| $\Delta m^2_{21}/10^{-5}$ eV$^2$ | $7.41^{+0.21}_{-0.20}$ | 6.81→8.03 | $7.41^{+0.21}_{-0.20}$ | 6.81→8.03 |
| $\Delta m^2_3/10^{-3}$ eV$^2$ | $2.505^{+0.024}_{-0.026}$ | 2.426→2.586 | $-2.487^{+0.027}_{-0.024}$ | -2.566→-2.407 |

Table 1.1: Results of the global $3\nu$ oscillation analysis, in terms of best-fit values and allowed 1 and $3\sigma$ ranges for the $3\nu$ mass-mixing parameters. The CP violating phase is taken in the (cyclic) interval $\delta_{CP} \in [0, 360]^\circ$, while the mixing angles are defined in the interval $\theta_{ij} \in [0, 90]^\circ$. Estimations are shown for both normal ordering (NO) and inverted ordering (IO). Note that $\Delta m^2_3 = \Delta m^2_{31} > 0$ for NO and $\Delta m^2_3 = \Delta m^2_{32} < 0$ for IO as visible also in 1.5. Table adapted from [28].

- **Octant of $\theta_{23}$ mixing parameter:** The octant of angle $\theta_{23}$ is still unknown, which translates into asking if $\theta_{23} < 45^\circ$ or $\theta_{23} > 45^\circ$. This question can be studied by reactor and accelerators neutrino experiments. The topic is important since it would allow to understand if the mass state $m_3$ contains more $\nu_\mu$ or $\nu_\tau$.

In particular, the search for CP violation in the leptonic sector might be linked with the baryon number asymmetry in the Universe, which is mainly formed by matter while antimatter is just a small fraction. The conditions which could have generated this asymmetry were expressed by Sakharov[75] and are known as *Sakharov conditions*:

- C and CP symmetries violation;
- Baryon number violation;
- Interactions out of thermal equilibrium.

The matter-antimatter imbalance, at a level of few particles per $10^{10}$ photons[76], is responsible for the matter present in the known Universe. The actual amount of CP violation observed in the baryonic sector of the SM is not enough to explain the matter-antimatter imbalance[77]. An

additional mechanism would rely on leptonic CP violation in a mechanism called leptogenesis[78]. In models introduced to explain the observed neutrino masses, hypothetical heavy partners to neutrinos would have been copiously present in the early Universe and subsequently decayed. In the presence of CP violation, these decays could have generated the observed matter-antimatter asymmetry[79].

### 1.7.1 Next generation of neutrino oscillation experiments

The answer to the questions still present in neutrino physics will be the focus of the next generation neutrino experiments. In this section I will briefly describe the reactor neutrino experiment JUNO in China and the next generation of accelerator neutrino experiments Hyper-Kamiokande in Japan and DUNE in the USA.

**Long Baseline Neutrino experiments**

- **DUNE** The Deep Underground Neutrino Experiment (DUNE) is based on a neutrino beam provided by the new LBNF neutrino facility at Fermilab[80]. The complex is expected to deliver 1.2 MW for 120 GeV protons[81]. The experiment will have the far detector 1300 km away from Fermilab and located 1.5 km underground at the Sanford Underground Research Facility (SURF) in South Dakota. The far detector will be equipped with a large liquid argon time projection chamber (LArTPC) with a total mass of almost 70 kt reached in two Phases: (i) Phase I is expected to use 2 LArTPCs of 17 kt each (20 kt total fiducial volume) and 1.2 MW beam, while in Phase II a total amount of 4 modules are expected (4×17 kt, 40 kt fiducial volume) and a beam power larger than 2 MW[82]. The liquid Argon technology provides the tool to perform a image-like reconstruction of neutrino interactions. A near detector will be placed 574 m away from the absorber, in order to characterize the intensity and the wide spectrum of the neutrino beam. The main goals of DUNE are (i) a sensitivity to CP violation better than $3\sigma$ over 75% domain of $\delta_{CP}$, (ii) neutrino mass ordering thanks to mass effect due to the long baseline, (iii) the search for supernova neutrino bursts, (iv) proton decay and (v) other physics Beyond the Standard Model. The far detector can also be used to study atmospheric neutrinos and the near detector is suitable for the study of neutrino-nucleus cross section.

- **Hyper-Kamiokande** The design of Hyper-Kamiokande[73] is a cylindrical tank with a diameter of 74 m and height of 60 m. The detector uses pure water as a target with a total mass of 258 kt, with a fiducial mass of 187 kt equal to eight time the Super-Kamiokande's fiducial mass. The detector will be placed on a different mine with respect to Super-Kamiokande, but at the same distance L = 295 km and at the same off-axis angle (2.5°). The near detector will be the same of T2K phase II, which will be presented in the next chapter, equipped with a Magnetic field for charge reconstruction. The J-PARC facility is expected to provide a beam of 30 GeV protons with a power of 1.3 MW. The main physical goals of Hyper-Kamiokande are similar to the ones expected by DUNE: (i) CP violation using both atmospheric neutrinos at the far detector and neutrino beams with a statistical significance at $3\sigma(5\sigma)$ for 76%(57%) of $\delta_{CP}$ parameters space; (ii) astrophysical neutrino observations for example from the Sun and the Supernovas, (iii) proton decay searches.

DUNE and Hyper-Kamiokande rely on different target technologies, baselines and neutrino energy spectra with a factor 5 of difference between the two experiments. For this reason, the two experi-

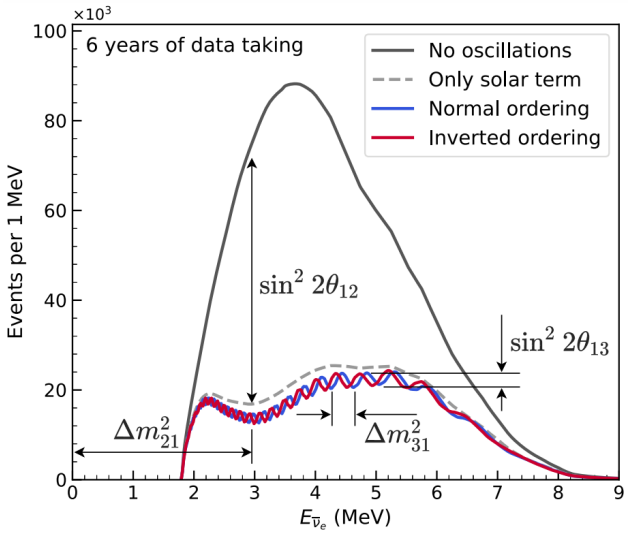


Figure 1.13: JUNO reactor anti-neutrino energy spectrum after 6 years of data taking under the assumption of no oscillations (black line) or oscillations: (i) modulation depending only on $\sin^2 2\theta_{12}$ (gray dashed line), (ii) full oscillation in vacuum for NO (blue line) and (iii) full oscillation in vacuum for IO (red line). The lines are drawn under the assumption of perfect energy resolution. Picture from [83].

ments can be considered as complementary. For example, the shorter baseline in Hyper-Kamiokande is such that the matter effect is less prevalent than DUNE, hence the latter is more sensitive to the mass ordering determination. For the same reason, Hyper-Kamiokande should be more sensitive to the measurement of CP-violating phase in combination with external inputs for mass ordering, for example from the next generation experiment JUNO. The expected statistical significance for CP violation for Hyper-Kamiokande is presented in the next chapter.

### JUNO

The Jiangmen Underground Neutrino Observatory (JUNO)[83] is a multi-purpose neutrino experiment located in China. It is placed 52.5 km away from two nuclear power plants with a total thermal power of 26.6 $GW_{th}$ in a 700 m deep site. The detector is filled with 20 kt of an ultra-pure liquid scintillator. The scintillation light is readout by 17612 20-inch PMTs and 25600 3-inch PMTs, with an expected energy resolution of 3% at 1 MeV. The main goal of the experiment is to determine the neutrino mass ordering by reconstructing the energy spectrum of the reactor electron anti-neutrino. Such baseline is chosen to minimize the $\bar{\nu}_e$ survival probability. In this condition, the "slow solar oscillations" cause the global minimum, while "fast atmospheric oscillations" cause the superimposed ripples. The absolute sign of $\Delta m^2_{31}$ causes a shift in the position of the ripples in the neutrino spectrum different for NO and IO. JUNO is expected to distinguish between the two scenarios and therefore arriving to the solution of one of the neutrino open questions at $3\sigma$.

# Chapter 2

# The T2K Experiment

The Tokai-to-Kamioka (T2K) experiment is a long baseline neutrino experiment located in Japan. T2K uses a muon neutrino or antineutrino beam generated at J-PARC facility in Tokai, which is directed towards the near detector complex ND280 and the far detector Super-Kamiokande 295 km away in Kamioka mine, as summarized in picture 2.2.

The peculiar characteristic of T2K experiment among the long baseline neutrino experiments

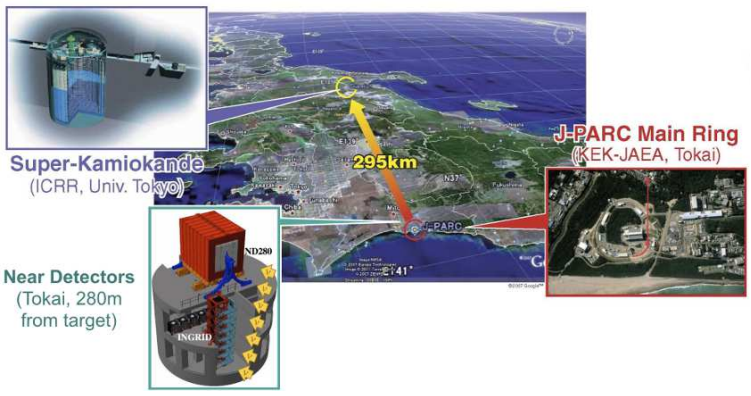


Figure 2.1: Sketch of T2K the Experiment, in which the accelerator, the near detector complex and the far detector are highlighted.

consists in using the *off-axis* technique. The near and far detector are on a line which is tilted by

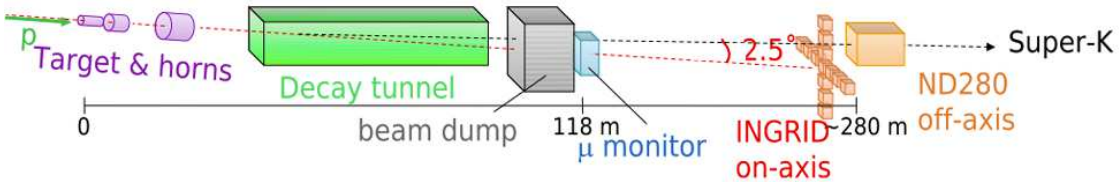


Figure 2.2: Sketch of T2K the Experiment main facilities, with a focus on the tilt angle between the beam direction and Super-Kamiokande.

2.5° with respect to the beam direction, allowing to select neutrinos or antineutrinos with an energy spectrum peaked at 600 MeV/c and to reduce high energy tails, as shown in figure 2.3. The cut of high energy tails in neutrino spectrum helps in excluding background reactions typical of higher

energy regions, where the interacting neutrino energy is more difficult to determine with respect to quasi-elastic scattering interactions. The technique is based on the kinematics of pion decay. Considering the ideal case of a pure pion beam, the decay of a positive charged pion is given by the reaction $\pi^+ \rightarrow \mu^+ + \nu_\mu$, with the presence of a neutrino in the final state. By computing the momentum of neutrinos according to the two body decay kinematics, the emission spectrum for neutrinos as a function of its angle of emission $\theta$ with respect to the initial direction of the pion has a maximum that changes with its energy:

$$\theta_{max} = \frac{E^*_{\nu},_{max}}{E_\nu} \sim \frac{30 \text{ MeV}}{E_\nu} \tag{2.1}$$

in which $E^*_{\nu},_{max}$ is the maximum energy of the neutrino in the rest frame and $E_\nu$ is its energy in the laboratory frame. Thanks to such relation, by selecting a particular off-axis angle, it is possible to select the peak of neutrino energy spectrum, as showin in the bottom plot of figure 2.3. The off-axis angle of 2.5° is selected to narrow the neutrino energy $E_\nu$ distribution in relation with the local maximum of electron neutrino appearance and the minimum of muon neutrino survivability.

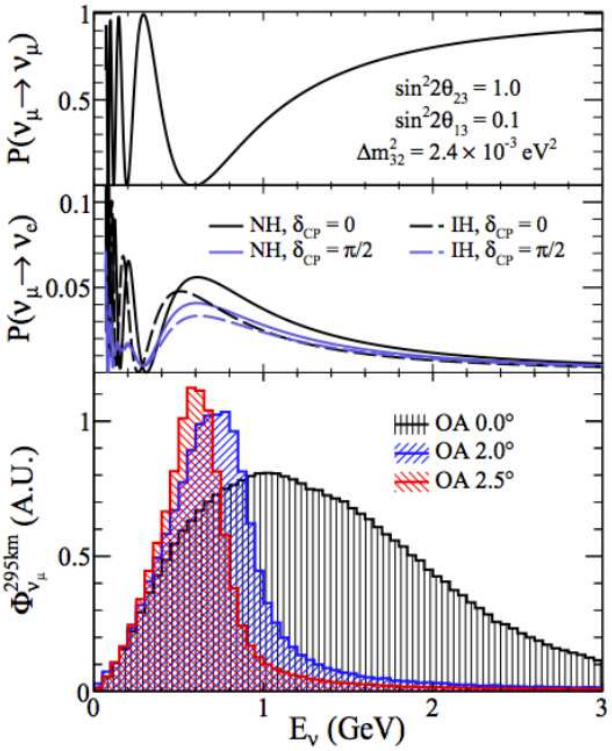


Figure 2.3: The muon neutrino survival probability (top) and electron neutrino appearance probability (middle) at 295 km as a function of neutrino energy. The bottom plot shows the unoscillated spectrum at the far detector for three off-axis angles. The appearance probability is shown for two values of the phase $\delta_{CP}$, and for normal (NH) and inverted (IH) mass hierarchies.

The JHF-Kamioka (now T2K) neutrino project proposal was published in 2001 with the idea of combining the new J-PARC facility with the expertise developed for the KEK-to-Kamioka (KEK) long baseline experiment[84]. After the construction of the dedicated facilities, including the Near Detector ND280, T2K started its data taking in 2010. Already in 2011, T2K presented a first indication of $\nu_\mu \rightarrow \nu_e$ oscillation. The T2K achievements and fields of interest focus on the determination

of neutrino oscillation parameters, in particular: (i) measurement of $\theta_{13}$ with the determination of its incompatibility with 0, (ii) precision measurements of atmospheric oscillation parameters $\theta_{23}$ and $\Delta m^2_{32}$, for which T2K was awarded the "Breakthrough Prize in Fundamental Physics" in 2015, and (iii) the hunt for the estimation of $\delta_{CP}$.
After over 10 years of operation using alternatively both muon neutrino and antineutrino beams, selected with Magnetic horns as explained later, T2K was the first experiment to report a measurement of $\delta_{CP}$, rejecting at $3\sigma$ a large part of the phase space including the relevant region of $\delta_{CP} = 0, \pi$ which correspond to the conservation of CP symmetry[85].
T2K Physics program includes the search for sterile neutrinos and the study of neutrino-nucleus cross section, which is a major source of systematic uncertainty for the experiment oscillation analysis. In the last few years, a second phase of T2K was proposed (T2K-II) which consists in an upgrade of its beam line and its near detector ND280, with an increase of the beam power and the installation of a new target and tracking system. Since 2027, the new water-based Cherenkov detector Hyper-Kamiokande is expected to start its operation. ND280 is expected to continue its work as a part of the new Hyper-Kamiokande program for beam neutrinos data taking.

## 2.1 Neutrino Beam

The high intensity beam used by T2K experiment is produced by the Japan Proton Accelerator Research Complex (J-PARC) in Tokai, Ibaraki. The facility is equipped with three main parts: (i) a linear accelerator (LINAC), (ii) a rapid-cycling synchrotron (RCS) and (iii) a main ring (MR) described detailed in [86].
T2K neutrino beam is produced starting from the accelerations of $H^-$ up to 400 MeV in the LINAC. Then, the anions are converted into $H^+$ by stripping two electrons thanks to charge-stripping foils. The cations enter the RCS where they are boosted up to 3 GeV. About 10% of bunches are injected into the MR and dedicated to the Neutrino Experimental facility, while the remaining bunches are supplied to the muon and neutron beamline for the Material and Life Science Facility. The MR accelerates the protons in a set of 8 bunches to the required energy of 30 GeV. At this point, the protons are extracted. The MR presents two extraction point: slow for the hadron beamline and fast for the Neutrino beamline by means of 5 kicker magnets. The beamline presents a power of about 750 kW.

### 2.1.1 The neutrino beamline

Neutrino beamline is constituted by two main sections: a primary beamline in order to bend the proton beam into its final direction towards Kamioka thanks to dedicated magnets, and a secondary beamline devoted to the conversion of protons to neutrinos via interaction with a graphite target and the consequential production of secondary particles. A schematic view of the beamline is reported in figure 2.4.
The primary beamline presents three main parts: (i) preparation, (ii) arc and (iii) focusing.

- The preparation section is dedicated to tune the extracted proton beam with 11 normal conducting magnets in order to be accepted by the arc section.
- In the arc section, the beam is bent by an angle of 80.7° pointing to Kamioka with a radius of curvature of 104 m. The line uses 14 doublets of superconducting combined functions magnets (SCFM).

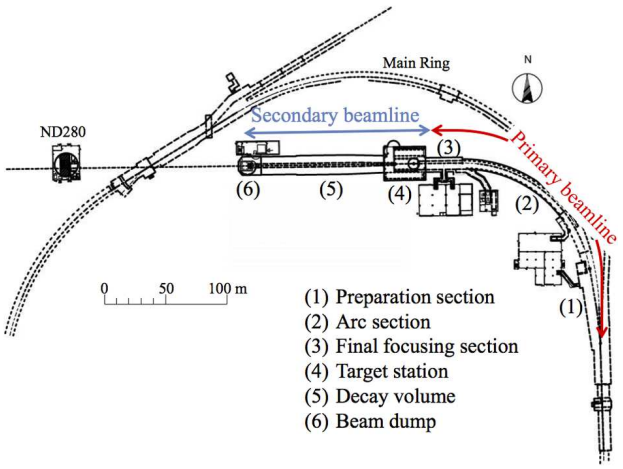


Figure 2.4: The neutrino beamline at J-PARC facility. Picture from [67].

- In the focus section, 10 normal conducting magnets are used for focusing the beam onto the target and to direct it downward by 3.637°.

Throughout the beamline, the quality, position and intensity of the beams are monitored by several beam monitors. The uncertainty on intensity monitoring is about 2% in the absolute intensity and 0.5% of fluctuation in relative intensity. The position is estimated with a precision better than 450 $\mu$m, while the beam profile is known with a systematic uncertainty of about 200 $\mu$m.
At this point, the beam enters in the secondary beamline, which is separated by the primary beamline by a titanium-alloy window. The secondary beamline is divided in four parts: (i) a target station, (ii) a decay pipe, (iii) a beam dump and (iv) muon monitors, with the first three parts contained in a helium gas vessel at 1 atm, in order to suppress pion absorption and to reduce the production of tritium and nitrogen oxide.
The helium vessel target station contains a graphite collimator, the target and three magnetic horns. The equipment is shielded by means of 2 m thick iron and 1 m thick concrete blocks. The production target is made of a graphite rod with a diameter of 2.6 cm and a length of 91 cm and it is enclosed by a titanium container filled with gaseous helium. The system is designed to survive thermal shocks due to the presence of $3.3\times10^{14}$ protons/pulse. The target is placed inside the inner conductor of the most upstream horn to achieve a high efficiency in focusing the newly-produced secondary particles. There are a total of 3 magnetic horns, consisting of two coaxial aluminum conductors. They are designed for a 320 kA pulsed current with a maximum of 2.1 T magnetic field, for maximizing the focus of secondary particles with low momentum and high emission angle. The focusing increases the number of neutrinos peaked at 0.6 GeV at the far detector by a factor of 16.
The decay volume is a 94 m long tunnel with a vertically elongated rectangular cross section that allows to vary the off-axis angle from 2.0° to 2.5°. At the same time, charged particles with the unwanted sign are de-focused by the same Magnetic field.
The beam dump is placed at the end of the decay volume, is composed by graphite blocks with aluminum cooling modules. The helium vessel and the beam dump are inaccessible due to their large activity and are designed to survive the thermal stress from a 3∼4 MW beam.

## 2.2 The Near Detector Complex

The T2K experiment near detector facility (ND280) is located 280 m away from the interaction target. The near detector is dedicated to the study of the unoscillated neutrino beam composition, energy spectrum and interaction rate. The facility houses two main detectors, INGRID and ND280, which are placed in a pit with a depth of 37 m, designed to allow the placement of such detectors at different off-axis angles. A schematic view of the pit is reported in figure 2.5. On top, the ND280 magnetized detector is visible, in which the magnet is open and the internal target and tracker part is revealed. Below, INGRID detector is visible. This view does not include the newly installed detectors developed for the T2K Phase II. A detailed description of T2K Experiment before the upgrade is reported in [67].

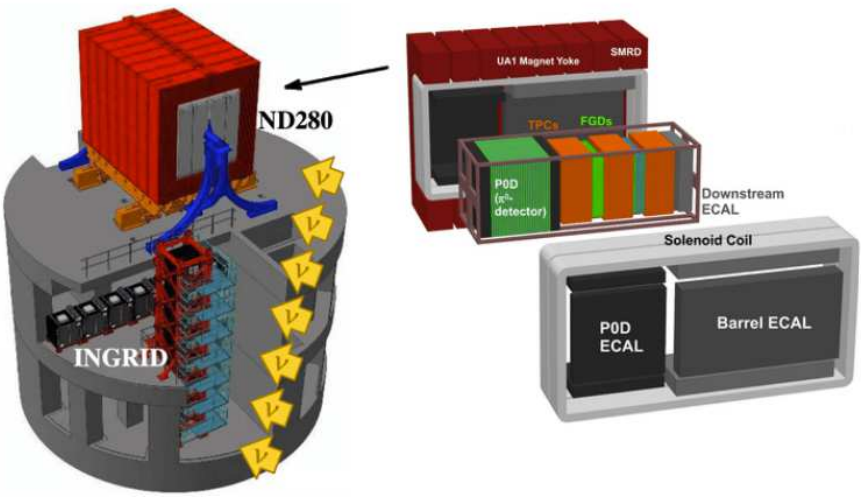


Figure 2.5: A scheme of the hall housing the detectors in the ND280 facility at J-PARC. On the right, an exploded view of ND280 detector configuration as it was until 2023 is visible.

### 2.2.1 INGRID

The Interactive Neutrino GRID (INGRID) detector[87] is placed on-axis and is dedicated to the monitoring of neutrino beam intensity and direction inside the pit. It is composed by several modules as shown in figure 2.6, which consist of a sandwich structure of nine iron plates and eleven tracking scintillator planes. They are surrounded by scintillating panels that act as a veto for interactions taking place outside the module.
Each tracking plane is formed by 24 scintillator bars in the horizontal direction glued to 24 perpendicular bars in the vertical direction, for a total number of 8448. The dimensions of the scintillator bars used for the tracking planes are 1.0 cm × 5.0 cm × 120.3 cm. Each veto plane consists of 22 scintillator bars segmented in the beam direction. The dimensions of those scintillator bars are 1.0 cm× 5.0 cm× 111.9 cm (bottom sides) and 1.0 cm× 5.0 cm× 129.9 cm (top, right and left sides). The total number of channels for the veto planes is 1144, which gives a total of 9592 channels for INGRID as a whole. INGRID was calibrated using cosmic ray data on the surface and in the pit. The mean light yield of each channel is measured to be larger than 10 photoelectrons per 1 cm of MIP tracks.
An additional module named Proton Module with different characteristics is installed to improve

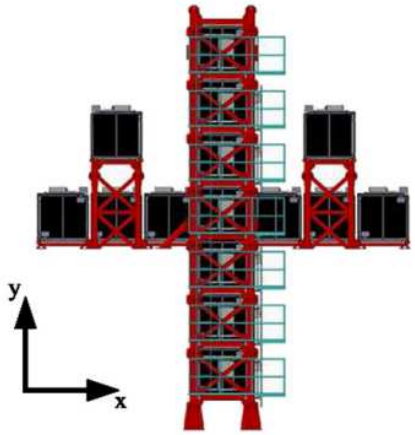


Figure 2.6: A scheme of the front view of INGRID detector. Picture from [67].

the detection of muons along with the protons produced in INGRID by the neutrino beam through the quasi-elastic channel interaction. In such module, no iron plane is included.

### 2.2.2 ND280

ND280 is the magnetized off-axis near detector of T2K[67]. It is dedicated to the estimation of: (i) muon neutrino flux, (ii) spectrum, (iii) electron neutrino contamination, which represents a non-removable background with a magnitude of 1%, and (iv) rate of exclusive and inclusive reactions for both muon and electron neutrinos.
ND280 is an ensemble of detectors which exploits different technologies in order to achieve the mentioned goals: it is a combination of tracking detectors used for particle identification and momentum estimation and calorimetric ones for energy loss estimation. ND280 designs allow to use magnetic field for charged particles particle identification and momentum reconstruction. Near and far detector in T2K use different materials as target and different technologies for particle detection. This information is a crucial aspect for Super-Kamiokande, in which no similar possibility is available.
ND280 design experienced an upgrade, completed in 2024 with the modification of target and tracking system close to the main interaction target. In the next sections, the detectors composing ND280 before the upgrade will be described. Later, a description of the new detectors installed for ND280 upgrade will follow.

#### UA1 Magnet

The ND280 off-axis detector is contained inside the old CERN UA1/NOMAD magnet. The magnet provides a dipole field used at a working regime of B=0.2 T in order to measure particle momenta and determine the sign of their charge. The magnet consists of water-cooled aluminum coils, which create the horizontally oriented dipole field, and a flux return yoke. The dimensions of the inner volume of the magnet are 7.0 m $\times$ 3.5 m $\times$ 3.6 m and the total weight of the yoke is 850 tons. The coils are made of aluminum bars with 5.45 cm $\times$ 5.45 cm square cross sections, with a central 23 mm diameter bore for water to flow. The coils are composed of individual "pancakes" which are connected hydraulically in parallel and electrically in series. The gaps of magnet yoke house the Side Muon Range Detector (SMRD).

The evaluation of the magnetic field direction and intensity is crucial for several of the detectors in ND280. In 2009, a mapping of the field took place and allowed to determine the performances of the magnet. As an example, the magnetic field intensity is reported in figure 2.7 for the central

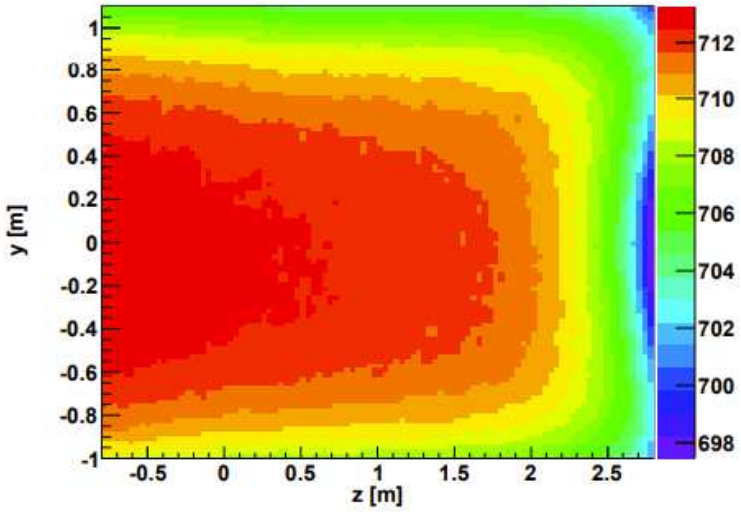


Figure 2.7: Magnetic field map for the central plane (x=0) of the magnet. Magnetic field values are expressed in Gauss. Picture from [67].

plane of the detector in the location occupied by the vertical Time Projection Chambers, being z the axis parallel to the beam direction. Measurements were performed at a value of B=0.7 T and they show that the field inhomogeneities are not negligible, especially for detectors like TPCs, in which the tracks are detected via the drift of electrons from ionization in the active volume.

### Side Muon Range Detector (SMRD)

The side muon range detector is designed to: (i) record muons escaping at large angle with respect to beam direction and (ii) their momenta; (iii) trigger muons entering in ND280 detector from outside and (iv) identify beam related events due to interactions with material surrounding the detector. It consists in 440 organic scintillator modules inserted in 1.7 cm air gaps between 4.8 cm thick steel plates, which are the magnet return yoke. The geometry of the detector is designed to fit the gaps in the return yoke of the magnet. The scintillating light is collected by a WLS fiber from both extremities of the scintillator, then the signal is readout by a total of 4016 MPPCs. SMRD components are shown in figure 2.8.

### Electromagnetic Calorimeter (ECal)

The electromagnetic calorimeter is a sampling calorimeter that surrounds the inner detectors. It is made of plastic scintillator layers divided by lead absorber sheets and it provides an almost integral cover of the inner detectors. The ECal is designed primarily to reconstruct $\pi^0$ particles forming inside ND280 with information on energy of the escaping particles. ECal modules are formed by a series of scintillator bars with a cross section of 4.0 cm $\times$ 1.0 cm with a 2.0 mm $\times$ 3.0 mm hole running through the bar. They are made of polystyrene doped with 1% PPO and 0.3% POPOP. WLS fibers pass through the hole of each bar to collect the scintillating light and readout by MPPCs. The bars are arranged in a layer and glued to a lead sheet absorber. The total amount of

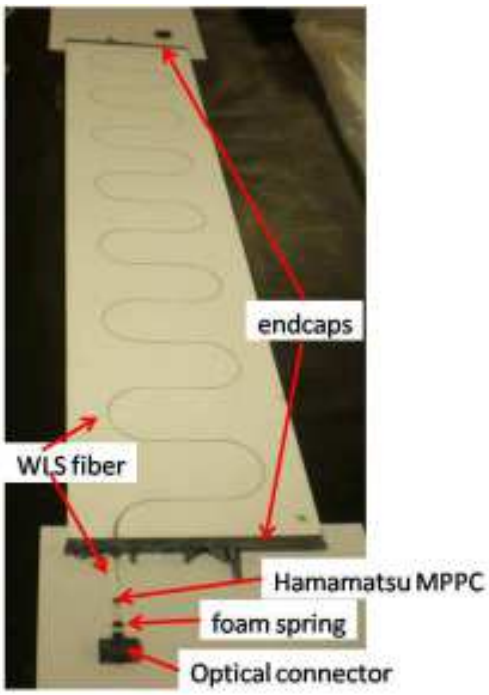


Figure 2.8: SMRD components before assembling. Picture from [67].

scintillating layers is limited by the space availability inside the magnet. The downstream and barrel modules contains enough layers of scintillator and lead to achieve a radiation length of $\sim 10X_0$. An additional module in the upstream region was placed before the ND280 target, in order to act as a veto and collect light of backward escaping particles. Such module was modified due to lack of space during the installation of ND280 upgrade.

### Pi-zero Detector (P0D)

P0D detector was primarily designed to measure the neutral current process $\nu_\mu + N \rightarrow \nu_\mu + N + \pi^0 + X$ on a water target, which is one of the main background sources for the $\nu_e$ appearance searches. The detector was formed by layers of x and y planes of scintillating bars, divided by fillable water bags used as a target and lead and brass sheets. Each bar is readout by a WLS fiber. The possibility to empty the water bags allows to compare the events with and without the presence of water, enabling the estimation by difference of the water cross section. The detector segmentation enables the detection of charged particles and electromagnetic showers. A schematic view of a P0D section is visible in figure 2.9. P0D is formed by 40 scintillating modules, each one formed by two perpendicular arrays of triangular-shaped scintillator bars. The total dimension of the active target is 2103 mm $\times$ 2239 mm $\times$ 2400 mm.
The detector is divided into 4 main regions: the upstream (and central) water targets, which are a sandwich of 13 (12) water bag layers and 13 (12) brass sheets 1.5 mm thick; two ECal modules which alternate scintillator layers with 7 lead sheets 4 mm thick.

### Fine Grained Detectors (FGD)

The two Fine Grained Detectors perform two main tasks: (i) to provide target mass for neutrino interactions and (ii) to track the charged particles from the interaction vertex. FGDs are made

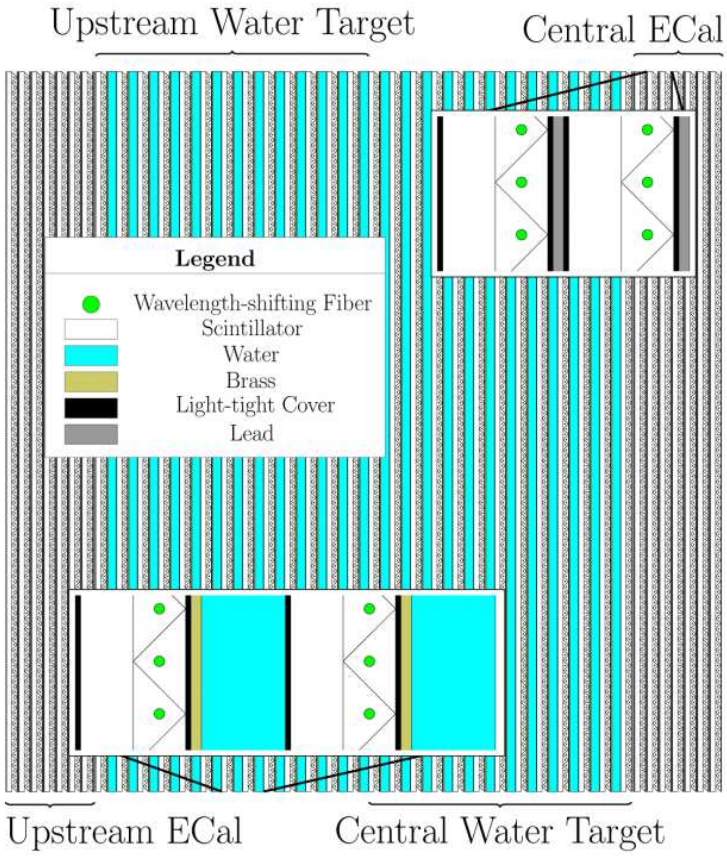


Figure 2.9: Schematic view of P0D structure. Four macro-regions are highlighted by labels and are characterized by the presence of layers with different materials. Picture from [67].

of 9.61 mm × 9.61 mm × 1864.3 mm extruded polystyrene scintillator bars oriented in x and y direction. The total dimension of a single FGD is 2300 mm × 2400 mm × 365 mm for a total of 1100 kg of target material and a schematic view is reported in figure 2.10. The first FGD is composed by planes in x and y directions made of 192 bars, with the outer surfaces glued to G10 sheets to provide structural support. The second FGD is formed by 7 scintillators XY modules alternating with six 2.5 cm thick water layers. Water is contained in hollow corrugated polycarbonate bars sealed at the end. Spilling of water is prevented by maintaining the inner part below the atmospheric threshold by vacuum pumps. A comparison of the interaction rates between the two FGDs with identical geometry allows to determine separately the cross section on carbon and on water.

### Time Projection Chambers (vTPCs)

The inner part of ND280 old setup is completed by the presence of 3 time projections chambers (TPCs), which are now referred to as *vertical*-TPCs to distinguish them from the recently installed *High Angle*-TPCs.
vTPCs are designed to provide three crucial information: (i) number and orientation of charged particles traversing their volume; (ii) momentum of charged particles due to the presence of magnetic field and (iii) the amount of ionized charge left by traversing particles, in order to reconstruct their energy loss per unit of length for particle identification. The mentioned features are fundamental to achieve the identification of charged particles, which is necessary to estimate the $\nu_e$ contamination

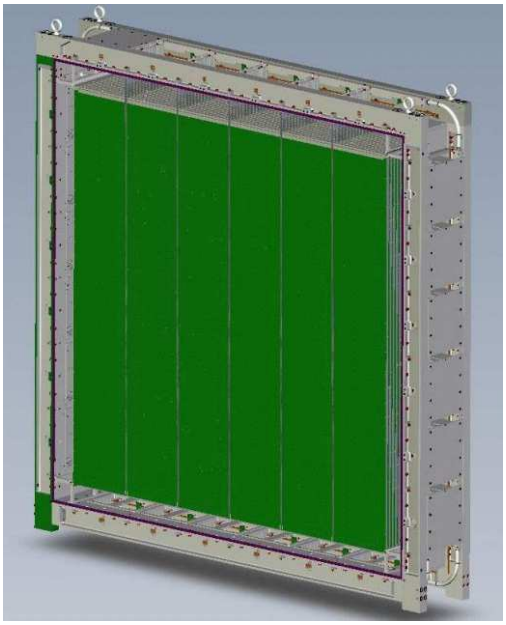

Figure 2.10: Schematic view of a FGD, in which the cover was removed. The modules (in green) are arranged in XY planes perpendicular to the beam direction. On the top, six mini-crates with electronics and their cooling lines are visible. Picture from [67].

in the neutrino beam, and to select high purity neutrino samples. Furthermore, the determination of particle momenta allows to reconstruct the event rate of incoming neutrinos as a function of energy prior to oscillation.
Each vertical TPC is composed by an inner volume that contains an argon-based drift gas and an outer volume filled with $CO_2$ as insulating medium. The inner walls are made of composite panels with copper-clad G10 skins, while the outer walls are made of composite panels with aluminum skins since they serve different purposes. The inner box provides a uniform electric field in the active volume thanks to the presence of a 11.5 mm pitch copper strips pattern and a copper cathode, which are visible in figure 2.11.
The TPCs are equipped with 12 bulk MicroMegas sensors per endplate for a total of 72 MicroMegas, which multiply and collect the electrons produced in the active volume and drifted towards the readout plane.
Each MicroMegas has a total surface of 342 mm $\times$ 359 mm, which is segmented in a grid of pads with sides 7.0 mm $\times$ 9.8 mm. The incoming electrons are multiplied in a 128 $\mu$m thick gap between the pads plane and a stainless steel wires spaced with a pitch of 63 $\mu$m. The micromesh is kept at a fixed distance by a grid of pillars (12 per pad) and a 2 mm coverlay at the border. The active area is 93% of the sensor surface. The signal is sampled by custom ASICs called "AFTER". Each AFTER ASIC shapes the signals and buffers them into 511 time-bin switched capacitor arrays.
The gas system is designed to keep a stable mixture in the inner volume and at a larger pressure than the outer volume. The inner gas mixture is formed by three components Ar:$CF_4$:$iC_4H_{10}$ in a proportion 95:3:2, chosen for: (i) its high speed, (ii) low diffusion and (iii) good performance with MicroMegas chambers.
The calibration of TPCs is performed thanks to the presence of a diffuse light of a 266 nm laser to illuminate small aluminum disks which are glued to the central cathode surface, to estimate the electron drift velocity and evaluate distortions of electric and magnetic fields.

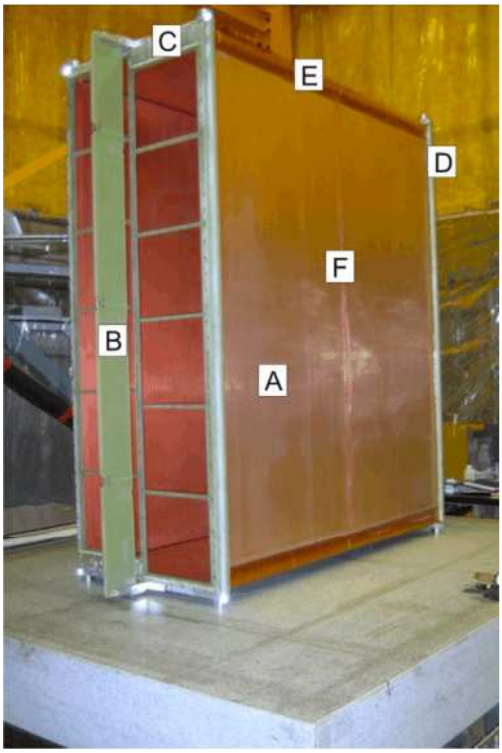


Figure 2.11: View of one inner vessel of vertical TPCs and its components: (A) vessel walls, (B) module frame stiffening plate, (C) module frame, (D) inner box endplate, (E) field reducing corners and (F) central cathode location. Picture from [88].

TPCs provide a three dimensional reconstruction by combining the time of electron arrival to the anode with the position of the signal on the segmented anode, with a spatial resolution in the MicroMegas plane of about 0.7 mm, which is sufficient to achieve the required goal for momentum resolution estimation. In addition, TPCs are capable of provide PID for charged particles, with a particular focus on discriminating electrons from muons. The measured energy loss per unit length is used to calculate the *pull*, $\delta_E(i)$, the number of standard deviations the measurement is away from the expected value for particle type i at the observed momentum. The energy deposition resolution is (7.8±0.2)%, hence the probability of identifying a muon as an electron is 0.2% for $-1<\delta_E(e)<2$ and tracks below 1 GeV/c as shown in picture 2.12.

### 2.2.3 The far detector: Super-Kamiokande

Super-Kamiokande is a water based Cherenkov detector placed in Kamioka mine, 295 km away from J-PARC site. The site is located in mount Ikenoyama under 1000 m of rock (2700 m water equivalent). The detector is dedicated to the study of proton decay and of neutrinos generated in the atmosphere, in the Universe or from J-PARC accelerator as far detector for T2K.
As shown in picture 2.13, Super-Kamiokande geometry consists of two volumes separated by a cylindrical stainless steel structure. The outer shell of the detector is a cylindrical stainless-steel tank with a diameter of 39 m and an height of 42 m, with a capacity of more than 50 kt. The volume is divided into two parts by a cylindrical support structure that optically insulates the two parts, which are separated by 50 cm of dead volume. The inner detector (ID) has a diameter of 33.8 m and an height of 36.2 m, filled with 32 kt of water. The light is collected by 11 146 inward-facing

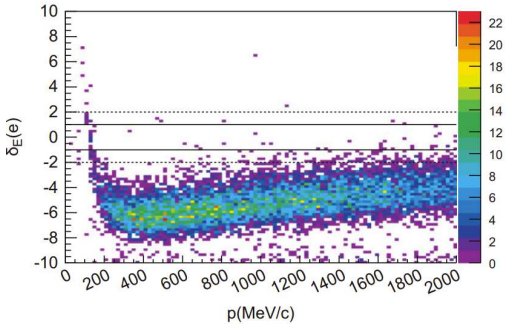


Figure 2.12: Energy loss *pull* for electron hypothesis on a sample of traversing muons as a function of particle momentum. Picture from [88].

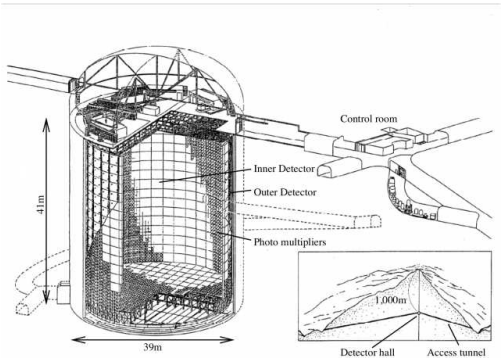


Figure 2.13: Schematic view of Super-Kamiokande and its location under the mount Ikenoyama.

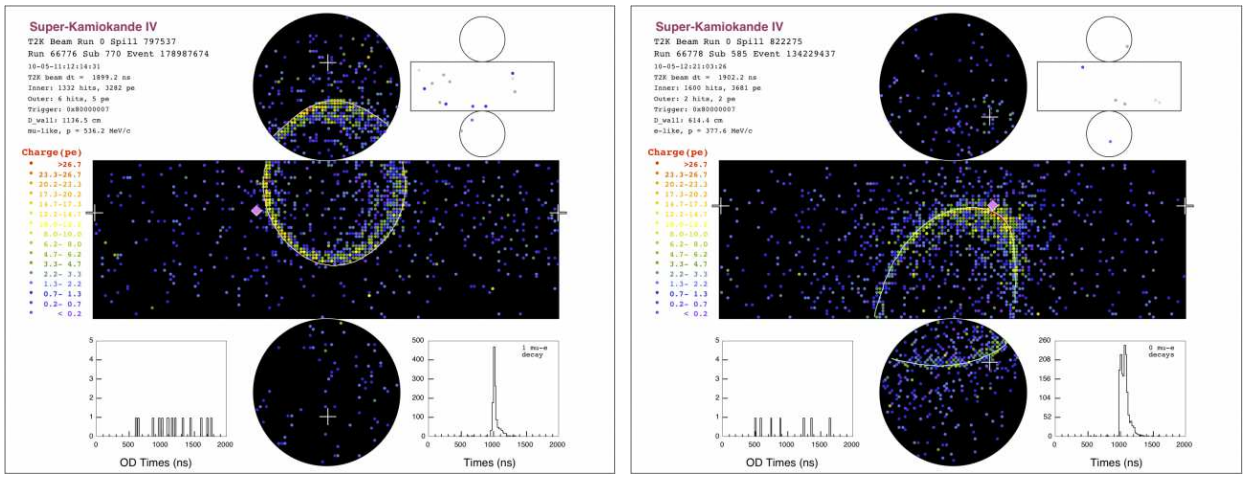


(a) (b)

Figure 2.14: Examples of a muon-like ring (left) and a electron-like ring (right), which are recognizable by the sharpness of the light ring.

50 cm MPTs, which cover about 40% of the inner surface.
The outer detector (OD) is an active veto counter against particles coming from outside and it serves also as a shield for neutrons and $\gamma$-rays generated in the sorrounding rocks. It is instrumented with 1885 outward-facing 20 cm PMTs. OD is capable of reaching almost a 100% rate of cosmic rays background rejection.
T2K relies on the far detector to detect muon neutrinos and electron neutrinos after the oscillation phenomenon, by counting the number of charged current quasi-elastic (CCQE) interactions that produce a charged lepton of the respective flavor. Charged particles are detected thanks to the Cherenkov phenomenon, in which charged particles traversing a medium with a refraction index n at a speed greater than the speed of light ($\beta > \frac{1}{n}$) produce a cone of light.
The possibility to discriminate between muons and electrons is based on the difference between their propagation through the water. Muons are more massive, therefore when scattering are less prone to modify their direction, while electrons are lighter and scatter in a more pronounced way. Hence, the Cherenkov cone for muons is sharper, while electrons produce a *fuzzier* cone. The Cherenkov light is collected by the PMTs of ID, from which the time of arrival and their intensity are recorded. Such information are used to reconstruct (i) the vertex position, (ii) the direction of the charged particle and (iii) the kind of particle. For a muon with a momentum of 1 GeV/c, the typical vertex resolution is 30 cm, the angular resolution is 3° and the energy resolution is 3%. Differently from ND280, Super-Kamiokande is not equipped with a magnetic field, so it cannot discriminate the sign of the charge of the particles.
The event reconstruction in Super-K is divided into four phases: vertex pre-fit, PMT hit clustering, single-ring reconstruction, and multi-ring reconstruction.

- First, an initial vertex is reconstructed thanks to the timing information of the PMTs hits;
- second, a Hough transform of the PMTs charge distribution is used in order to look for ring candidates;
- as a third step a PID algorithm is used for classification of muon-like or electron-like candidates. An event might contain one or more rings: for single ring events, the misidentification

rate of e/$\mu$ PID is less than $\sim 1\%$ when the visible energy is $E_{vis} < 1330$ MeV [89]. the reconstructed momentum for each particle is determined by the charge assigned to the Cherenkov ring caused by the particle.

- Similarly to the single ring fit, the multi-ring fit aims to find events with more than one charged particle, for example adding a $\pi^+$-like hypothesis. The fit is repeated until the likelihood does not improve by adding new rings into the fit.

Additionally, decay electron signals produced by the pion or muon decay chains are tagged using the delayed signals. When neutrons produced in the neutrino interaction are captured by protons in nuclei, they emit a gamma ray with 2.2 MeV, which can be a background for the decay electron tagging.

**Gadolinium loading** In pure water, the direct detection of neutrons is a challenging task, since they do not emit Cherenkov light. Therefore, a decision was made to dope the pure water medium with Gadolinium, using a Gadolinium Sulfate. Gadolinium presents a cross section for thermalized neutrons about $10^5$ larger than Hydrogen, with an expected capture rate of about 50% after the first loading[90]. After the second Gadolinium loading[91], the Gadolinium concentration was measured to be 333.5±2.5 ppm via an Atomic Absorption Spectrometer (AAS), while the neutron capture efficiency is estimated to be 75%. The capture of neutrons by Gadolinium nuclei will emit a total of about 8 MeV through de-excitation from excited nuclear levels. The high energy photons emitted in the process will interact with the water atoms. Hence, the signal from the Cherenkov radiation of produced electrons is registered by SK PMTs with some delay and, consequently, the antineutrino events can be reconstructed based on the observation of the double signal from the charged lepton followed by the neutron capture fingerprints.

## 2.3 Latest T2K Oscillation results

The T2K experiment has provided important results throughout its activity for some of the oscillating parameters: (i) a first indication of a non-zero value of $\theta_{13}$ through the observation of $\nu_e$ appearance[92], (ii) an accurate estimation of $\theta_{23}$ and most recently (iii) first hints towards a violation of CP symmetry in the leptonic sector, excluding at $3\sigma$ almost half of $\delta_{CP}$ domain[85]. The latest release of T2K oscillation analysis results with a statistics of $3.6\times10^{21}$ protons on target (POT) are described in [69] and summarized in table 2.1, with and without the constraints from neutrino reactor experiments.
Regarding the $\delta_{CP}$ parameter, the T2K results are still in favor of almost-maximal violation of CP with a slight difference in value depending on the mass ordering as shown in figure 2.15. The figure shows the number of $\nu_e$ and $\bar{\nu_e}$ reconstructed events at Super-K, compared with the expected results for oscillation models with different values of oscillating parameters as reported on top of the figure.
T2K results are also in favor of the upper octant solution to $\theta_{23}$ value ($\pi/4 \leq \theta_{23} \leq \pi/2$), and the normal ordering is favored as shown in both $\Delta\chi^2$ distributions. The determination of $\delta_{CP}$ and $\theta_{23}$ are still open questions and the hints showed by T2K are a promising result, but still far away from a conclusive statement as demonstrated by $\Delta\chi^2$ distribution in figures 2.15c and 2.16b. The next upgrade of T2K and the construction of Hyper-Kamiokande are huge steps for increasing the number of events and decreasing the systematic and statistical uncertainties in the next future.

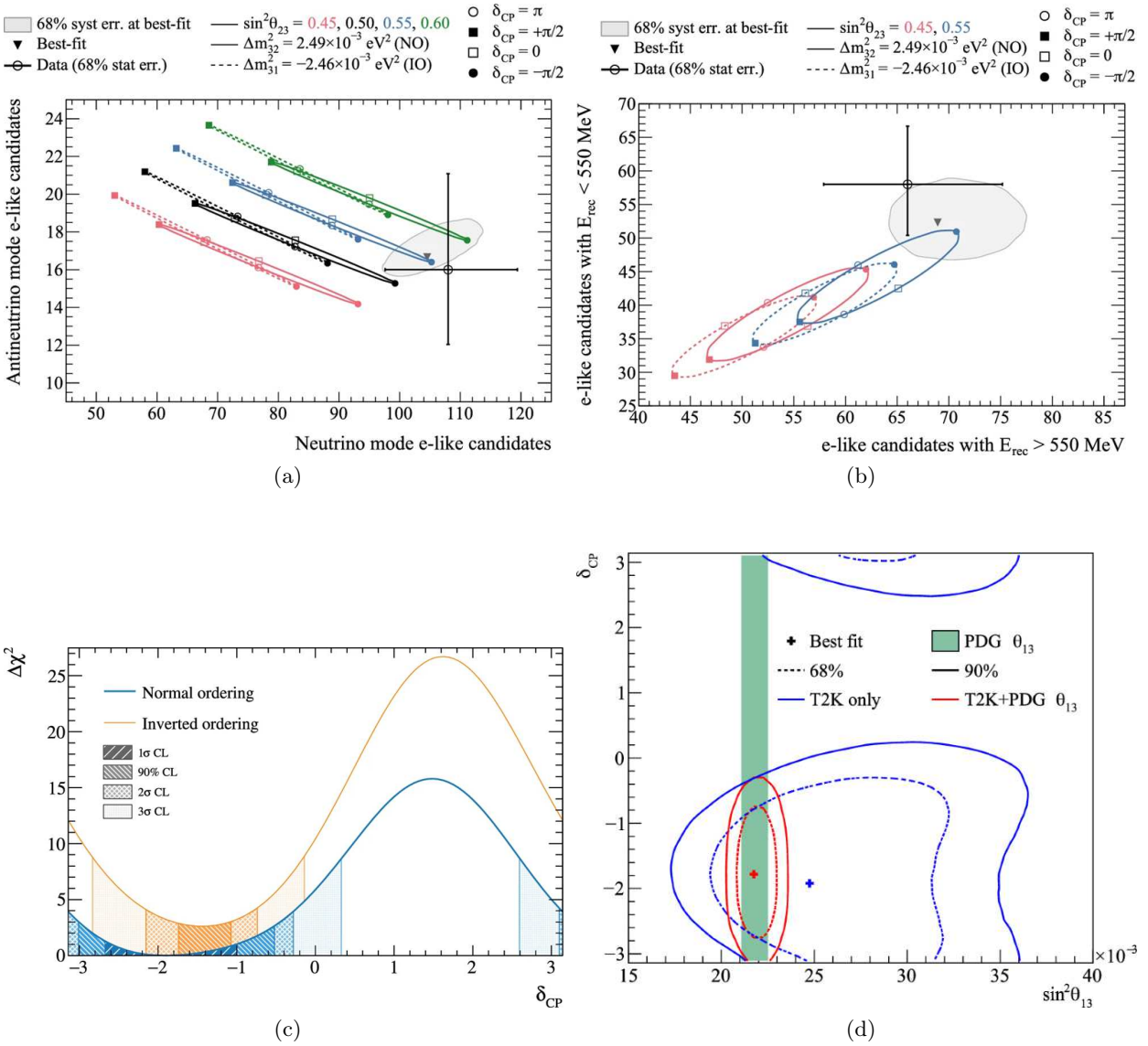


Figure 2.15: Top left plot shows the comparison of measured $\nu_e$ and $\bar{\nu_e}$ appearance at Super-K with the expected values from models with several $\delta_{CP}$ and $\sin^2(\theta_{23})$ values. Top right plot shows a data/models comparison dividing the events based on neutrino energy. Bottom left plot highlights the excluded regions at several values of $\sigma$ for both NO and IO, while the bottom right highlights the importance of reactor constraint: it represents the 68% and 90% credible intervals from the marginalised $\sin^2(\theta_{13}-\delta_{CP}$ posterior distribution with (red) and without (blue) the reactor constraint (green band) applied, marginalised over both mass orderings. Picture from [69].

| Parameter | With reactor constraint | | Without reactor constraint | |
|---|---|---|---|---|
| | Normal ordering | Inverted ordering | Normal ordering | Inverted ordering |
| $\delta_{CP}$( rad. ) | $-1.97^{+0.97}_{-0.62}$ | $-1.44^{+0.56}_{-0.59}$ | $-2.22^{+1.25}_{-0.81}$ | $-1.29^{+0.72}_{-0.83}$ |
| $\sin^2\theta_{13}/10^{-3}$ | - | - | $28.0^{+2.5}_{-6.8}$ | $31.0^{+3.0}_{-6.0}$ |
| $\sin^2\theta_{23}$ | $0.561^{+0.019}_{-0.038}$ | $0.563^{+0.017}_{-0.032}$ | $0.467^{+0.106}_{-0.018}$ | $0.466^{+0.103}_{-0.019}$ |
| $\Delta\ m^2_{32}/10^{-3}\ (eV^2)$ | $2.494^{+0.041}_{-0.058}$ | - | $2.495^{+0.041}_{-0.058}$ | - |
| $\lvert\Delta m^2_{31}\rvert/10^{-3}\ (eV^2)$ | - | $2.463^{+0.042}_{-0.056}$ | - | $2.463^{+0.043}_{-0.055}$ |

Table 2.1: Results for the oscillation parameters from the fit to data with and without the reactor constraint in the frequentist analysis, with the confidence intervals estimated using the constant $\Delta\chi^2$ method.

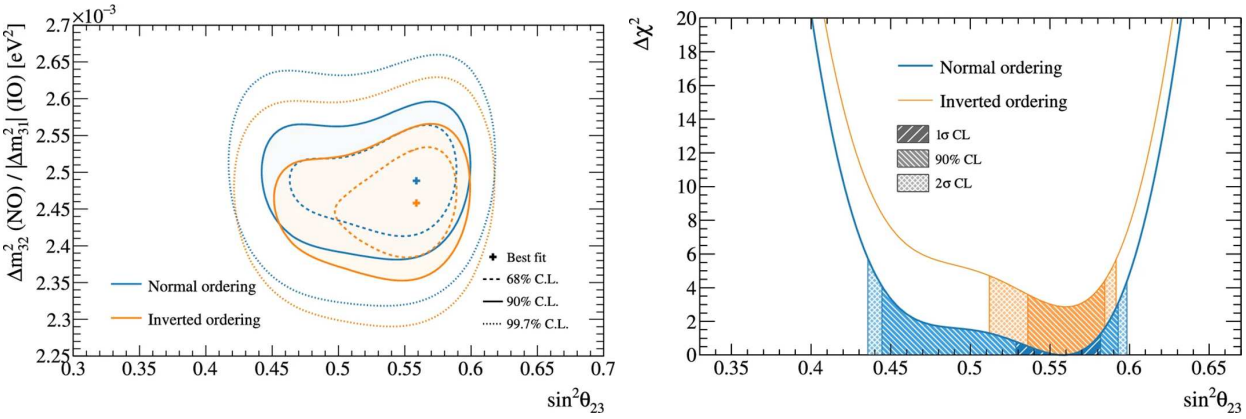


(a) (b)

Figure 2.16: Left plot shows the confidence regions in $\sin^2(\theta_{23}) - \Delta m^2_{32}$ ($|\Delta m^2_{31}|$ in IO) for the data fit with the reactor constraint applied, obtained with the constant $\Delta\chi^2$ method, where in each mass ordering hypothesis a fixed mass ordering is assumed. On the right plot, The $\Delta\chi^2$ distribution in $\sin^2(\theta_{23})$ for fitting to the data with the reactor constraint applied. Pictures from [69].

## 2.4 T2K Phase II

In the last years, the T2K Collaboration prepared a new phase of data taking with increase statistics and improved detector performances. The goals of the experiment will be to improve the estimations on atmospheric oscillation parameters and to obtain a confirmation on the hints regarding the CP symmetry violation in the leptonic sector.
For this purpose, an upgrade of the beamline and of the near detector ND280 were planned and recently achieved. Furthermore, the construction of Hyper-Kamiokande detector would provide a larger statistics at the far detector by a factor of 10.

#### Upgrade of the neutrino beam

T2K Phase II is expected to reach a beam intensity of 1.3 MW in the next years and the beamline has been upgraded to withstand such increase in intensity[93]. At the moment of the submission of this work, the achieved beam power was 0.8 MW. Among the required improvements, there are: (i) improvement of the helium cooling system in the target and of the water cooling for beam line components, (ii) development of a new beam window, (iii) improvement of the horns electrical components for increasing the current and (iv) several adjustments to manage an increase in the radioactivity of the whole beamline.

### 2.4.1 ND280 Upgrade

The presence of a larger number of candidate events, which provides smaller statistical uncertainties, requires an improvement in the systematic uncertainties. The ND280 configuration presented in the previous section reached a systematic uncertainty of about 6%, while the proposed goal for the new ND280 setup is 4% for T2K-II and up to 3% when Hyper-Kamiokande will begin its operations.
The previous ND280 design presented two main limitations. First, the efficiency in the forward region is excellent, but it drops significantly for particles at angles larger than 40% with respect to beam direction as shown in figure 2.17, in which the acceptance for ND280 is compared to the one of Super-K. In fact, in order to precisely determine the properties of a lepton emitted by a neutrino interaction, its track has to be reconstructed in one of the three TPCs[94]. On the other hand, Super-Kamiokande provides an isotropic $4\pi$ reconstruction, highlighting a mismatch between the phase space of the near and far detector. Second, the efficiency for selecting electron neutrino events at momentum smaller than 1 GeV/c is quite poor, due to low efficiency at large angles and a large contamination caused by converted photons as shown in figure 2.18. The new configuration is designed to provide: (i) full polar angle acceptance for produced muons, (ii) target mass of few tons, (iii) high tracking efficiency for low energy pions and protons for event topology recognition, (iv) enhance neutron detection (thanks to Super-FGD) and (v) highly efficient time of flight detector to reconstruct the direction (backward/forward or inward/outward) of tracks traversing the TPCs.

The new design shown in figure 2.19 is characterized by the installation of three new detectors, which replace the P0D detector: (i) an active fine grained scintillator detector (super-FGD), (ii) two time projection chambers located at large angles with respect to beam direction (HA-TPCs) and a (iii) time of flight detector (TOF) composed by 6 panels of scintillator bars which surround the two new detectors mentioned previously. The new configuration achieves a full polar angle acceptance for muons produced in charged current interactions.

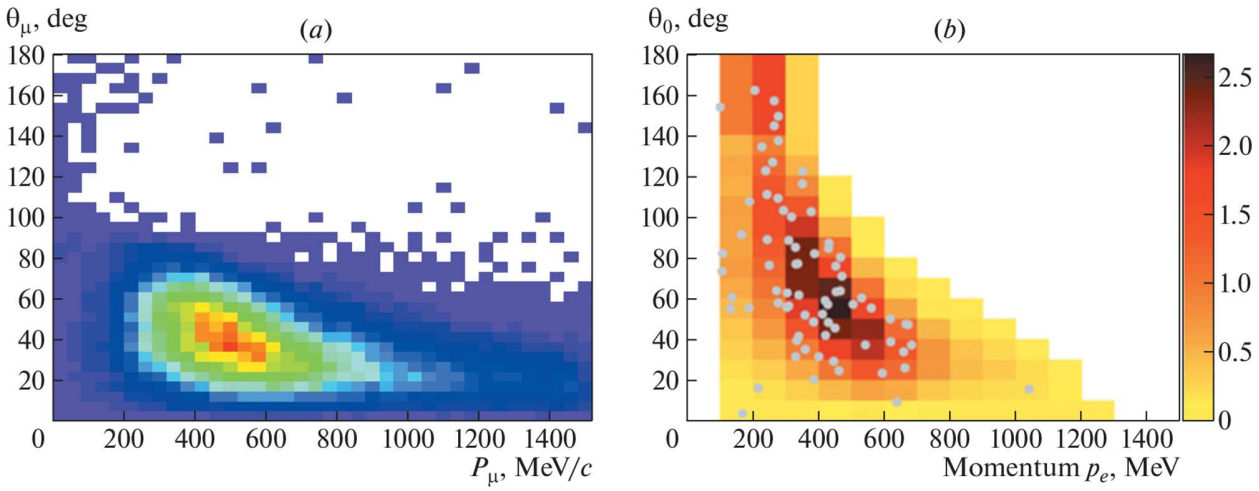


Figure 2.17: Reconstructed momentum and angle for muons selected at ND280 (a) and electrons selected at Super-K (b). Picture from [94].

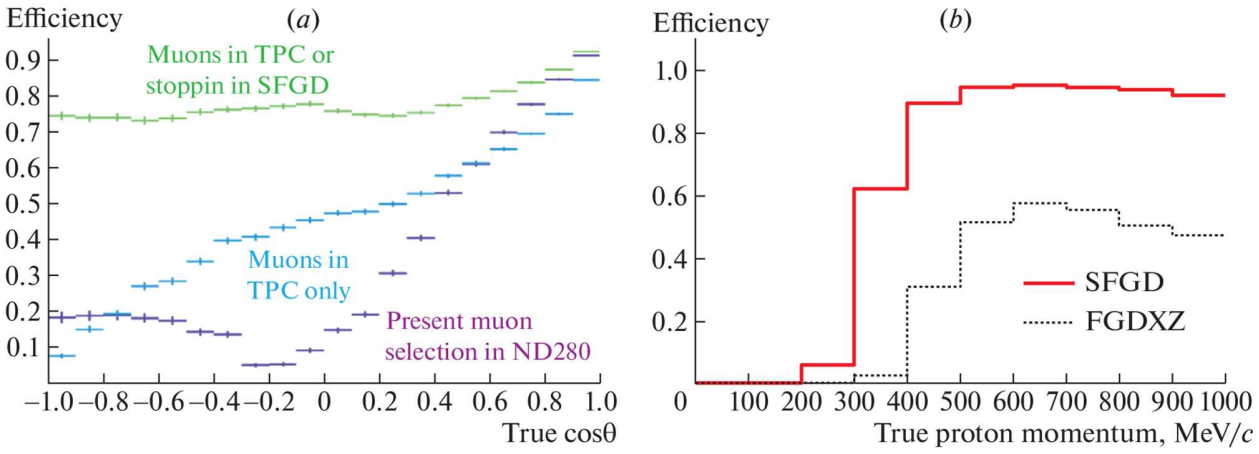


Figure 2.18: ND280 upgrade efficiency in reconstructing muons (a) and protons (b) where FGDXZ are the current FGDs of ND280. Picture from [94].

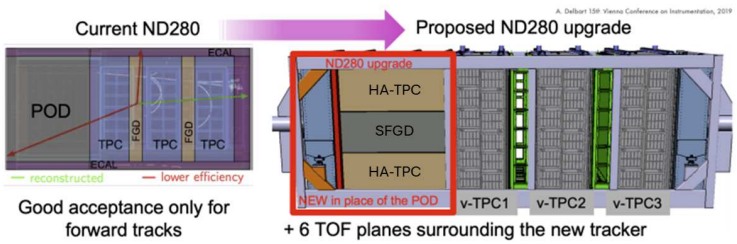


Figure 2.19: Comparison of previous (left) and upgraded (right) designs for ND280 detector.

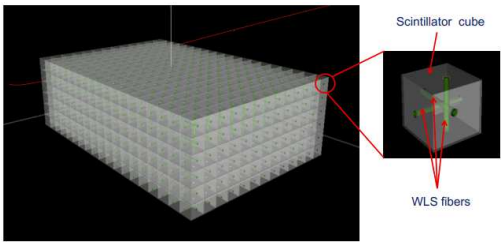


Figure 2.20: Scheme of Super Fine Grained Detector. On the right, a focus on a single cube is visible, with the holes for WLS fibers insertions on three directions.

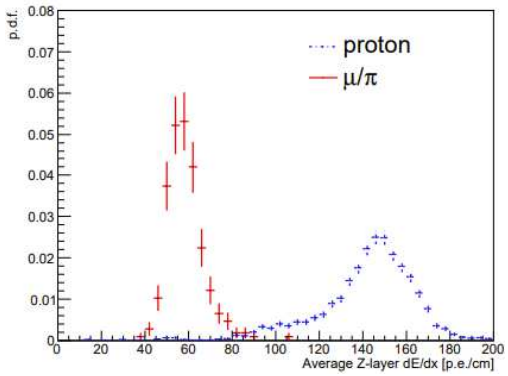


Figure 2.21: Comparison of dE/dx for protons, muons and electrons at a momentum of 0.8 GeV/c. Picture from [95].

### The Super Fine Grained Detector (SuperFGD)

SuperFGD is the new active target for neutrino interaction in ND280 near detector. The detector is composed by independent cubes of plastic scintillator with 1 cm side and arranged in a parallelepiped shape with 192 × 192 × 56 cubes. The signal is collected in three directions by WLS fibers, that pass through holes in each cube and are readout by MPPCs. The detector contains the remarkable amount of about 2 000 000 cubes and 58 000 readout channels for an active mass of about 2 tons. A picture of the detector is shown in figure 2.20.

Differently from FGDs, the SuperFGD allows to reconstruct a 3D image of a track and, due to its segmentation and low mass number material, it is able to reconstruct particles with short range in the active volume like low momentum protons. In addition, it has a fast intrinsic time resolution of about 0.6 ns for a MIP. The performances of Super-FGD have been tested in two test beams at CERN, the latter with a prototype composed by 9216 cubes arranged in arrays of 28 × 8 × 48 cubes. The time resolution for a single channel was evaluated to be 1.14 ns, while the dead time is of the order of 200 ns. Such amount of time is short enough to allow the detection of the consequent Michel electrons following a muon decay in a cube. A study on energy deposition shows the possibility to perform a PID based on dE/dx, as reported in figure 2.21 for protons versus muons and electrons. In addition, dE/dx resolution for a single cube expressed as $\sigma$ over mean value $\mu$ of 25% is sufficient to resolve one MIP from two MIPs equivalent events such as two co-linear tracks through the same set of cubes[95]. The resolution on dE/dx improves on the number of layers traversed by a track, up to a value of about 10%. The detector was successfully installed inside the ND280 pit in 2023 and was used successfully in beam runs since November 2023.

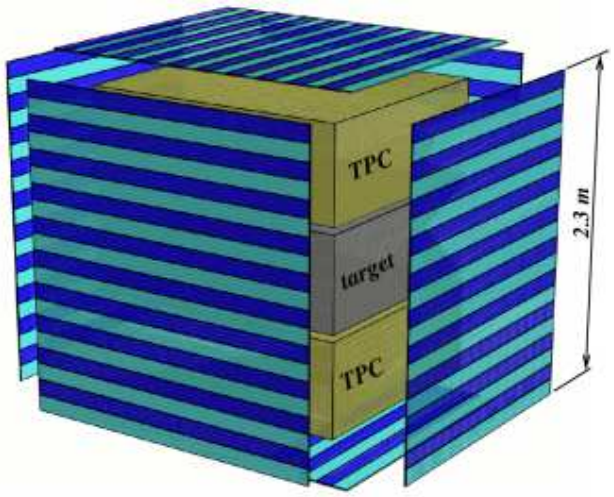


Figure 2.22: Placement of TOF panels around the new tracker of ND280.

### Time of Flight (TOF)

The Time of Flight detector aims to measure the crossing time of charged particles in ND280 and thanks to timing information in SuperFGD it can provide an estimation on particle direction. The detector is formed by 6 panels of plastic scintillator bars, which surround the volume occupied by SuperFGD and HA-TPCs as show in in figure 2.22. The bars have a dimension of 200 cm (or 230 cm) $\times$ 1 cm $\times$ 12 cm depending on which side of the new tracker they are placed. The scintillation light is then collected at the bar ends by MPPCs. Plastic scintillator was chosen to provide precision timing: a resolution better than 500 ps is required for direction determination and a few hundreds of ps are necessary to enhance the PID capabilities of SuperFGD and HA-TPCs. In particular, discrimination between muons/electrons or protons/positrons in the energy range 0.1-0.3 GeV and 1-2 GeV respectively are not possible relying only on energy loss reconstruction.

### High Angle Time Projection Chambers (HA-TPCs)

High angle time projection chambers are two newly installed detectors placed on the two large faces of Super-FGD and are designed to provide optimal (i) tracking performance for momentum reconstruction and (ii) energy loss reconstruction for particle identification of particles escaping the Super-FGD at large angle with respect to the beam direction.
HA-TPCs will be the focus of the next chapters, while a summary of its innovative characteristics might be described as:

- low density and low Z material for reduced interaction probability, but at the same time providing optimal mechanical and insulating properties;
- reduced wall dimensions with respect to vTPCs for reduced dead volume;
- use of resistive MicroMegas sensors as readout, which aim to achieve a spatial resolution better than 800 $\mu$m with pads size of about 1 cm $\times$ 1 cm.

The TPCs required also the design and the installation of a new gas system, that was prepared at CERN and shipped to J-PARC. It is dedicated to (i) the mixing of the three elements composing

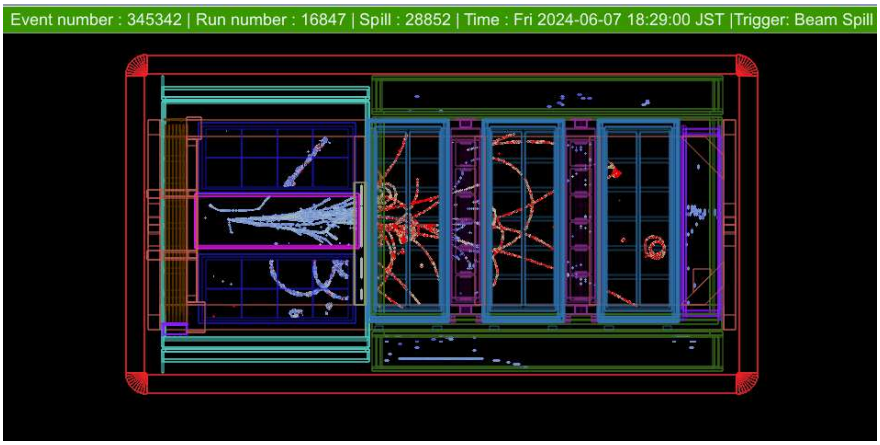


Figure 2.23: Event display of an event with the upgraded ND280 detector (beam coming from left). On the left side, the primary interaction vertex is within the Super-FGD. Most of the particles move in the forward region towards FGDs and vTPCs, while few of them are directed at large angles to HA-TPCs on both sides of Super-FGD.

the *T2K gas*, (ii) circulating the gas in all the TPCs, keeping the contamination under control and to (iii) recirculate the majority of the exhaust gas.

#### ND280 Upgrade status

The installation of the new detectors in ND280 was completed in April 2024, with the installation of the second HA-TPC. Since the installation, a period of data taking with beam runs were performed starting in May and a second one started in November. An example of an event detected by the new ND280 is reported in figure 2.23, which shows tracks passing through multiple detectors.

## 2.5 Beyond T2K

The newly upgraded ND280 detector is expected to serve also as near detector for Hyper-Kamiokande, which will provide a target mass 10 times greater than Super-Kamiokande. In addition, a new water based detector at J-PARC is planned and will improve the near detector performances by providing the same detection technology of the far detector.

### 2.5.1 Hyper-Kamiokande

Hyper-Kamiokande is part of the new generations of neutrino detectors and as Super-Kamiokande will be based on detection of Cherenkov light in pure water. The distance from production target will be 295 km as T2K, at the peak of Mt. Nijyugo, with 1750 meters-water-equivalent of overburden. Hyper-K is expected to search for proton decay events, with a world-leading sensitivity owing to the large water mass. At the same time, the detector will measure oscillations of atmospheric and solar neutrinos and accelerator neutrinos from J-PARC using ND280 as near detector. The detector will have a cylindrical shape with an inner and an outer detector for a total diameter of 68 m and an height of 71 m, with a 217 kt mass of water in the inner detector (ID). The fiducial volume is 188.4 kton, about 8 times more than Super-K. The outer detector (OD) is a shell about 1 m wide and will sorround the ID. It is expected to be instrumented with 3600 8 cm diameter PMTs in order to

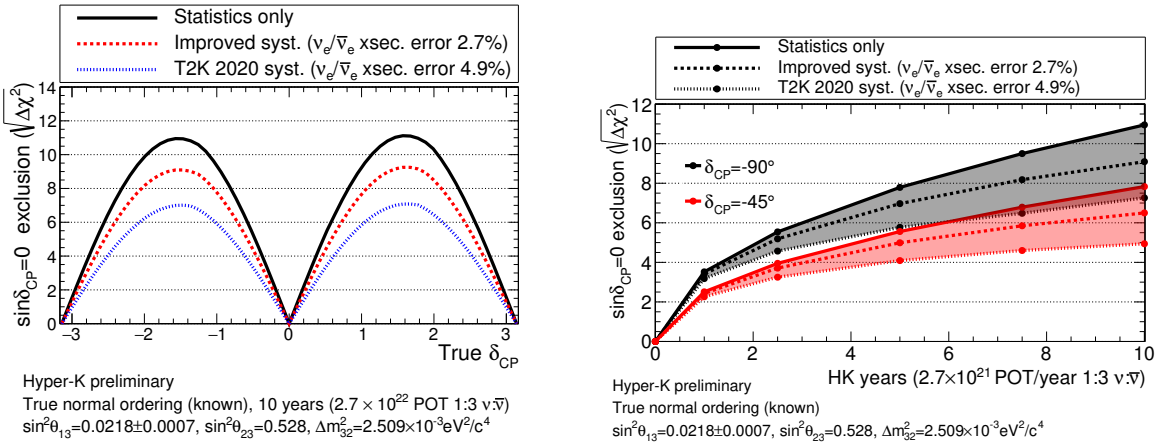


(a) (b)

Figure 2.24: Left plot refers to the significance level to exclude CP conservation at Hyper-K after 10-year assuming the reported oscillation parameters. Right plot shows sensitivity to CPV as a function of data-taking time for two values of $\delta_{CP}$. "Physics Official Plots" from Hyper-K Collaboration.

detect and veto charged particles. The ID will be instrumented with about 20 000 50 cm diameter PMTs and 1000 multi-PMT photonsensor modules. The total photo-cathode coverage is about 20% of the whole surface, compared to 40% in Super-K, however the light collection efficiency of the 50 cm PMTs is doubled.
Hyper-Kamiokande is expected to collect $2.7\times10^{21}$ POT of data per calendar year, with a partition of 1/4 exposure in Forward Horn Current (neutrino mode) and 3/4 in Reverse Horn Current (anti-neutrino mode). The expected number of muon netrino events of CCQE type is about 10 000, with a similar amount of muon antineutrino events. For the electron appearance channel, about 2000 CCQE electron neutrino events are expected, compared to 800 electron antineutrino ones, assuming $\delta_{CP} = -1.601$. These samples will allow Hyper-K to exclude $\delta_{CP}$ conservation at $5\sigma$ for 60% of true values for $\delta_{CP}$. The ratio of 1:3 between FHC and RHC is chosen in order to obtain a $\delta_{CP}$ resolution mainly independent on the constraint on $\sin^2\theta_{13}$ from external reactor constraints. Taking into consideration the assumed running plan for Hyper-K, a $5\sigma$ discovery on CP violation might be achieved with 3 years of data taking if MO is known and CP violation is maximal, otherwise with no external input on MO and maximal CPV the expected required time would be 6 years. In fact, Hyper-K is sensitive to mass ordering (MO) in atmospheric neutrinos events. A summary of Hyper-K sensitivy on CP violation is reported in figure 2.24.
Regarding the octant determination for $\theta_{23}$, the wrong octant can be excluded with a significance of $5\sigma$ for $\sin^2\theta_{23} < 0.45$ and $\sin^2\theta_{23} > 0.57$. Hyper-K will be able to measure $\Delta m^2_{32}$ better than 0.5% and, with the input of reactor experiments, $\sin^2\theta_{13}$ with a predicted slight improvement with respect to reactor experiments.

### Intermediate Water Cherenkov Detector (IWCD)

The Intermediate Water Cherenkov detector is expected to be realized as a new water based near detector about 850 m away from the beam production at J-PARC as a part of the Hyper-K Experiment. The detector is expected to have a cylindrical shape with an inner detector diameter of 7 m and an height of 8 m, for a total water mass of 600 t (300 t fiducial volume) and it is planned to install about 500 multi-PMTs detectors. A sketch of the detector is reported in figure 2.25.

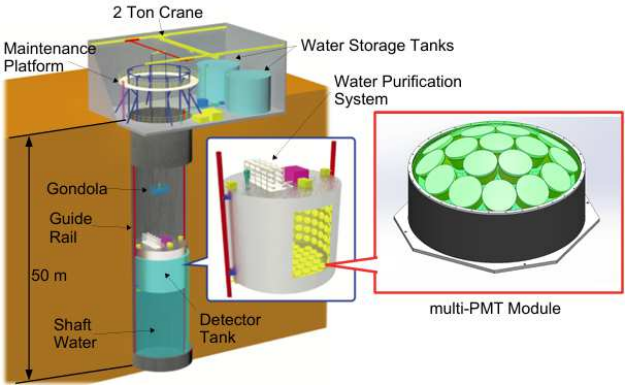


Figure 2.25: Sketch of IWCD experiment.

IWCD can provide high statistics of electron or muon neutrinos and antineutrinos samples. Additionally, the vertical mobility of the detector allows for measurement of unoscillated muon neutrino flux at off-axis angles from 1° to 4°, providing neutrino samples with energy spectra peaking between 0.4 GeV to 1 GeV. The extraction of large samples of $\nu_e$ and $\bar{\nu_e}$ with high purity is helpful for constraining the relative $\nu_e/\nu_\mu$ interaction cross section uncertainties of the neutrino event prediction

$$\frac{\sigma(\nu_e)/\sigma(\nu_\mu)}{\sigma(\bar{\nu_e})/\sigma(\bar{\nu_\mu})}, \tag{2.2}$$

where the current T2K theory-driven is 3%. Additionally, the measurement of $\nu_e$ events helps to constrain the intrinsic $\nu_e$ flux deriving from the decay of muons and kaons.

# Chapter 3

# HA-TPCs

HA-TPCs are an important part of the ND280 detector upgrade. Their ambitious design is based on the recently developed resistive MicroMegas detector as sensor and on the application of a custom designed composite material structure from industry sector to particle physics. Since the publication of the technical design report in 2018[96], the steps towards the installation of HA-TPCs at J-PARC in 2023 and 2024 were characterized by several test beams campaigns on prototypes and several cosmic rays data taking on the final detectors. The HA-TPC prototypes performances are reported in [97] and [98]. In this chapter, a brief introduction on TPCs will be presented and an overview on HA-TPC design and performances will be discussed. Then, in next chapters the focus will be shifted towards the HA-TPC structural part, called field cage, with a description on its performances and challenges faced in its realization and characterization.

## 3.1 Particle detection with gaseous detectors

Gaseous detectors use a gas medium as a target of interaction between a traversing charged particle and the gas molecules due to the Coulomb force. When moving through matter, a charged particle loses energy due to multiple inelastic processes of excitation and ionization that depends on the energy of the particle. As a result, part of the gas molecules will be in an excited state and in a fraction of them an electron will be removed, creating a positive ion and a free electron pair. In gas at the condition used in HA-TPC, usually the yields of excitation processes, luminescence or scintillation photons are not intense enough to be detected. For this reason, this description will be neglected. On the other hand, the free electrons generated by the traversing particles can be collected and multiplied thanks to the presence of electric fields.
The number of primary ion-electron pairs released in a gaseous target is described by:

$$N_T = \frac{\Delta E}{W_I} \tag{3.1}$$

where the total energy loss in the medium $\Delta E$ and the average energy per ion-electron pair production $W_I$ (usually between 20 and 40 eV) are defined.
The energy loss due to Coulomb interactions for charged particles are summarized in the so called Bethe-Bloch equation[28]:

$$\frac{\Delta E}{\Delta x} = -\rho \frac{2KZ}{A\beta^2} \left[ \ln \left( \frac{2mc^2\beta^2}{I\left(1-\beta^2\right)} \right) - \beta^2 - \frac{C}{Z} - \frac{\delta}{2} \right]. \tag{3.2}$$

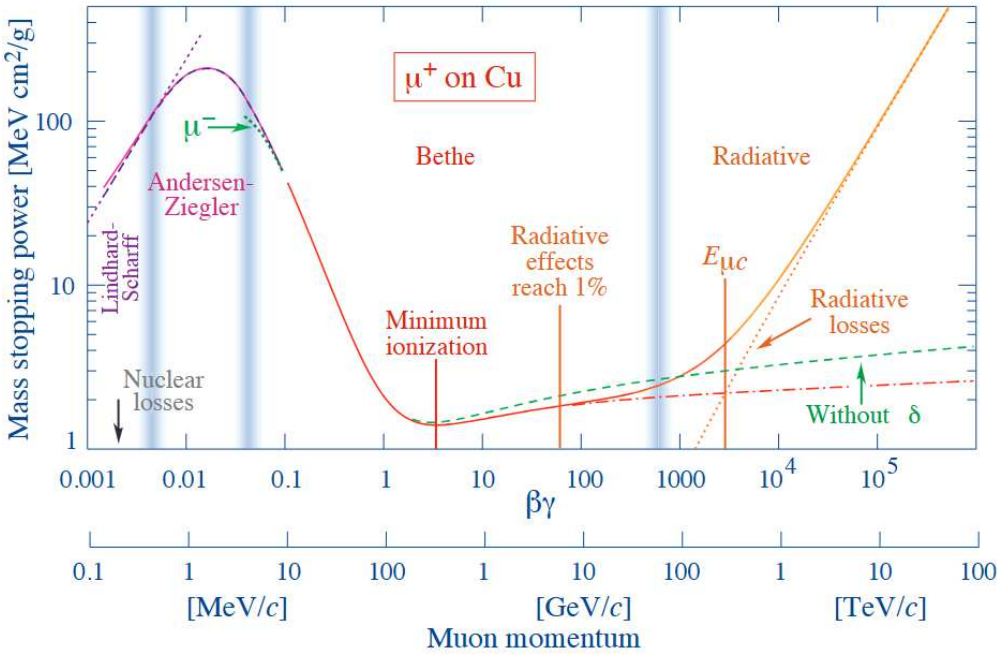


Figure 3.1: Differential energy loss for a positive muon in a copper medium as a function of its momentum. Picture from [28].

The equation 3.2 shows that the differential energy loss depends on: the particle (i) velocity $\beta$ and (ii) its electric charge contained in parameter K, and the medium (i) atomic number Z, (ii) mass number A and (iii) density $\rho$. Additional terms are present in order to consider the inner shell correction (C/Z), since the ionization efficiency decreases for deeper electronic layers due to screening effect and a density effect correction ($\delta/2$) from a collective interaction between the medium and the Coulomb field of the particle in ultra-relativistic regime. The differential energy loss for an anti-muon in a copper medium is shown in figure 3.1 as a function of its momentum. The plot shows that at low momenta the differential energy loss increases up to a local maximum and successively it decreases as $\propto 1/\beta^2$, reaching a minimum. In the minimum region, the particle is called Minimum Ionizing Particle (MIP). Successively, the differential energy loss increases due to relativistic effects.
The differential energy loss described by the Bethe-Bloch equation represents an average value, while single measurements present a variance that depends on both the particle and the medium properties. A large contribution to the variance is given by the probability of creating energetic secondary electrons, named $\delta$-electrons, that are able to ionize effectively the medium molecules. The presence of $\delta-$electrons in an event might cause a smearing of the ionization trails along the particle line of flight, with a worsening of the detector reconstruction capabilities. The normalized deviation from the most probable energy loss $\Delta E_{MP}$ is

$$\Delta = \frac{\Delta E - \Delta E_{MP}}{\xi}, \tag{3.3}$$

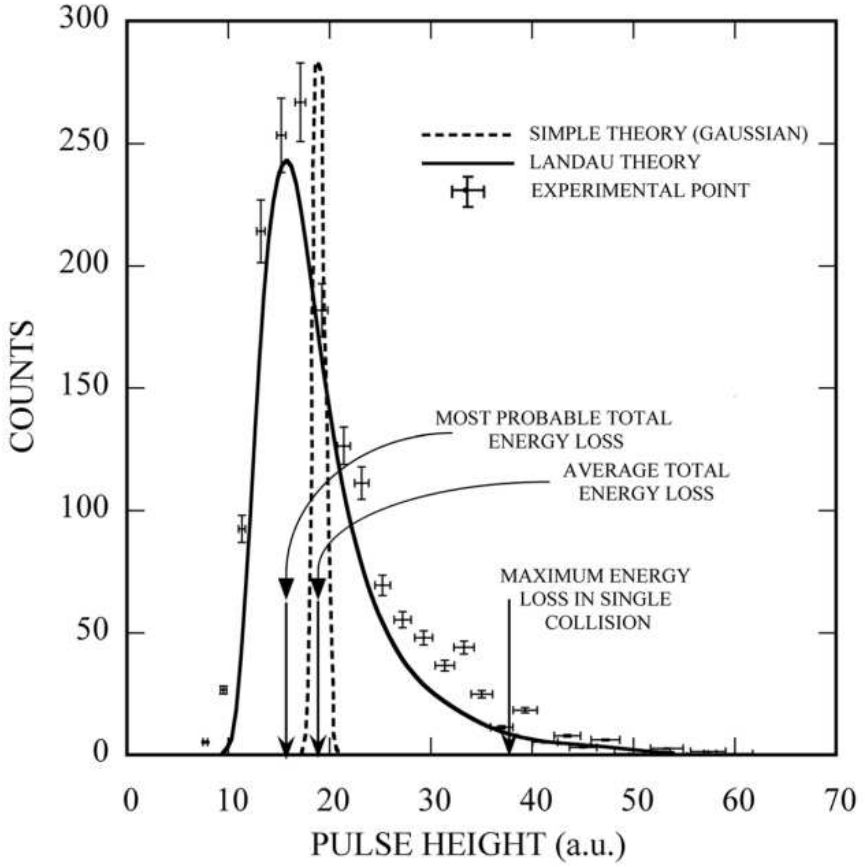


Figure 3.2: Comparison between experimental data and Landau theory calculation (solid line) of energy loss in thin sample of gas. The dashed line shows the Gaussian expectation for the same average energy loss. Picture from [100].

in which the parameter $\xi = K\frac{Z}{A}\frac{\rho}{\beta^2}x$ is defined[99]. The total energy loss is described by

$$f(\Delta) = \frac{1}{\sqrt{2\pi}} e^{-\frac{1}{2}(\Delta + e^{-\Delta})}, \tag{3.4}$$

that presents a typical high energy tail. Such distribution is named after the Russian physicist Landau. An example of such shape is reported in figure 3.2 compared to experimental data. A Gaussian distribution (dashed line) is clearly incompatible with the observed values.

## 3.2 Drift of electrons in gases

Free electrons moving in a gas with no external interference thermalize with the medium molecules at a thermal velocity according to Maxwell-Boltzmann law:

$$F(\varepsilon) = 2\sqrt{\frac{\varepsilon}{\pi(KT)^3}} e^{-\frac{\varepsilon}{KT}}, \tag{3.5}$$

where $k$ is the Boltzmann constant [101]. It follows that the average velocity is given by

$$\overline{v} = \sqrt{\frac{8kT}{\pi m}}, \tag{3.6}$$

with an average value at room temperature of about $10^7 \frac{\text{cm}}{\text{s}}$. A free electron in a gaseous detector might (i) be neutralized by a ion, (ii) be absorbed in the walls or (iii) attached to a molecule due to collisions. The latter usually is negligible for noble gases, but it becomes relevant for electronegative molecules. In oxygen, the average time needed for a thermal electron to be attached is about 200 ns. A localized distribution of particles moving in a gas diffuse symmetrically due to collisions according to a Gaussian distribution after a time $t$ as

$$\frac{dN}{N} = \frac{1}{\sqrt{4\pi Dt}} e^{-\frac{x^2}{4Dt}} dx, \tag{3.7}$$

in which $D$ is a diffusion coefficient. One might define the linear diffusion as $\sigma_x = \sqrt{2Dt}$.
In gaseous detectors, the information is usually carried by the free electrons which are directed towards sensors thanks to the use of an electric field. In ND280, a magnetic field is also present, therefore the motion of electrons in gas is influenced by both $\mathbf{E}$ and $\mathbf{B}$, according to:

$$m\frac{\mathrm{d}\mathbf{u}}{\mathrm{d}t} = e\mathbf{E} + e\left[\mathbf{u} \times \mathbf{B}\right] - K\mathbf{u}, \tag{3.8}$$

where $m$ and $e$ are electrons mass and charge, $\mathbf{u}$ is its velocity vector and $K$ describes frictional forces in the medium. Langevin introduced the concept of considering the term $K\mathbf{u}$ as a stochastic average over the random collisions of drifting particles, considering the ration $m/K$ as a characteristic time $\tau = m/K$. Introducing this simplification in 3.8, a solution for $\mathbf{u}$ is found:

$$\mathbf{u} = \frac{e}{m}\tau|\mathbf{E}|\frac{1}{1+\omega^2\tau^2}\left(\hat{\mathbf{E}} + \omega\tau\left[\hat{\mathbf{E}} \times \hat{\mathbf{B}}\right] + \omega^2\tau^2\left(\hat{\mathbf{E}} \cdot \hat{\mathbf{B}}\right)\hat{\mathbf{B}}\right), \tag{3.9}$$

in which the term $\omega^2 = (e/m)^2\,\mathbf{B}^2$ is introduced and is called Larmor frequency. For $\omega\tau = 0$, the equation 3.9 simplifies in the relation

$$\mathbf{u} = \frac{e}{m}\tau\mathbf{E} = \mu\mathbf{E}, \tag{3.10}$$

in which the proportional factor between velocity and electric field is defined as mobility $\mu$. This linear relation depends on the fact that up to very high fields, the average energy of electrons is almost not modified.
The intensity and direction of electric and magnetic fields influence greatly the velocity vector. In gaseous detector where the track reconstruction depends on the electrons drift position and timing it is crucial to guarantee uniform values for B and E in the drift volume. A typical setup for TPCs is the one where magnetic and electric fields are parallel. In this case, the relation simplifies to the same case described in 3.10, even though the results arise from different simplifications.
In the case of only an electric field involved, using a classic approach it can be derived that a relation between mobility and diffusion stands as shown in

$$\frac{D}{\mu} = \frac{\varepsilon_k}{e}, \tag{3.11}$$

where $\varepsilon_k$ is a phenomenological quantity defined as characteristic energy of electrons. In the thermal case, $\varepsilon_k = kT$. From this relation, an estimation for the linear standard deviation along the drift direction is found:

$$\sigma_x = \sqrt{\frac{2\varepsilon_k}{e}\frac{x}{E}} = \sqrt{\frac{2\varepsilon_k}{e}\frac{P}{E}\frac{x}{P}}, \tag{3.12}$$

where the dependence on the ratio between the electric field $E$ and the gas pressure $P$ is explicited. This ratio is defined as reduced electric field.
The addition of a magnetic field parallel to the electric one does not modify the effect on the velocity nor the longitudinal diffusion. In a cloud of electrons, the magnetic field modifies the usual linear path between two collision to circular trajectories which leads to a net decrease of the drift velocity with the exception of $\mathbf{E} \parallel \mathbf{B}$, where the drift velocity is unaffected as shown in equation 3.8. It can be shown that the transversal diffusion is reduced by a factor depending on $\omega\tau$:

$$\sigma_{Transveral} = \frac{\sigma_{Longitudinal}}{\sqrt{1+\omega^2\tau^2}}. \tag{3.13}$$

### Particle identification in gaseous detectors

The ionization caused by a charged track crossing a gaseous volume is an important information, since it depends on the type of particle and its energy. As previously shown in equation 3.2, the ionization distribution presents large tails that neither a proper mean nor variance exists. Given a number of pulse-height measurements on one track it is possible to measure a *strength of the ionization* I, that might be written as

$$I = Z^2 F_{g,m}(u), \tag{3.14}$$

where: Z is the atomic number of the particle; $F_{g,m}(u)$ is a parameter that depends on the gas mixture and its density. However, I depends also on the track length and the number of samples. By dividing $F_{g,m}(u)$ for its minimum value $F_{g,m}(u_{min})$ a curve which is approximately independent on the manner of ionization measurement

$$F_{g,m}^{(norm)}(u) = \frac{F_{g,m}(u)}{F_{g,m}(u_{min})} \approx F_g(u) \tag{3.15}$$

Typical distributions of $F_g(u)$ in Argon for: electrons, muons, pions, kaons and protons are shown in picture 3.3. Such distributions are identical to each other on logarithmic scale and are shifted with respect to one another by the logarithm of the particles masses ratios.

The simultaneous measurement of the momentum and the ionization of a particle results in a point in figure 3.3. Particle identification occurs when, considering the measurement errors, this point can be associated with one of such curves. For a good particle identification, both the vertical separation between the curves and the uncertainty $\delta I$ related to the ionization measurement are crucial.
In a particle experiment, a determination of the ionization as a function of the particle velocity is done with identified particles over a range of momenta, for example in test beams campaign or using cosmic rays events. The mathematical description of the ionization curve does not assume a closed mathematical form in many of the formulated theories (e.g. Bethe, Bloch). As reported in [101], in literature a description of measured ionization curve is given by:

$$F_g(u) = \frac{p_1}{\beta^{p_4}}\left\{p_2 - \beta^{p_4} - \ln\left[p_3 + \left(\frac{1}{\beta\gamma}\right)^{p_5}\right]\right\} \tag{3.16}$$

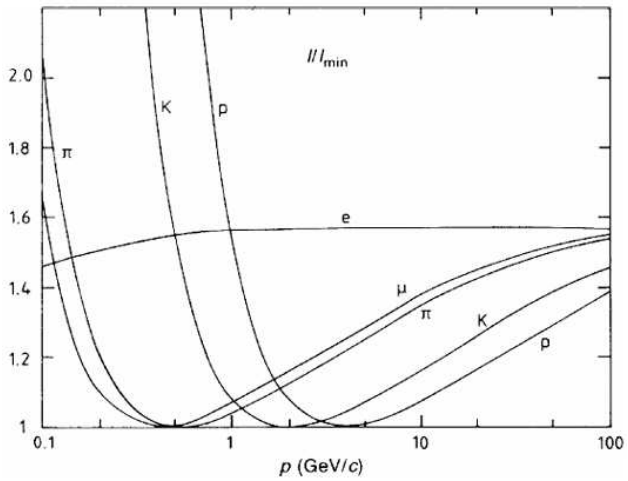


Figure 3.3: Most probable values of the ionization (normalized to the minimum value) in argon at ordinary density as function of the momenta of the known stable charged particles. Picture from [101].

in which five free parameters $p_i$ are present and $\beta = u/c$, $\gamma^2 = 1/(1-\beta^2)$.
Ionization measurements in various cells of a detector are usually entirely independent, neglecting the rare case of forward going $\delta-$rays that transports the ionization from one cell to the next ones. Considering $n$ independent ionization samples, one would like to derive a suitable estimator for the strength of ionization in a cell. The average of all $n$ values is subjected to a large fluctuation due to the non-finite average and variance of the Landau distribution 3.4. A good estimator might be derived from a fit to the shape of the measured distribution or from a subsample excluding the very high measured values. A simplified method is defined as *truncated mean*, in which the estimator for the signal strength $\langle S \rangle_\eta$ given a cut-off parameter $0 < \eta < 1$ is estimated by using the $\eta \cdot n$ lowest values among the $n$ signals $S_i$

$$\langle S \rangle_\eta = \frac{1}{m} \sum_{j=1}^{m} S_j, \tag{3.17}$$

where $m$ is the integer closest to $\eta \cdot n$. In many experiments, the truncated mean method is chosen over the fit to the ionization curve for its simplicity and similar performances.
The power of particle separation for a certain gas and readout sensors is the crucial point of the experiment. For example, in T2K TPCs the particle identification is performed by comparing the expected $F_g^i$ assuming that the particle is $i = e, \mu, \pi, p$ with the measured value as explained later in this chapter.

## 3.3 Time Projection Chambers

The design of gaseous detector may vary substantially depending on the experiment goal. In cases where the event separation is tied to the maximum drift time, the drift volume is kept relatively small. In cases where there are low rate events, long drift length can be used instead, providing a three dimensional track reconstruction of the traversing particle.
The Time Projection Chamber (TPC) was proposed by David Nygren[102][103], a drift chamber providing simultaneously non-projective track recognition, momentum measurement and particle

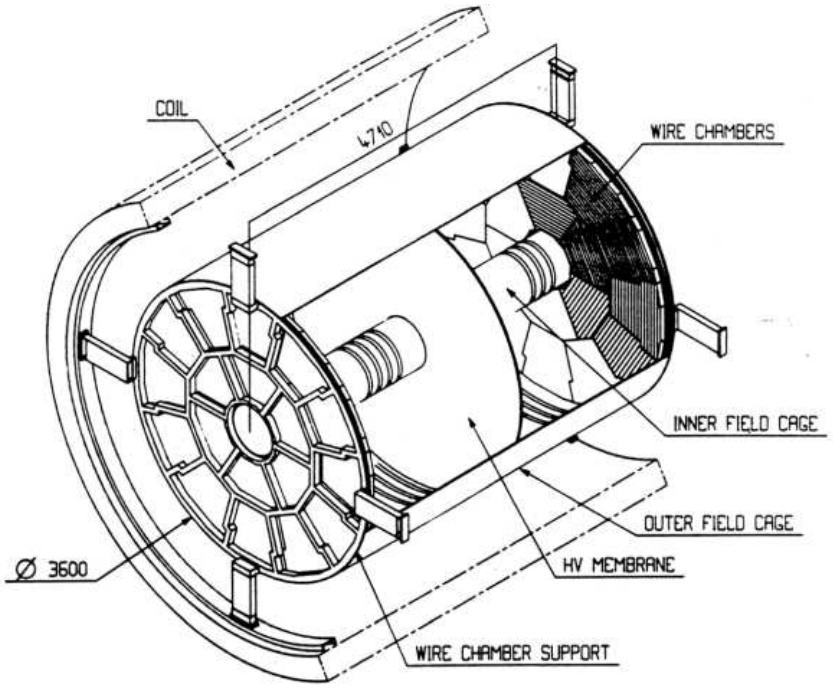


Figure 3.4: Drawing of ALEPH TPC structure. Picture from [105].

identification in a compact device[104]. TPCs consist in large volumes of gas with field shaping electrodes, terminating on one side with sensors for signal collection where electrons are drifted thanks to the presence of an electric field. The presence of a magnetic field reduces the transversal diffusion and might help in the localization of the drifted electron cloud.
Time projection chambers were used in several colliding beam and fixed target experiments due to their imaging capabilities for events with a large number of tracks involved. Since their memory time is of the order of tens of microseconds, they were used typically in (i) electron-positron storage rings (e.g. LEP at CERN and TRISTAN at KEK), (ii) low rate fixed target experiments (e.g. TRIUMF in Vancouver) and (iii) high multiplicity heavy ions collisions (e.g. ALICE TPC at CERN). A typical design consists in a central cathode and two halves with two instrumented endcaps at the two extremities. Usually the active volume is contained in a cylindrical structure named field cage which is also devoted to the shaping of the electric field, as shown by the scheme of ALEPH TPC in figure 3.4. In recent experiments, the readout is performed thanks to the presence of Micro Pattern Gaseous Detectors (MPGDs), that gradually replaced the detection by means of wires in gaseous TPCs. T2K experiment is using bulk MicroMegas detectors for vertical TPCs and resistive MicroMegas for the newly installed HA-TPCs that will be described in the next section.

## 3.4 The High Angle Time Projection Chambers (HA-TPCs)

During their years of data taking, the TPCs already installed in ND280[88] proved successful in providing crucial information for T2K for event reconstruction:

- 3D track reconstruction;
- charge measurement;

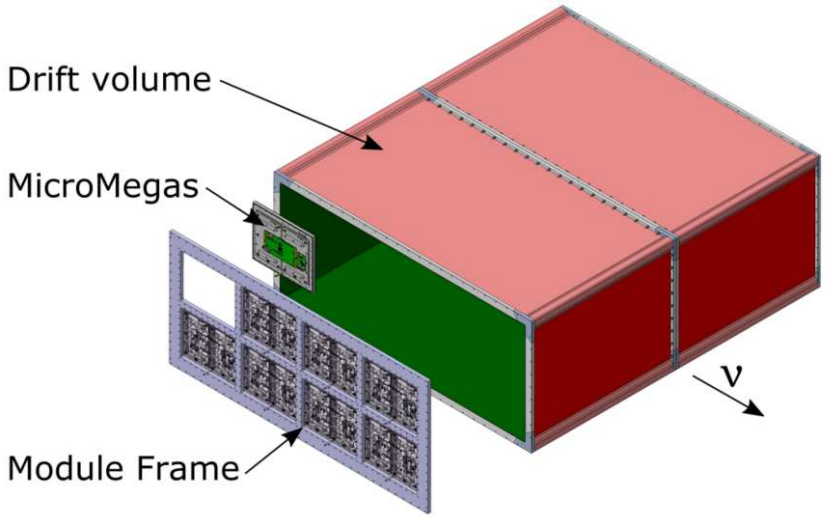


Figure 3.5: Sketch of a HA-TPC, in which one of the two instrumented anodes is visible, while the other is on the back. The cathode is placed in the middle of the active volume, corresponding with the visible flange. Picture from [96].

- momentum measurement;
- particle identification by a combination of dE/dx and momentum estimation.

Also, the performances are particularly remarkable for particles in the range of few hundreds of MeV/c up to few GeV/c, the energy of interest of ND280. Considering the previous reasons, the design of ND280 upgrade included two new TPCs (HA-TPCs) placed at the sides of the new active target SFGD, in a region where particles might reach energies as low as 200 MeV/c.
As already stated for vTPCs, HA-TPCs are designed for track reconstruction and particle identification with a particular attention in the separation between electrons and muons, to evaluate and quantify $\nu_e$ contamination in the $\nu_\mu$ beam.

### 3.4.1 HA-TPC structure

HA-TPCs are composed by two parallelepiped-shaped field cages with a common cathode in the middle and two active readout planes on the two extremities as shown in figure 3.5. The overall TPC dimension is about 2.0 m × 0.8 m × 1.8 m with a drift length of about 1 m per side. The nominal longitudinal electric field is equal to 275 V/cm, and its direction is such that it is aligned with the magnetic field given by UA1 magnet. Each of the anode is instrumented with 8 MicroMegas sensors that covers almost entirely the available surface and are supported by an aluminum frame. The active volume is filled with the so called *T2K gas*, a mixture of Ar:$CF_4$:i$C_4H_10$ = 95:3:2, in which electrons have an expected drift velocity of about 7.8 cm/$\mu$s. Hence, if an electron starts its drift at the cathode, the total drifting time is about 12 $\mu$s. Therefore, the number of samplings is set at 511 with a sampling frequency of 25 MHz that can be adjusted.
Each component of the HA-TPCs will be described in the next sections, with the exception of field cages, which will be described in the next chapter.

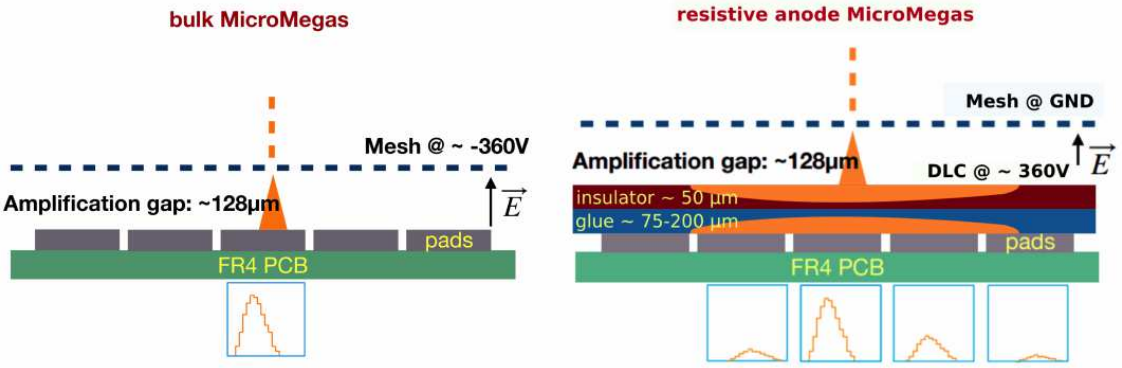


Figure 3.6: Sketch of a bulk Micromegas (left) and a resistive Micromegas (right).

### 3.4.2 Resistive Bulk MicroMegas Modules

In HA-TPCs, the drift electrons are collected and multiplied by an evolution of the micro-mesh gaseous chambers (MicroMegas) described by Giomataris in 1996[106]. A MicroMegas consists of a mesh (e.g. of woven steel) that separates a small gaseous amplification gap with a thickness of $\sim$ 100 $\mu$m from the active volume. In this region, the electric field is much more intense than in the rest of the TPC, in order to create avalanches to multiply the drifting electrons reaching the anode. In HA-TPCs, the magnitude of electric field in the active volume is $\sim$ 27 kV/m, while in the amplification region is set to $\sim$ 2700 kV/m. The amplification gap is delimited on the other side by a segmented plane that is devoted to charge collection. The plane is usually divided in pads with the dimensions of few to tens millimeters sides, in order to achieve an optimal spatial reconstruction. In each pad, the signal is induced by the drift of ions moving in the amplification region: usually electrons move very fast, hence their signal is too quick.
In recent years, resistive MicroMegas were developed with the instertion of a resistive layer between the amplification gap and the pads. This layer protects the pads from discharges that arise due to the very intense electric field in the amplification gap. Secondly, the presence of a resistive layer, in which free charges might spread, generates signal also in pads not directly hit by an avalanche. Therefore, by reconstructing the signal in more pads it is possible to achieve a good spatial resolution even with a less dense grid of readout channels.
MicroMegas belong to the Micro-Pattern Gaseous Detectors (MPGDs) category, which share similar purposes with different technology. Similar to MicroMegas, Gas Electron Multipliers (GEMs) are often used in TPCs. They consists in a series of planes with small holes ($\sim$ hundreds of $\mu$m diameter) in order to generate an intense local electric field for electron multiplication, that can be enhanced by placing multiple GEM planes. The advantage of MicroMegas is the presence of the mesh, that is able to capture the majority of ions created in the amplification gap, thus reducing the amount of positive free charge moving from the amplification gap to the TPC volume.
The sensors used as a readout of HA-TPCs are called Encapsulated Resistive Anode MicroMegas (ERAM), which feature the mentioned resistive layer for charge spreading. The production of ERAMs was performed by CERN/EP-DT-EF department. A detailed description of ERAMs production and characterization might be found in [107] and [108]. A schematic view of a ERAM section is reported in figure 3.6. ERAMs consist of a 42 $\times$ 34 cm$^2$ detector segmented into pads with sides 11.18 mm $\times$ 10.09 mm arranged into a 36 $\times$ 32 grid, for a total amount of 1152 pads. By summing all ERAMs, the total amount of output channels is 36 864. The pad plane is covered by a resistive layer made made of an insulated 50 $\mu$m Apical polymide foil pressed with 150 $\mu$m of

glue. On top, diamond-like carbon (DLC) is deposited by electron beam sputtering. Eventually, a SD45/18 woven stainless steel mesh is placed on top of the detector and supported by insulating pillars at a nominal distance of 128 $\mu$m, forming the amplification gap. A very large electric field ($\sim$2 700 kV/m) is set at the two sides of the amplification gap, creating local avalanches for a mean gain of about a factor of 1000. Due to the small gap and high field, the ions move very swiftly to the mesh and induce fast signals on the anode and are then mostly collected by the mesh. Electrons move to the DLC and spread on top of it according to the diffusion equation:

$$\frac{\partial \rho(r,t)}{\partial t} = \frac{1}{RC}\Delta\rho(r,t), \tag{3.18}$$

where $\Delta$ is the Laplace operator, $\rho(r,t)$ is the charge density function, R is the sheet resistance of DLC and C is the capacitance determined by the spacing between anode and readout planes. RC is usually denoted as $\tau$. The mathematical description of signal formation is presented in [109]. Considering a point-like source depositing on the DLC plane at $r = 0$ and $t = 0$, the spreading assumes a Gaussian distribution

$$\rho(r,t) = \frac{1}{4\pi(t/\tau)} e^{-r^2/4(t/\tau)}. \tag{3.19}$$

However, the ideal case approximation of a delta like deposition of charge does not take into account the transversal and longitudinal diffusion of electrons in the avalanche. For such reason, in the detector modeling, the charge density function is described by a initial Gaussian distribution:

$$\rho(r,t) = \frac{Q_e}{2\pi\sigma^2(t)} e^{-r^2/2\sigma^2(t)}, \tag{3.20}$$

in which $\sigma(t) = \sqrt{\frac{2t}{RC} + \omega^2}$, $\omega$ is the initial width of the charge deposition and $Q_e$ is the initial charge after multiplication.
In order to allow the charge spreading on more than one pad, a sheet resistance of about 400 k$\Omega/\square$ is chosen. The total charge collected by a single pad $Q_{pad}(t)$ is given by the integration of the charge density function over the pad surface. The output signal S(t) of ERAMs module is given by the convolution of the derivative of $Q_{pad}(t)$ and the electronic response function $ADC^D(t)$:

$$S(t) = \frac{dQ_{pad}(t)}{dt} * ADC^D(t) = Q_{pad}(t) * \frac{ADC^D(t)}{dt} \tag{3.21}$$

due to the properties of convolution.
The ERAMs characterization was performed at CERN in a dedicated test bench equipped with a $^{55}$Fe X-ray source and a 50 cm $\times$ 50 $\times$ 15 cm$^3$ plastic gas chamber, in which a scan over the ERAM pads is performed. From each spectrum, the average and the variance of the main peak are extracted. An example of ERAM-30 characterization is reported in figure 3.7 for both gain and resolution.

Due to charge spreading on DLC, a X-ray event that generates an avalanche on a pad usually record signals also for the neighbor 8 pads. A simultaneous fit of the signal according to equation 3.21 is used to estimate the value of RC locally.

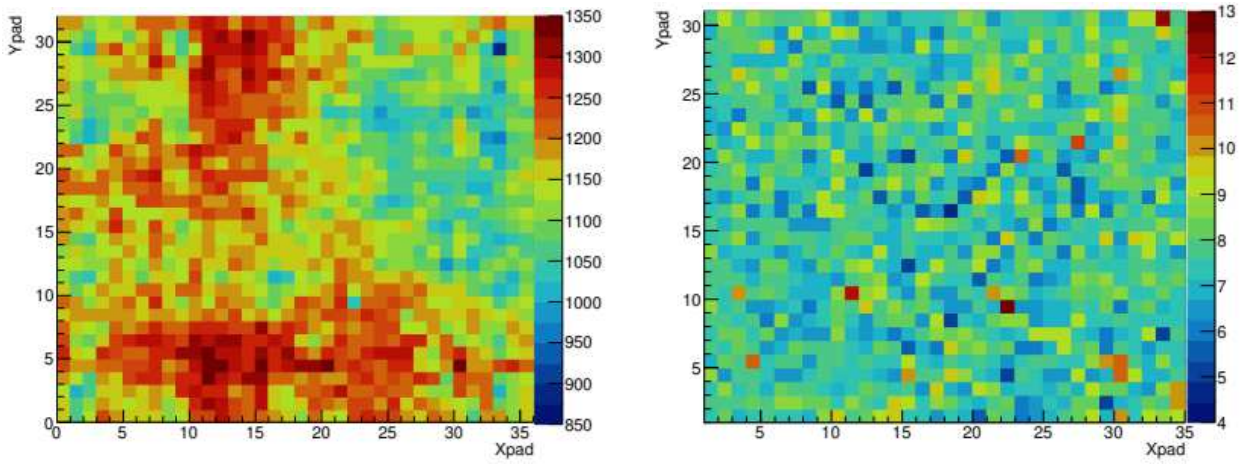


(a) (b)

Figure 3.7: Mean and variance of the main $^{55}$Fe peak for each pad in ERAM-30. Pictures adapted from [107].

### 3.4.3 Electronics

The readout electronics is based on the AFTER chip, described in [110], operated at a sampling frequency of 25 MHz, a peaking time of 200 or 412 ns and a gain such that 4096 ADC counts are reached for a pulse current carrying 120 fC of charge. Each ASIC reads 72 electronics channels connected to an array of 9 × 8 pads. Each detector module holds three kinds of electronic boards:

- Two Front-End Cards (FECs), with 576 channel each, that converts the analog signal in digital format using an octal-channel analog to digital converter. Each FEC hosts eight AFTER ASICs;
- a Front-End Mezzanine card (FEM), that controls the two FECs and performs elementary data processing (offset correction, zero-suppression and temporary data storage);
- a Power Distribution Card (PDC), that performs a local conversion of the externally provided higher voltage (24 V) to 4-5 V used by FECs and FEMs.

Shielding covers are designed to allow the operation of electronics inside the UA1 magnet. A scheme of ERAMs and the related electronics are reported in figure 3.8. All data from the two HA-TPCs are collected and sent to the Trigger and Data Concentrator Module (TDCM). The response of a Dirac current pulse is found to be proportional to:

$$f(t; w_s, Q) = e^{-w_s t} + e^{-\frac{w_s t}{2Q}} \left[ \sqrt{\frac{2Q-1}{2Q+1}} \sin\left( \frac{w_s t}{2} \sqrt{4 - \frac{1}{Q^2}} \right) - \cos\left( \frac{w_s t}{2} \sqrt{4 - \frac{1}{Q^2}} \right) \right]. \quad (3.22)$$

The response used in 3.21 is found from previous equation by introducing a proportionality factor

$$ADC^D(t; w_s, Q) = \frac{ADC_0}{Q_0} \frac{f(t; w_s, Q)}{f_{max}(w_s, Q)}. \quad (3.23)$$

The test and calibration of FECs is performed using an on-board pulser, to extract the parameters of the AFTER chip model $w_s$ and $Q$. In addition, the linearity response of electronics is tested.

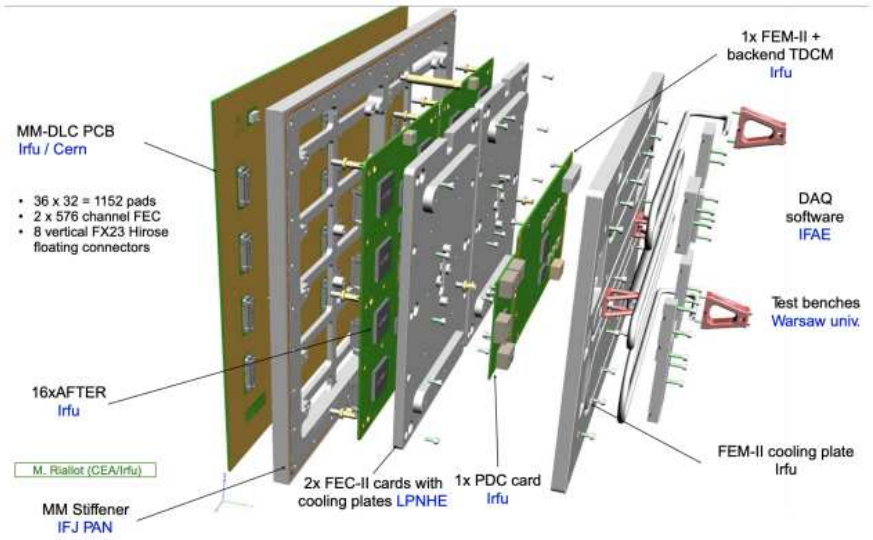


Figure 3.8: Schematic view of an ERAM module and the related electronics.

As a result, the linearity coefficients obtained from all the channels of two FECs shows a uniform response with differences in linearity between neighbor ASICs better than 3%.

### 3.4.4 Gas system

The upgraded configuration of ND280 includes five TPCs, with a total gas volume of 18.4 $m^3$. The presence of $CF_4$ in the gas mixture, the system is based on gas recirculation, with a fresh injection of gas of about 10%. In order to mantain the contamination of $O_2$, $CO_2$ and $H_2O$, the baseline circulation of gas flow is set to 1 volume exchange every 6 hours.
The gas system is connected to the 5 gases used by TPCs: Ar, $CF_4$ and $iC_4H_{10}$ as active volume; $CO_2$ for insulation and $N_2$ to control pneumatic valves. The gas system is designed to properly mix the mentioned gases and the circulation is designed in a closed loop for keeping under control the operational costs.

### 3.4.5 Gas Monitoring Chambers (GMCs)

The gas flowing in the TPCs is monitored by the presence of dedicated GMCs, which are designed to provide estimations of drift velocity and gas amplification over time. In particular, the gas properties depend on the contaminant concentration monitored by the gas system and on the pressure and temperature of the system. It can be shown that the relative change of gain in ND280 pit is mainly due to the change in the atmospheric pressure which alters the gas density.

## 3.5 Assembly and installation of HA-TPCs

Once the characterization and validation tests on each part of HA-TPCs showed the possibility to proceed, the detectors were assembled at CERN.
First, the procedure required the installation of the cathode on one of the two field cages, then thanks to supporting tables the two field cages composing an HA-TPC were aligned and fixed together with the use of G10 screws. In the region near the cathode, the presence of metallic parts

Figure 3.9: Picture from inside the TPC in which the mesh is visible (left).

would create an increase in the local electric field that might seriously affect the HA-TPCs safety requirements. In between the two sealed flanges, the gas tightness is ensured by means of two O-rings placed in dedicated grooves. A third and deeper groove is designed to house an insulating panel, in order to increase the possible path of the charge from the cathode to the external shielding placed at ground. Tests on mechanical and gas tightness performances of HA-TPCs structure were performed and the results are presented at the end of the next chapter.
Successively, the module frames were mounted on the field cages and sealed with aluminum plates. After a very attentive cleaning process, the TPC structure was transferred to a clean room for the installation of ERAMs. A particular attention was used in order to reduce the possibility of having grains of dust on the ERAM surfaces, which might cause local discharges and alterations of RC values. Inside the clean room, the aluminum plates on the module frame were removed and replaced with ERAMs. A look from the inside of HA-TPCs can be seen in picture 3.9. After a preliminary leak test with helium, the HA-TPC was moved outside of the clean room and a long term leak test was performed. Eventually, the high voltage connector is installed on the central flange to supply the HV to the cathode through a dedicated passage on the flange. The central flange was then wrapped in a Mylar insulating film and covered by an aluminum foil, which connects the shieldings on the field cages. A picture of a HA-TPC ready before cosmic data taking is shown in figure 3.10.
HA-TPCs were shipped to J-PARC in two different moments, since the detector components were produced and assembled in subsequent periods. The first HA-TPC reached J-PARC in August 2023, while the second arrived in April 2024. The final setup of ND280 basket before the installation of the last TOF panels is visible in figure 3.11.

## 3.6 Reconstruction in HA-TPCs

HA-TPCs are designed to provide an estimation of a charged track momentum and its energy loss, which is used as a discrimination for particle identification.
The signal collected by ERAMs, see equation 3.23, is stored as amplitude over time and it is called *waveform*. Waveforms are the fundamental steps from which the reconstruction algorithms are

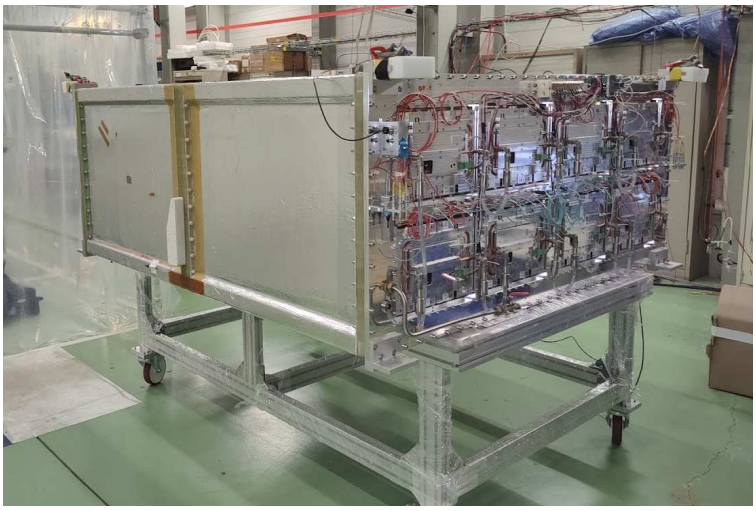

Figure 3.10: Picture of the first HA-TPC at CERN. On the right, one endplate is visible, in which FECs and FEMs are mounted on ERAMs.

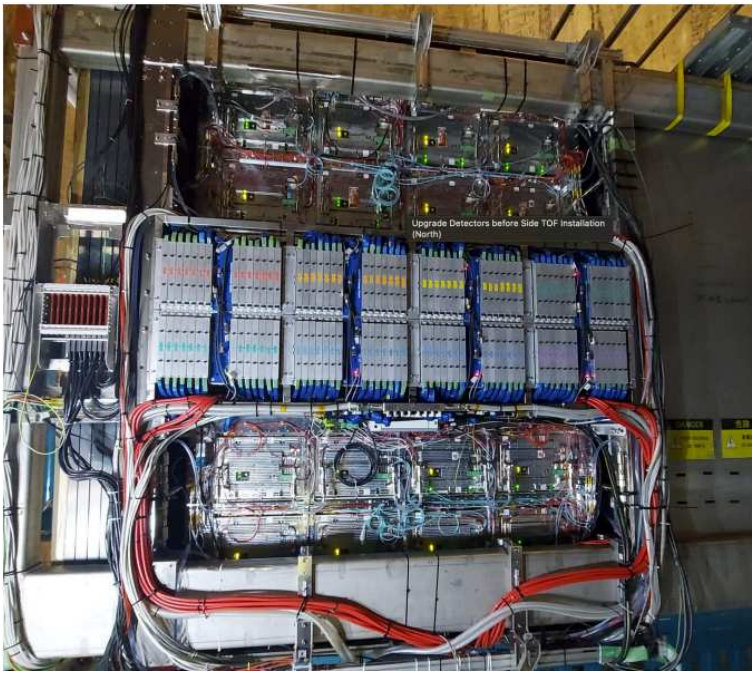


Figure 3.11: Picture of the SFGD (middle) and the two HA-TPCs on top and bottom installed in the ND280 basket in April 2024.

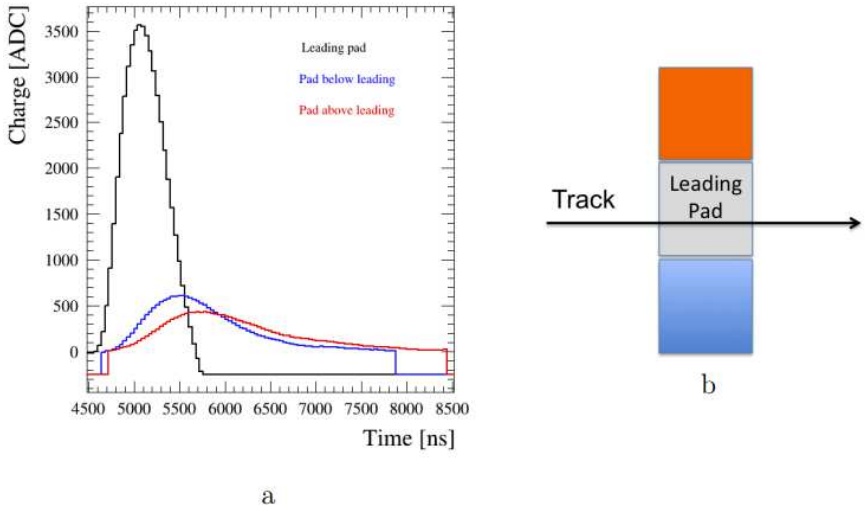


Figure 3.12: On the right a vertical cluster with a leading pad and two secondary pads is shown, with an horizontal track crossing the leading pad. On the left, the corresponding waveforms are visible with a clear difference between the leading and secondary pads. Picture from [97].

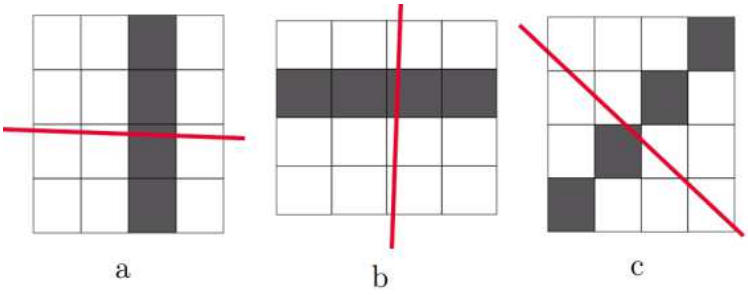


Figure 3.13: Shapes of cluster used for spatial reconstruction with horizontal (a), vertical (b) and diagonal (c) orientations. Red line represents the typical inclination of tracks for which each cluster is used. An additional cluster direction similar to (c) is used for diagonal tracks moving with negative slope in ERAMs plane. Picture from [111].

developed. Usually, pads whose signal is due to the direct development of avalanches in the gap region are referred to as *leading pad*, while pads in which the signal is due to charge spreading on DLC are called *secondary pads*. Waveforms of leading pads are usually larger with respect to secondary pads and the time interval from the trigger to their peak is compared with information from other detectors in ND280 to determine the starting position in the drift direction. For secondary pads, the peak is usually delayed in time and therefore they are not reliable for the estimation of the drift distance. A typical example of such differences is reported in figure 3.12, in which the signal for a leading pad and two secondary pads are shown. In order to reduce the memory size of an event, signals are cut once they fall below a threshold calibrated per each channel (∼250 ADC). A signal over a certain threshold (usually 250 ADCs) collected by a pad in a short amount of time (usually about few tens of sampling times) is associated with a *hit*, which are identified by looking for local maxima in a channel signal. In the 512 sampling time window, multiple tracks might release signal in a single pad. A maximum is identified if the previous 5 time bins and the next 5 bins are smaller than it. An example is reported in 3.14. Therefore, it is possible that in a single event, a single

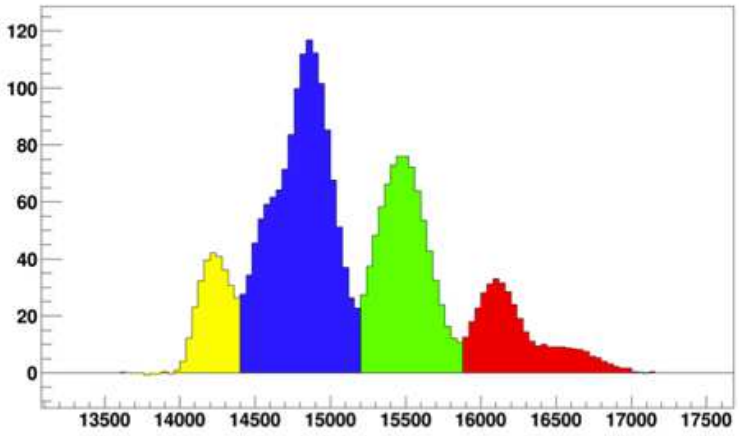


Figure 3.14: Example of waveform segmentation for several maxima in a channel. Picture from T2K-TN-466.

pad might be associated with more than one *hit*. Tracks are identified by grouping hits using the TRex algorithm, based on A* path-finding algorithm. TREx separates each event into patterns and finds the edges and junctions, points where two or more tracks intersect, within each pattern. The algorithm connects the junctions and edges by finding paths using A* algorithm. Tracks are required to give a continuous signal on an endplate (no gaps are allowed). Due to charge spreading, it might happen that two tracks are recognized as one since their signals are not enough separated. Once hits are grouped into patterns, neighbor hits are arranged in clusters, whose shape depends on the local estimation for direction of the track projection in the ERAM plane. Clusters might be oriented horizontally, vertically or diagonally as shown in picture 3.13, with the following limits:

- -90° $\leq \theta <$-60° or 60° $\leq \theta <$ 120° (vertical tracks);
- -60° $\leq \theta <$-28° (diagonal tracks going down);
- -28° $\leq \theta <$ 28° (horizontal tracks);
- 28° $\leq \theta <$ 60° (diagonal tracks going up).

### 3.6.1 Spatial reconstruction

The three dimensional reconstruction of track position is fundamental for the particle momentum estimation due to the presence of magnetic field. The transverse momentum resolution in HA-TPCs is estimated by using the Gluckstern formula[112]:

$$\frac{p_T}{\sigma_{p_T}} = \sigma_{ZY} \frac{p_T}{qBL^2} \sqrt{\frac{720}{N_P + 4}}, \tag{3.24}$$

which shows that the resolution is inversely proportional to (i) the charge magnitude, (ii) the field strength B, (iii) the track projection length L and (iv) the number of equidistant independent observations $N_P$, which in HA-TPCs are assumed to be the clusters. On the other hand, the resolution is directly proportional to (i) the transverse momentum $p_T$ itself and (ii) the point resolution in the transverse plane $\sigma_{ZY}$, also named *spatial resolution*.
Spatial resolution was estimated in several test beams and cosmics data taking with HA-TPCs

prototypes and full scale detectors. The latest validated algorithm for spatial reconstruction is called *log(Q) method*, which is an empirical method for the estimation of the track position in each single cluster.
Applying the log(Q) method requires sorting the pads in a cluster in decreasing order according to their maximum amplitude $Q_{max,i}$ (denoted from now on as $Q_i$), with $i = 0, ...n-1$ referring to the $(i-1)-th$ pad. Usually, the cut on the number of allowed pads in a cluster (named *multiplicity n*) is set to 4. For larger multiplicity, it is likely that such cluster might be due to multiple tracks recognized as one or the presence of $\delta$-rays, since the spreading does not cause significant signals after about a centimeter.
Successively, the ratio of $Q_i$ are computed in order to obtain the track position estimation. For n=2, only one ratio is possible, while for $n = 3$ there are two important values: (i) $L_{10}$=log$(Q_1)$/log$(Q_0)$ and (ii) $L_{21}$ =log$(Q_2)$/log$(Q_1)$. If the track is close to the edge of two pads, then it is more likely that the information obtained from $L_{10}$ is more useful for the position reconstruction, otherwise if $L_{10}$<-1.2 then the ratio $L_{21}$ is used for the estimation of the track displacement from the center of the leading pad in the axis perpendicular to the cluster orientation. In the two cases, the displacement $dx$ is obtained as:

$$dx = \alpha_{10} L_{10}^3 + \beta_{10} L_{10} + \frac{\text{pad}}{2} \tag{3.25}$$

or

$$dx = \alpha_{21} L_{21}^3 + \beta_{21} L_{21} \tag{3.26}$$

in which $\alpha_{10}, \beta_{10}$ and $\alpha_{21}, \beta_{21}$ are empirical parameters estimated on cosmics data and "pad" is the pad dimension in the direction of the cluster (i.e. width, height or diagonal). The direction of the shift $dx$ is assumed positive if it is towards top or right of the leading pad center depending on cluster orientation. For example, if in equation 3.25 $L_{10} = 0$ (i.e. $Q_0 = Q_1$), then the track is expected to pass on the edge of the leading pad $dx = \frac{\text{pad}}{2}$, in which the shift $dx$ is toward the pad with the second highest maximum amplitude $Q_1$.
Once the position estimation in each cluster is obtained, the information on ERAM planes is combined with the timing information in order to obtain a point in 3D space. Those points are fitted with a helix, from which the radius R and the center of the circumference $(Z_0, Y_0)$ drawn by the track in the transversal plane are estimated. The radius R is linked to the particle momentum by the Larmor equation:

$$R = 3.3\text{m} \frac{(\gamma m v_T)/(\text{GeV/c})}{(|q|/e)(\text{B}/T)} \tag{3.27}$$

in which $e$ is the magnitude of the elementary charge.
Once the helix fit is performed, for each cluster the residuals between the reconstructed coordinates of the cluster and the corresponding coordinates from the fitted track are computed as

$$r = \sqrt{(y_{\text{rec}}^{\text{cluster}} - Y_0)^2 + (z_{\text{rec}}^{\text{cluster}} - Z_0)^2} - R, \tag{3.28}$$

where $R$ is the radius of the helix. A sketch of a residual for a single cluster is reported in figure 3.15.

The performance of spatial reconstruction algorithm is evaluated by computing the root mean square (RMS) of the distributions of the residuals $r_j$ of each cluster $j$ point estimation with respect

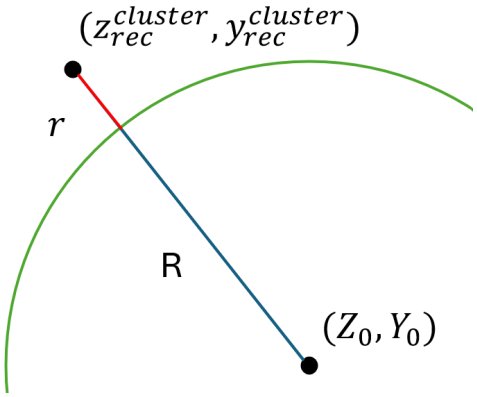


Figure 3.15: Example of a residual (red line) for a single cluster once helix fit is performed (green line). The typical radius R of the helix is greatly reduced for an improved visualization.

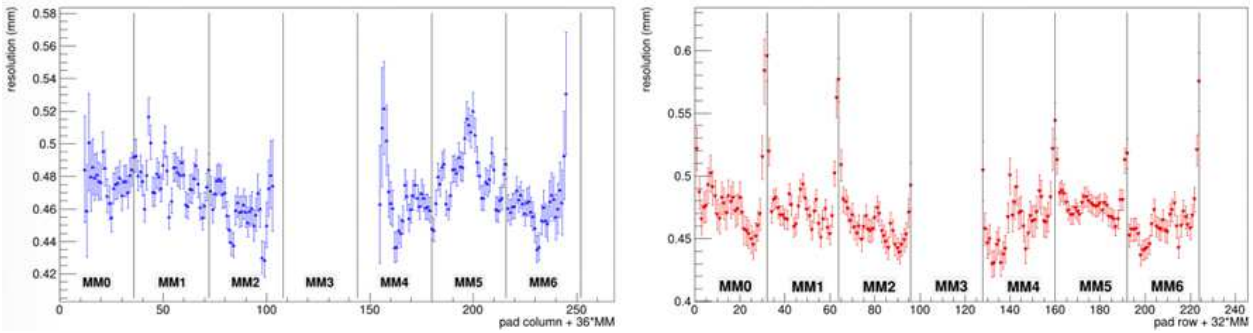


Figure 3.16: Spatial resolution as a function of MMs column (left) and row (right). Pictures from T2K-TN-466.

to the trajectory from the helix fit:

$$(\text{resolution})^{\text{RMS}} = \sqrt{\frac{1}{N_{clusters}} \sum_{j=1}^{N_{clusters}} r_j^2}. \tag{3.29}$$

The spatial resolution has been estimated in the HA-TPCs using $10^4$ muons from cosmic rays events collected at CERN. The resolution as a function of MMs columns and rows are reported in figure 3.16. Since the distributions of collected tracks is not homogeneous due to the placement of scintillator panels for trigger, the resolution is not computed for MM3 and MM7.

The spatial resolution is expected to improve near the anode and to consistently worsen at large drift distances due to charge diffusion while drifting. A study on spatial resolution as a function of drift distance was performed with the same dataset and compared to simulation as reported in figure 3.17. The experimental points were fitted with the function

$$\sigma(d_d) = \sqrt{\sigma_0^2 + C_{diff}^2 / N_{eff} d_d}, \tag{3.30}$$

where: (i) $C_{diff}$ is the transversal diffusion constant and (ii) $N_{eff}$ is the number of effective electrons[113]. Simulated points show a similar trend to experimental data, but the spatial res-

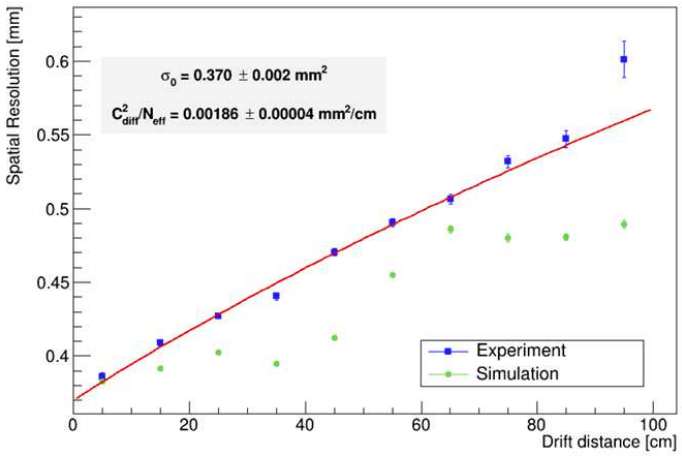


Figure 3.17: Spatial resolution in data (blue) and MC simulations (green) for HA-TPCs as a function of drift distance. Pictures from T2K-TN-466.

olution is consistently better.

### 3.6.2 Estimation of Energy Loss per unit of Length (dE/dx)

The energy deposition of charged tracks in HA-TPCs and the momentum information are used for identification of charged particles, mainly muons or electrons (and their anti-particles in anti-neutrino mode). In this section I will describe the method developed for DESY test beam in 2021[98][111] named $WF_{sum}$, even if other methods are currently under development.
The reconstruction algorithm is still based on the clustering procedure used for spatial reconstruction. However, rather than using the maximum amplitude of single waveforms, the waveforms of pads are summed time bin per time bin:

$$WF^j_{sum}(t) = \sum_{i=0}^{n} WF^j_i(t) \tag{3.31}$$

and the maximum of $WF^j_{sum} = WF^j_{sum}(t_{max})$ is taken for each cluster j=1,...,N. In this way, the goal is to avoid the double counting due to charge spreading from the leading pad to secondary pads, whose peaks are delayed in time. For this reason, the definition of $WF^j_{sum}$ as a direct sum of the individual maxima $Q_i$ is discarded. As seen in figure 3.2, in which the Landau distribution is presented, a way to reduce the fluctuations in energy loss estimation is to compute a truncated mean of the energy deposit $C_T$. Clusters are sorted in ascending order according to their $WF^j_{sum}$ and the largest ones are excluded from the computation by a cut-off on the percentage of clusters by a parameter $\alpha$:

$$C_T = \frac{1}{\alpha N} \sum_{j}^{\alpha N} WF^j_{sum} \tag{3.32}$$

in which the optimal $\alpha$ value was estimated to be about 0.7. Therefore, 70% of clusters are kept for dE/dx estimation, avoiding the ones with larger charge deposit. In addition, the dE/dx estimation requires to take into account the length of the track in a cluster, which is particularly important for diagonal clusters due to their particular shape. In the two extreme cases, a track might pass near

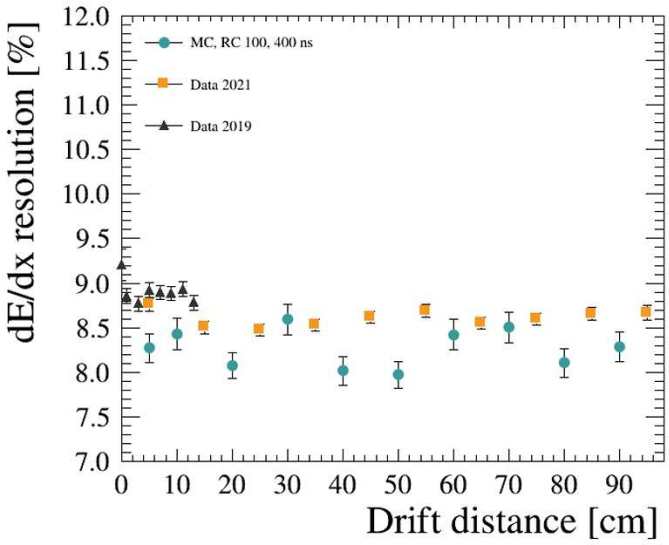


Figure 3.18: dE/dx resolution as a function of drift distance for HA-TPC prototypes in 2019 (black) and 2021 (orange) compared with simulated data (light blue). Picture from [111].

the vertex of a leading pad or along the pad diagonal with a difference in length up to about 1.5 cm. For this reason, once the track is reconstructed, the estimator $WF^j_{sum}$ is normalized to the expected value for a segment of 1 cm. A summary of dE/dx resolution estimation for HA-TPC prototypes as a function of drift distance is shown in figure 3.18, with a comparison between data and Monte Carlo simulations. The estimated resolution is almost uniform in the whole drift distance and better than 10%. An in depth study on spatial resolution and dE/dx capabilities of full scale HA-TPCs is in preparation at the moment of the submission of this work.

Particle identification in HA-TPCs is particularly important for distinguishing electrons and muons, a task which requires a dE/dx resolution better than 10% for a $3\sigma$ separation for electrons and muons hypotheses. For a given particle, the energy loss per unit of length in gases changes as a function of its momentum as shown in figure 3.1. In HA-TPCs, the energy loss per unit of length is parametrized by the expression

$$C_E = \frac{p_0}{\beta^{p_3}} p_1 - \beta^{p_3} - \log\left[p_2 + \frac{1}{(\beta\gamma)^{p_4}}\right], \tag{3.33}$$

which represents the expected dE/dx under a given particle hypothesis as parametrized in equation 3.16. As reported in detail in [111], the parametrization of dE/dx for muons, electrons and protons were generated using the "nd280Geant4Sim" framework presented in the next section. The produced samples were subsequently processed with "detResponseSim" and "hatRecon" in order to simulate an electronics response and reconstruct the tracks in HA-TPC. Muons were simulated with kinetic energies ranging from 0.05 GeV/c to 2.1 GeV/c, incrementing in steps of 50 MeV/c. Similarly, electrons and protons were simulated within the energy range of 0.1 GeV/c to 2.1 GeV/c in steps of 200 MeV/c. In total, 2000 particles were generated for each energy sample. The dE/dx distribution for muons and electrons in MC simulations is shown in figure 3.19. The particle identification is performed by introducing the *pull*

$$\delta_E(i) = \frac{C_T - C_E(i)}{\sigma_E(i)}, \tag{3.34}$$

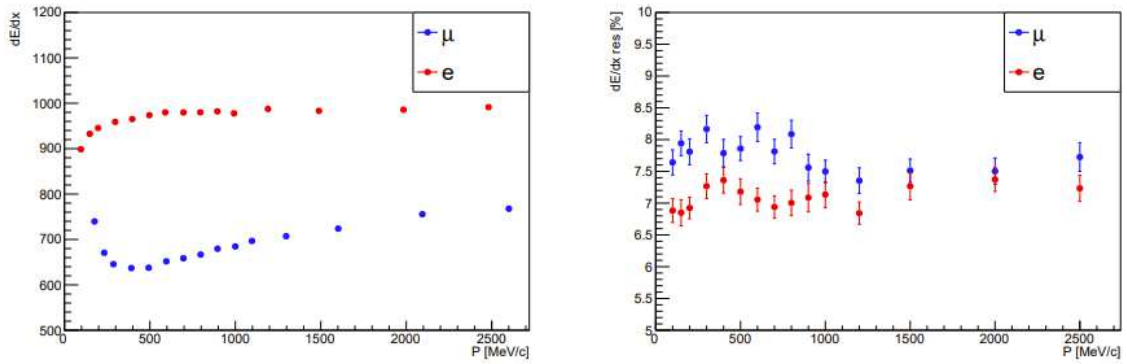


Figure 3.19: Estimator of dE/dx for electrons and muons in simulations as a function of particle momenta on the left. On the right, the resolution for dE/dx estimation related to the same population is reported. Pictures from [111].

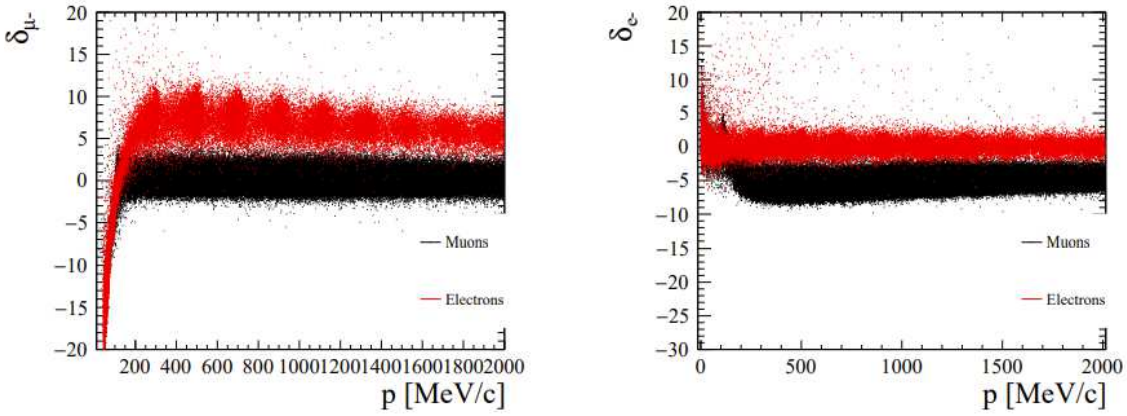


Figure 3.20: Pulls distributions for muon and electron hypotheses applied to a muon (left) and electron (right) simulated samples. Pictures from [111].

in which the measured $C_T$ is compared with $C_E$ for each of the five particle hypotheses $i$ = electron, muon, pion, kaon and proton. Pulls for muon and electron hypotheses are shown in picture 3.20, in which the correct hypothesis follows a Gaussian distribution centered in zero excluding the particle at momenta below 200 MeV/c. The pulls for electrons and muons show a good separation capabilities for momenta above about 200 MeV/c.

## 3.7 Simulation of HA-TPCs

The simulation of events in HA-TPCs is included in ND280 Software framework. The first step is performed by GEANT4[114], which simulates the passage of particles through matter: in the case of HA-TPCs, the position of primary ionization clusters in gas are generated. In order to consider the fluctuation in ionization, the PAI model with a 1 mm step is used[115]. Secondly, the drift of electrons is performed numerically, taking into account the non-ideal values of electric and magnetic field maps. The position and arrival time of each ionization electron are distributed on the sensors plane using a Gaussian distribution due to a transverse diffusion of $\sigma_{trans} = 286\ \mu m/\sqrt{cm}$ and a longitudinal diffusion of $\sigma_{long} = 210\ \mu m/\sqrt{cm}$. Once an ionization electron arrives to the ERAM,

the amplification is simulated based on the ERAM gain G. The process is performed by considering a Polya distribution.
Signal formation in ERAMs is simulated by considering the 2D charge spreading mechanism presented in section 3.4.2 and it requires particular optimization since it could become particularly time consuming. In fact, two methods are introduced to reduce the amount of computation needed. First, the pad is divided in a regular grid of subpads (e.g. 5×5) and all the avalanches that should happen inside the same subpad are merged. The final charge Q is computed as the sum of the each single contribute.
Secondly, the convolution operation introduced in 3.21 is pre-computed and tabulated considering: (i) a unit charge, (ii) a fixed RC value, (iii) a grid of coordinates for the arrival position on the ERAM plane, dividing the pad in a set of subpads with a tunable step. The standard value is set to a 10×10 grid of subpads. The process is repeated for each electron reaching the ERAM plane. The waveform $WF(t)$ is obtained by multiplying the waveform obtained for a unit charge $WF_{unit}(x_i, y_i; t)$ by the the total charge $Q_i$ in a single subpad obtained in the previous step:

$$WF(t) = \sum_{i}^{grid} Q_i WF_{unit}(x_i, y_i; t). \tag{3.35}$$

The main approximation in the method is the assumption that the charge in an avalanche arrives at the center of each subpad.

## 3.8 Test beams for HA-TPC prototypes

The technologies involved in the realization of HA-TPCs were tested throughout the years with several test beam campaigns since 2018. Firstly, an ERAM prototype was mounted in the former HARP TPC field cage, which is a 2 m long and 0.8 m diameter cylindrical volume that provides 1.5 m drift region. The cathode and Micromegas were mounted on the opposite edges of the cylinder and cathode was set at 25 kV, providing a drift field of 167 V/cm. The experimental setup was exposed to a beam of electrons, muons, pions and protons at T9 experimental area at CERN. As reported in [116][117], the energy resolution of $\sim$ 9% for electrons and $\sim$ 11% for pions was estimated, while spatial resolution was estimated to be better than 500 $\mu$m at the largest drift distance. Successively, in 2019 a prototype of ERAMs has been designed, built and exposed to an electron beam at the DESY II test beam facility[97]. The data have been used to characterize the charge spreading and to produce a RC map. Spatial resolution better than 600 $\mu$m and energy resolution better than 9% are obtained for all incident angles, in compliance to the requirements for ND280 Upgrade. In the test beam, a prototype of field cage was not yet ready. Successively, other two beams test were performed in 2021 at DESY[98] and at CERN now with the final version of the field cage for HA-TPCs, but on a smaller scale for validation before starting the production.
The DESY prototype was equipped with an ERAM connected to four Another Readout Cards (ARCs) electronics cards, differently to the actual electronics setup presented in this chapter. The field cage prototype was designed to house just a single ERAM, but with the same drift length of the actual HA-TPCs. A test beam was performed in DESY facility T24 experimental area, where a superconductive magnet was available in order to create a magnetic field up to 1 T. A beam of electrons up to 4 GeV in energy was used for characterize the detector performances. The detector was able to rotate thanks to a mechanical support designed for such purpose. As shown in picture 3.21, spatial resolution better than 800 $\mu$m and dE/dx resolution better than 10% are observed for all the incident angles and for all the drift distances of interest. All the main features of the data

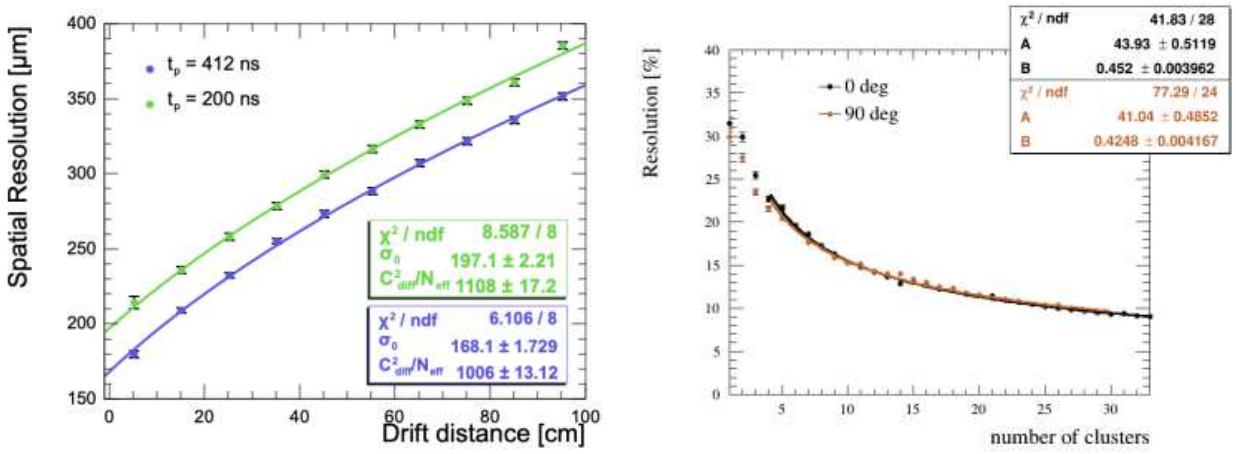


(a) (b)

Figure 3.21: Perfomances of HA-TPCs prototype at 2021 DESY test beam[98]. Left picture shows spatial resolution as a function of drift distance, while right picture shows the energy loss resolution as a function of number of clusters in a track as defined in 3.13 (vertical or horizontal option).

are correctly reproduced by the simulation and these performances fully fulfill the requirements for the HA-TPCs of T2K. The last test beam for HA-TPCs was performed in 2022 at CERN. Initially, a test with the full scale HA-TPCs was expected, however due to a major delay in field cage preparation, the test beam was performed with a replacement able to host 8 ERAMs at the same time. The substitute field cage is referred to as *mock up* since it was designed to perform only mechanical tests and its electrical properties were not optimal. In addition, the walls are formed by only G10 panels, increasing the radiation length of incoming particles.
The full scale prototype was placed in T9 experimental area at CERN, where it was exposed to a beam of electrons, muons, pions and protons produced by Proton Synchrotron (PS) accelerator. A picture of the setup is reported in figure 3.22.

As summarized in [111] and reported in figure 3.23, even with a non-optimal field cage, the full scale prototype showed optimal results for the electron sample: (i) spatial resolution better than 500 $\mu$m and (ii) dE/dx resolution better than 8%. Additionally, the dE/dx for different kind of particles were compared as a function of energy with similar results.

**Personal contribution to test beams** I contributed to the 2021 DESY test beam in several key areas: (i) the assembly and commissioning of the field cage and prototype TPC at INFN Legnaro National Laboratories (LNL), (ii) the preparation and commissioning of the gas system at LNL, and (iii) the commissioning and data taking of the prototype TPC at DESY. These activities were completed before I began my Ph.D. program, as documented in my Master's thesis [118]. Regarding data analysis of the DESY test beam, I contributed to the study of the $E \times B$ effect caused by non-uniformities in the DESY magnet.

The same instrumentation was later used in the 2021 CERN test beam, where I additionally contributed to setting up a silicon strip tracker for 2D track reconstruction, alongside preparing the TPC prototype and participating in data taking. For data analysis, I was involved in aligning the silicon tracker with the TPC.

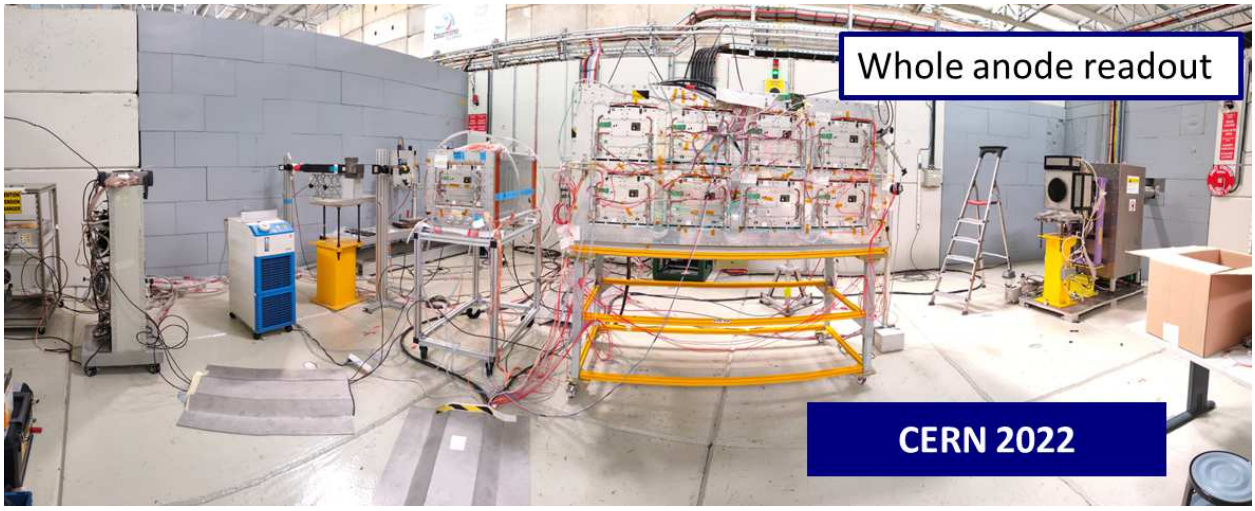


(a)

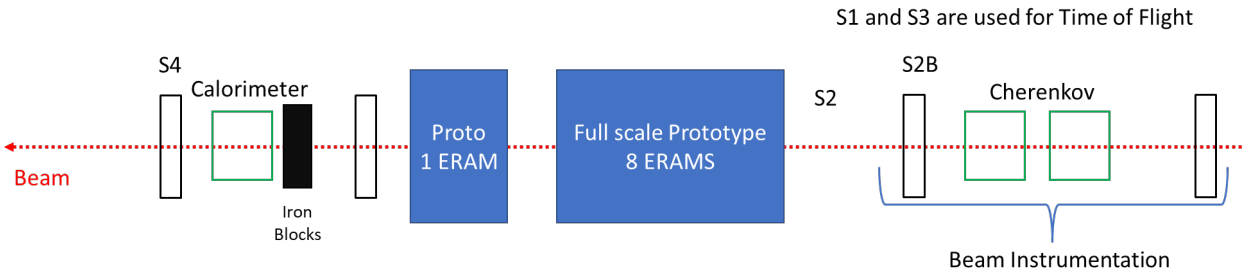


(b)

Figure 3.22: On top, a picture of CERN 2022 test beam setup is reported. In the center, the HA-TPC prototype with a single full scale field cage instrumented with 8 ERAMs is placed near to the small prototype used for DESY 2021 and CERN 2021 test beams. On the left of the picture, the gas rack containing the gas analysis branch is visible. The bottom picture is a schematic view of the detectors involved in the test beam and included in the trigger logic development.

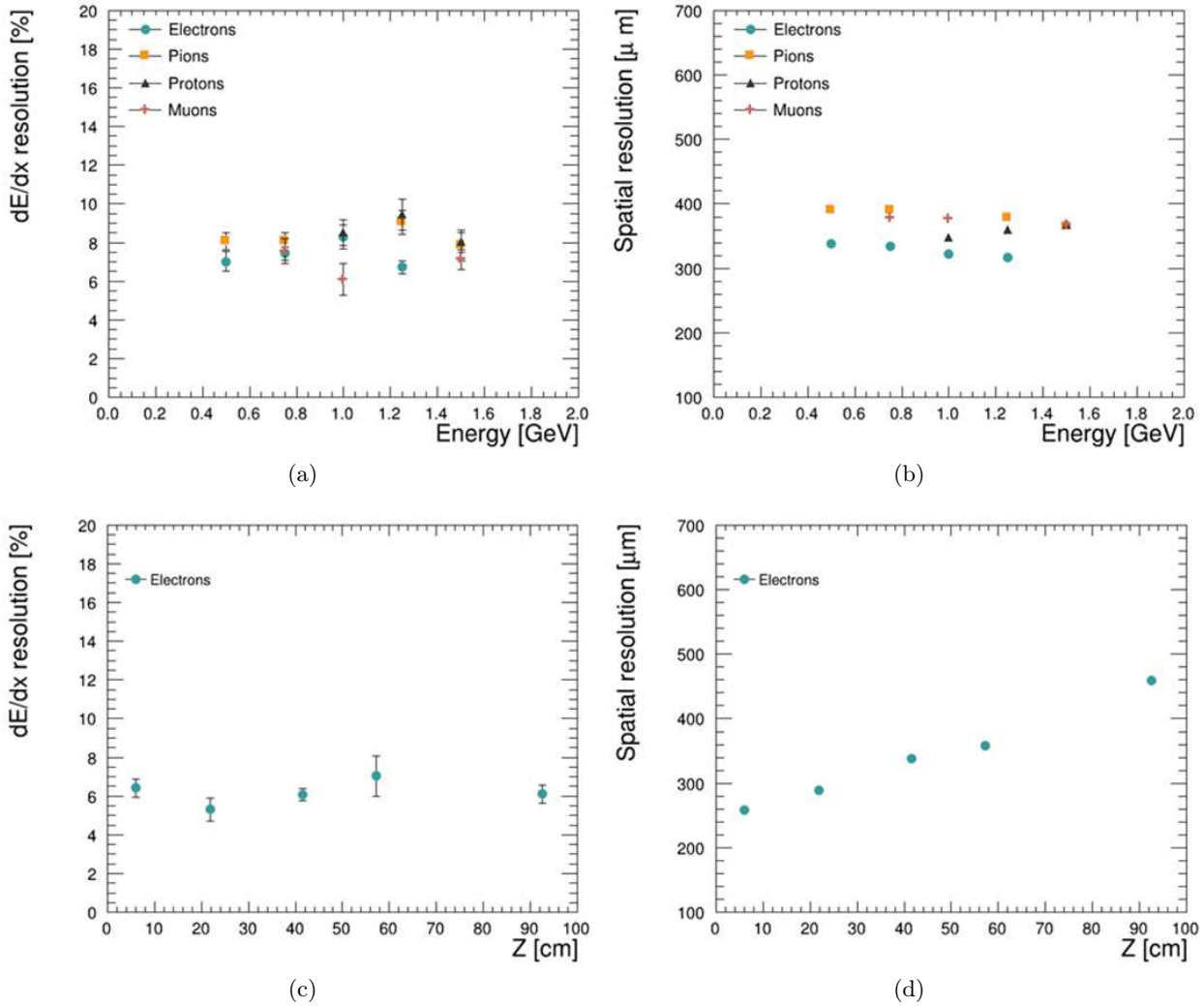


Figure 3.23: Perfomances of HA-TPC full scale prototype at 2022 CERN test beam. Top picture shows dE/dx resolution as a function of particle energy for $e, \mu, \pi, p$, while top right picture shows the spatial resolution. Bottom left and right pictures show the dE/dx and spatial resolutions for electrons sample as a function of drift length Z. Pictures from [111].

For the 2023 CERN test beam, my contributions included: (i) setting up the gas system to achieve the required gas properties and quantify contaminant levels (oxygen and water), as detailed in [119], (ii) implementing a trigger system based on time coincidences among fast detectors along the beamline to enable online selection of electrons, muons, pions, or protons based on their Time of Flight, and (iii) actively participating throughout the entire data-taking period, also serving as the gas and trigger expert.

# Chapter 4

# Field cage of HA-TPC

Field cages present a structure based upon lightweight composite materials that have been chosen to satisfy the required mechanical and electrical properties for HA-TPC, reducing the total interaction length of traversing particles as well as the dead volume with respect to the vertical TPCs already present in ND280.
Field cages present a hollow box shell-shaped structure, in which each layer serves a different role. The innermost part is dedicated to the shaping of Electric Field from cathode to anode. The uniform voltage drop is obtained by two layers of copper strips linked by two voltage dividers as reported in figure 4.1 . In each layer, copper strips are 3 mm wide and placed with a pitch of 5 mm. Each

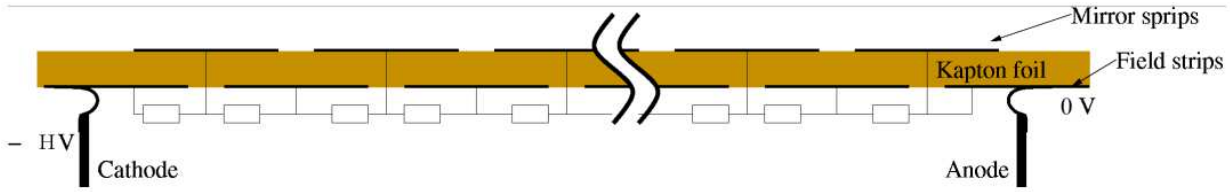


Figure 4.1: Schematic view of a cross section of the field cage, with focus on the strips. Two voltage dividers connect all the strips from cathode to anode.

strip covers the perimeter of the cage transversely to drift direction, thus carrying the same Voltage value along their area. The 197 strips in the layer facing the active volume are called "field strips", while the 196 strips on the other layer are called "mirror strips" and it is possible to access them thanks to copper pads traversing the insulating material. Strips in the two layers are staggered in such a way to overlap by 0.5 mm. Two voltage dividers that run on the drift direction of the field cage connect alternatively "field"-"mirror" strips by using 5 MΩ for a total of 393 SMD resistors. Each couple of strips is connected by two resistors for redundancy, with a total equivalent resistance of 1 GΩ. In this section, I will provide a detailed description of the construction of a field cage, emphasizing the innovative materials and procedures used. This is for two main reasons. First, I was actively involved in designing and manufacturing some of the most critical components, as well as in quality control. Second, the details presented here will serve as reference for the subsequent work in this thesis.
Mechanical and Electrical specifications for the HA-TPCs field cages follow:

- low density and low Z material to reduce multiple scattering and conversion processes. The structure is designed to improve the result for vertical TPCs of 4% radiation length;

- high structural integrity against over pressure, gravitational and thermal loads;
- high degree of electric field uniformity, with a required relative inhomogeneity $\frac{\Delta E_{drift}}{E_{drift}} \leq 10^{-3}$ at 1.5 cm away from the walls;
- adequate inner surface smoothness to prevent discharges caused by "point effect";
- walls materials able to stand the electric field component perpendicular to the layers;
- very low permeability to atmospheric gas components which affects negatively the drift of electrons, with a requirement for $O_2$ component lower than 10 ppm;
- negligible vapour pressure of contaminants emanating from material exposed to the drift volume.

The mentioned requirements led to the choice of composite materials for the field cage, due to the possibility to combine layers with different properties. Besides, composite sandwich structures are also commonly used in the industry, thus their production processes are well established and relatively cheap.

## 4.1 Field cage Structure

The field cage walls are designed to meet electrical and mechanical specifications while maintaining a thickness of only 4 cm and a total radiation length of approximately 2%. The Vertical TPCs in ND280 have a dead volume of about 12 cm and a total radiation length of 4%; therefore, the HA-TPC field cages represent a significant technological improvement. A schematic view of a cross-section of the field cage is reported in figure 4.2, and the thicknesses of each layer are summarized in table 4.1, along with an approximated computation of the expected radiation length $X_0$ which is estimated to be $X_0 \sim 2.5\%$.

| Material | Nominal Thickness [mm] | Radiation Length $X_0$ [%] |
|---|---|---|
| Copper | ∼0.035 | 0.2 |
| Aluminum | 0.15 | 0.2 |
| Kapton (Polymide film) | 0.475 | 0.2 |
| Twaron (Aramid Fiber Fabric) | 4 | 1.4 |
| HoneyComb Nomex (Aramid honeycomb) | 35 | 0.2 |
| Total | ∼40 | 2.2 |

Table 4.1: Summary of materials thickness which compose the field cage walls. Values for radiation length are reported in [120] and computed starting from single nuclei values when not available for a specific material.

The arrangement of layers close to the inner volume is shown in the top side of figure 4.3, while the outer region is shown on the bottom side. The layer facing the inner volume is called strip foil and it is produced by CERN Micro-Pattern Technologies service. First, a thin layer of copper is deposited on a Kapton[1] surface 5 m long and about 0.5 m wide, then the layer is chemically etched

[1] Kapton is a registered trademark of DuPont company.

in order to leave rectangular shaped strips, assuring parallelism at micrometer level between them. After that, two of those layers are glued one on top of the other, thus creating a double layer of strips. Finally, the strip foil is completed by joining two of those composite layers side by side in order to cover the whole drift length, which is 1 m wide. A view of one of the strip foils used for field cage productions is reported in figure 4.4. The construction of the field cage is summarized in the next section.

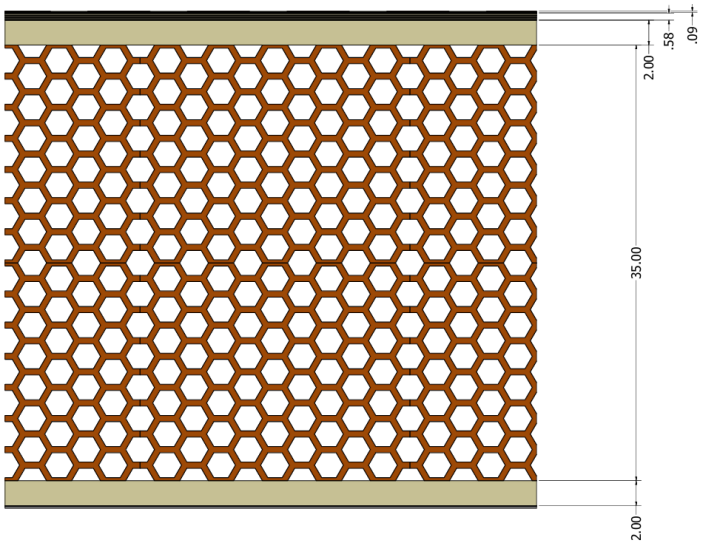


Figure 4.2: Schematic view of a cross section of the field cage on scale, with the side facing the inner volume on top. Quotations are reported in mm.

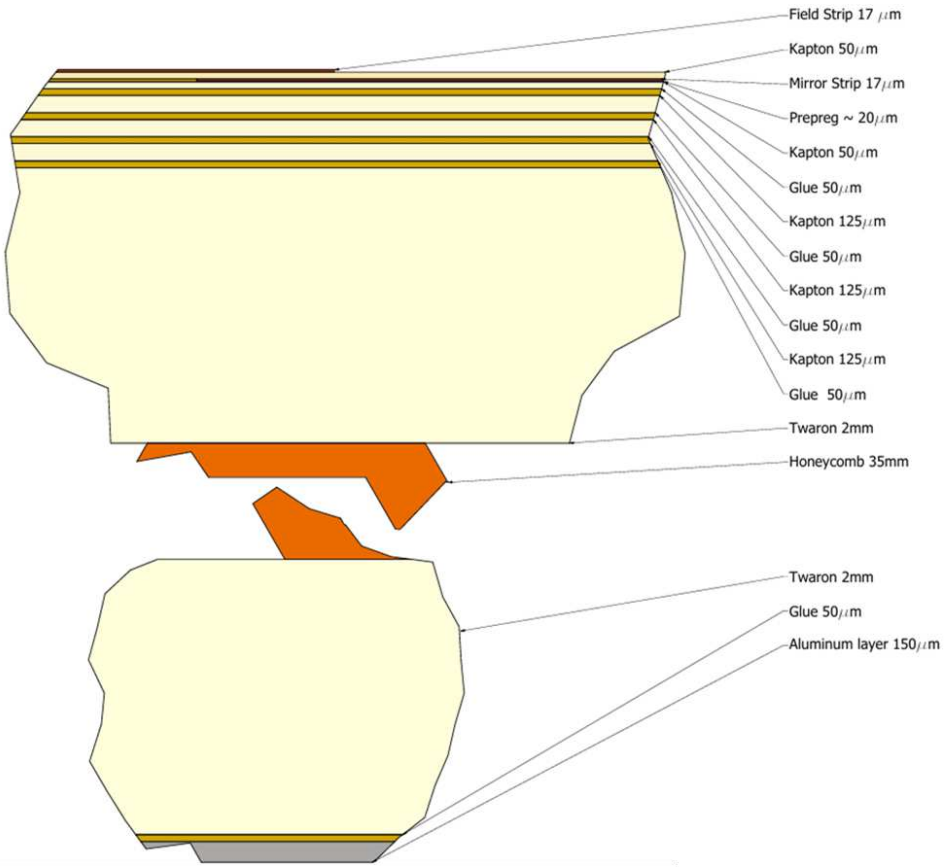


Figure 4.3: On top, a detailed view of the field cage wall is shown. Due to the large intensity of electric field in this region, several Kapton layers are glued together as insulation. On the other side, an aluminum layer is applied to shield the system from possible charge accumulation and field distortions.

Figure 4.4: Picture of a strip foil with field strips side facing the observer. The strip foil is 5 m long and 1 m wide and it covers the whole internal perimeter of the field cage. In the center of the strip foil, the junction line of the two parts composing the strip foil is visible parallel to the long sides.

The design of field cages has been carefully studied since 2018 with the realization of the first small scale prototype, with the same drift length and the possibility to house a single ERAM. The small scale prototype was tested in two test beams at DESY and at CERN in 2021. The construction of the prototype served as a proof of principle for both the feasibility and the required performances. Indeed, the prototype showed excellent gas tightness, electrical insulation and mechanical properties, while the construction procedure was refined to improve the final result.

The first full-scale field cage (hereafter referred to as FC0) was successfully constructed and met the mechanical and gas-tightness requirements. However, a flaw in the production process at the company's facility resulted in a significant issue with the electrical insulation of the layers beneath the strip foil. A detailed analysis of this issue will be presented in the next chapter. The design of subsequent field cages was successfully modified to incorporate additional insulating material layers between the strip foil and the Twaron[2], enhancing redundancy. A picture comparing a small scale prototype and a full scale field cage is visible in 4.5.

## 4.2 Field cage production

The construction of the field cage is a lengthy process that involves the layup and installation of multiple materials, all of which must meet stringent electrical and mechanical requirements. Several factors must be considered crucial during this process.

For instance, deformations in the field cage geometry can alter the direction of the electric field in the drift region. Furthermore, if the parallelism of the flanges is not maintained, this can lead to misalignment between the anode and cathode, resulting in a distortion of the electric field.

Electrical field distortions and high-voltage breakdowns can be induced by leakage currents, which may occur due to the presence of contaminating (low-resistivity) materials trapped between

[2] Twaron is a registered trademark of Teijin Aramid company

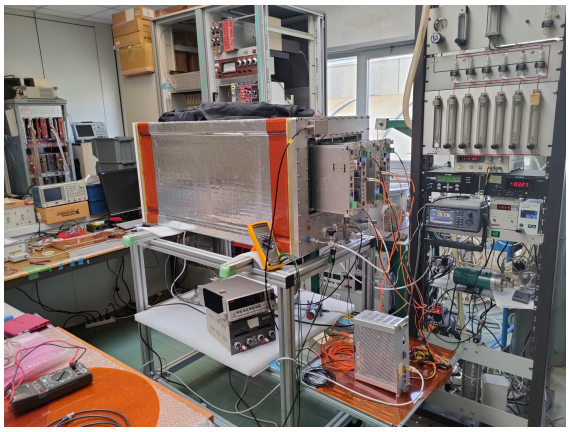

(a)

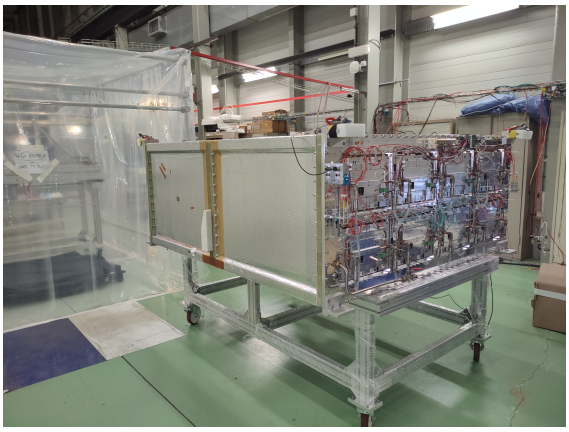

(b)

Figure 4.5: Comparison of HA-TPC prototype on left 4.5a with the old ARC electronics installed and full scale HA-TPC on right 4.5b. Each HA-TPC endplate houses 8 ERAMs module. The total lateral surface covered by the HA-TPC is 5 times larger than the prototype, which is designed for only 1 ERAM.

the layers, particularly near the inner surface. These contaminants, such as trapped humidity or air bubbles, can compromise the integrity of the field cage.

Through building small-scale prototypes and addressing an issue related to unexpected extra currents at high voltage, as experienced with the aforementioned FC0, we gained valuable insights into potential mechanical and electrical issues. These experiences enabled us to understand, prevent, and address these problems in the final design of the field cages.

While an in-depth analysis of the issue with FC0 is presented in the next chapter, in this chapter, we describe the production of the four field cages used to assemble the two new HA-TPCs for the ND280 Upgrade. These field cages were manufactured by NEXUS Projectes, S.L. according to our final design and the manufacturing procedures and quality assurance methods agreed upon with the company.

As mentioned, the field cages are hollow boxes made of solid dielectric material walls, constructed using composite materials techniques. This involves layering various materials (such as polyamide sheets, fiber-fabric peels, and honeycomb panels as peel spacers) over a metallic mold and bonding them under controlled temperature and pressure conditions in an autoclave. The mechanical strength of these laminated structures is further reinforced by embedding G10 flanges, where the cathode and anode plates will be fixed, as well as G10 angular bars along the four longitudinal edges.

**Mold** The mold consists in the metallic structure necessary for supporting the layers during construction phases and providing the geometry reference system for accurate layup procedure. It is designed and manifactured to achieve a surface planarity better than about $100\mu m$. The first step in the field cage construction process is to prepare the mold surface by coating it with a demolding layer

**Strip foil placement** The strip foil is positioned on the mold with the field strips facing the mold. It is then temporarily fixed using residue-free tape, ensuring that the two extremities on the

short side are aligned such that the ends of each strip are aligned and matched with an accuracy better than $50\mu m$. A detailed view of the strip foil layup on the mold is shown in Figure 4.6a. Since a strip foil consists of two foils juxtaposed along the long side (see Figure 4.4), perfect alignment may not be achieved at every point along the junction between the strip ends. Figure 4.7a provides a magnified view of this junction region, where the strip foil extremities are aligned. The Kapton layer, visible in the lower part of Figure 4.4, has been trimmed to create a small gap between the two extremities, which is subsequently filled with epoxy resin.

Once a satisfactory alignment is achieved, the strip foil is secured again with tape, and a vacuum bag is applied to evacuate the gap between the strip foil and the mold. This step prevents the formation of bubbles that could compromise surface planarity and ensures that the strip foil remains in place during subsequent steps.

However, a small amount of residual air trapped beneath the strip foil may still form bubbles, which can pose two potential issues: (i) degradation of electrical insulation due to the creation of unintended conductive paths for free charges in the air, and (ii) deformation of the wall caused by the additional volume occupied by the bubbles. Moreover, trapped air may expand during high-temperature processing steps.

To mitigate these effects, residual air bubbles were removed by puncturing the coverlay with a needle, and the holes were subsequently sealed with Kapton tape. Finally, any dust deposited on the strip foil surface was removed using antistatic cloths.

After positioning the strip foil, rectangular Kapton sheets 125 $\mu$m thick are placed on top of the coverlay in three layers and bonded using epoxy resin, which is cured at room temperature. To minimize water content and prevent degradation of the material's insulating properties, the Kapton layers were desiccated for 12 hours before use. The bi-component epoxy resin consists of Resoltech 1050T and hardener 1054S with a mass ratio of 100:32.17. According to Resoltech datasheets [121], once applied as a thin film, the resin stays in a gel state for about 12 hours. Resin and hardener are mixed for a few minutes and then put in a vacuum for degassing. During the application of Kapton foils, bubbles trapped in between the layers are removed with the aid of Teflon spatulas. In the corner region, the placement of additional Kapton layers was not feasible, as their thickness prevented them from bending to the required radius of curvature. Instead, multiple strips of Kapton tape were applied in several layers until the same thickness as the central regions was achieved.

**Resin curing** Successively, epoxy resin is applied on the whole surface, which is squeezed by a Peel-Ply tissue that can be removed once the resin has been cured. After that, a vacuum bag is applied on the strip foil at its extremities near the yellow plasticine visible in figure 4.6b. At this point, vacuum is applied and the field cage is placed into an autoclave. The pressure is set at 6 bar at a temperature of 30 °C for a period of 12 hours. The temperature is chosen after careful and conservative consideration of both curing procedure and materials thermal expansion. The mold is made of Aluminum, while the cage layers are made of copper and Kapton, which expand due to thermic effect at different rates and might cause unwanted stress on materials. In this region of the field cage walls the insulating performances of Kapton are crucial, therefore any unwanted and unpredictable change in its state due to the action of pressure and temperature has to be prevented. In addition, once the layers are glued, it is impossible to remove them and it is also very challenging to measure their resistivity without damaging the field cage. After curing in autoclave, the mold is returned into clean room and vacuum bag and Peel-Ply are removed. A visual inspection of the layers is performed, in order to identify the presence of bubbles or imperfections in the resin

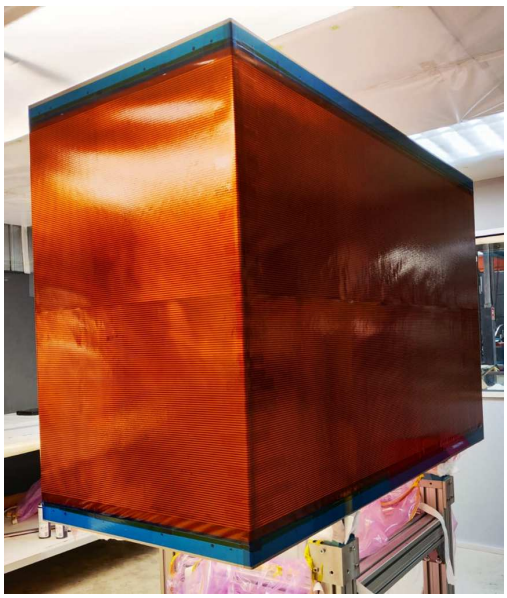

(a) Strip foil placement on mold

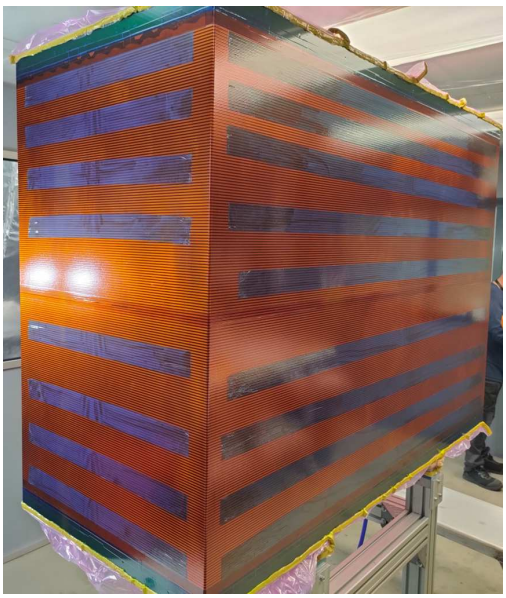

(b) Strip foil on mold after application of vacuum

Figure 4.6: Strip foil placement on mold before 4.6a and after 4.6b vacuum bag is applied. Vacuum is obtained by pumping out the air in between strip foil and mold with the aid of holes in the mold surface. The system is sealed by means of vacuum bags attached to the strip foil extremities as shown in figure 4.6b. Strip foil is kept in place with the aid of tape which will be removed in the next stages. In figure 4.6b the tape on coverlay is temporarily placed to stretch the strip foil and avoid the formation of wriggles.

(a) Mirror strips alignment

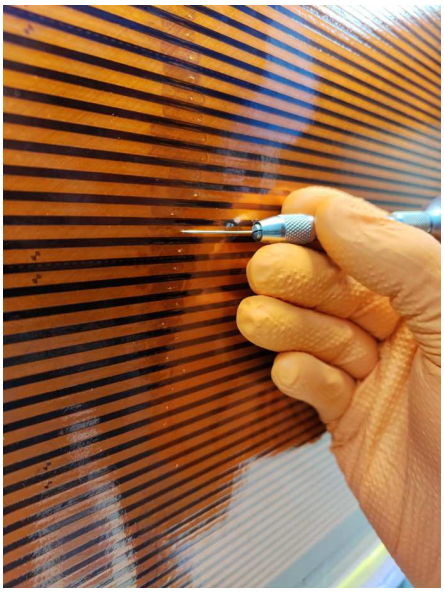

(b) Removal of air bubbles trapped in strip foil

Figure 4.7: In figure 4.7a the two extremities on the short side of the strip foil are aligned with the accuracy of few hundreds of micrometers before the application of vacuum. Once the vacuum is applied, bubbles might form inside the strip foil, which are removed as shown in figure 4.7b.

application as reported in figure 4.8. At this stage, tests to evaluate the surface resistance of the cured resin on Kapton is performed. Once the required properties are verified, it is possible to move forward and apply the Twaron peel layer.

### 4.2.1 Resin resistivity

In addition to estimating the resistivity of the layers, multiple resin batches utilized in the production of the field cages were also analyzed. For each lamination procedure applied to the prototype field cage (proto-FC), several square samples composed of a resin and hardener mixture were prepared to evaluate their surface and volumetric resistivity. These samples were subjected to applied voltages of up to 10 kV. With respect to tests on proto-FC, a different set of electrodes was prepared, based on copper tape on low resistivity rubber. Optimal adhesion on sample resin surfaces was ensured by the use of vacuum bags or extraweights (see for instance figure 4.9). Before commencing field cage production, tests were conducted on samples from each new epoxy batch to assess resin quality in terms of resistivity and to detect potential low-resistivity contaminants, such as carbon fibers. Additionally, several preliminary measurements were performed to evaluate the impact of slight imbalances in the resin-to-hardener ratio or suboptimal curing temperatures on epoxy resistivity. Each sample has a thickness of about 2 mm and side length of about 40 cm. Unless specified, the resin sample is cured at room temperature.

**Volumetric resistivity** The measurements of sample volumetric resistivity are reported in figure 4.10, which includes an example of tests performed for resins cured at room or larger temperature and on the same resin used for Kapton and Twaron lamination. The measured current in figure 4.10

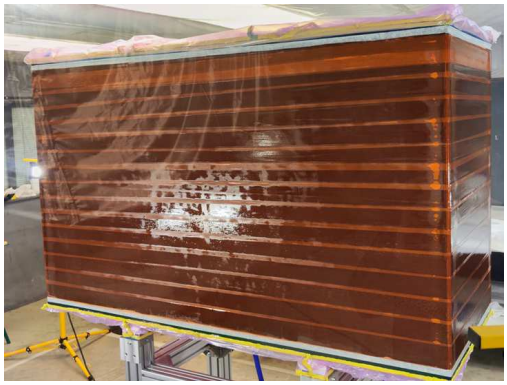

(a) Mold and Kapton layers wrapped in Peel-Ply after curing in autoclave.

(b) Mold and Kapton layers after Peel-ply removal.

Figure 4.8: Once the mold and the applied layers are placed in the clean room after curing in autoclave, the vacuum bag and the Peel-Ply layer in figure 4.8a are removed. The large pressure applied to the system forces the glued layers against the rigid mold and the strip foil. Few defects are still possible, such as trapped bubbles or inhomogeneity in the resin placement as reported in figure 4.8b.

(a)

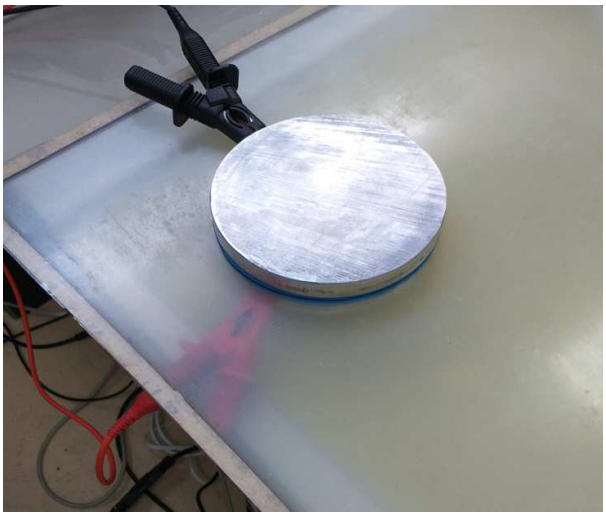

(b)

Figure 4.9: Set of electrodes used for resin surface resistance 4.9a and volumetric resistance 4.9b.

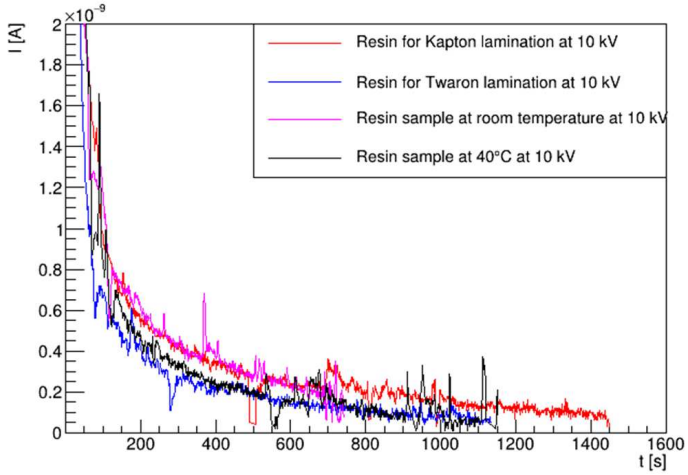


Figure 4.10: Current over time for volumetric resistivity measurements for resin samples realized with resin from Kapton (red) and Twaron (blue) lamination. The other two samples are made with the same resin but with room temperature (magenta) and 40°C (black) curing temperatures.

usually shows an initial transient period, followed by a slow transition to a plateau that is eventually reached in the next hundreds of seconds by two of the four samples. For estimating the plateau value for the current, the tails of the curves reaching a stable regime are considered and are fitted with a horizontal line. In the cases where a plateau was not reached, an upper limit is estimated by fitting the tail at large times analogously to the other samples. The estimation of volumetric

| Dataset | Voltage [kV] | Current [pA] | $\rho_{vol}$ [Ω·cm] |
|---|---|---|---|
| Twaron lamination | 10 | $220 \pm 2$ | $(7.133 \pm 0.007) \cdot 10^{16}$ |
| Kapton lamination | 10 | $252 \pm 1$ | $(6.223 \pm 0.002) \cdot 10^{16}$ |
| Room T curing | 10 | $348 \pm 4$ | $(4.520 \pm 0.006) \cdot 10^{16}$ |
| 40°C curing | 10 | $330 \pm 2$ | $(4.760 \pm 0.003) \cdot 10^{16}$ |

Table 4.2

resistivity is then performed by considering a nominal thickness of 2 mm and a voltage applied of 10 kV. The estimated volumetric resistivity reported in 4.2 satisfies the required resistivity values. Resistivity measurements on proto-FC are performed in the 1 kV range, which is not suitable for such small currents, therefore the two estimations should not be compared. Besides, the data hints to the fact that with additional time the current might had stabilized at lower values.

**Surface resistivity** The resin samples are prepared in a mold placed on a metallic surface, while the other face is exposed to air. For this reason, the surface in contact with the metallic surface is smooth, while the one exposed to air presents tiny irregularities and might be potentially exposed to contamination during the curing time. Therefore, the estimation of the surface resistivity on the samples might give different results on the two sides. Results are summarized in figure 4.11, in which the measurements are performed on the surface exposed to air during curing, in order to have the resistivity estimation for the worst case scenario. All samples show a similar behavior with small

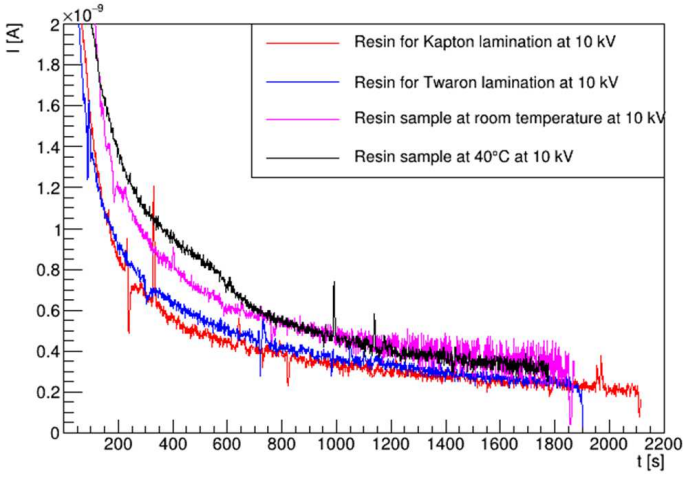


Figure 4.11: Current over time for surface resistivity measurements for resin samples, realized with resin from Kapton (red) and Twaron (blue) lamination. The other two samples are made with the same resin but with room temperature (magenta) and 40°C (black) curing temperatures.

differences in the time needed for reaching a stable value. The value for current plateau and the estimated surface resistivity are obtained as in previous paragraph and they are reported in table 4.3. Each sample shows a similar value for surface resistivity, while in some cases the estimated

| Dataset | Voltage [kV] | Current [pA] | $R_S$ [$\Omega/\square$] |
|---|---|---|---|
| Twaron lamination | 10 | $84 \pm 1$ | $(9.9 \pm 0.1) \cdot 10^{14}$ |
| Kapton lamination | 10 | $104 \pm 5$ | $(8.0 \pm 0.4) \cdot 10^{14}$ |
| Room T curing | 10 | $169 \pm 7$ | $(4.9 \pm 0.2) \cdot 10^{14}$ |
| 40°C curing | 10 | $96 \pm 5$ | $(8.7 \pm 0.4) \cdot 10^{14}$ |

Table 4.3

value might be larger since the measurement was stopped early before reaching a stable plateau. In every sample, the value satisfies the requirement for proceeding in the field cage production.

### 4.2.2 Assessment of layers resistivity

The estimation of layers resistivity has been introduced in the construction procedure to evaluate the volumetric and surface resistivity of the inner layers in the early stages of field cage production. Measurements have to be performed with electrodes that do not leave traces once applied to surfaces in order to avoid contamination. In addition, since the mold is in a vertical position, it is not straightforward to ensure a proper contact between the electrodes and the field cage layers. For the mentioned reasons and due to the very large values of resistances at play, the electrodes were made by copper tape installed on rubber shapes and the contact between them and the layers was realized by enforcing vacuum on a region around the electrode.
The first layer that was tested is the strip foil once applied to the mold. For this purpose, a Megger insulator tester is used as a DC source and as an amperometer.

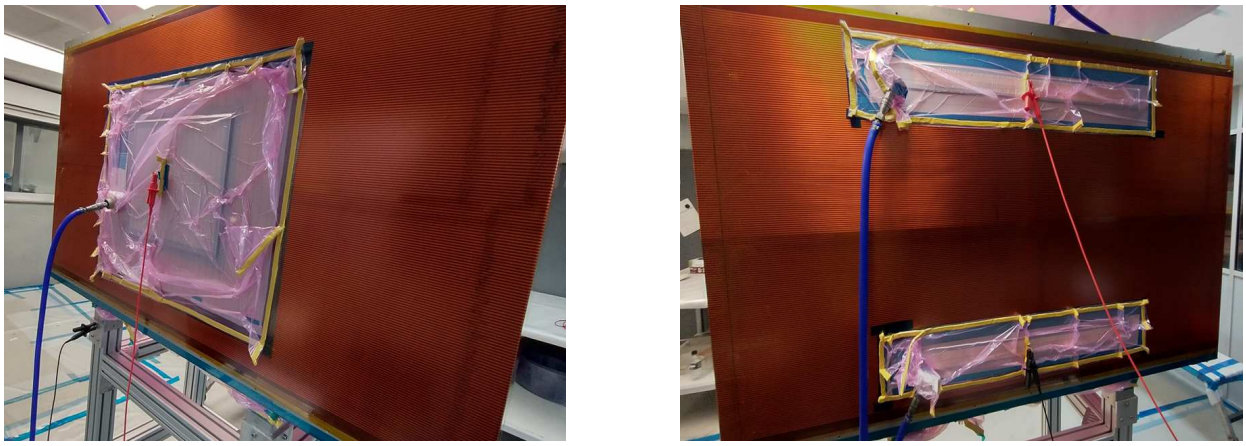

(a) (b)

Figure 4.12: Picture of setups for volumetric resistivity measurement of proto-FC layers. Picture 4.12a shows the large 40×50 cm$^2$ electrode applied on the coverlay and pushed against it thanks to vacuum. One end of the insulator tester is connected to the electrode, while the other is applied to the support. Analogously, picture 4.12b shows the two long electrodes in separated vacuum bags. The two cables are connected to the insulator tester.

### Volumetric resistivity

For the evaluation of the volumetric resistivity, two different tests are performed with different electrode configurations. First, a 40×50 cm$^2$ electrode is applied onto the coverlay and a vacuum bag is placed on top of it. In this setup, the hot extremity (HV) of the voltage generator is applied to the square electrode, while the cold extremity (not referred to as "ground" since the tester does not propagate the ground reference of the power line) is applied to the mold metallic frame. This setup aims to measure the resistance through the whole strip foil thickness. As a second method, two rectangular shaped electrodes 5 cm wide and 1 m long are applied on the coverlay at a distance of about 60 cm and a vacuum bag is applied to each one. The two electrodes are then connected to the Megger insulation tester. In this configuration, the aim is to measure any hypothetical current flowing inside the strip foil along the drift direction, in parallel with the current flowing on the mold and traversing the strip foil volume twice. In case of good insulation, the expected resistance at play is at least comparable with the smallest current measurable by the insulation tester, thus a lower limit can be found. Besides, since a proper shielding of the system of such dimensions is difficult to provide, the presence of humidity or other contaminant can lower the measured resistance. A picture of the two setups is reported in figure 4.12. Since the mold is in contact with the field strips side of the strip foil, it is likely that the pads for accessing the mirror strips are touching the mold, therefore halving the distance between the two electrodes of the circuit. A comparison between the results obtained from the two setups is not straightforward due to the mentioned differences and assumptions. However, by creating a simplified model of the two setups, the order of magnitude of the two estimations for the volumetric resistivity should give the same results.
For the setup with the large 40×50 cm$^2$ electrode, the volume traversed can be divided into two halves. The first one corresponds to the coverlay and it is enclosed in between the electrode and the mirror strips which act as an intermediate electrode between the square electrode and the mold. The second half is delimited by the mirror strips and the mold. A sketch of the strip foil section is

visible in figure 4.13.

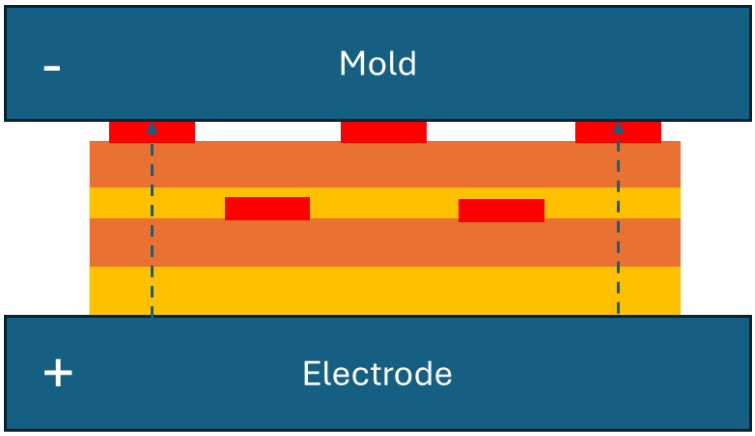


Figure 4.13: Sketch of strip foil section (not on scale) with the expected path for current from the electrode to the mold.

For the first half, the effective surface between the two electrodes to be used in the Ohm's law is given by the intersection of the area of the square electrode and the mirror strips one, so about $A_1 \sim 40 \times 50 \times \frac{3}{5} = 1200$ cm$^2$, in which the factor $\frac{3}{5}$ is given by the strips width over the pitch. For the second half, the whole length of the mirror strips has to be considered since the whole mold is approximately at the same potential. In this case, the surface area for Ohm's law is $A_2 \sim 80 \times A_{strip} = 80 \times 0.3 \times 500 = 12000$ cm$^2$. The total resistance is given by the series of the two halves.
For the setup with long electrodes $A_1$ and $A_2$ are different since the electrodes are 5 cm wide. In this case $A_1 \sim 5 \times 80 \times \frac{3}{5} = 240$ cm$^2$, while $A_2 \sim 10 \times A_{strip} = 10 \times 0.3 \times 500 = 1500$ cm$^2$. The total resistance is given by:

$$R_{square} = R_1 + R_2 = \rho_{vol} \left( \frac{d_1}{A_1} + \frac{d_2}{A_2} \right) \tag{4.1}$$

where $d_1$ and $d_2$ are the thicknesses of the two halves, while for long electrodes $R_{long} = 2 \times (R_1 + R_2)$ since the strip foil has to be traversed twice.

### Surface resistivity

The estimation of surface resistivity of proto-FC layers is performed by using two concentric circular electrodes as shown in figure 4.14. The electrodes are made with the same materials as those used for measuring the volumetric resistivity. They are kept in place by using Kapton tape and then sealed inside the same vacuum bag in order to ensure optimal electrical contact. For two concentric circular electrodes with radius of the inner circle $r_1 = 8$ cm and inner radius of the larger electrode $r_2 = 17$ cm, the surface resistivity is

$$R_s = \frac{2\pi}{\ln \frac{r_2}{r_1}} \times R_{meas}. \tag{4.2}$$

The surface resistivity is estimated primarily to promptly detect the presence of contaminants after the lamination of the inner layers.

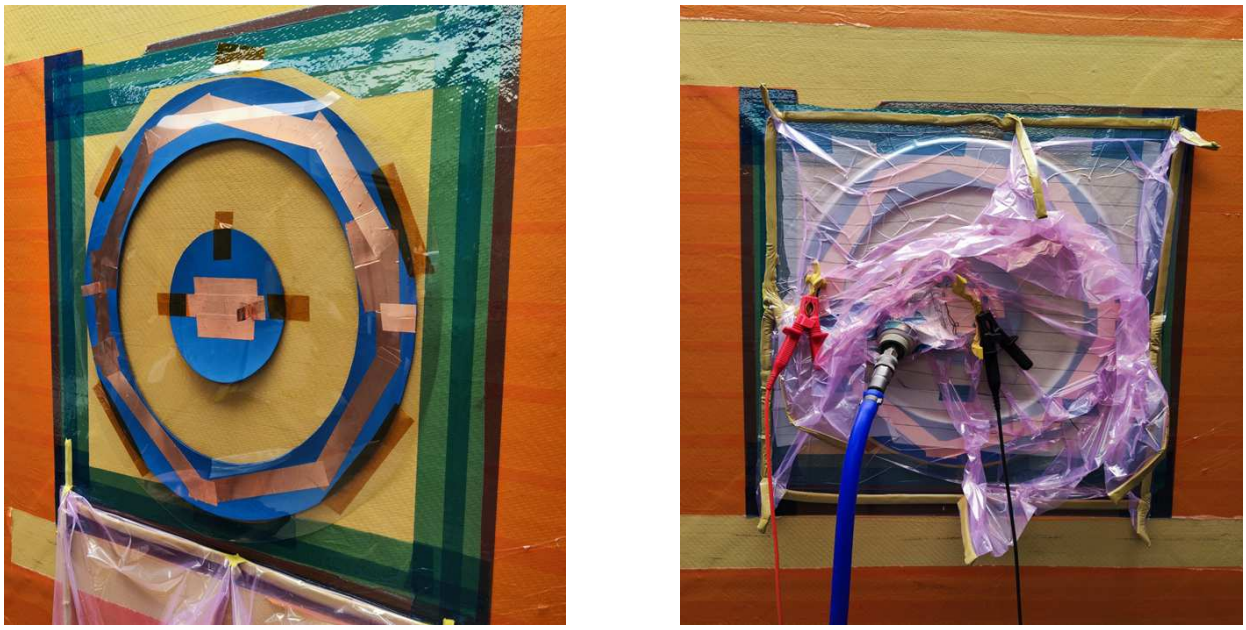

(a) (b)

Figure 4.14: Electrode for surface resistivity estimation of proto-FC layers. Picture 4.14a shows the electrode held in place on the inner Twaron layer by Kapton tape. Picture 4.14b shows the sealing with vacuum bag. Two pieces of copper tape connect the electrode with the insulator tester through two small openings.

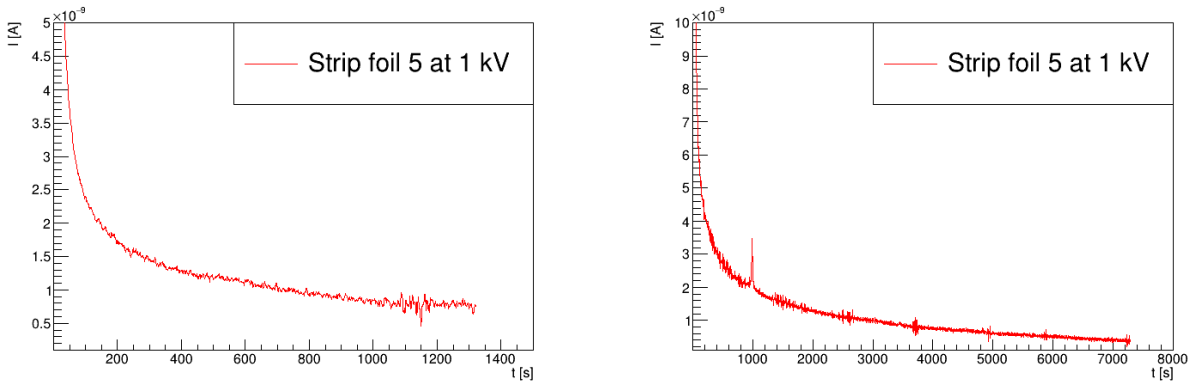


(a) (b)

Figure 4.15: Current as a function of time for volumetric resistivity estimation of strip foil at 1 kV for square electrode configuration on 4.15a and long electrodes configuration on 4.15b. Both plots reach a plateau value that is given by the tester.

### 4.2.3 Strip foil resistance

Once the strip foil is placed on the mold, the layers resistance is measured. Due to the large resistances at play and the possibility of having large capacitances between the mold and the strips, the measured current is expected to present a steady decrease, until it eventually reaches a plateau. The plateau might depend on the limit of the insulator tester or on parasitic leakage currents. In both cases, reaching a plateau means that the system satisfies the required resistivity level at tested stage. At first, measurements are performed directly on the coverlay as shown in figure 4.12.

The estimation of the strip foil volumetric resistivity under the assumptions of (i) grounded and (ii) floating mirror strips is summarized in 4.4. Both cases show that the estimated resistivity

| Method | Voltage [kV] | Resistance [Ω] | $\rho_{vol}^{floating}$ [Ω·cm] | $\rho_{vol}^{gnd}$ [Ω·cm] |
|---|---|---|---|---|
| Square | 1 | $(0.409 \pm 0.002) \cdot 10^{12}$ | $(10.8 \pm 0.4) \cdot 10^{17}$ | $(0.9813 \pm 0.004) \cdot 10^{17}$ |
| Long | 1 | $(2.50 \pm 0.02) \cdot 10^{12}$ | $(8.71 \pm 0.04) \cdot 10^{17}$ | $(1.201 \pm 0.006) \cdot 10^{17}$ |

Table 4.4

is compliant with the expected one from pure Kapton materials datasheet, showing no critical degradation of strip foil materials at this stage of field cage production, allowing to proceed to the next steps.

For surface resistivity, the value is summarized in table 4.5, which is around one to two orders of magnitude larger than the value estimated for resin samples in 4.3. In this case, a possible explanation might derive from the fact that the two electrodes are tightly sealed and put under vacuum by the presence of a plastic bag. In this way, current might leak across the plastic bag causing an underestimation of surface resistivity. It should be noted that the chosen method is the only feasible approach given the challenging operating conditions of the electrodes, where leakage currents are particularly difficult to control.

| Voltage [kV] | Current [pA] | $R_S$ [$\Omega/\square$] |
|---|---|---|
| 1 | $956 \pm 2$ | $(8.72 \pm 0.02) \cdot 10^{12}$ |

Table 4.5

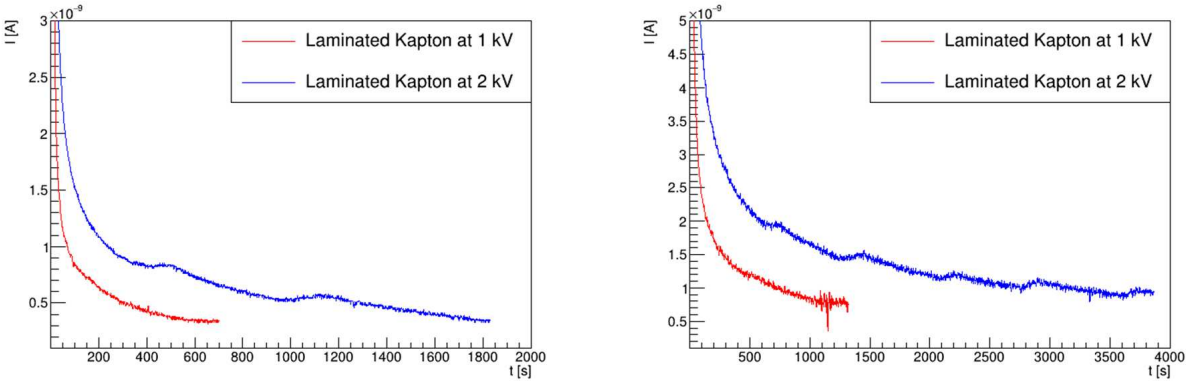


(a) (b)

Figure 4.16: Current as a function of time for volumetric resistivity estimation for the proto-FC formed by strip foil and laminated Kapton layers at 1 kV and 2 kV for square electrode configuration on 4.16a and long electrodes configuration on 4.16b. At 1 kV, both plots reach a plateau value that is given by the tester, while at 2 kV the configuration 4.16b appears to stay at a larger value. The resistance is estimated by fitting the tail of the curves with a horizontal line.

### 4.2.4 Laminated Kapton

Measurements are repeated once the additional Kapton layers are glued to the strip foil. The volumetric resistance measurements at 1 kV and 2 kV are reported in figure 4.16. In both cases a plateau is reached and the few current spikes are due to little electrical perturbations of the system. The voltage values are chosen to avoid possible damage to the materials due to large electric fields between the two faces of the strip foil.

The resistances and the volumetric resistivities are reported in table 4.6, considering both cases in which mirror strips are at the same potential of the mold $\rho_{vol}^{gnd}$ or floating $\rho_{vol}^{floating}$[3]. The estimations obtained from this tests are at maximum one order of magnitude away from the datasheet value for Kapton, therefore it was possible to proceed to the next steps. The estimation of surface resistivity $R_S$ is obtained by applying a voltage of 1 kV between the two electrodes and the results are reported in table 4.7, in which equation 4.2 is used. The trend in figure 4.17 is similar to figure 4.6, with a first part in which the current steadily decreases into a plateau. Measurements have been performed one after the other, therefore the second time it might be possible that the lower current is due to the fact that the material is still polarized and therefore it reaches a plateau much faster. Indeed, the blue curve in figure 4.17 is still decreasing at a much slower rate.

[3] Errors on thickness and on electrodes area are difficult to estimate, so only the error on current measurement by the insulation tester is used in the error estimation. Therefore, the statistical error reported here is a clear underestimation of the uncertainty on resistivity value. However, the goal of these measurements is to give an approximate feedback on the volumetric resistivity, which will be studied in detail in the next sections.

| Method | Voltage [kV] | Resistance [Ω] | $\rho_{vol}^{floating}$ [Ω·cm] | $\rho_{vol}^{gnd}$ [Ω·cm] |
|---|---|---|---|---|
| Square | 1 | $(1.276 \pm 0.007) \cdot 10^{12}$ | $(30.9 \pm 0.2) \cdot 10^{17}$ | $(0.245 \pm 0.001) \cdot 10^{17}$ |
| Square | 2 | $(2.171 \pm 0.004) \cdot 10^{12}$ | $(52.52 \pm 0.09) \cdot 10^{17}$ | $(0.4168 \pm 0.0007) \cdot 10^{17}$ |
| Long | 1 | $(2.916 \pm 0.007) \cdot 10^{12}$ | $(8.859 \pm 0.02) \cdot 10^{17}$ | $(0.1120 \pm 0.0007) \cdot 10^{17}$ |
| Long | 2 | $(5.74 \pm 0.02) \cdot 10^{12}$ | $(17.4 \pm 0.05) \cdot 10^{17}$ | $(0.2205 \pm 0.0007) \cdot 10^{17}$ |

Table 4.6

| Voltage [kV] | Current [pA] | $R_S$ [Ω/□] |
|---|---|---|
| 1 | $120 \pm 1$ | $(6.93 \pm 0.05) \cdot 10^{13}$ |
| 1 | $276 \pm 1$ | $(3.02 \pm 0.01) \cdot 10^{13}$ |

Table 4.7

In both datasets reported in table 4.7, the surface resistivity is larger than the case of strip foil only. Even if the applied procedure is the same, the surface in which the electrodes are applied is different. On the strip foil coverlay, the surface is very smooth, while after Kapton lamination the surface is rougher due to the resin flowing inside the pores of the Peel Ply. Therefore, the surface resistivity might be larger due to a worse contact between the surface and the vacuum bag. In summary, the large value for the surface resistivity excludes any contaminant in the lamination of the Kapton, which was confirmed also in the measurements of the resin batches.

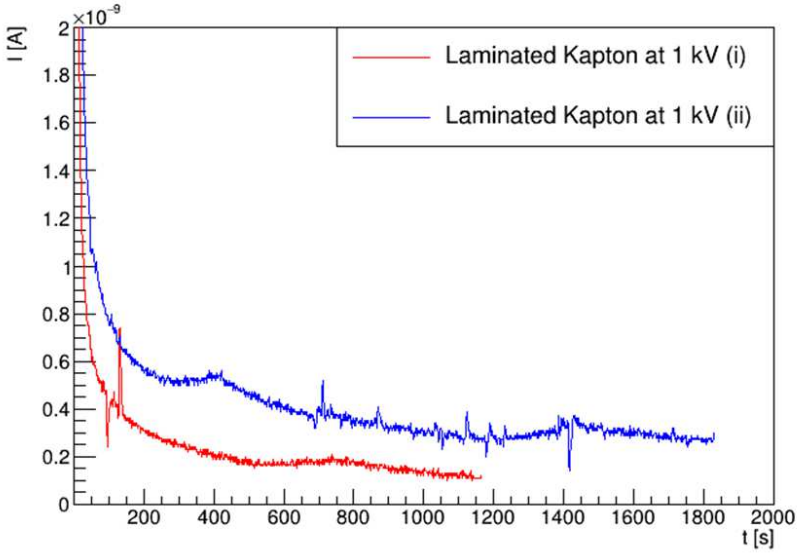


Figure 4.17: Surface resistance of laminated Kapton layers on strip foil, measured with concentric circular electrodes at a voltage of 1 kV.

**Twaron layers** The next step in the procedure is the application of several layers of Twaron on top of the last glued Kapton layer. A Twaron roll is cut with predetermined shapes in order to cover the whole surface with overlapping layers for a total nominal thickness of 2 mm. The resin used is identical to the previous step. Once the Twaron layers are applied, two independent layers of Peel-Ply are applied to the whole surface. On top of them, a vacuum bag is placed and vacuum is applied. The mold is put again in autoclave under the same environmental conditions used for the previous step.
The strip foil, the Kapton layers and the Twaron layers placed until this point are the most important for the overall performance of the field cage. For this reason the insulating properties of the strip foil, Kapton and Twaron layers are measured and reported in this chapter, while the properties of such layers for FC0 are reported in the next one.

**Fiberglass structure installation** At this stage, the mechanical structure forming the field cage skeleton must be installed. The Peel-Ply used during the curing of the Twaron layers is removed from the sides to allow for the placement of the structure, which consists of G-10 fiberglass bars shaped as a parallelepiped. This structure is manufactured by Orvim SRL (TV, Italy). The side regions are thoroughly cleaned to ensure proper contact between the laminated Twaron layers and the G-10 bars, which are then bonded using a high-viscosity adhesive along all vertical and horizontal edges of the field cage. At the bottom, four horizontal metallic beams are fixed to the mold, serving as both a reference and a support structure for the bottom G-10 rectangular base. Once the base is secured atop the metallic beams, vertical G-10 bars are positioned to form the four corner supports of the field cage. Subsequently, the top G-10 rectangular base is placed, followed by the fixation of four additional horizontal metallic beams to the mold, which provide alignment and stability for the top G-10 base. Each G-10 bar is coated with high-viscosity epoxy resin before being positioned, and additional epoxy is applied to fill any gaps between the assembled G-10 skeleton and the previously laminated Twaron layer, ensuring the required gas tightness of the cage. To facilitate uniform resin distribution and complete gap filling, the mold is turned upside-down. The metallic beams are also essential at this stage to maintain the position of the G-10 structure while the epoxy is still curing, preventing any displacement when the mold is turned upside down. After curing, the excess epoxy is removed, and the structure is treated with sandpaper to ensure a smooth surface. A picture of the field cage at this stage is shown in Figure 4.18.

**Nomex HoneyComb** After the installation of the fiberglass bars, the next step is the preparation of the Nomex HoneyComb. Nomex HoneyComb is a lightweight, high strength and nonmetallic honeycomb core material manufactured from aramid fiber paper with a hexangular cell shape. After the honeycomb is formed, it is coated with a heat resistant phenolic resin to increase its strength and thermal properties. It exhibits a high strength-to-weight ratio, exceptional stiffness against compression along the cell direction, and excellent bondability[122]. In order to glue the HoneyComb to the Twaron layer, a different type of resin is used with respect to the previous steps. The new mixture is obtained by mixing the resin Resoltech 3350 and the hardener 3357 on a mass ratio 100:45. This resin is faster than Resoltech 1050T and is particularly resistant to the propagation of micro-cracking and is well adapted to bondings subject to important cycles of fatigue[123].
Before gluing, the HoneyComb is heated at 100°C in order to reduce the water content analogously to all the other materials. The resin mixture is applied to the four surfaces delimited by the fiberglass flanges and then the HoneyComb sheets are placed. Following the same procedures as in previous steps, Peel-Ply layers are applied as well as vacuum bags. The whole system is transferred in an

Figure 4.18: View of the G-10 bars installed on the sides of the proto-field cage on top of the inner Twaron layers. The faces are sanded in preparation for the installation of the HoneyComb.

oven and kept for 8 hours at a temperature of 30°C. A picture of the proto-FC once removed from the oven is reported in figure 4.19.

**External Twaron layer** Once the curing step is completed, Twaron layers are prepared again to cover the whole surface as already described. Twaron sheets are heated at 120 °C for 2 hours. After that, Resoltech 3357 is applied to the HoneyComb with a roll, while a mixture of Resoltech 1050T is prepared as already explained for Twaron lamination. After a further period in autoclave, the whole system is transferred into an oven at a temperature of 40°C for 64 hours. This stage completes the lamination Phase of the field cage construction

**Machining of the Field Cage Flanges** The laminated field cage, still attached to the mold, is transported to the milling company Valmoll (Spain), where high-precision, large-aperture machines are used to mill the flange regions. During this process, the O-ring grooves are created, and the flanges are shaped to their final, precise geometry by using the mold as accurate reference.

**Latest stages of Field Cage building and quality controls** After milling, the field cage is returned to NEXUS, where the mold is removed carefully to avoid any damage to the inner surface

Figure 4.19: View of the proto-FC with HoneyComb installed on the four faces. On top of it, the external Twaron layers will be laminated.

of the cage, where the field strips are exposed.

At this stage, a thorough inspection of the inner surface is conducted. In some cases, air bubbles were observed on the inner surface. Although the phenomenon was limited to very small regions, it needed to be addressed, both for achieving design surface weaviness and for avoiding further damages to the surfaces. For example, given that the HA-TPCs were to be transported to Japan via air freight, they would be subjected to atmospheric pressures as low as 0.7 bar during the flight. Under such conditions, the air trapped within the bubbles at 1 bar could expand, potentially causing damage to the strip foil. The procedure for eliminating these bubbles involves two primary steps. Initially, two pinholes are created at separate points within the bubble. Subsequently, one of the pinholes is connected to a needle filled with resin, while the other is linked via a pipe to a vacuum pump. The pump removes the trapped air and allows the resin to be drawn into the emptied gap. This procedure proved successful and was applied to all such defects.

Preliminary tests are also conducted at this stage on the field cage to check the electrical insulation between the strips. In a few cases, accidental short circuits between adjacent field and mirror strips were found. The precise location of the short circuit is determined by exploiting the small resistance of the 5-meter-long strips (approximately 1 $\Omega$). A potential difference is applied to both ends of the field strip, and the potential of the adjacent mirror strip is measured relative to one of the field strip ends. Since the potential drop is linear along the strips, the precise location of the short circuit can be identified.

In some cases, visual inspection at the short circuit location revealed defects such as a pinhole through the $50\mu m$ thick Kapton foil, allowing electrical contact between the field and mirror strips. This type of defect was resolved by removing the copper in the pinhole region with ferric chloride, filling the pinhole with epoxy, and restoring the electrical continuity of the field strip.

In other cases, the short circuit was found at one of the two foil edges, resulting from the trimming of the strip foil edges to match the exact mold perimeter length. During the cutting process, the scissors bent both the field and mirror strips, bringing them closer together than the nominal 50 $\mu$m thickness of the Kapton foil along the cut line. This issue is resolved by using ferric chloride to remove the last 1 mm of copper along the edge of the strip, covering the 1-meter region where the two edges of the foil meet.

After curing and addressing potential electrical defects, the electrical insulation between strips is assessed. The measured electrical resistance at 1 $kV$ between adjacent field-field and field-mirror strips is on the order of 1 TΩ, indicating sub-nA leakage currents, which are compatible with superficial leakage due to humidity. This level of insulation is well within the specifications, and it is expected to improve further during HATPC operations, as the cages are sealed and humidity is removed from the inner surfaces.

At this stage, the final external layer, consisting of a few tens of micrometers of thin aluminum foil, is laminated. This layer serves as the field cage's electrical shield and external ground layer. The application of this layer allows to check the electrical insulation between the cage strips and the shielding. The measured electrical resistance (often referred to as "Mantle" resistance) at 10 $kV$ is on the order of 1 TΩ, indicating a few $nA$ of leakage current, which is consistent with superficial leakage due to humidity. This level of insulation is already within the specified limits and is expected to improve further during HATPC operation, when the cages are sealed and humidity is removed from the inner surfaces.

Similar insulation measurements are carried out at later stages (see Section 4.7), after the completion of the HATPC assembly process, to further validate the electrical performance and ensure the continued integrity of the insulation.

During the final, but crucial step, the surfaces are finished, with particular attention given to polishing the flanges using ultrafine sandpaper, up to P3000 grit. This ensures that the necessary surface requirements are met and guarantees the required gas tightness when the cage is sealed with O-rings where the two open sides of the cage are closed with the End-Plate on the Anode side and a symmetric Field Cage on the Cathode side.

## 4.3 Cathode

The central cathode (figure 4.20) is a Copper-clad G10/ROHACELL[124] panel constructed from 1 mm copper-clad G10 laminated onto both surfaces of 10 mm (nominal) thick ROHACELL, giving a total nominal thickness of 12 mm. A frame is constructed from G10 bars, which are glued, screwed together and machined to match the measured ROHACELL thickness. The frame is then loaded with ROHACELL and laminated to both copper-clad G10 sheets at the same time. More details on cathode preparation can be found in [96], while a picture of one of the cathode sides is reported in 4.20a.The cathode is initially covered with a plastic film to prevent copper oxidation. This protective film is removed before the cathode is installed onto the field cage. The planarity of the cathode is measured by the CERN metrology service, after which it is glued to one of the two field cages, ensuring that its intermediate plane coincides with the flange surface. The design allows for a 1 cm gap between the cathode and the wall, as the gas is shared between the two field cages. This gap is also necessary to ensure electrical insulation of the cathode from the flange and to minimize leakage currents flowing from the cathode to the external shielding through the flange. To further minimize these leakage currents and to maintain a proper distance between the cathode at high potential and the external shielding, both field cages' cathode flanges are equipped with, in addition to the two 8 mm thick grooves for the O-rings, a 30 mm groove. This groove acts as a gas and surface charge labyrinth, effectively lengthening the path for any potential leakage currents.

## 4.4 Field cages assembly

In order to complete the structure of one TPC, two field cages have to be assembled together. A sketch of the junction point is reported in figure 4.21. First, the cathode is aligned and secured

(a)

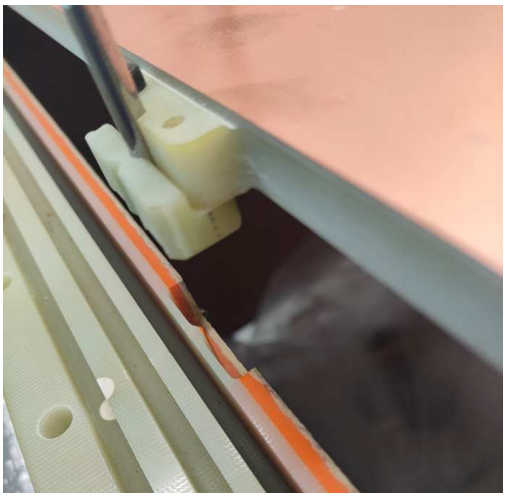

(b)

Figure 4.20: Left image 4.20a is a view of one of the two Copper-plated faces of the cathode. In this picture, the protective film is still applied. The cathode is secured to the field cages with six supports placed on the perimeters, as shown in picture 4.20b.

on one field cage using plastic screws and epoxy. Next, two O-rings are placed in the dedicated grooves to ensure gas tightness. After that, a 60mm height Teflon band is inserted into the third 30 mm deep groove. The three grooves, the O-rings and the Teflon band, as mentioned previously, are intended to extend the electrical path length from the cathode to the ground, helping to further isolate the cathode from the external shielding and to reduce leakage currents caused by charge movement either supported by the gas or due to superficial phenomena.

At this point, the two field cages must be put together. The procedure is very delicate, since a mistake in the alignment of the two flanges might damage the O-rings by pinching them. Eventually, the two flanges are secured together by means of G10 screws, since metallic pieces cannot be used in such a delicate spot. The cathode is then connected with two wires to the closest field strip on both field cages

Once the field cages are secured, the high voltage connector is installed in the central part of the TPC. The connector is used to provide the operating voltage to the cathode, while its case is designed to provide electrical insulation and protection from environmental conditions (e.g. air humidity). At such large voltages, it is important to reduce water permeability and to reduce the irregularities on the hot wire that might cause discharges. Small pointed defects may cause local intense electric fields which lead to corona effect, consisting in discharges caused by the ionization of air molecules. The continuous series of local discharges can damage the wire and modify the amount of current flowing in the field cages voltage dividers and therefore the drift field. A sketch of the custom developed connector is reported in figure 4.22. The wire coming from the power supply is connected as shown in figure, then the hot wire passes through a hole in the flange sealed by a feed-through realized in polyether ether ketone (PEEK). The wire is then soldered directly to the cathode. The connector case is sprayed with anti-corona varnish to prevent discharges.

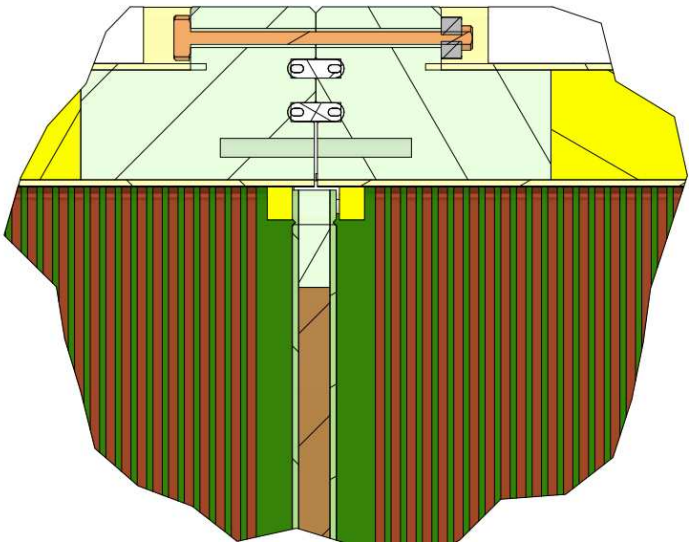

Figure 4.21: The picture is a sketch of the junction section. Starting from bottom, the cathode is visible, which expands symmetrically in both field cages inner volume. Between the cathode and the wall there is a small gap for gas passage. In the flange, three groves are present. The innermost one is used for insulating purposes, while the other two host an O-ring each. Eventually, on the external part G10 bolts hold the field cages in place.

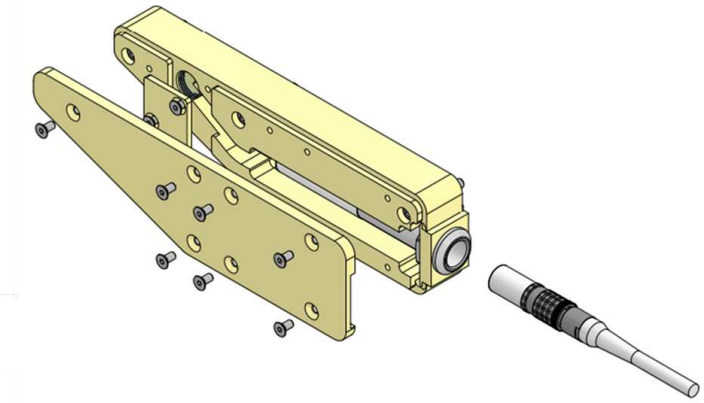

Figure 4.22: The picture is a sketch of the HV connector. High voltage is fed from the wire on the right to the standard socket, which extends for about 10 cm inside the connector case. Then, from the hot end, a copper wire is soldered and connected to the cathode thanks to a feed-through. The case is then closed by plastic screws.

## 4.5 Field cage validation

In this section, the tests performed to validate the field cages properties in the case of (i) a single cage and (ii) once field cages are assembled are reported.
For each single field cage, the surface flatness is evaluated by the NEXUS and CERN metrology services independently. Besides, the electrical insulation in between strips is tested before and after the installation of the voltage divider.
Once the field cages are validated, the cathode is installed and two field cages are jointed together

to form the structural part of the HA-TPC. The internal alignment of the system is evaluated by CERN metrology service, in order to control the parallelism between the cathode surfaces and the readout planes and their orthogonality to the drift direction. Successively, the gas tightness is evaluated by sealing the volume with aluminum plates on the module frame. The field cage mechanical and electrical properties are thoroughly verified at NEXUS and at CERN in order to confirm the compliance with the required performances. Then, the structural deformation due to under-(over-)pressure is estimated and compared with simulations. As a last test before ERAM sensors installation, the deformation of the system due to external weight placed on top of the TPC is studied and compared with the simulation.

### 4.5.1 Metrology

The evaluation of the inner surface of the field cages is performed at NEXUS and at CERN in order to check:

- surface planarity;
- opposite walls parallelism;
- adjacent walls orthogonality;
- cathode surfaces planarity;
- distance of last strip from flanges;
- flanges smoothness and planarity.

The listed items concerning field cage walls are crucial for ensuring the parallelism of the electric field to the drift direction and to identify defects during the production phase. The smoothness and planarity of flanges is important to guarantee a proper contact between the two field cages or with the module frames for optimal gas tightness.

**Surface planarity** A full 3D survey of each field cage was conducted using a high-precision laser measurement system with an accuracy of 80$\mu$m across a volume of several cubic meters. The measurements were compared against the nominal 3D CAD model.

Overall, the displacement from the nominal design in critical regions did not exceed $\pm$ 300$\mu m$ for any of the cages, with a variance of less than $\pm$ 100$\mu m$. These results confirmed that all cages met the required specifications.

In some cases, consistent but acceptable geometric distortions were observed in critical regions. As illustrated in Figure 4.23, certain areas exhibited deviations of up to 800$\mu m$, from the nominal plane, with deformations gradually varying along the wall.

Such distortions may result from residual mechanical stresses in the field cage structure due to material expansion and contraction during curing cycles. Despite careful selection of the fiber-fabric type for the Twaron peel and an optimized layup sequence-where four fiber-fabric layers are oriented at 0°, 45°, 90°, and 135°-these deformations cannot be completely eliminated. They represent an intrinsic limitation of the current state-of-the-art manufacturing technology.

Additionally, while the field cages are fabricated in a vertical orientation (with the drift direction aligned vertically), they are operated in a horizontal position and supported at different points. This change in orientation introduces further geometric distortions, which were measured to be within 300$\mu$m/m per meter.

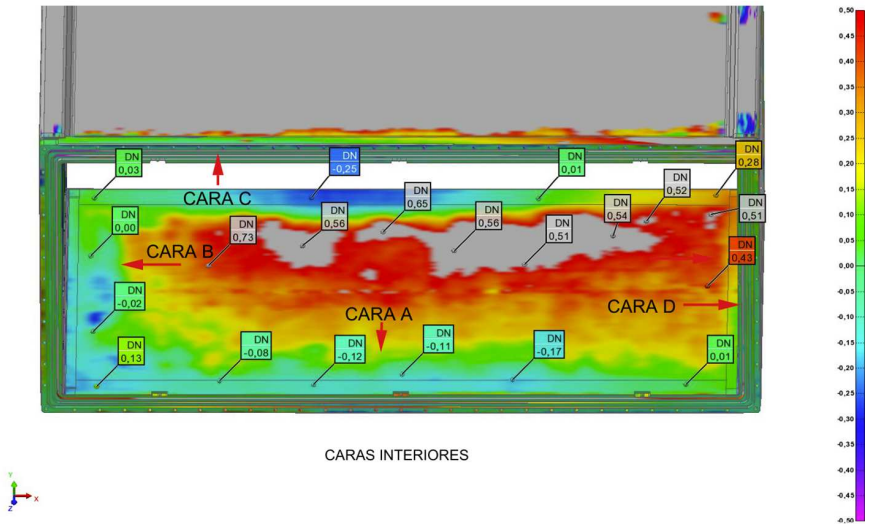


Figure 4.23: Measurement of field cages planarity performed at NEXUS. Color scheme represents the deviation from ideal planar surface in millimeters.

**Walls parallelism** A second type of test is performed to evaluate the distance between the corresponding points in two opposite walls, which is a way to check that the field cages can be considered as a parallelepiped within the required constraints. The distances over 15 points for two large walls and two small walls are measured, while only the 5 of them in the central zone along the drift direction are reported respectively in figure 4.24 and figure 4.25. The values show a very good agreement between the set of distances along the whole surfaces, with a maximum deviation of 0.46 mm over an average distance of about 705 mm for the large sides and a maximum deviation of 0.93 mm over an average distance of about 1750 mm for the small sides, which is an impressive results considering the challenging construction procedure. Furthermore, the slight differences in the total distance seem to depend mainly on the planarity deformations of the walls, while there is no evident global trend on such measurements.

**Cathode planarity** Cathode structure is different from field cage walls and is realized by a different company, so its planarity might differ from the field cage one. The measurements were performed by metrology service at CERN and are reported in figure 4.26 for one of the two cathodes. The picture shows two horizontal regions in which the cathode surface is bending towards the observer and one central zone in which the opposite effect is visible. This deformation might derive from the procedure in which the copper layers are applied on the underneath supports which are not filling the whole inside volume. As for field cage walls, the cathode deviations from the ideal planar surface is at most 0.806 mm. Picture 4.26 contains also measurements of the cathode flange planarity. From the measurements performed, the top right corner in the picture differs about 0.3 mm away from the bottom right corner, hinting towards the fact that the plane of the flange is slightly tilted from the expected vertical plane. However, the deviation can be neglected and the the flange do not present large local deformations but only the mentioned global effect is present.

**Last strip placement** The position of the closest field strip to the anode flange is relevant since it is useful to estimate the orientation of the plane identified by the strip with respect to the ERAMs plane. Therefore, a tilt between the two planes might correspond to a deviation of the electric field

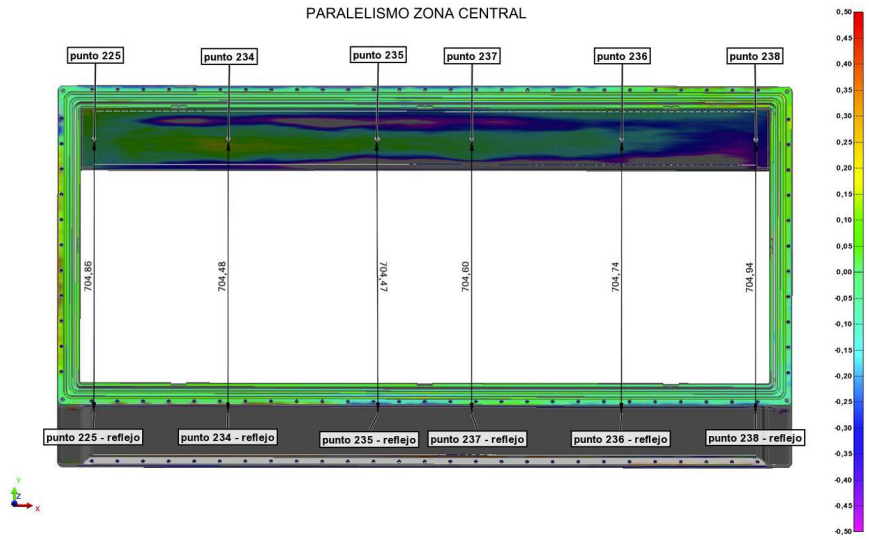


Figure 4.24: Measurement of distances between series of two points on the two opposite large area sides of the field cage. Colour scheme represents the deviation from ideal planar surface in millimiters.

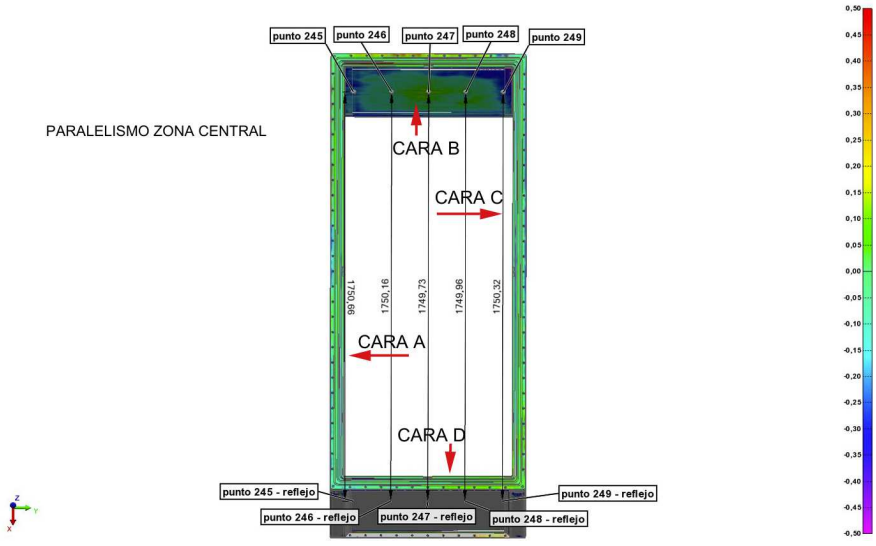


Figure 4.25: Measurement of distances between series of two points on the two opposite small area sides of the field cage. Colour scheme represents the deviation from ideal planar surface in millimiters.

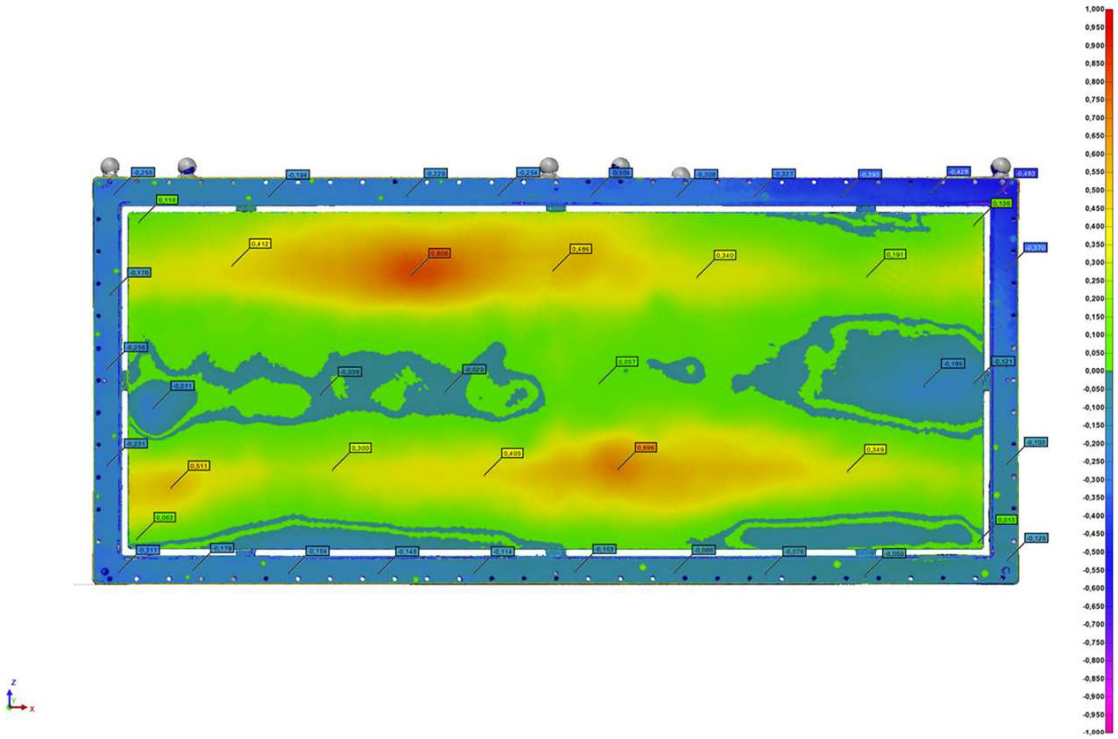

Figure 4.26: Measurement of cathode and flanges planarity performed by CERN metrology service. Colour scheme represents the deviation from ideal planar surface in millimeters.

from its ideal direction. The measurement is performed by NEXUS and an example is reported in figure 4.27. The differences between the nominal position and the measured ones are mainly of the order of few hundreds of micrometers, while the maximum deviation is about 0.4 mm. Such deviation is recorded for the angle in which the two ends of the strip foil are meeting, in which is the most delicate point for alignment on the first step of field cage production. Therefore, the handling of the strip foil might have caused this small deviation from the nominal position, which is still satisfying the alignment requirements.

**Insulation test** In order to test the insulating properties of the strip foil and the materials below, two series of 10 mirror strips are soldered together in different parts of the strip foil. Then, a Megger insulation tester S1-1068 is used to give a potential up to 10 kV between the two electrodes.

## 4.6 Validation of mechanical properties

The performances of field cages wall under mechanical stress is evaluated by performing a load test and by applying over and under pressure in the inner volume. In addition to safety concerns, the estimation of the deviation from the planarity of field cages walls is an important parameter for electric field deformation.

### 4.6.1 Load test

Load tests are performed on the final configuration of the HA-TPCs, in which two field cages and the cathode are jointed together. The two field cages system is placed on three supports corresponding

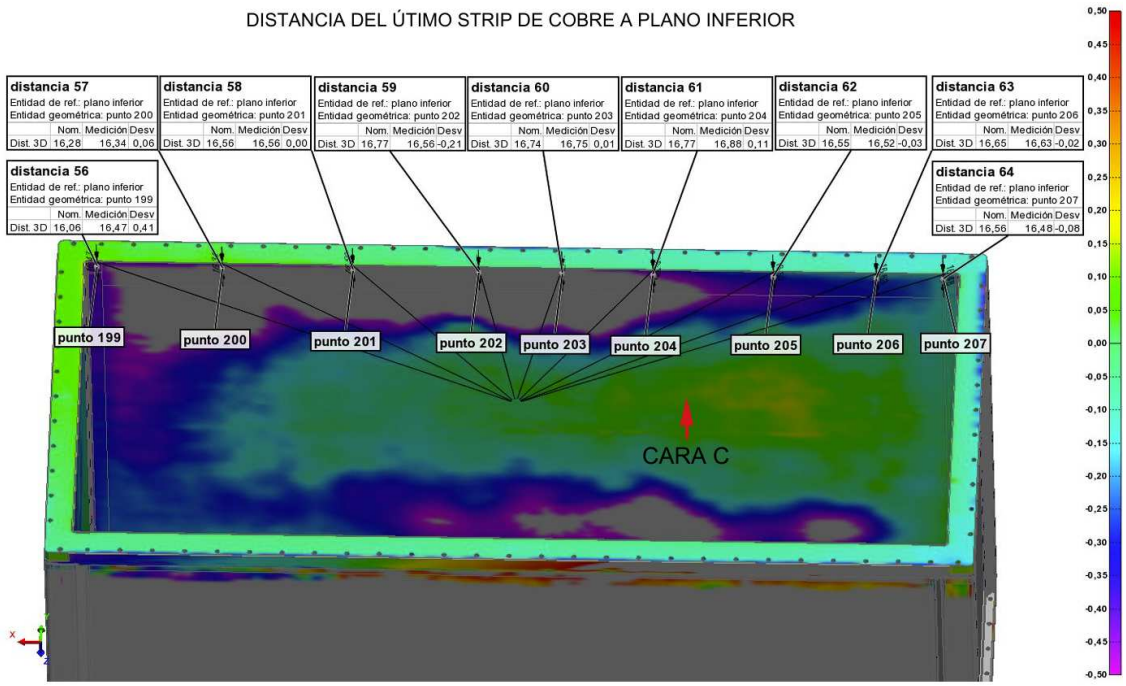


Figure 4.27: Measurement of the distance between the last field strip and the anode flange for a side of a field cage.Colour scheme represents the deviation from ideal planar surface in millimeters for the visible part of field cage walls.

to three of the four bottom corners. This configuration is chosen (i) to ensure planarity and (ii) to allow the middle flanges to bend. Then, weights are applied on different places on the flanges in the upper side of the TPC. A reference point is set on the lateral side of the TPC in the middle flange. The displacement of the reference point under the additional weight is measured and its compliance with the required safety norms is evaluated.
The results reported refer to the first HA-TPCs, composed by FC1 and FC2. Since the production of field cages was sequential, a first load test was performed on the system composed by FC0 and FC1. The test was repeated later on the final configuration for the bottom HA-TPC composed by FC1 and FC2. The two setups are different, since FC0 was already modified. In fact, in order to assess the resistive properties of the internal Twaron layer, the strip foil was removed. Once the measurements were performed, a thick fiberglass panel was glued to every inner surface of the FC0, likely making it more rigid. The results are reported in figure 4.28, in which a similar behaviour between the two setups is visible. The two setups proven to withstand loads of at least 200 kg placed on the upper part of the junction, in which the two field cages are jointed by G10 screws. Once the weights were removed, the two field cages went back to their original position with no permanent structural modification. The data were fitted with a line and the deflection rate has been estimated in table 4.8, in which a slightly larger flexibility is reported for *FC1+FC2*, very likely due to the fiberglass panels installed on FC0. The results of the tests show that from a mechanical point of view the production protocol for field cages leads to items with similar and reproducible mechanical properties. The results were considered compliant with the related safety regulations.

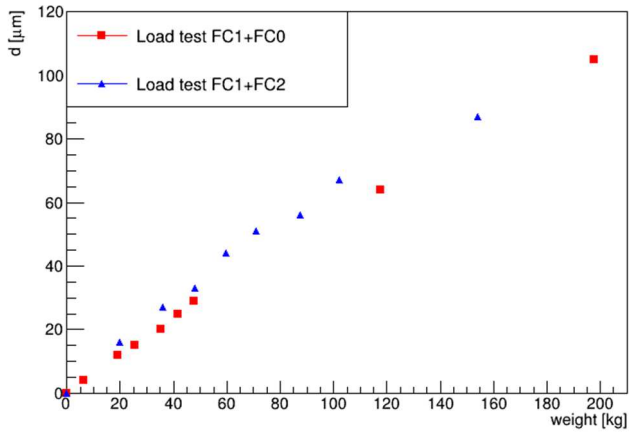


Figure 4.28: Load test for setups *FC0+FC1* (red) and *FC1+FC2* (blue). The two setups show similar deflection rates and have been tested up to 200 kg.

| System | Deflection rate $[\frac{\mu m}{kg}]$ |
|---|---|
| FC0+FC1 | 0.527±0.007 |
| FC1+FC2 | 0.57±0.03 |

Table 4.8

### 4.6.2 Walls deformation due to gas pressure

The evaluation of field cages deformation under the action of overpressure or underpressure is relevant for both safety concerns and physical performances. Even if HA-TPCs are expected to work under a slight over-pressure of few mbars, they are designed to withstand an overpressure regime up to 20-30 mbar, that is equivalent of a force of $3{\times}10^3$ $\frac{N}{m^2}$, which is the force per unit of area applied by a weight of about 310 kg. As seen in the load test case, the application of weights can displace the structural position of field cages and therefore modifies the planarity of field cages walls. This effect will translate into a modification of the electric field direction, in particular in the region close to the walls.
In order to evaluate this effect, the final setup of bottom HA-TPC (*FC1+FC2*) was sealed with two module frames. The openings designed to house ERAMs were closed by metallic plates of similar dimensions instead. Successively, the whole system internal pressure is modified and the displacement of walls and flanges is recorded and the corresponding datasets are summarized in figure 4.29. A fit to a line is performed excluding the data points in which a plateau is reached and the slope of each fit is reported in table 4.9. In both field cages, the deflection of walls with large surfaces is larger by an order of magnitude with respect to the small ones, which is the case also for the flanges on the long side of the cathode at the junction. By comparing the properties of both field cages, a similar behavior is reported for both topside walls, while for the side walls the comparison is unclear. Considering only the points in which there is a movement of the wall, the deflection rate is compatible. However, for the short side a plateau is reached in a long range of $\Delta p$, while the large surface walls are still moving after reaching the end of $\Delta p$ range. Measurements can be compared with the mechanical simulations performed at the design stage of the field cage, in which

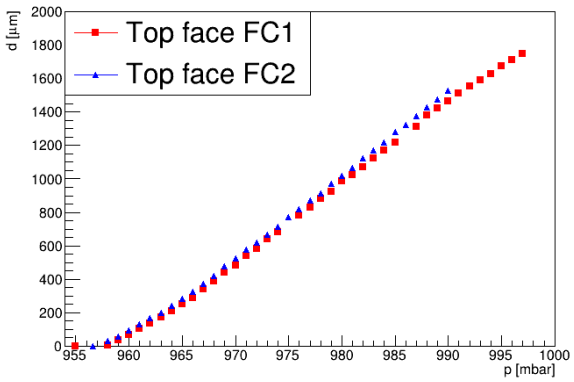


(a)

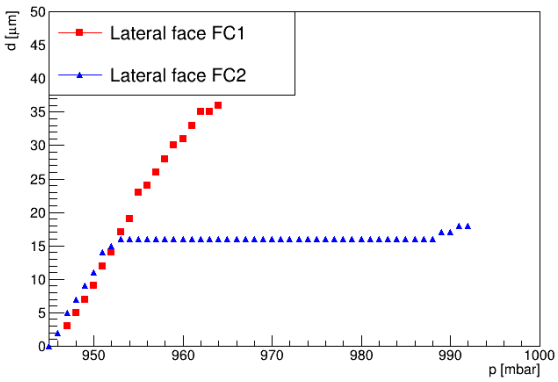


(b)

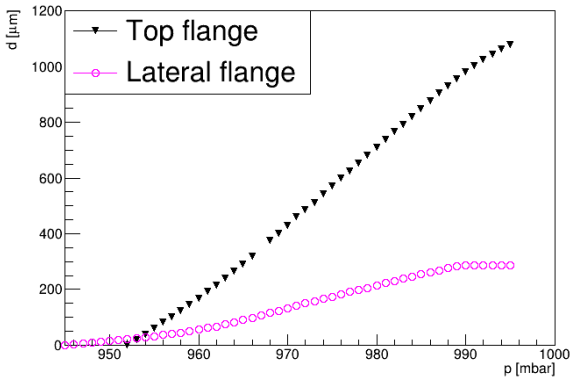


(c)

Figure 4.29: Displacement as a function of the internal pressure is reported. The outer pressure was measured to be around 970 mbar, however its accuracy is not relevant, since the important parameter is the structural deflection rate. Central position for field cages walls on one of the large faces 4.29a and on one of the short faces 4.29b. Figure 4.29c reports the displacement for flanges on the cathode side, which are jointed by fiberglass screws.

| Position | Deflection rate $[\frac{\mu m}{mbar}]$ |
|---|---|
| Top FC1 | 48.4±0.2 |
| Top FC2 | 50.0±0.2 |
| Side FC1 | 2.43±0.07 |
| Side FC2 | 2.20±0.07 |
| Top Flange | 27.5±0.1 |
| Side Flange | 8.31±0.03 |

Table 4.9

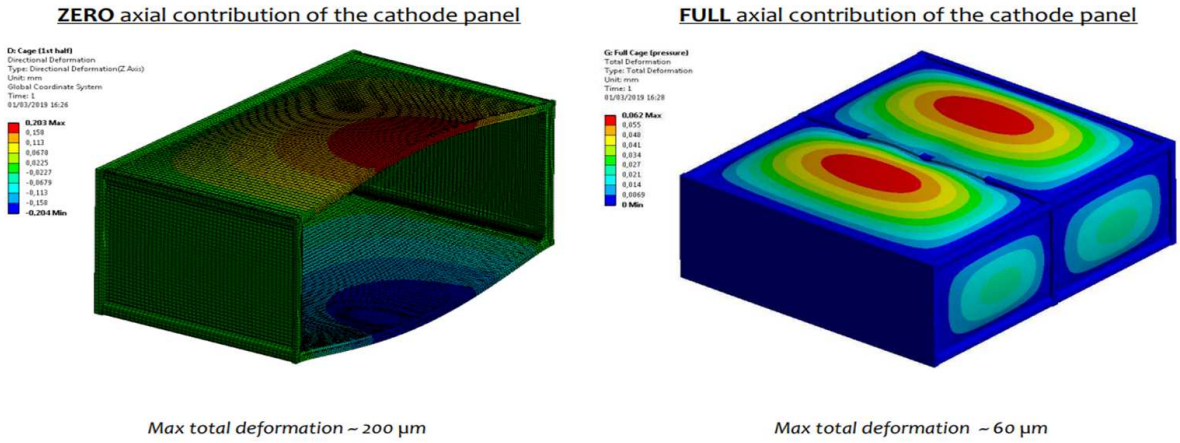


Figure 4.30: Simulation of field cages response to overpressure of 10 mbar in the hypothesis of free (left) and constrained (right) middle flange by the action of cathode. Picture from [96].

a maximum displacement of about 230 $\mu$m was found at a $\Delta p$ of 10 mbar [96]. The results from simulation are reported in figure 4.30, in which a factor of 2.5 of overestimation for the structure flexibility was used. The finite element simulations were performed using two different assumptions: (i) the flanges in the middle are rigid and strongly constrain the walls movement; (ii) the flanges are free to move under the action of over/under-pressure. Measurements on the flanges in figure 4.29c show that cathode is only partly reducing the whole top surface movement, showing a behavior in between the two hypotheses. This different property might explain why the large surface walls are displaced by over a factor 2 more than in the simulation. However, even if there is a discrepancy between the two estimations, the performance of the HA-TPC satisfies the requirements and the effect of this deformation on the electric field might be evaluated in further studies.

## 4.7 Electric properties of the field cages

The final step of evaluation for the electric properties of the field cages is performed by accurately assessing the currents flowing on the voltage dividers.
As an initial test, once the voltage divider is soldered to the field cage, the quality of the soldering is checked for each individual resistor. The test is conducted at 70 V and 150 V, which are representative of the voltage drop across a single resistor under the operating conditions of the HA-TPC. Indeed, by dividing the overall voltage of about -27 kV by the total number of resistors the expected $\Delta V_{single} \sim 70$ V. As an example, a plot of the measured resistance values for a single voltage divider at 70 V is reported in figure 4.31. The histogram is fitted with a gaussian distribution with centroid $R_{FC4} = (5.08818 \pm 0.00007)$ MΩ. The picture shows that the soldered resistances did not present any anomalous behaviour. Subsequently, the voltage dividers are analyzed as a whole. For this measurement, the hot polarity is connected to the cable in the feed-through, while the cold electrode is connected to the strip closest to the anode side. This process is performed at 10 kV on both field cages, and the results from both are found to be identical within the sensitivity of the insulation tester, as shown in figure 4.32a.

In addition, the insulation between the inner side of field cages and the external shielding (Mantle resistance) is estimated (see Paragraph 4.2.4). For this estimation, the hot polarity is connected to the cable in the feed-through, while the cold polarity is connected to the aluminum shielding of

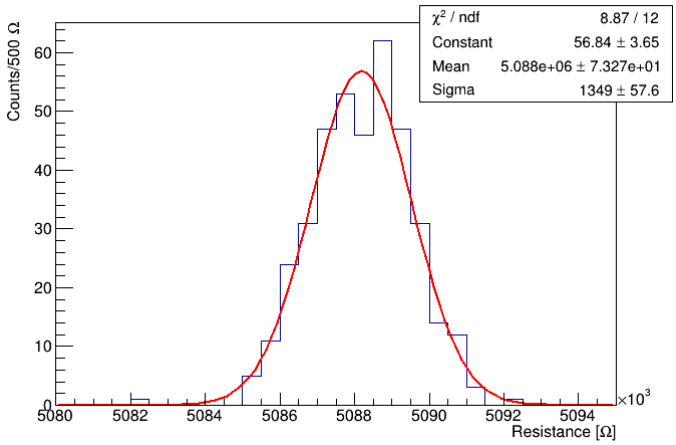


Figure 4.31: Distribution of measured resistance values for a single voltage divider in FC4 at 70 V.

FC1. In order to exclude further contributions to the leakage current, the FC2 shielding is guarded, along with the module frames on both field cages. Therefore, in this configuration, we are expected to estimate the current flowing through the FC1 walls. Two additional paths are still possible: (i) through the connector case and the external gap between the cathode flanges and the aluminum shielding; (ii) through the grooves in the cathode side from the inner part to the external part of the field cages junction. This measurement is able to constrain such leakage currents, whose potential presence is a major concern for the stability of HA-TPCs over time. In order to increase the path length of potential currents through the junction, a groove is placed in addition to the two housing O-rings for gas tightness, as showed in figure 4.21. The measurement is performed over a time period of 10 hours at a voltage of 10 kV (figure 4.32b) and it shows a continuous decrease of the measured current until reaching a plateau, which is fitted with a horizontal line. The estimated current is equal to $I_{leak} = (3808.2 \pm 0.4)$ pA, from which the estimated resistivity is R=$(2.6259 \pm 0.0003) \times 10^{12}$ Ω, that is about 3 order of magnitude larger than the voltage divider resistance. However, the measured current is about one order of magnitude larger than the sensitivity of the device, hence the estimated value is not an upper limit and the leakage is present. Therefore, the leakage current has to be evaluated and monitored over time at the working regime of about 27 kV.

## 4.8 Summary

The field cages for HA-TPCs present an innovative design based on composite materials that greatly differs from the one used in vTPCs. The use of composite materials allow to: (i) have minimal dead volume, (ii) a reduced radiation length of the order of $\sim 2.5\%$ and (iii) optimal mechanical and electrical properties.
The construction procedure was presented, highlighting the tests performed at every step. The tests include: (i) the assessment of the insulating properties of the field cages inner layers and of the applied resins; (ii) the evaluation of field cages structure compliance with its original design thanks to NEXUS and CERN metrology services; (iii) the evaluation of the field cage mechanical properties.
Those tests assured that field cages comply with the required performances, and that the issue observed in FC0 was understood and positively resolved.

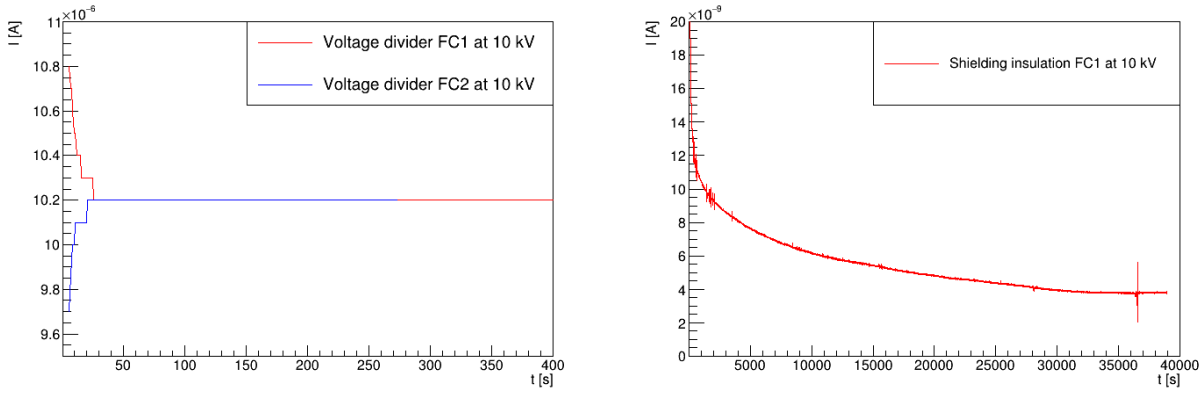


(a) (b)

Figure 4.32: Measurement of current flowing through the voltage divider resistances for FC1 and FC2 at a voltage of 10 kV in figure 4.32a. On the right in figure 4.32b, the leakage current at 10 kV from the feed-thorugh to the shielding of FC1 is reported. The two plots estimate the alternative paths from cathode to ground, in which the leakage to the shielding is negligible as intended.

# Chapter 5

# Characterization of Field Cage response

This chapter is dedicated to the study of the first full-scale field cage, referred to as *FC0*, which was not used in the construction of the HA-TPCs due to critical issues with its insulating properties. Understanding the anomalous behavior of FC0 was a priority at the time of its discovery, as it could have indicated a fundamental flaw in the field cage design and a serious potential failure for the HA-TPCs project.

A comprehensive analysis was conducted on each component involved in the field cage production, along with studies of FC0's inner layers made possible by the removal of the strip foil. The collected measurements were compared with a model of parasitic electrical conduction mechanisms through the inner layers of FC0, suggesting the possibility of degradation in the insulating properties of Kapton and Twaron. This degradation could create an alternative path for currents flowing through the voltage divider that connects the copper strips.

As a consequence of the detailed investigation described in this chapter, the source of the issue was identified not as a field cage design flaw but as a defect in the production process at the company's facility. During a pause in production, in the COVID period, a large amount of anti-static spray was applied to keep one of the inner layers of the cage clean. Specifically, the water-based, low-resistivity anti-static spray was absorbed into the 25-micrometer-thick Kapton layer (the so-called coverlay) that is glued onto the mirror strips on the backside of the strip foil. This contamination subsequently affected the Twaron layer, which was later laminated on top of the coverlay.

As a result, a parasitic current path was formed, extending from the cathode to the anode and providing low-resistivity access to all the strips. This unintended conduction route was embedded within the cage wall, confined to the first few hundred micrometers.

As described in this chapter, through detailed electrical characterization, the development of a mathematical model, and subsequent design improvements, this issue was successfully understood and resolved. The design and production process of the subsequent field cages was modified to incorporate additional insulating material layers between the strip foil and the Twaron, enhancing redundancy.

As a result, four new field cages were produced, as discussed in Chapter 4, and were used in the assembly of the two HA-TPCs at CERN. The HA-TPCs were later installed at J-PARC. Recently, the first field cage, FC0, was recovered and will be repurposed for electric field measurements at CERN.

## 5.1 Validation of High Voltage response

After the delivery of FC0 at CERN, the 800 resistors that connect the strips are soldered and tested. Then, a test on the field cage current response was performed. A DC Power Supply was used to provide a voltage up to 30 kV in negative polarity. The current was measured using both the Supply internal amperometer and an external Multi-meter, applied to the ends of a load resistence of 10 kΩ, which is negligible with respect to the total resistance of the voltage divider.
The test detected a deviation from the linear response, with a current excess that was steeply increasing when approaching voltages close to the working regime at about -27 kV. The tests raised serious concerns regarding the stability of the first field cage. The total current $I_{tot} = I_{linear} + I_{extra}$ can be expressed as a sum of the expected current for an ohmic conductor and an extra-current, that represents an unexpected deviation from the ideal circuit of the voltage divider. The total current has been measured with voltage values ranging from 1 kV to 15 kV as reported in figure 5.1. The deviation from the ideal case shows a consistent behavior across different voltages. Furthermore, for applied voltages of absolute values larger than 25 kV, a permanent modification on the absolute value of the total current is noticed once the measurements are repeated even at lower voltage values.

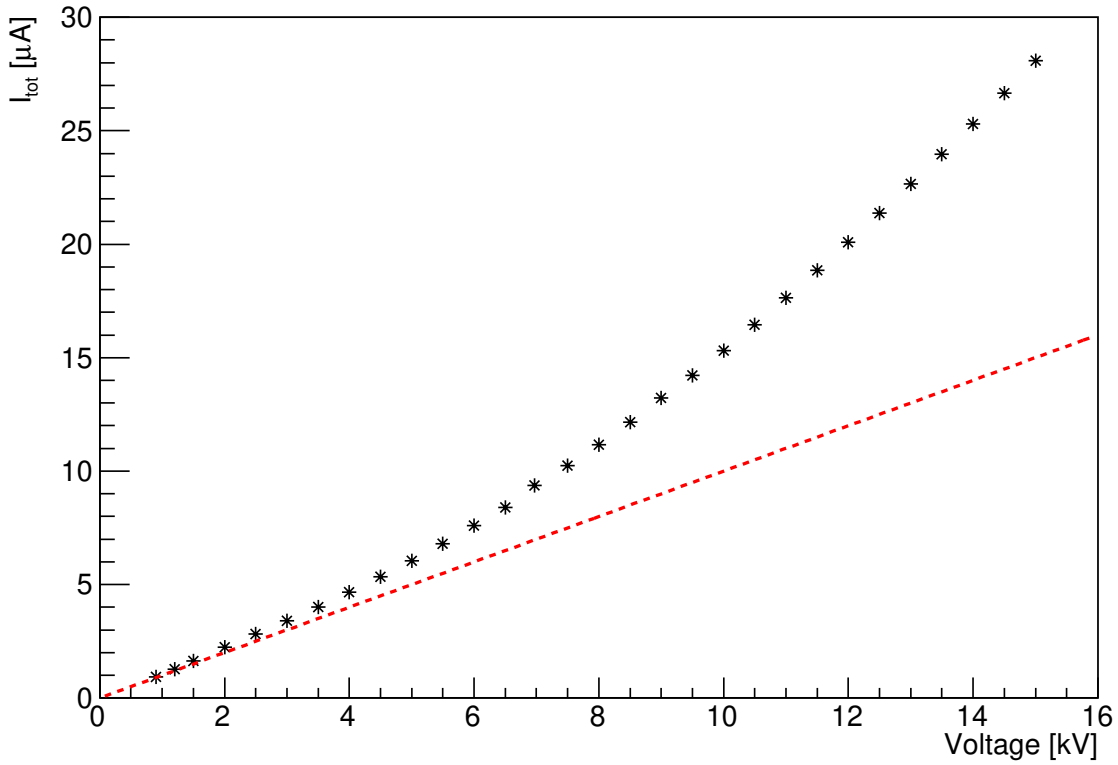


Figure 5.1: Measured total current (star points) compared to the simple ohmic model which consider only the voltage divider (red dashed line) of 1 GΩ.

The dependence over time of the total current has been studied by setting the voltage at 15 kV. In figure 5.2 it is possible to observe a first regime in which the current is steadily decreasing due to

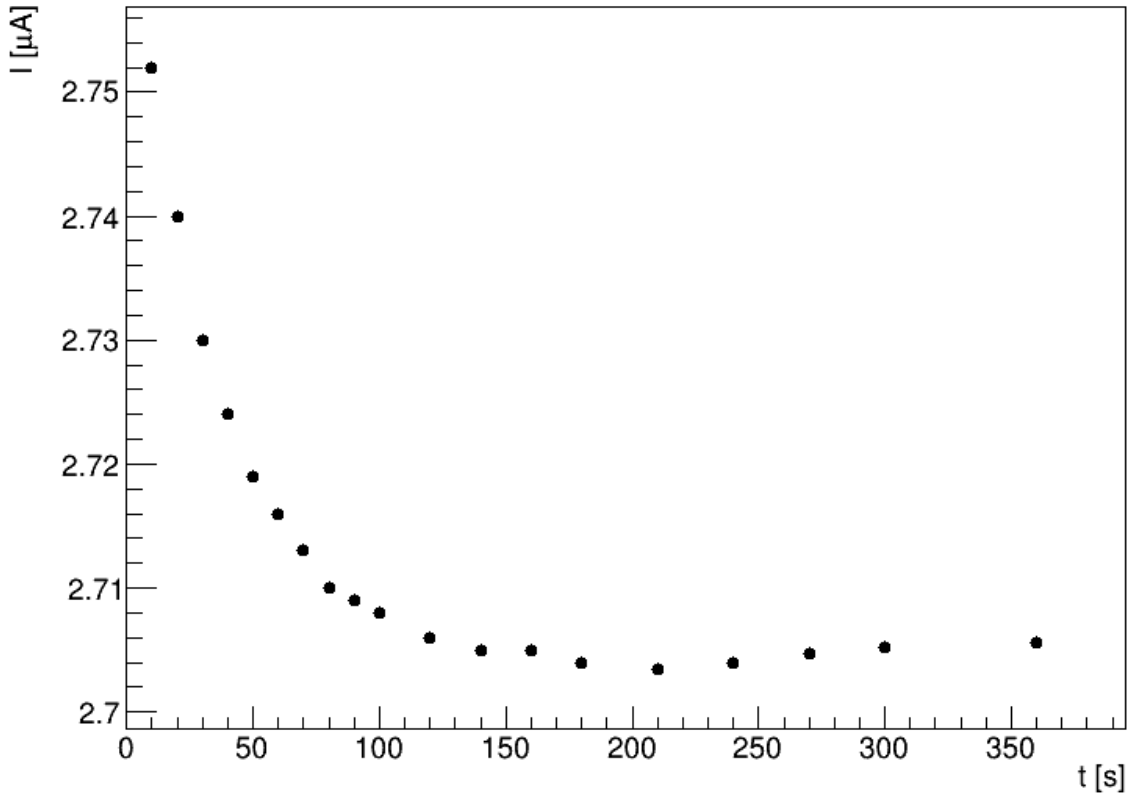


Figure 5.2: Measured total current over time using a voltage of 15 kV over a nominal total resistance equal to 1 GΩ.

capacitance and polarization phenomena, while an asymptotic behavior is seen at longer times due to the conduction through the voltage dividers and possible other paths.

### 5.1.1 Possible sources

The higher value of total current could be interpreted as a lower effective resistance, due to the availability of alternative paths for the current in parallel to the installed voltage divider. The phenomenon might derive from the involvement of either electrical parts characterized by large RC values or dielectric relaxation phenomena. However, no such extra current effects were noticed at any level when operating a field cage prototype built with the same procedure, but differing by the transverse dimensions of the inner volume (42x42 $cm^2$ instead of 175x84 $cm^2$), with FC strips length (and surface) of about one fifth of FC0.

A model that explains the presence of other paths inside the FC0 other than the voltage divider requires two major elements:

- a layer with resistivity much lower than its nominal value;

- a way for the free charges to access such layer, that need to pass through the Kapton coverlay. This also implies the 25 $\mu m$ Kapton sheet used in the FC0 construction to present a much smaller resistivity with respect to its nominal value.

Therefore, in order to have the presence of an extra current according to the mentioned mechanism, we need the presence of (i) *vertical* and (ii) *horizontal* conduction mechanisms. Several investigations were performed in order to test the field cage materials of the strip foil and underneath layers, with particular attention to the layers close to the voltage divider:

- Kapton coverlay of the strip foil;
- Twaron layer glued to the strip foil, referred to as internal Twaron.

The modelization and the measurements reported in the following sections aim to study the nominal and anomalous operating conditions, trying to estimate the contribution of each layer to the observed phenomenon.

## 5.2 Measurement on FC0 voltage divider

Once the presence of an extra current was observed as reported in figure 5.1, other two kinds of measurements were performed. First, the value of the resistance between two consecutive field strips has been measured along the strip foil. The dataset is shown in figure 5.3a, in which a clear deviation from the expected measurement is seen, with a deviation up to few percents from the expected value. Their distribution differs substantially from the observed values for FC4, in which a proper insulation from layers below the strip foil has been ensured. The mean value for FC4 resistances corresponds to $R_{FC4} = (5.088 \pm 0.001)$ M$\Omega$, with a variance for resistance distribution values of about 1 k$\Omega$.

A second set of measurements have been performed by providing a fixed voltage of 5 kV along the

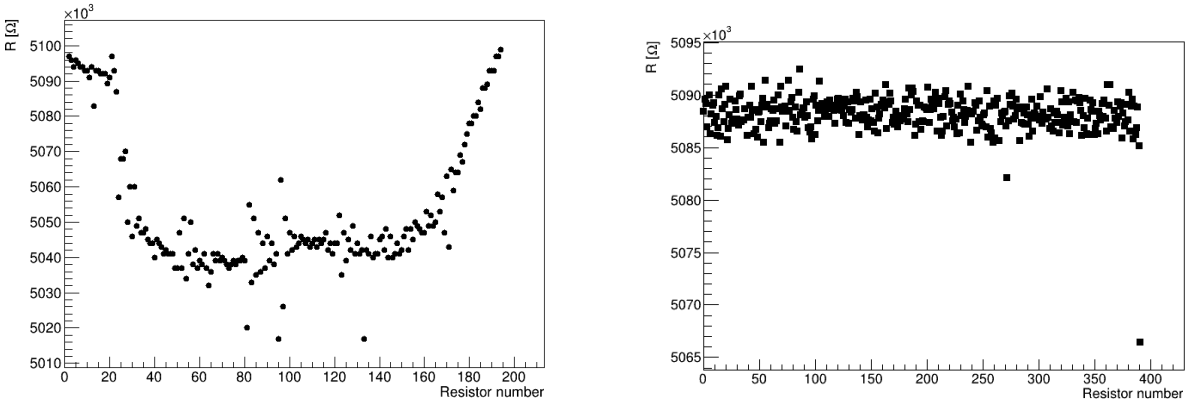


(a) (b)

Figure 5.3: Comparison of measured value of resistances for two different field cages. Picture on left 5.3a represents the total resistance between two consecutive field strips on FC0 at 140 V, while picture on right 5.3b shows the resistance between two adjacent strips (mirror-field) at 70 V with only one voltage divider soldered for FC4. The number of measurements for 5.3a is half 5.3b, but both plots cover the whole drift length.

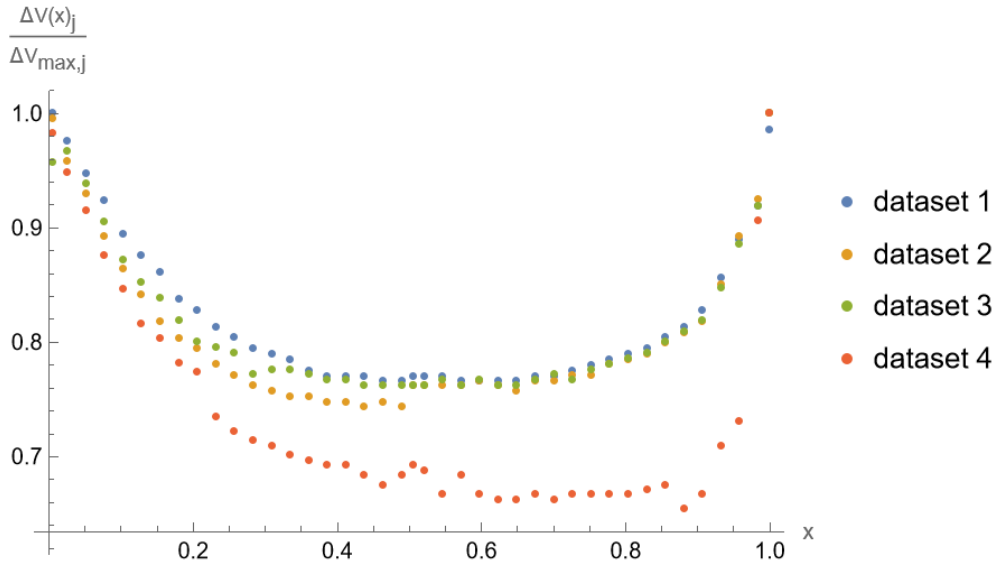


Figure 5.4: Plot of difference of potential between two successive strips on different points along the Field Cage with a tension of 5 kV applied to the voltage divider, normalized to the variation at the edge for each dataset j = 1,2,3,4.

voltage divider and by sampling the potential drop $\Delta V$ from one strip to the following along the drift volume using a Keithley Series 2400 Source Measure Unit, which is able to measure difference of voltages up to 1000 V [125]. The first three datasets were collected under the same conditions, while the fourth one was collected once the voltage was raised to 25 kV and then brought back to the lower value of 5 kV as shown in figure 5.4. Datasets 1,2,3 are similar while dataset 4 behaves differently. This hints to the fact that the field cage might have suffered a modification of its properties once exposed to such value of high voltage, which is still lower than the expected working regime of 27.5 kV.

## 5.3 Model

The behavior of FC0 is not compatible with the case of an ideal voltage divider, as seen in the previous sections. Therefore, a model of the field cage electrical response to a direct current in a steady state is presented as an alternative explanation. A sketch of the FC0 section of the walls is reported in figure 5.5. In the FC0, the internal Twaron layer is glued directly to the strip foil. The separation between mirror strips, where the current on the voltage divider flows, and the Twaron layer is ensured by the 25 $\mu$m thick Kapton layer. In this section, the hypothesis of a non insulating Twaron layer is introduced and a modelization of the equivalent electrical system is performed. In such a system, the current in the voltage divider may flow along new paths through the Kapton coverlay and across the Twaron layers. A schematic view of the system under this assumption is reported in figure 5.6. The structure of the field cage is periodic along the drift length and it consists in an a pattern of alternating field and mirror strips. Since field strips are further away from the Twaron layer with respect to mirror strips, their contribution as a path in parallel towards the Twaron layer can be neglected. The model is based on the characteristics resistivity of three materials: (i) voltage divider resistors with an expected value R of about 2.5 M$\Omega$ for two neighboring strips, (ii) Kapton volumetric resistivity K and (iii) Twaron surface resistivity T.

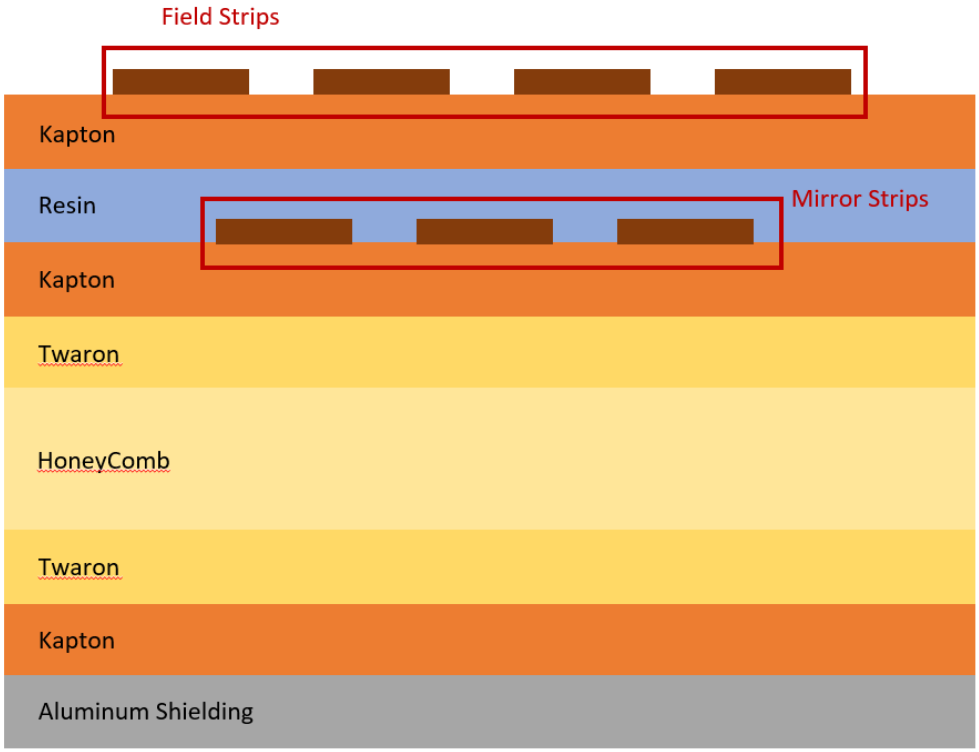


Figure 5.5: Sketch of the Field Cage walls from inner part on top to the external Aluminum shielding. Not on scale.

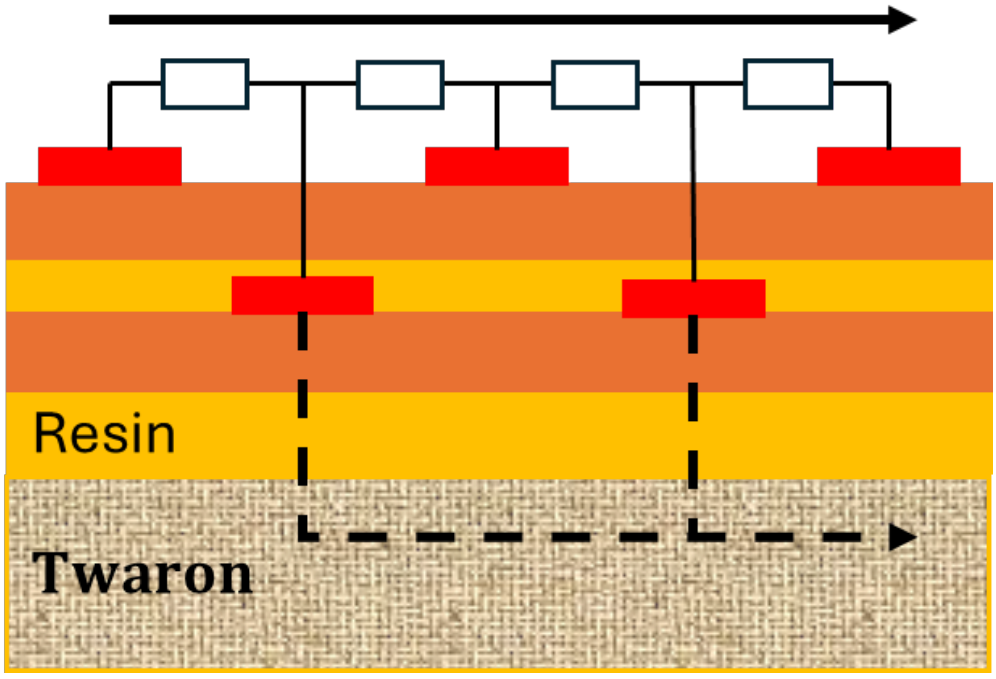


Figure 5.6: Sketch of possible paths for current on Field Cage walls.

The field cage design allows to access the entirety of field strips, while the mirror strips can be accessed only through copper pads that are placed on the same surface of field strips. Therefore, the design does not allow to directly probe the layers below the mirror strips without compromising the Field Cage properties in a irreversible manner.
The model can be used to compare the measured values of resistances in figure 5.3a and $\Delta V$ in figure 5.4 with the predicted values, which are presented in the next sections.

## 5.4 Local measurements of voltage divider resistors

The presence of an alternative path for the current implies that the measured resistance across two consecutive field strips is not necessarily proportional to the resistance on the voltage divider. In fact, several contributions to the measured current are at play. In the setup presented in figure 5.3a, the resistance between two successive mirror strips is evaluated with a multimeter and no external voltage is applied along the voltage divider by a DC power supply. The measured resistance is given by the series of resistances field-mirror-field strips on the voltage divider for a total nominal value of 5 MΩ. However, the presence of alternative paths along the field cage might lower the measured value which can be considered as *effective resistance* $\mathrm{R}_{eff}$. Thanks to the presence of those alternative paths, it is possible to find an estimation for K and T from the measured value $\mathrm{R}_{eff}$ by modeling the system under examination.
As a first approximation, the current is considered to reach the Twaron layer by passing through the coverlay only starting from mirror strips which are closer to Twaron with respect to field strips. Then, the current injected by one of the multimeter electrode might reach the other electrode by (i) passing directly in the voltage divider or (ii) passing through Kapton and Twaron layers and then through the voltage divider on the nearby strips. The estimation of the magnitude of the second contribution might help in assessing the local values for K and T.
The model of the circuit for this kind of measurement is reported in figure 5.7. The two ends of the multimeter are connected to two field strips. The least resistive path is the one in the voltage divider composed by two resistances R. The middle node in the figure is the mirror strip, which is connected to Twaron through the Kapton coverlay with resistance K. At first order, the alternative path continues towards the Twaron layer with resistance T and it is connected to the closest mirror strip through the coverlay again. By including additional strips, it is possible to find new paths for the current. Due to the placement of the cathodes, the presence of additional $n$ paths can be interpreted as a lower effective resistance for the coverlay $\mathrm{K}^{(n)}$.
According to this model, the effective resistance at order $n$ $\mathrm{R}_{eff}^{(n)}$ is given by the relation for two parallel resistances

$$\frac{1}{R_{eff}^{(n)}} = \frac{1}{2R} + \frac{1}{2R + 2K^{(n)} + 2T} \tag{5.1}$$

in which the contribution from additional loops is given by $\mathrm{K}^{(n)}$.
An analytical form for $\mathrm{K}^{(n)}$ can be found by solving a recursive equation which is given by:

$$K^{(0)} = K, \tag{5.2}$$

$$\frac{1}{K^{(1)}} = \frac{1}{K} + \frac{1}{2R + K^{(0)} + T}, \tag{5.3}$$

$$\frac{1}{K^{(n)}} = \frac{1}{K} + \frac{1}{2R + K^{(n-1)} + T}. \tag{5.4}$$

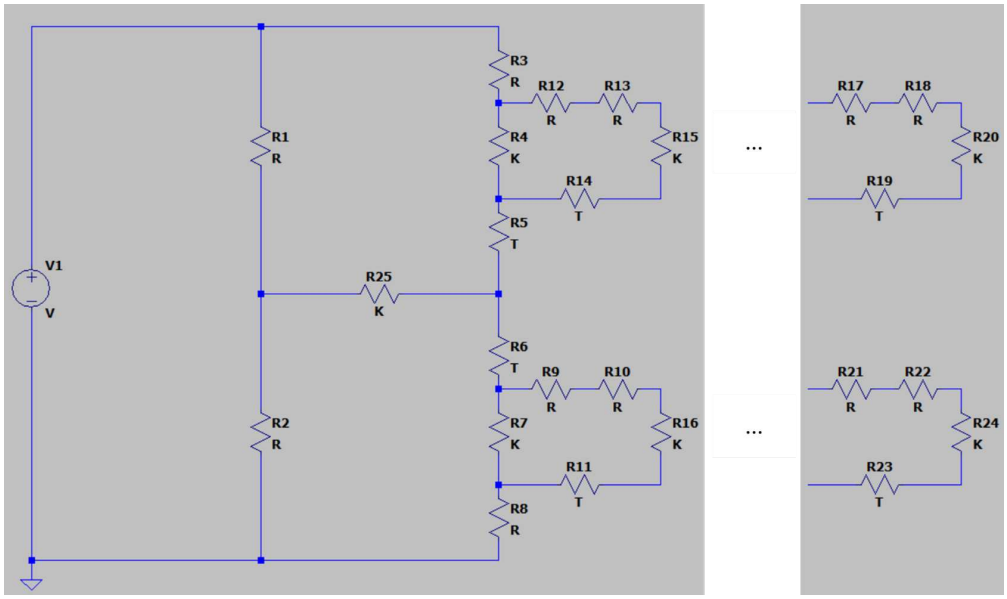


Figure 5.7: Sketch of the possible paths for current for a voltage applied at two successive field strips. The resistance between field-mirror strips is called R≃2.5 MΩ, while K and T are the respective Kapton and Twaron resistivity for a single cell. The additional loops represent the n-term correction due to the presence of additional cells on the two side of the voltage divider.

Equation 5.4 is solvable analytically, but its form is complex. By dividing the equation in the numerator N and denominator D, such that $K^{(n)} = -K\frac{N}{D}$:

$$\begin{aligned} N = &-\sqrt{2R+T}\sqrt{4K+2R+T}\left(-\frac{2K+2R+T-\sqrt{2R+T}\sqrt{4K+2R+T}}{K^2}\right)^n + \\ &+(2R+T)\left(-\frac{2K+2R+T-\sqrt{2R+T}\sqrt{4K+2R+T}}{K^2}\right)^n - \\ &-\sqrt{2R+T}\sqrt{4K+2R+T}\left(-\frac{2K+2R+T+\sqrt{2R+T}\sqrt{4K+2R+T}}{K^2}\right)^n - \\ &-(2R+T)\left(-\frac{2K+2R+T+\sqrt{2R+T}\sqrt{4K+2R+T}}{K^2}\right)^n \end{aligned}$$

and the denominator D is

$$\begin{aligned} D = &(\sqrt{2R+T}\sqrt{4K+2R+T})\left(-\frac{2K+2R+T-\sqrt{2R+T}\sqrt{4K+2R+T}}{K^2}\right)^n - \\ &-(2(K+R)+T)\left(-\frac{2K+2R+T-\sqrt{2R+T}\sqrt{4K+2R+T}}{K^2}\right)^n + \\ &+\sqrt{2R+T}\sqrt{4K+2R+T}\left(-\frac{2K+2R+T+\sqrt{2R+T}\sqrt{4K+2R+T}}{K^2}\right)^n + \\ &+(2(K+R)+T)\left(-\frac{2K+2R+T+\sqrt{2R+T}\sqrt{4K+2R+T}}{K^2}\right)^n. \end{aligned}$$

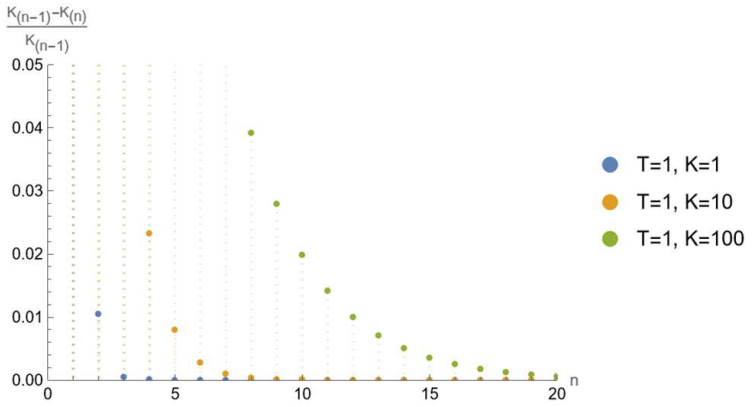


Figure 5.8: Relative difference for $K_{eff}$ at the $n^{th}$ and $(n-1)^{th}$ orders for different values of Kapton coverlay resistance and same Twaron resistance value.

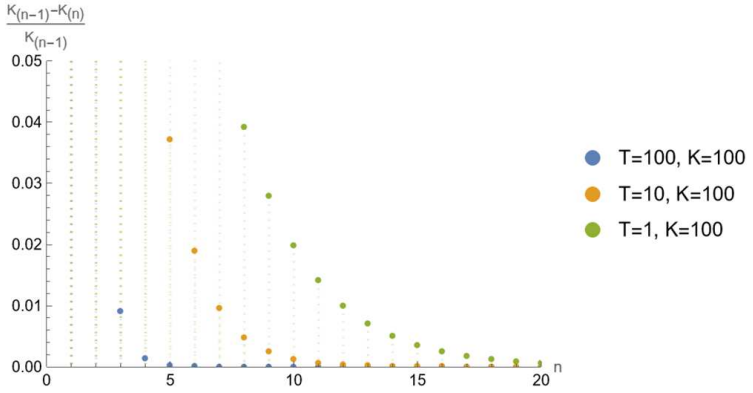


Figure 5.9: Relative difference for $K_{eff}$ at the $n^{th}$ and $(n-1)^{th}$ orders for same values of Kapton coverlay resistance and different Twaron resistance values.

A possible way to simplify the analytical form for $K^{(n)}$ is to find at which order the inclusion of additional loops becomes negligible. By expressing the value of K and T in units of R, i.e. imposing R=1, the plots 5.8 and 5.9 and show the relative difference for $K_{eff}$ at the $n^{th}$ order with respect to the $(n-1)^{th}$ one, considering different order of magnitudes for K and T. In plot 5.8, $K_{eff}$ is corrected already by only few percents after two loops if K and T are similar, while if K is much larger than T more loops are required to reach a stable point, since the coverlay is preventing the current from reaching easily the Twaron layer. Then, the same plot reported in figure 5.9 is performed for a large value of K and with different T, in which the relative difference is smaller at any loop when K and T are similar. In this case, when K and T are both much larger than R, the relative correction becomes smaller since their contribution is quite small at any level.
Once a model for $K_{eff}$ is found, it is possible to estimate the values for K and T starting from $R_{eff}$, which is expressed in equation 5.5. Depending on the strip position on the field cage, for the model in figure 5.7, a different number of loops might be considered on the two sides of the voltage divider, in particular if a resistor is placed near the edges of the field cage. The relation might be

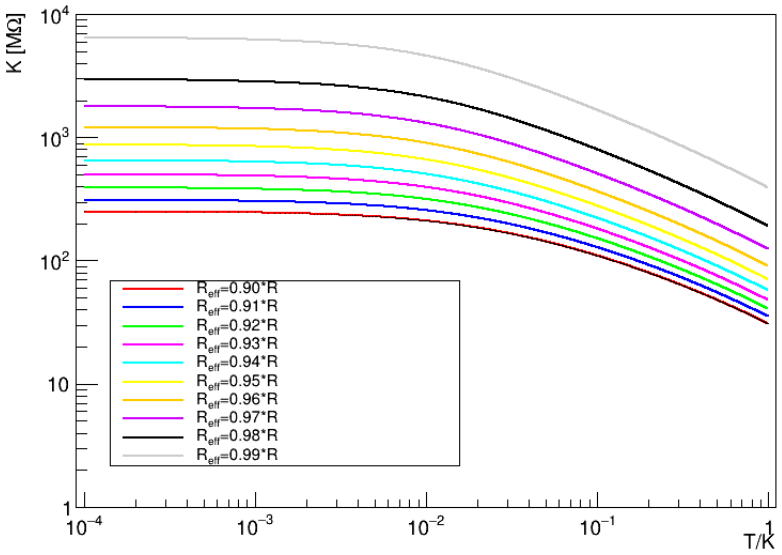


Figure 5.10: Estimated value for K at for a given value of $R_{eff}$ as a function of parameter $\lambda$.

arranged to express the relation as a ratio of K and T over R, as in previous model:

$$\frac{R_{eff}}{2R} = \frac{1 + \frac{K^a_{eff}+K^b_{eff}}{2R} + \frac{T}{R}}{2 + \frac{K^a_{eff}+K^b_{eff}}{2R} + \frac{T}{R}}, \tag{5.5}$$

in which a and b are the two sides of the voltage divider identified by the strip under examination. Unfortunately, the relation presents a degeneracy in the simultaneous determination of K and T. A sensible solution to this problem is to consider the degradation of both Kapton and Twaron insulating properties as proportional in each point of the cage. Under this assumption, it is possible to express T=$\lambda$K, with $\lambda$ uniform all along the field cage. In this way, the total number of parameters is reduced from 2N, in which N is the number of measured resistances between two consecutive field strips, to N+1: (i) N parameters for estimating local K and scale parameter $\lambda$. The system still presents a degeneracy that has to be determined in an external way. For example a possible assumption is to consider $\lambda$ equal to the ratio between the measured Twaron and Kapton resistivity. The expected value for K considering $\lambda$ in a interval which spans over two orders of magnitudes is reported in figure 5.10. Each curve represents the expected value for K at different values of $\frac{R_{eff}}{R}$, spanning from 0.9 to 1. When parameter $\frac{R_{eff}}{R}$ is approaching 1, the estimated value for K is increasing at a faster rate with respect to the case in which $\frac{R_{eff}}{R}$ is close to 0.9. Since the dependence of $R_{eff}$ from K cannot be analytically inverted, the estimation of K is found by the bisection method. The figure also shows that below a given value for $\lambda$, K is practically constant, which means that in the condition T$\gg$K, a modification in T does not affect K. The effect might introduce a large uncertainty in the estimation of T from this measurement. In order to estimate the variation of K and T according to $\lambda$, the values for $R_{eff}$ in the middle of the cage are fitted with a horizontal line. Successively, the values of $K_{central}$ and $T_{central}$ are computed for $10^{-4} \leq \lambda \leq 1$, since $\lambda$ is derived from measurements with large uncertainties. The points (K,T) are summarized in figure 5.11. The plot shows that the variation of $\lambda$ implies a large variation for both K and T.

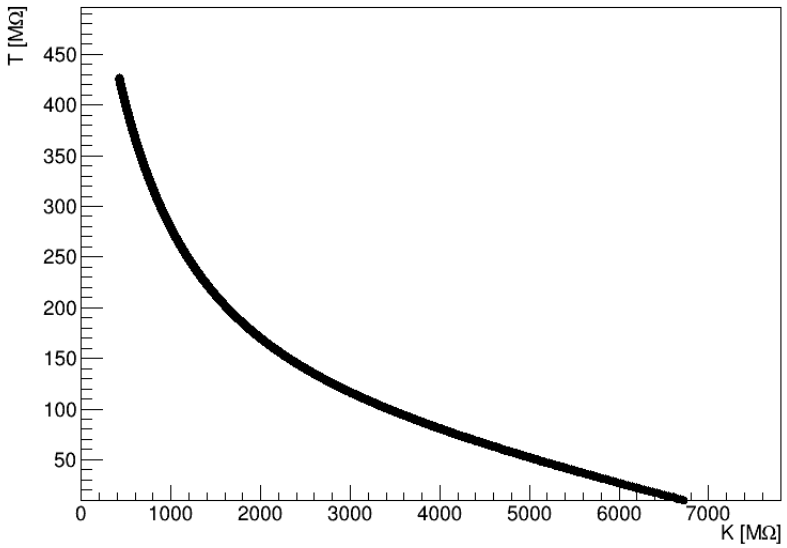


Figure 5.11: Estimated value for K and T with $10^{-4} \leq \lambda \leq 1$ using as $R_{eff}$ the fitted value in the middle of FC0.

An additional constraint to further reduce the degrees of freedom of the system might be introduced by using information obtained from data: (i) resistivity of Kapton and Twaron using components from FC0 and additional new samples and (ii) the total extra current on the whole field cage presented in figure 5.1. From those two kinds of measurements, an estimation for parameter $\lambda$ can be obtained if one consider two additional assumptions: $\lambda$ is assumed uniform over the whole field cage and non dependent on the voltage applied to the system. The next sections are dedicated to the estimation of Kapton and Twaron resistivities, as well as their dependence on the magnitude of the Electric field applied to the samples.

## 5.5 Estimation of Twaron Resistivity

Kapton and Twaron are well known materials used respectively for their known insulating and mechanical properties. A comparison of the results from the model with studies on single components of field cage 0 was performed. In particular, the measurements focused on three components:

- Kapton sheets and once part of Strip Foils;
- Resin samples with different mixtures;
- Twaron layers in both internal and external parts of the Field Cage walls.

The goal of these studies is to break down the overall conduction mechanism into two main components as reported in figure 5.6:

- Vertical Conduction through the Kapton coverlay of the strip foil;
- Horizontal Conduction through the thin layer of Twaron glued with resin to the coverlay;

and to study them independently. To separate the two effects, the strip foil was removed from FC0. The results obtained are summarized in the next section and are compared to results for the successive Field Cages where a correction to the design was applied.

### 5.5.1 Twaron properties

Twaron is a brand name for a type of aramid fibers, a class of materials used for their heat-resistance properties and their incredible tensile strength. They are used in many different fields, such as body armor fabric, marine cordage and in lightweight materials for public use (tennis racquets, cars...). Twaron was chosen for the realization of Field Cages due to many positive properties of the material[126]:

- excellent strength-to-weight ratio;
- excellent thermal stability;
- good chemical resistance;
- long lifetime;
- electrically non-conductive.

In particular, the last point is crucial for the realization of the field cage, where the uniformity of the Electric field in the drift region is a priority.
As reported in figure 5.5, Twaron layers are placed on both sides of the Honeycomb layer. To distinguish between them, the Twaron layer placed towards the active volume will be called internal Twaron, whereas the layer on the other side will be referred to as external Twaron. Since the two layers are applied using material from the same batch, a difference in the electrical properties between the two is a strong indication for the supposed degradation of the internal layer electrical properties. Since the layers are not directly exposed, the Strip Foil and the external shielding were partially removed as shown in picture 5.12. The now exposed Twaron layers can be studied to understand if there is a difference in the electrical properties between the two samples. However, it should be worth mentioning that even if the layers on top were removed, the resin used to glue them together is still present and will modify the performances. Since the resin used for every layer is the same, the tests will show a possible contamination of the resin and the Twaron together.
As shown in figure 5.12a, due to the dimension of the Field Cage, the only way to perform resistivity measurements is to install electrodes made of copper tape, which can be arranged according to the desired geometry. Since the Twaron layer was placed along the whole Field Cage surface with a thickness of few millimeters, the physical dimension at play in the model presented in 5.6 is the sheet resistance.

#### Sheet Resistivity

Sheet resistance is defined as the resistance of a square piece of thin film with electrodes placed at two opposite sides. One interesting property is due to the fact that squares with different side will have the same resistance, as long as other phenomena are not at play. For this reason, a small sample of the Twaron layer might be used to estimate the whole Field Cage resistance. Considering

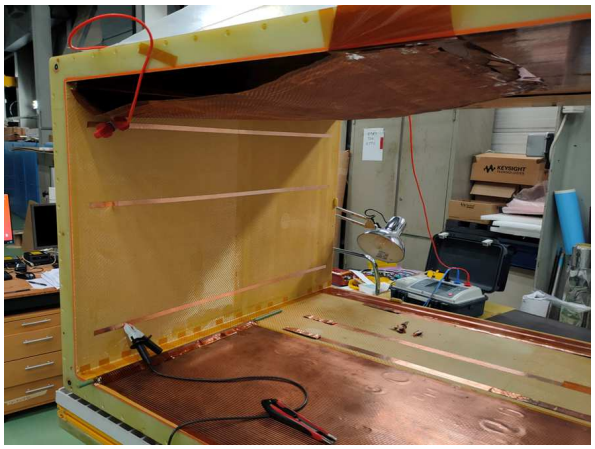

(a) Internal Twaron layer

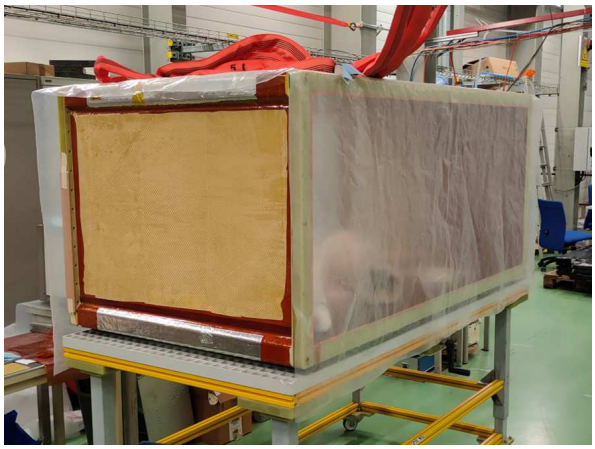

(b) External Twaron layer

Figure 5.12: Picture of internal Twaron layer 5.12a that is visible after removing the Strip Foil still partly present. Few copper tape electrodes are already applied to measure the surface resistance. On the right side, a picture of the external Twaron layer is present 5.12b, in which the external shielding and Kapton layers were removed from the Field Cage 0.

a three dimensional conductor of width W, length L and thickness t, the resistance is defined as in equation 5.6.

$$R = \rho \cdot \frac{L}{A} = \rho \cdot \frac{L}{Wt} \tag{5.6}$$

Combining resistivity $\rho$ with thickness $t$, equation 5.6 can be rewritten as in equation 5.7 in which the surface resistivity $R_s$ is introduced.

$$R = \frac{\rho}{t} \cdot \frac{L}{W} = R_s \cdot \frac{L}{W} \tag{5.7}$$

The relation for a thin layer holds as long as the current is travelling *on* the surface of the layer and not *through* it. Due to its definition in 5.7, the unit of measurement of sheet resistivity $R_s$ is $\Omega \cdot \frac{m}{m} = \Omega$, but since it is involved in the study of resistivity of square samples, it is usually noted with the units of *resistance per square* $\Omega/\square$ .
As seen in figure 5.1, the Field Cage response in current depends on the voltage applied across the drift length with a non linear behaviour. For this reason, it is important to estimate the Twaron resistivity applying Electric fields whose magnitude is comparable with the expected working regime of the Field Cage. It is important to remind that the layers involved in the leakage current have resistivity values very far from the definition of conductors or semiconductors. Nevertheless, such values are still relevant when compared to the total resistance value of the voltage divider which is about 1 $G\Omega$. For this purpose, advanced instrumentation is needed to estimate such low values of resistance.
To fulfill this request, a Megger Insulation Tester with a High Voltage DC Supply up to 10 kV was used. This tool is able to measure resistance values up to 30 T$\Omega$ with an accuracy of 5% in the range 1 M$\Omega$ to 3 T$\Omega$.

### 5.5.2 Twaron surface Resistivity

In this section, the focus is on the estimation of Twaron surface resistivity after large values of time, thus neglecting the evolution over time of the current collected by the instrumentation. Datasets were collected in different points of the Field Cage. As reported in figure 5.12, in one of the two short sides of the Field Cage, both Twaron layers were exposed. Copper tape electrodes were placed with the same setup on both sides and the total current was measured over time. The results in figure 5.13 show a clear difference in the behaviour of the internal and external samples. Since

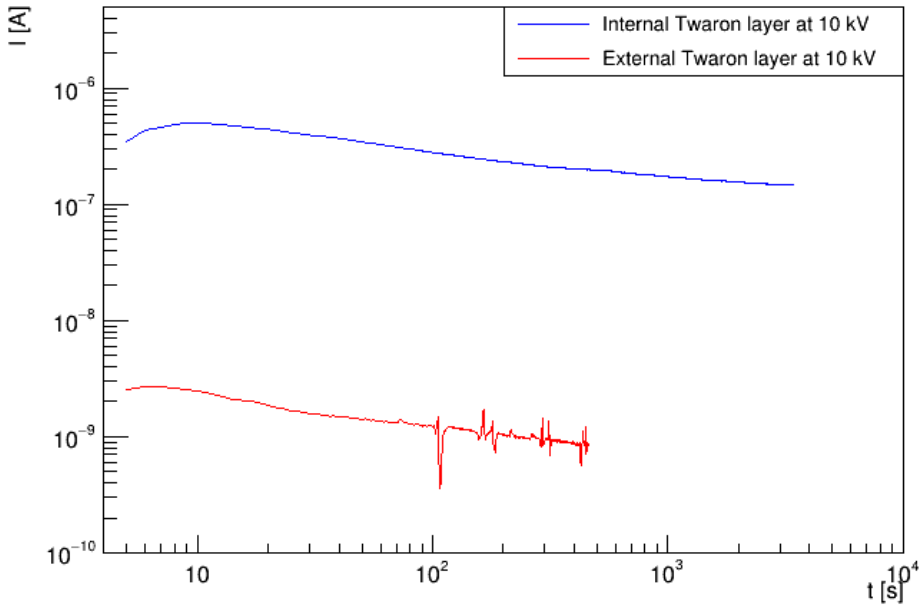


Figure 5.13: Total current measured on the internal (blue) and external (red) Twaron layers on surfaces with the same width and length.

the surfaces covered in this test have the same width and length, the graph 5.13 shows a direct comparison between the two surface resistivities $R_s^{int}$ and $R_s^{ext}$. However, the Twaron used for both layers belonged to the same batch so a corruption on the material is greatly disfavored. On the other hand, it is possible that the two layers were treated with different procedures when installed on the mold for the Field Cage construction.
Since the removal of the external shielding was a difficult procedure, the study of the external Twaron surface resistivity measurement was limited to the mentioned region. On the internal side, the removal of the damaged Strip Foil was simpler and it was also necessary in view of a possible refurbishment of the whole Field Cage with another Strip Foil. In this way, other zones of the internal Twaron layer were studied, using electrodes of different sizes. The results on the internal Twaron layer are summarized in figure 5.14. In order to compare samples with different geometries, the current per square is computed and the datasets are reported as a function of the Electric field on the thin layer. Each column represents the time evolution of the current over time, therefore, points with markers of the same shape belonging to different datasets are sampled at the same time from the starting measurement. For each single dataset, the current after 10 minutes is up to one order of magnitude lower than the initial value recorded at 15 s. Besides, the current per

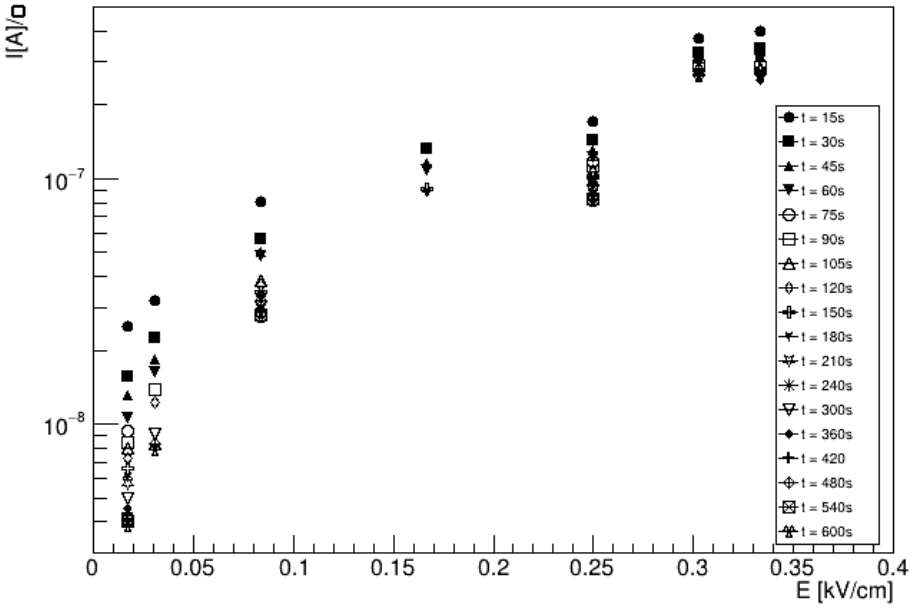


Figure 5.14: Current per square measured as a function of Electric field applied across the two electrodes and as a function of time. Each vertical series of points belong to the same dataset, in which the current is sampled over time. In order to facilitate the comparison among different datasets, points of the same style are taken at the same instant.

square depends greatly on the Electric field applied between the two electrodes, since varying the magnitude of the Electric field of a factor 20 the current per square changes up to two order of magnitudes considering the points at t=600 s. For the external Twaron layer a similar study has been performed and it is reported in figure 5.15. In this case, the total value of the current is much lower than the one reported in figure 5.14. In addition, the dependence on the intensity of Electric field is not significant. However, the time evolution of current recorded by the system is still present. The intensity of the Electric field studied by these measurements is compatible with the values at which the internal Twaron layer is exposed when reaching the working regime in the Field Cage. Assuming a voltage applied of -27 kV across the drift region of about 1 m, the total Electric field is about 0.27 $\frac{\text{kV}}{\text{cm}}$. However, the datasets collected and used for the model fitting described in figure 5.4 had a voltage of 5 kV, for a value of Electric field equal to 0.05 $\frac{\text{kV}}{\text{cm}}$. Since the current per square seems to saturate at around 0.3 $\frac{\text{kV}}{\text{cm}}$, that value of I(t=600 s) is taken for the working regime, while at 5 kV a current of I(t=600 s)$\sim 10^{-8}\frac{A}{\square}$ is assumed due to the steep increase of current in picture 5.14 for similar Electric field magnitudes. From that measurement and given the value of Electric field, the estimation of surface resistivity for the internal Twaron layer is

$$R_S^{int}(25\text{ kV}) = 1.2 \times 10^{11}\ \Omega, \tag{5.8}$$

$$R_S^{int}(5\text{ kV}) = 5 \times 10^{11}\ \Omega, \tag{5.9}$$

while for the external Twaron layer no dependance on the magnitude of the Electric field is

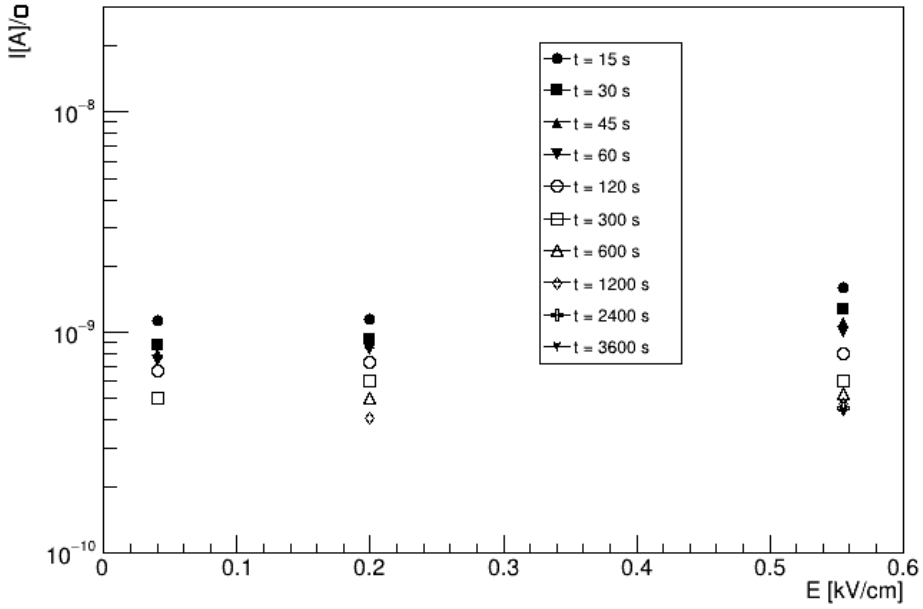


Figure 5.15: Current per square measured as a function of Electric field applied across the two electrodes and as a function of time. Each vertical series of points belongs to the same dataset, in which the current is sampled over time. In order to facilitate the comparison among different datasets, points of the same style are taken at the same instant.

observed. From measurements summarized in figure 5.12b, the surface resistivity is

$$R_S^{ext} = 2.49 \times 10^{13}\ \Omega. \tag{5.10}$$

From thise estimation, one might derive the estimated resistance across the same distance travelled on the voltage divider for joining two next to next mirror strips. Since the pitch is 0.5 cm, the resistance for such interval is summarized in table 5.1. The estimation for the internal Twaron is

| Dataset | $R_{strip}$ [MΩ] |
|---|---|
| Internal Twaron (30 kV) | 120 |
| Internal Twaron (5 kV) | 600 |
| External Twaron | 24900 |

Table 5.1

very close to the resistance on the voltage divider from mirror strip to mirror strip, which could explain the presence of an alternative path below the strip foil.

## 5.6 Test of "Vertical" Conduction Mechanism

The following paragraph is dedicated to the study of the conduction through the kapton layers that compose the strip foil. The tests are focused on the study of kapton volumetric resistivity and of the application of this estimation to the field cage specific case.
The properties of Kapton are summarized in the datasheet published in DuPont websites. Considering a thickness of 25 $\mu$m, the nominal volume resistivity at 23°C and 50% Relative Humidity reported is $\rho = 1.7 \times 10^{17}$ $\Omega$cm. Considering two copper strips as electrodes on two opposite faces of a 25 $\mu$m thick Kapton layer, the resistance is computed according to:

$$R = \rho \cdot \frac{l}{A} \simeq 2.8 \times 10^{12} \Omega \tag{5.11}$$

The nominal value is much larger than the resistance along the voltage divider, so a degradation of the kapton film is required to explain an increase in the measured total current, according to the hypothesis presented in the previous model.

### 5.6.1 Methods

The measurements are performed with to a Megger diagnostic insulation resistance tester, used also for the testing of Twaron, whose electrodes are attached to aluminum electrodes. In particular, for the test of volumetric resistivity of square samples, two 15cm diameter round aluminum electrodes are used. In addition, since the strip foil presents copper strips on both sides, the strips themselves were also used as electrodes.

### 5.6.2 Kapton Volumetric Resistivity

The volumetric resistivity of Kapton has been tested using different setups. Firstly, two layers of kapton 25 $\mu$m and 50 $\mu$m were tested with round copper electrodes at different voltages as shown in picture 5.16. Each measurement was sampled at fixed period of time, therefore the time evolution of the measured currents might be compared. Considering the 25 $\mu$m thick kapton sample, the current is much higher than the case at 50 $\mu$m after the same amount of time. A possible explanation of the different behaviour is that the presence of same size defects is much more relevant in a thinner layer, due, for example, to the accumulation of charge on the two interfaces according to the peaks effect. Furthermore, a dependence on the Electric field is visible.
In the field cage, if the Twaron layer is floating and is a conductor, its voltage will be the medium value between the working regime and ground, i.e. around 13 kV. In such case, the Electric field across the coverlay might reach values up to

$$E_{max} \sim \frac{13 \text{ kV}}{25 \ \mu\text{m}} = 0.52 \frac{\text{kV}}{\mu\text{m}}, \tag{5.12}$$

which is one order of magnitude larger than the Electric field in datasets in figure 5.16 and it is larger than the dielectric strength of the material in AC according to the datasheet. This extreme condition is reached at the two edges of the field cage. As a lower limit approximation, since the Twaron layer sheet resistivity has been estimated and it is of the order of few M$\Omega/\square$, the current at t=600 s for the largest Electric field magnitude in figure 5.16a might be considered for estimating the kapton volumetric resistivity.

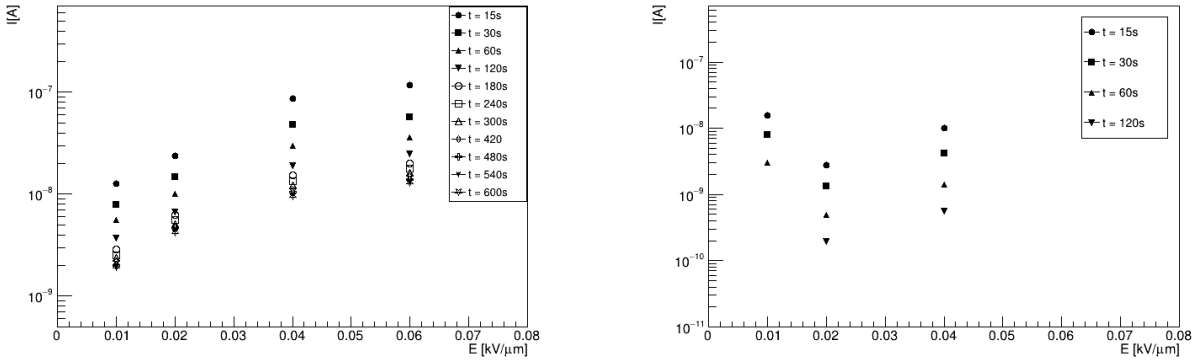


(a) (b)

Figure 5.16: Measured current through a Kapton foil of thickness 25 $\mu$m in picture 5.16a and 50 $\mu$m in picture 5.16b as a function of Electric field. Points with the same style are taken after the same time interval from the start of the measurement.

The estimated value for Kapton coverlay of thickness d is

$$\rho_{vol}(t = 600 \text{ s}) = \frac{V}{I(\text{t=600 s})} \times \frac{A}{d} = (8.87 \pm 0.05) \times 10^{14} \Omega\text{cm}, \tag{5.13}$$

which is about 150 times lower than the datasheet value.

### 5.6.3 Measurements on strip foils

A second set of measurements was performed directly on strip foils with different coverlay thickness. Furthermore, it was possible to compare the results for the strip foil removed from FC0 with newly produced strip foils. Those strip foils are called:

- strip foil 3, with a coverlay of 25 $\mu$m as strip foil 2 used in FC0;
- strip foil 4, with a coverlay of 125 $\mu$m;
- strip foil 5, with a coverlay of 50 $\mu$m,

following the production order. To avoid any possible damage to strip foil, the maximum applied voltage was 2000 V across any kind of coverlay, therefore the maximum Electric field achieved for thicker coverlays is smaller.
Strip foils are placed unrolled on top of an aluminum plate that covers the whole area, with the coverlay facing the aluminum plate. Then, two electrodes are created by soldering together 10 successive mirror strips on two sides of the strip foil and electrodes are connected to the Megger insulator tester. The summary of the current over time for the each strip foil is shown in figure 5.17. The strip foil removed from FC0 shows a clearly different behaviour with respect to strip foil 3 which has the same thickness, reaching a plateau at a much larger current than any other strip foil. This effect is visible on both halves of the strip foil 2, the one removed and placed on the aluminum plate and the one still glued to the field cage. This similarity might hint to the fact that the Twaron layer is behaving like a conductor given the high resistivity of the other components. The response

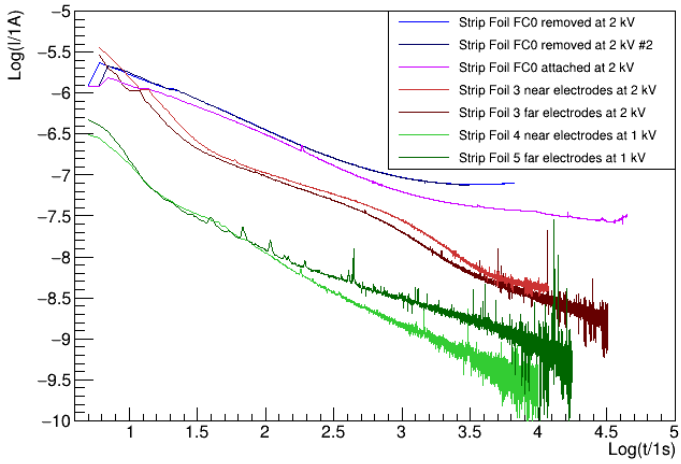


Figure 5.17: Current over time for each strip foil across the coverlay.

of strip foils 3 and 4, which present the two extremes in thickness is studied as a function of the Electric field through the coverlay.
In picture 5.18, the current over time up to t=600 s is reported for strip foils 3 and 4. The two graphs show that a newly produced strip foil with a coverlay of 25 $\mu$m behaves like a strip foil with a coverlay of 125 $\mu$m at the same magnitude of Electric field. However, the working regime for the thinner coverlay is 5 times larger than the thicker one and this difference might cause a breakdown in the thinner case at a larger voltage.
As in the previous paragraph, an estimation of the kapton volumetric resistivity can be performed. Given the geometry of the electrodes, according to the Ohm's Law the resistance is

$$R(t = 600 \text{ s}) = 2 \times \rho_{vol} \frac{d}{A} \tag{5.14}$$

using the same convention of equation 5.13. Hence, by fitting the current with a horizontal line once it reached at plateau, the volumetric resistivity measured on the coverlay of strip foil 3 is

$$\rho_{vol}^{SF3} = (1.392 \pm 0.001) \times 10^{17} \ \Omega\text{cm}, \tag{5.15}$$

which is the same order of magnitude as the value from the datasheet. The same procedure can be performed on the part of strip foil 2 removed from FC0, which leads to a volumetric resistivity for kapton equal to

$$\rho_{vol}^{SF2,removed} = (7.682 \pm 0.002) \times 10^{15} \ \Omega\text{cm}, \tag{5.16}$$

and

$$\rho_{vol}^{SF2,attached} = (0.21026 \pm 0.00006) \times 10^{15} \ \Omega\text{cm}. \tag{5.17}$$

The measurements performed on the strip foils showed that a newly produced strip foil behaves accordingly to the kapton nominal volumetric resistivity, regardless of the thickness of the coverlay. However, once the strip foil is used in the production of field cages, it is subjected to mechanical, thermal and electrical strains that might alter its integrity. The ability to resist to such alterations depends on the thickness of the kapton sheet.
In order to compare the experimental results with the prediction from the models, it is useful to

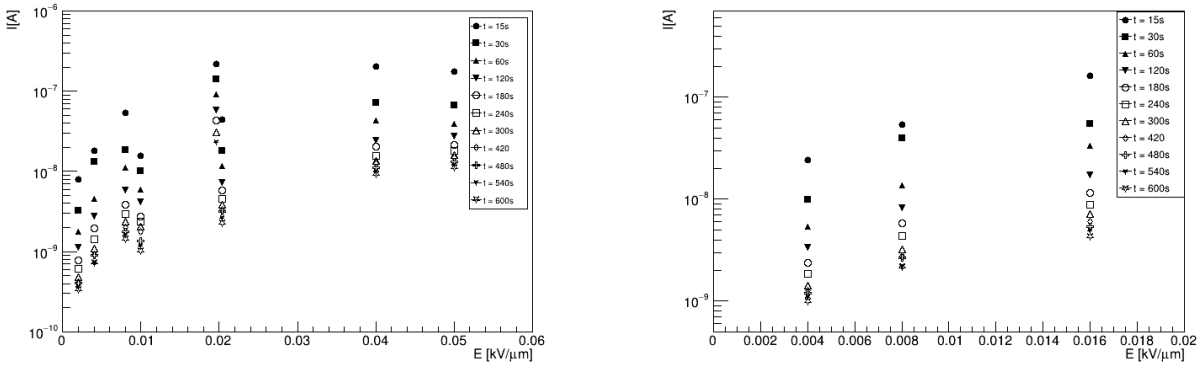


(a) (b)

Figure 5.18: Current over time for strip foil 3 in figure 5.18a and for strip foil 4 in figure 5.18b, as a function of Electric field applied through the coverlay. A particular attention has to be given to the x-axis range.

estimate the resistance of the coverlay between one mirror strip and the Twaron layer. Considering the area of a single strip equal to $A_{strip} = 150$ cm$^2$, the results are summarized in table 5.2. The values reported in table 5.2 are still much greater than the resistance on the voltage divider.

| Dataset | $R_{strip}$ [GΩ] |
|---|---|
| Kapton 25 $\mu$m, round electrodes | 14.79 ± 0.07 |
| Strip foil 2, removed | 128.03±0.03 |
| Strip foil 2, attached | 350.4±0.1 |
| Strip foil 3 | 2320 ± 2 |

Table 5.2

However, one must keep into account the fact that the measurements are performed with a voltage one order of magnitude smaller than the regime. It has been shown in picture 5.16 that the total current depends on the intensity of the electric field and that the behaviour is not linear. For such reasons, it is possible that in the FC0, the current flowing through the coverlay is much higher due to a higher voltage and a degradation of the kapton material due to local breakdown.

## 5.7 Fit of the model to Kapton and Twaron resistivity estimation

In the previous sections, the resistances K and T havenbeen estimated. Considering the worst case scenario for K, as summarized in table 5.2, and for the internal Twaron, reported in table 5.1, the estimation for parameter $\lambda$ is

$$\lambda = 8.11 \times 10^{-3}, \tag{5.18}$$

in the plateau region for T in figure 5.10. With these assumptions, it is possible to proceed with the fit of the model to the data presented in figure 5.3a. The estimated values for K and T are reported in figure 5.19. The pictures show that in the middle K and T are smaller than the ones near the

edge. In the central region, the resistances might be fitted with a horizontal line, which gives

$$K_{central} = (5400 \pm 100)\ \mathrm{M}\Omega \tag{5.19}$$

and

$$T_{central} = (44.1 \pm 0.7)\ \mathrm{M}\Omega. \tag{5.20}$$

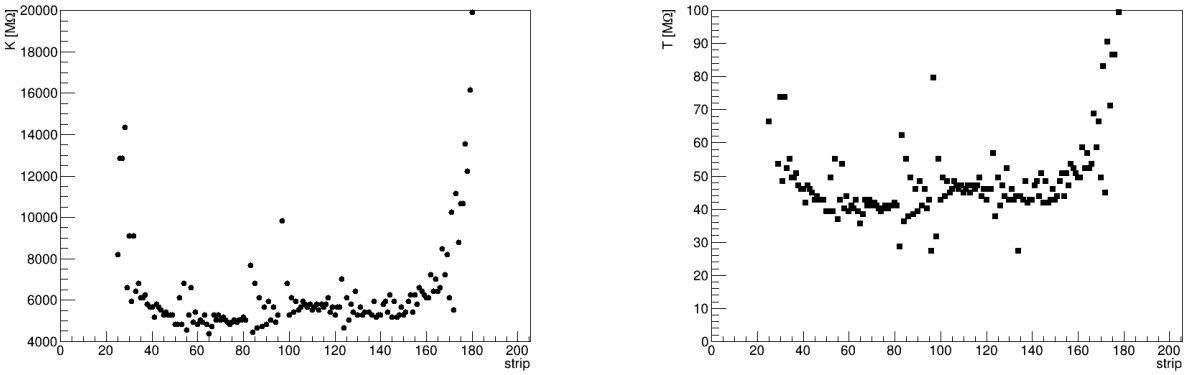


(a) (b)

Figure 5.19: Predicted value of K and T for each resistance measurement in FC0.

## 5.8 Continuous modelization of field cage

To estimate the Kapton and Twaron resistivity starting from the measurements of $\Delta V$ across two consecutive mirror strips reported in figure 5.4, it is necessary to model the behaviour of the field cage using the hypothesis of an alternative path for the current as seen in figure 5.6. Considering that the field cage contains about 400 strips, the distance across two consecutive mirror fields can be considered *small* with respect to the total drift length and it is named *dx*. The total distance is normalized to the total drift length, hence x$\in [0, 1]$.
Along this distance, it is possible to introduce resistivity per unit of length (i) R along the voltage divider, (ii) K across the Kapton coverlay and (iii) T along the inner Twaron layer. The three values are summarized in figure 5.20.

The current flowing on the voltage divider and on the Twaron layer are respectively called $I_1(x)$ and $I_2(x)$. The primary goal of this model is to evaluate the behaviour of $I_1(x)$ as a function of the position across the drift length, since it is linked to the uniformity of the Electric field in the drift direction, which is a fundamental requirement for obtaining a uniform drift velocity for ionized electrons.
In order to evaluate the behaviour of circuit in figure 5.20, the first Kirchhoff's law is applied to the net on the left on a clockwise direction:

$$V(x) - R\Delta x I_1(x) - V(x + \Delta x) - T\Delta x I_2(x) = 0 \tag{5.21}$$

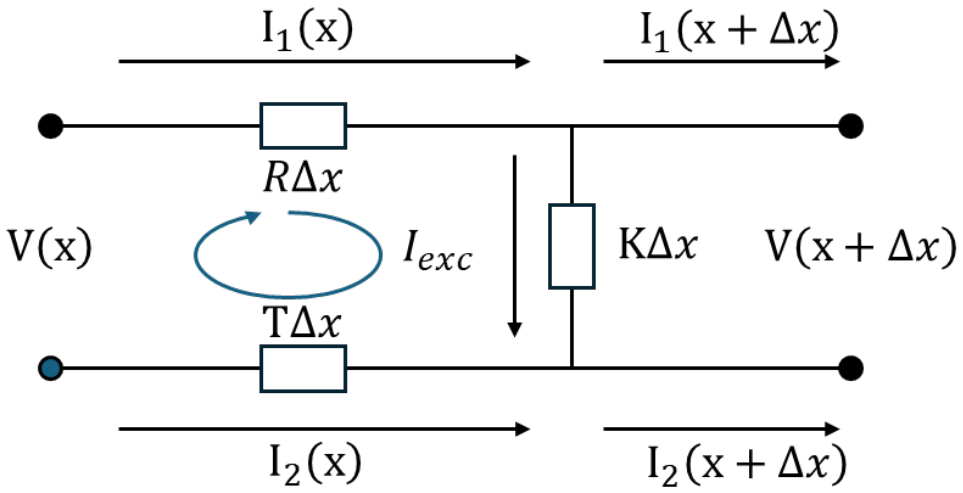


Figure 5.20: Schematic representation of hypothesized circuit.

while the second Kirchhoff's law is applied to the two nodes:

$$I_1(x) = I_{exc} + I_1(x + \Delta x) = K\Delta x V(x + \Delta x) + I_1(x + \Delta x) \tag{5.22}$$

$$I_2(x) = -I_{exc} + I_2(x + \Delta x) = -K\Delta x V(x + \Delta x) + I_2(x + \Delta x) \tag{5.23}$$

According to the interpretation of picture 5.3a presented in this chapter, K and T are estimated to be larger at the edges of the field cage and relatively constant in the middle as shown in picture 5.19. Therefore, in equations 5.21, 5.22 and 5.23, K and T should present a dependence on the x position $K \equiv K(x)$ and $T \equiv T(x)$. A first simplified solution to such equations is presented in the next section, in which the special case for K and T costant is introduced. Successively, a numerical solution for K(x) and T(x) is presented for the specific case of FC0.

## 5.9 Continuous solution for K and T homogeneous

This specific case holds considering only the field cage central part, excluding about 40 strips per side of the almost 400 strips. In this case, an analytical solution for the system is found. Considering this circuit as *small* with respect to the whole Field Cage length, i.e. $\Delta x \to 0$, the equations 5.21, 5.22 and 5.23 can be written as differential equations:

$$\begin{cases} \frac{dV(x)}{dx} + RI_1(x) - TI_2(x) = 0 \\ K\frac{dI_1(x)}{dx} - V(x) = 0 \\ K\frac{dI_2(x)}{dx} + V(x) = 0 \end{cases} \tag{5.24}$$

in which the relation $V(x + dx) \simeq \Delta x \frac{dV(x)}{dx} + V(x)$ has been used in equations 5.22 and 5.23. The system requires three additional constraints in order to provide a defined solution that keeps into account the geometry of the whole field cage.
A first condition is imposed by considering the symmetry of the field cage along the drift length, in which the current flowing from the voltage divider to the Twaron layer in the first half will behave in the same way but in opposite direction on the second half. Hence, in the middle point the net

current between the strip foil and the Twaron layer is null, i.e. the two ends of the branch are at the same voltage. A second constraint is imposed on the system by studying the circuit at the edges, in which the voltage divider and the path towards the Twaron layer converge into the branch which connects to the power supply. Since the current is injected on the strips, it is reasonable to assume that all the current at the edges is found on the voltage divider. As a last constraint, the total current flowing on the circuit has to be preserved and since the only path towards ground in the circuit is through the power supply, all the current that is flowing on the Twaron layer, at the edge it must return on to the voltage divider. As a summary:

$$\begin{cases} V(\frac{1}{2}) = 0 \\ I_2(0) = 0 \\ I_1(0) = I_1(1). \end{cases} \tag{5.25}$$

The set of linear differential equations 5.24 with additional constraints 5.25 has an analytical solution, which depends on the resistances R, K and T. The solution requires an additional constraint that links the model to the experimental condition, in which the current flowing into the system depends on the voltage $V_0$ applied to the circuit according to

$$V_0 = R \int_0^1 I_1(x) dx, \tag{5.26}$$

i.e. the overall voltage drop is equivalent to the sum of the potential drop in each infinitesimal resistance on the voltage divider. This voltage $V_0$ must not be confused with the one defined in 5.24: $V_0$ is the potential across the voltage divider, while V(x) is the voltage across the coverlay at a given position x along the drift length, as shown in figure 5.20. For such conditions, the expression for $I_1(x)$ is

$$I_1(x) = \frac{V_0}{R} \frac{R \cosh\left(\alpha\left(\frac{1}{2} - x\right)\right) + T \cosh\left(\frac{\alpha}{2}\right)}{\frac{2R}{\alpha} \sinh\left(\frac{\alpha}{2}\right) + T \cosh\left(\frac{\alpha}{2}\right)} \tag{5.27}$$

in which $\alpha = \sqrt{\frac{R+T}{K}}$ is defined. A first test to evaluate the function behaviour for limit cases in the middle of voltage divider, i.e. $\sinh\left(\frac{\alpha}{2}\left(\frac{1}{2} - x\right)\right) = 0$ When considering a perfectly insulated field cage, K will be much larger than R but two different possibilities are available: (i) K $\sim$ T and K$\gg$T, i.e. $\alpha \to 1$ and $\alpha \to 0$. It can be verified that the following relations hold:

$$I_1(0.5) \xrightarrow{K \sim T \gg R} \frac{V_0}{R}$$
$$I_1(0.5) \xrightarrow{K \gg T \gg R} \frac{V_0}{R}.$$

These expressions are in agreement with a field cage in which the only possible path for the current is the voltage divider.
On the other hand, other two interesting possibilities are found if one considers the case for (iii) $R \sim T \gg K$ or (iv) $R \gg T \gg K$ in which $\alpha \to +\infty$. Under those circumstances, since K is negligible, the conductive layer below the strip foil is not insulated from the circuit and it can be

shown that once again

$$I_1(0.5) \xrightarrow{R\sim T\gg K} \frac{V_0}{R}$$
$$I_1(0.5) \xrightarrow{R\gg T\gg K} 0,$$

since in the last case $\alpha \sim R^{\frac{1}{2}}$. In each case, the ratio of the currents flowing on the voltage divider and on the Twaron is different. The sum of the two currents $I_{tot}(x) = I_1(x) + I_2(x)$ can be used to define an effective resistance of the field cage, according to:

$$R_{eff} = \frac{V_0}{I_{tot}} \tag{5.28}$$

which can be compared to the graph 5.1 once the model is fitted to the data in picture 5.4. Since the resistance R is known and measurable, the model presents only two free parameters K and T, that might be expressed as a ratio of R by introducing $t$ and $k$ as:

$$\begin{cases} t = \frac{T}{R} \\ k = \frac{K}{R}, \end{cases} \tag{5.29}$$

while $\alpha$ can be expressed as $\alpha = \sqrt{\frac{1+t}{k}}$.
The relation 5.27 is rather complicated and at a first glance is not possible to evaluate how K and T are modifying the shape of $I_1(x)$. For this reason, an example of $I_1(x)$ for different orders of magnitude for k and t are reported in figures 5.21. The function changes drastically only when k and t are much smaller than 1, while in the other cases k and t slightly change the shape of the function in particularly near the edges of the circuit. The same exercise can be performed by

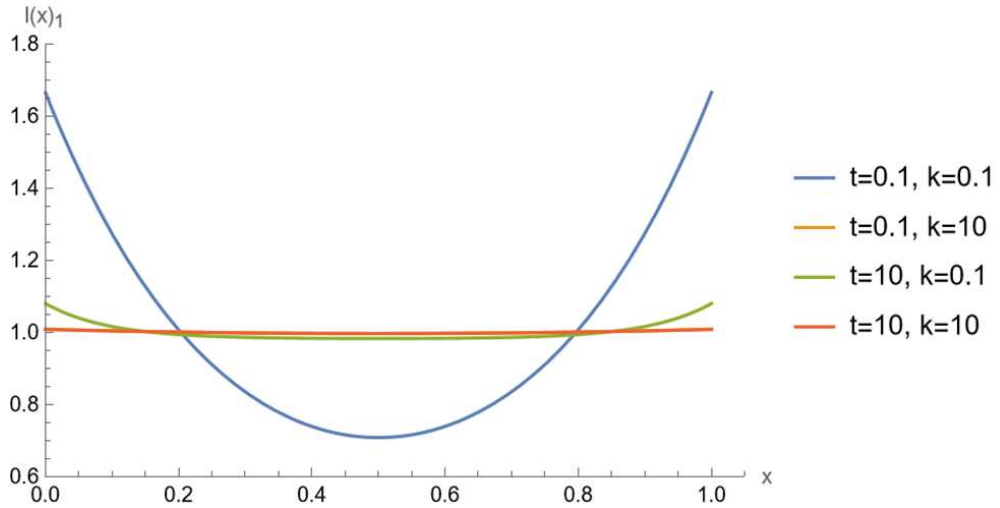


Figure 5.21: Current on the voltage divider $I_1$(x) for different order of magnitudes of k and t.

changing only one of the two parameters, as reported in figure 5.22. For k→0, current $I_1(x)$ tends to $\frac{t}{t+1} = \frac{T}{R+T}$. On the other hand, if k is large enough, the alternative path becomes inaccessible.

As a summary, from picture 5.21 and picture 5.22,it follows that the two parameters k and t

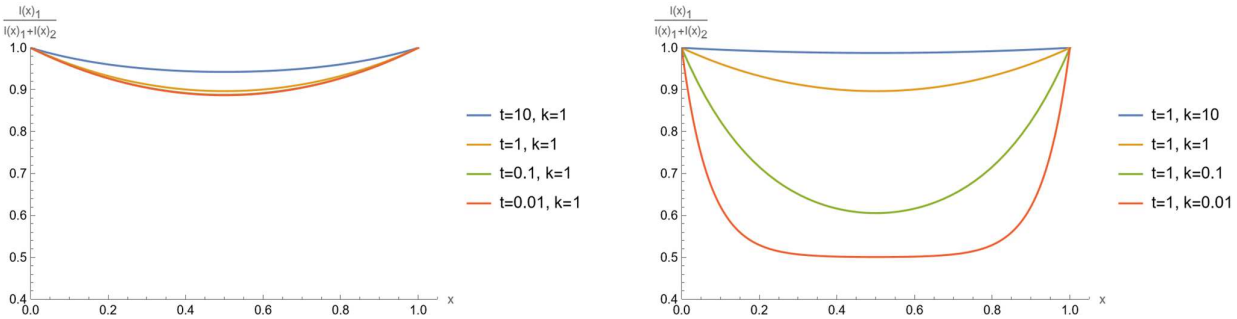


(a) (b)

Figure 5.22: Current on the voltage divider for different values of k and t. On the left picture 5.22a, four different hypotheses for t at different order of magnitudes are reported at the same k. On the right 5.22b, the same exercise is reported but for different k and same t. The two parameters act differently on $I_1(x)$.

shape the current on the voltage divider differently. Since k is directly proportional to the resistivity of the Kapton coverlay, it represents the opposition of the system to let the current flowing on the Twaron layer. For this reason, the smaller k, the steeper the increase or decrease rate of $I_1$ near the edges. The parameter t related to Twaron resistivity represents the limit case of current flowing on the Twaron layer. In order to have an extra current flowing in the field cage, both *vertical* and *horizontal* conduction mechanisms are required.

## 5.10 Model application to field cage

Once the soldering of the voltage dividers was completed, the only way to evaluate the field cage electrical properties was to measure the current flowing on the voltage dividers. Thanks to the model in 5.3, a predicted value for Twaron and Kapton resistivity can be obtained, since R is already known and can be checked by measuring the value of each single soldered resistance.
Therefore, the ratio $\frac{\Delta V(x)}{\Delta V(0)}$ can be related to $\frac{I_1(x)}{I_1(0)}$. Thanks to this relation, datasets can be fitted to find the values of k and t. Since datasets 1,2,3 are measured in the same conditions, their results are used for estimation the average $\bar{k}$ and $\bar{t}$, while dataset 4 is considered as a different estimation. The plot 5.4 shows an asymmetry between the two field halves of the field cage. Three kinds of fits are performed: one global and one for each of the two halves. The fits are shown in picture 5.23, while the estimation for k and t are reported in table 5.4. The results in table 5.4 show an agreement in the fits for datasets 1, 2, 3 for all the global fit and the fit on the *second* half. The fits for the other half field cage do not agree for the parameter t, with a relative difference of about 30% between the two extreme values. Dataset 4 show a degradation of the Kapton resistance in particular on the *second* half, in which k is one order of magnitude smaller than in datasets 1, 2, 3. The two halves of the field cage do not show a symmetry, since a global fit fails to describe properly the datasets in figure 5.4 as shown by the residuals plots in figure 5.24. In particular, the residuals for the global fit show a similar trend in each one of the datasets. A pattern in the fit is seen also for the individual fit on the *second* half of the field cage, while the fits for the *first* do not show any remarkable deviation from 0. The residuals for dataset 4 highlights the presence of an asymmetric degradation of the electrical properties. This effect might be explained by the presence of a contamination which a priori is not required to be homogeneous along the field cage.

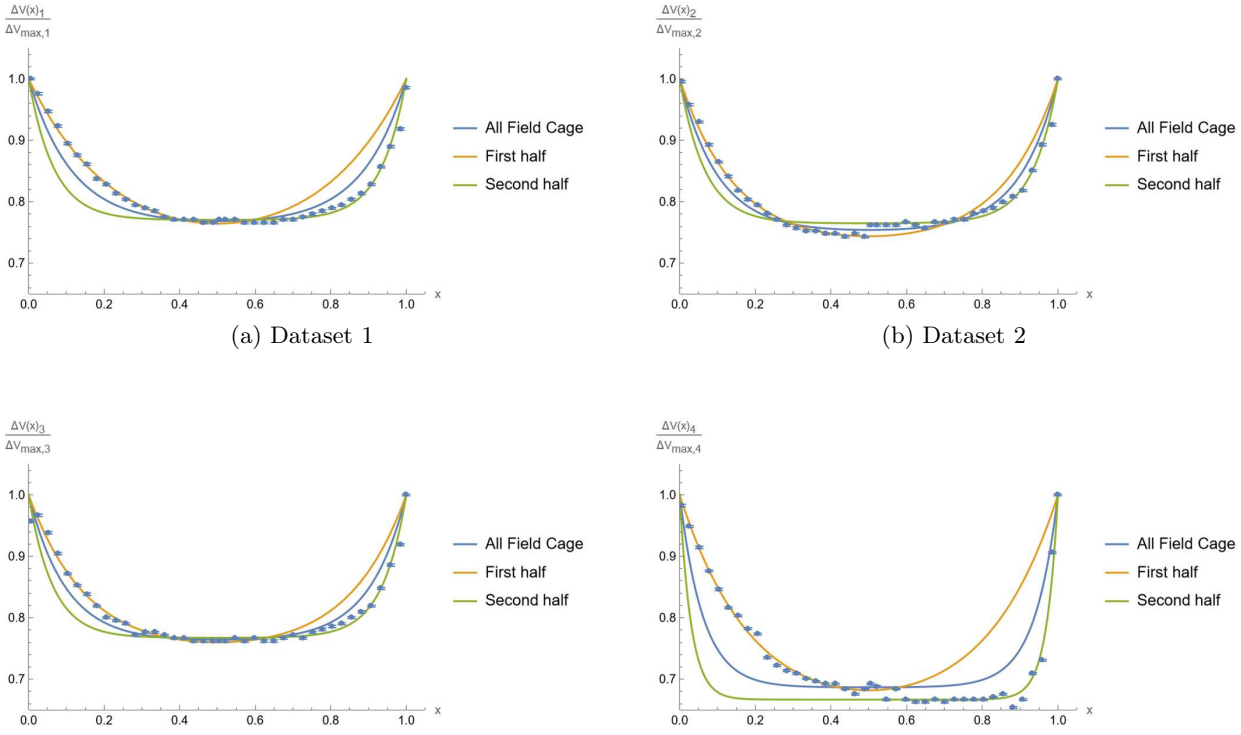


(a) Dataset 1

(b) Dataset 2

(c) Dataset 3

(d) Dataset 4

Figure 5.23: Comparison of datasets with the best fit from the model. Each figure contains a fit for all data points (blue), only first half (orange) and only second half (green). Datasets 5.23a,5.23b,5.23c present a much different behaviour with respect to 5.23d probably due to the modification of the Field Cage electrical properties once 20 kV of high voltage were reached.

Table 5.3: Summary of model fit to datasets as shown in figure 5.23.

| Dataset | $t_{all}$ | $k_{all}$ | $t_{first}$ | $k_{first}$ | $t_{second}$ | $k_{second}$ |
|---|---|---|---|---|---|---|
| 1 | 3.2±0.1 | 0.06±0.01 | 2.2±0.1 | 0.18±0.01 | 3.35±0.06 | 0.019±0.002 |
| 2 | 3.01±0.07 | 0.041±0.005 | 2.65±0.06 | 0.078±0.006 | 3.25±0.04 | 0.019±0.002 |
| 3 | 3.19±0.09 | 0.040±0.006 | 2.9±0.1 | 0.09±0.01 | 3.30±0.05 | 0.017±0.002 |
| 4 | 2.2±0.1 | 0.012±0.004 | 1.70±0.07 | 0.097±0.007 | 2.00±0.03 | 0.0028±0.0004 |

Table 5.4

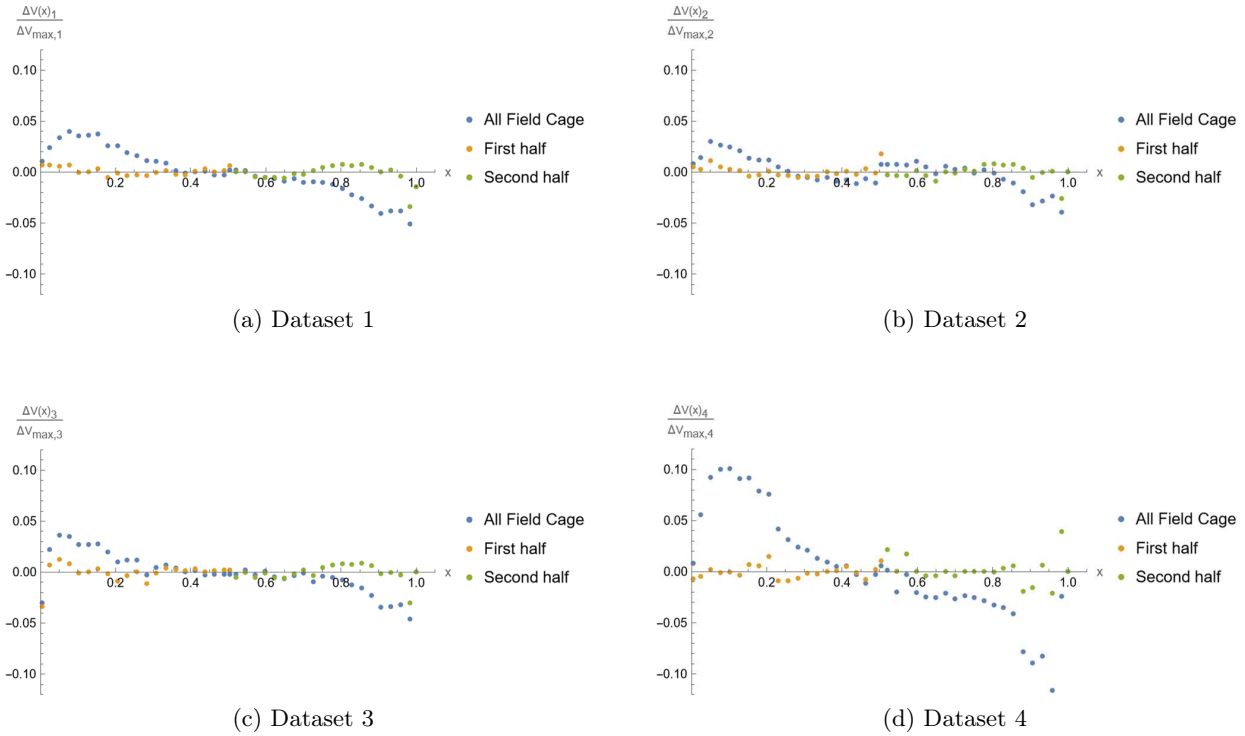


(a) Dataset 1

(b) Dataset 2

(c) Dataset 3

(d) Dataset 4

Figure 5.24: Plot of residuals referring to fits in figure 5.23 . Each figure contains residuals for all data points (blue), only first half (orange) and only second half (green).

The average estimation for k and t can be performed and it is summarized in table 5.5. The

| Dataset | $\bar{t}_{all}$ | $\bar{k}_{all}$ | $\bar{t}_{first}$ | $\bar{k}_{first}$ | $\bar{t}_{second}$ | $\bar{k}_{second}$ |
|---|---|---|---|---|---|---|
| 1-2-3 | 3.13±0.09 | 0.047±0.009 | 2.6±0.3 | 0.12±0.05 | 3.30±0.04 | 0.0183±0.0009 |
| 4 | 2.2±0.1 | 0.012±0.004 | 1.70±0.07 | 0.097±0.007 | 2.00±0.03 | 0.0028±0.0004 |

Table 5.5

estimated values for $\bar{k}$ and $\bar{t}$ might be used to compute the predicted total current and therefore the predicted resistance of the whole field cage $R_{eff}$ defined in equation 5.28. In order to do so, the total resistance of the field cage voltage divider is needed. As shown in the previous chapter, the total resistance for voltage dividers in FC1 and FC2 reported in figure 4.32a is equal to about $R \sim 980$ MΩ. With the values in table 5.5 and R, it is possible to estimate K and T and successively the total effective current as summarized in table 5.6

| Dataset | All [MΩ] | First half [MΩ] | Second half [MΩ] |
|---|---|---|---|
| 1-2-3 | 748±5 | 723±2 | 754±2 |
| 4 | 676±9 | 639±8 | 654±3 |

Table 5.6

As a comparison, at a voltage $V_0$= 5 kV, the measured current in three different instances was found to be between $I_{tot}$=5.8 $\mu$A and $I_{tot}$=6.1 $\mu$A after waiting at least 10 minutes before stopping the measurement, corresponding to an effective resistance in the range between 820 MΩ and 860 MΩ. Therefore, the results from the fit under the assumption of K and T homogeneous underestimate the effective resistance for about 15-30% depending on the considered dataset.

### 5.10.1 Resistance per single cell

In order to compare the results with data and other models, it is convenient to express the estimated quantity for K and T over the fundamental unit of the model, which is one *cell* drawn in scheme 5.20. Estimations in tables 5.4 and 5.5 are the values integrated over the whole field cage. In the field cage, there are 196 cells which are delimited by two next to next mirror strips. Since T increases with length, the values of $T_{strip}=\frac{T}{196}$, while K decreases with length, so $K_{strip}=196\times K$. The values in table 5.5 are modified according to the previous considerations and are summarized in table 5.7.

| Dataset | $\bar{T}^{strip}_{all}$ [MΩ] | $\bar{K}^{all}_{strip}$ [MΩ] | $\bar{T}^{strip}_{first}$ [MΩ] | $\bar{K}^{strip}_{first}$ [MΩ] | $\bar{T}^{strip}_{second}$ [MΩ] | $\bar{K}^{strip}_{second}$ [MΩ] |
|---|---|---|---|---|---|---|
| 1-2-3 | 16.0±0.4 | 9000±2000 | 13±1 | 23000±9000 | 16.8±0.2 | 3600±200 |
| 4 | 11.2±0.5 | 2400±800 | 8.7±0.4 | 19000±1000 | 10.2±0.2 | 550±80 |

Table 5.7

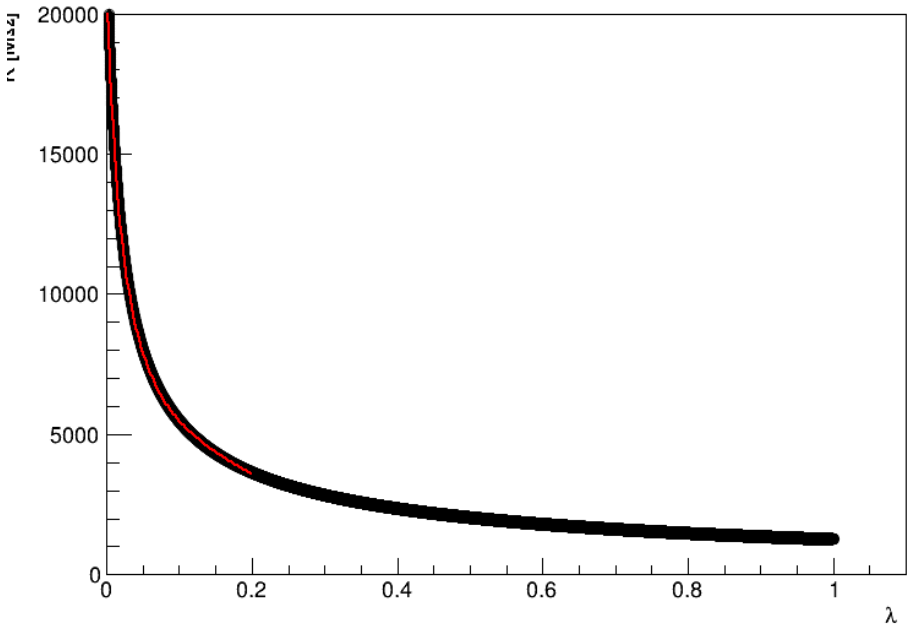


Figure 5.25: K as a function of $\lambda$ for data point i=13 in figure 5.3a. In red the fit for the empiric formula 5.30 is shown.

## 5.11 Field cage modelization for K and T inhomogeneous

The presence of inhomogeneity for K and T in the field cage might imply that the simplified model presented in the previous section might not predict the behaviour of FC0 once high voltage is applied on the voltage divider. Since an analytical solution cannot be obtained in this case, a numerical solution is found through the use of LTspice[1], a SPICE simulator software[127]. With such tool, the almost 200 loops presented in figure 5.20 can be drawn and a specific value to each resistor can be applied. In order to estimate K and T two assumptions have to be made. First, once again the proportionality between K and T along the field cage, i.e. $T_i = \lambda K_i$. From measurements in picture 5.3a, K and T depends both on $\lambda$, as shown in picture 5.11. Therefore, $\lambda$ can be estimated by requiring that the total current flowing through the voltage divider is the one measured in figure 5.1 for a given voltage.
Since the dependence of K on $R_{eff}$ reported in equation 5.1 is not analytically invertible, no analytical relation between K and $\lambda$ can be performed. However, it has been shown that for a relatively small range of $\lambda$ their relation can be fitted with the function

$$K(\lambda) = \frac{p[0]}{1 + p[1]\lambda + p[2]\lambda^2 + p[3]\lambda^3}. \tag{5.30}$$

An example of such relation is shown in graph 5.25 for data point i=13, in which the set of points ($\lambda$,K) identified as a solution for one of the points in 5.3a is fitted in the range $\lambda \in [0.0001, 0.2]$. The fit is performed for each of the data points and each parametric expression for K and T is inserted in the LTspice model. A DC voltage source is set at a voltage such that the expected

[1] LTspice is a registered trademark of Analog Devices

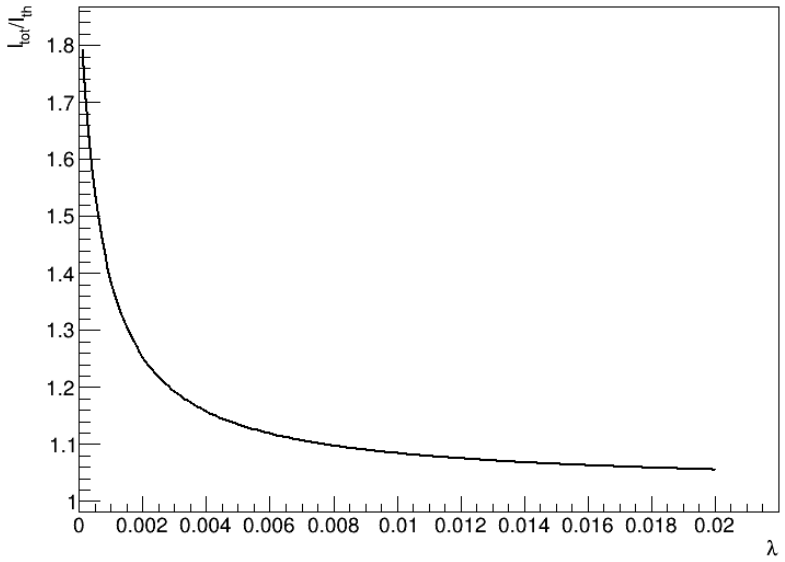


Figure 5.26: Total current output as a function of $\lambda$ in LTspice simulation of field cage model over the nominal current expected from the field cage voltage divider.

current output from the voltage divider is 1 A. The current output at the steady state is collected as a function of $\lambda$ and is reported in figure 5.26. At 5 kV, the total current is 16% larger than the nominal value, which according to LTspice simulation corresponds to $\lambda = 3.97 \times 10^{-3}$. The value differs from the one estimated using direct measurements on Kapton and Twaron samples by a factor of 2. Considering the assumptions made in this model, obtaining values in the same order of magnitude shows a consistency in the model introduced with respect to data.
Using the newly estimated value for $\lambda$, it is possible to find the values for ($K_i$,$T_i$) as in figure 5.19. The new estimation is reported in figure 5.27. In this case, the estimated value for Twaron resistivity is about half of the one in figure 5.19b. By fitting the central values with a horizontal line, the estimated values are

$$K_{central} = (4970 \pm 60)\ \mathrm{M\Omega} \tag{5.31}$$

and

$$T_{central} = (19.7 \pm 0.2)\ \mathrm{M\Omega}. \tag{5.32}$$

The trend of the current on the voltage divider from the LTspice simulation is reported in figure 5.28. The graph shows an asymmetry between the two halves of the field cage, which is similar to the trend shown in figure 5.4. As a comparison, the plot for $I_1(x)$ and $I_2(x)$ using the best fit parameters in the homogeneous case for K and T is shown in picture 5.29. In the homogeneous case, the predicted total current is about 22% larger than the nominal value, in contrast with the measured 16%.

## 5.12 Refurbishment of FC0

The study of the electrical properties of FC0 and its layers required a removal of the strip foil. The tests did not damage the mechanical structure of the field cage, so the feasibility of the installation

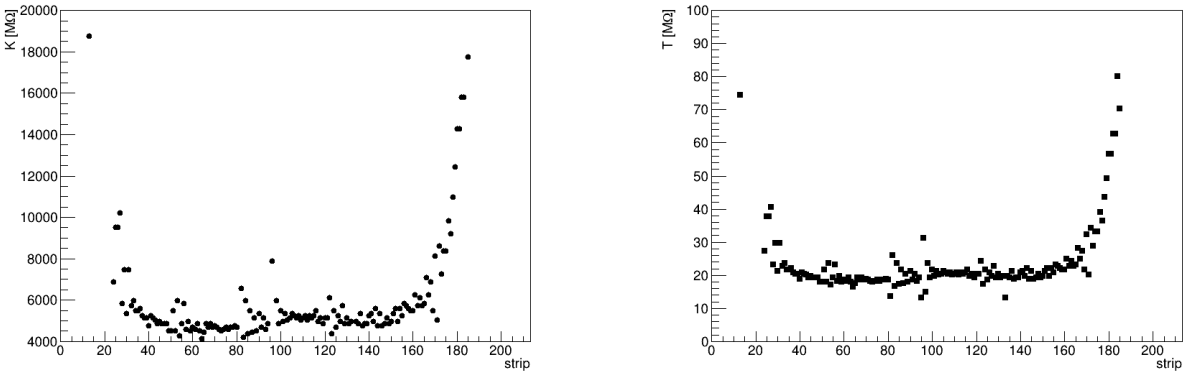


(a) (b)

Figure 5.27: Predicted value of K and T for each resistance measurement in FC0 using parameter $\lambda$ obtained from the LTspice simulation of the field cage.

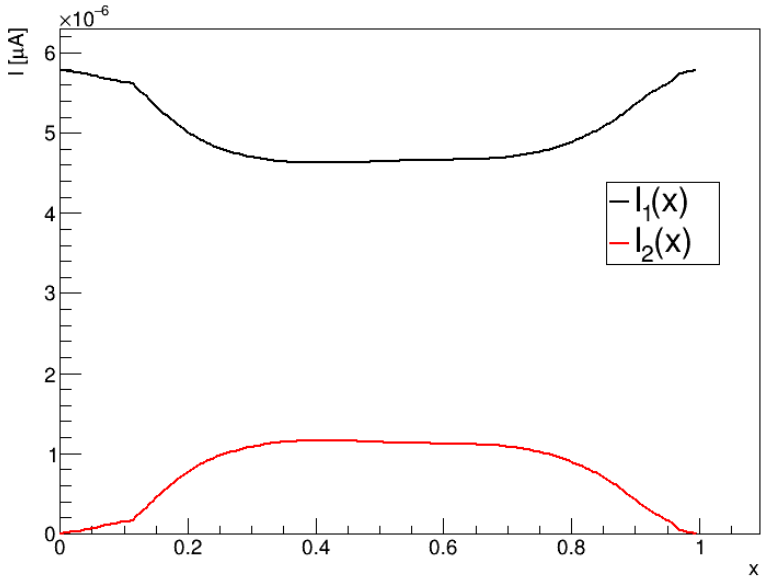


Figure 5.28: Predicted current on the voltage divider and on the Twaron layer according to LTspice simulation for $\lambda = 3.97 \times 10^{-3}$.

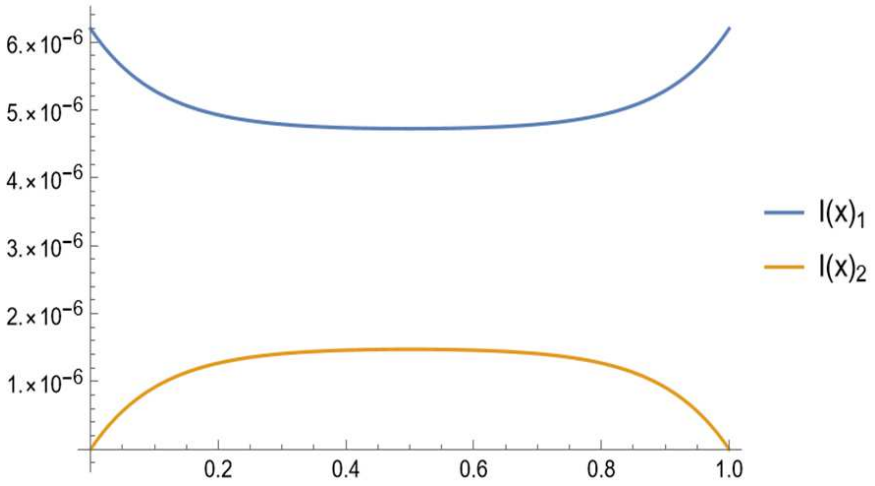


Figure 5.29: Predicted current on the voltage divider and on the Twaron layer for the best fit in the case of K,T homogeneous.

of a new strip foil was investigated.
Since the resistivity measurements proved that the internal Twaron layer is much more conductive than the external one, a better insulation in the interface with the strip foil is required. For this purpose, the envisaged solution consisted in the installation of fiberglass panels on top of the internal Twaron layer.
In order to keep the possibility to access the Twaron, a ring made of copper tape was installed near the flanges on both sides of the field cage. Successively, gluing of the fiberglass panels was performed. An electrical cable was soldered on the copper rings near the edges of the field cage, which were not covered by the fiberglass panels. After that, the edges were covered by an additional layer of resin, which was modelled to create a smooth transition in the junction between two panels. A comparison before and after the installation of fiberglass panels is reported in figure 5.30.

At this point, the strip foil is ready to be installed. A strip foil with a Kapton coverlay 125 $\mu$m thick was available, since it was discarded during the production of the other field cages. In fact, the thickness of the coverlay did not allow the foil to follow the curvature of the mold on the edges. The mold was designed for a much thinner coverlay of 25 $\mu$m and it proved to be working for a coverlay up to 50 $\mu$m. On the FC0, the new corners were designed to fit properly the increased thickness. A closer look to the detail on the corners of the field cage is reported in figure 5.32.

After the gluing of the strip foil, the resistors on the voltage dividers were soldered. The measurements performed on the resistors reported in figure 5.32 showed no deviation from the expected value, as opposite of what was reported for figure 5.3a. The fit of such values with a gaussian function gives as a result $R_{FC0}^{new}$=(2.54860 $\pm$ 0.00003) M$\Omega$. Therefore, the addition of fiberglass panels and the increased coverlay thickness proved successful in the insulation of the new strip foil with respect to the internal Twaron layer.
The placement of the two copper rings covering the whole perimeter at the level of the Twaron layer allows to check the resistance across the field cage in the region enclosed by the inner Twaron layer and the side of the fiberglass panels facing them. In order to avoid any possible damage to the newly refurbished FC0, a maximum voltage of 5 kV between the two rings is set and the current trend over time is collected, as reported in figure 5.33. Given the distance of 90 cm between the two rings and the overall length of 500 cm, the estimated surface resistivity is $R_s = (2.4 \pm 0.1) \times 10^{12}$

(a) (b)

Figure 5.30: Comparison between FC0 before (left) and after(right) the installation of a fiberglass panel to cover the internal Twaron layer and prepare strip foil installation. The Twaron layer was levigated and cleaned of visible impurities in order to facilitate the panels gluing.

(a) (b)

Figure 5.31: Details of the corner (left) of FC0, in which resin was added to increase the radius of curvature for proper gluing of the strip foil. On the right, a picture of the inner side of FC0 after the strip foil was glued.

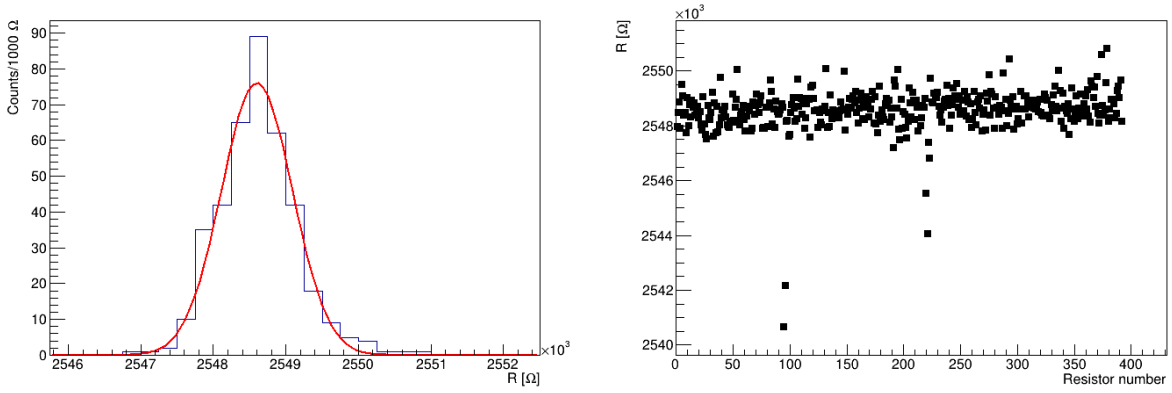


(a) (b)

Figure 5.32: Values of resistance between two neighboring strips along the drift length in the picture (left) and their fit with a gaussian distribution (right).

Ω/□, in between the estimated values for internal and external Twaron in FC0. Therefore, part of the contamination was removed when the strip foil was removed, while part of it is still present on the Twaron surface. The combination of new resin and the installation of fiberglass panels have greatly improved the insulating properties of FC0.

## 5.13 Summary

The first full-scale field cage (FC0) for the HA-TPCs exhibited a major issue after the installation of the two voltage dividers and subsequent electrical testing. The problem was characterized by a nonlinear relationship between the voltage applied across the field cage and the total current flowing through it. Specifically, the observed current exceeded twice the expected value under operational conditions. Additionally, for $|\Delta V| > 20$ kV, a permanent alteration in the insulating properties occurred, as an additional extra-current was detected even when the applied voltage was subsequently reduced. This unexpected issue posed a significant failure risk to the entire HA-TPC project.

This chapter illustrates a detailed investigation into the cause of this issue. The study involved: (i) resistivity measurements on the field cage and its inner layers and (ii) the development of a mathematical model to describe alternative conductive paths.

In FC0, experimental results clearly demonstrated that the insulating properties of the Kapton and Twaron layers near the voltage dividers were inconsistent with the nominal values reported in their datasheets and with those observed in the external Twaron layer, which originated from the same production batch as the inner Twaron layer. These findings support the hypothesis that a parasitic conductive paths was formed beneath and/or within the strip foil, likely due to suboptimal material treatment near the voltage dividers.

In the case of FC0 the issue was solved by insulating the compromised Twaron layer with thin G10 fiberglass panels and gluing a new strip foil onto the G10 panels. To address the issue in the case of the four final field cages, additional Kapton layers were inserted between the strip foil and the Twaron layer, alongside improved handling procedures for the inner layers. These modifications proved to be successful, as no extra current was observed in the final four field cages.

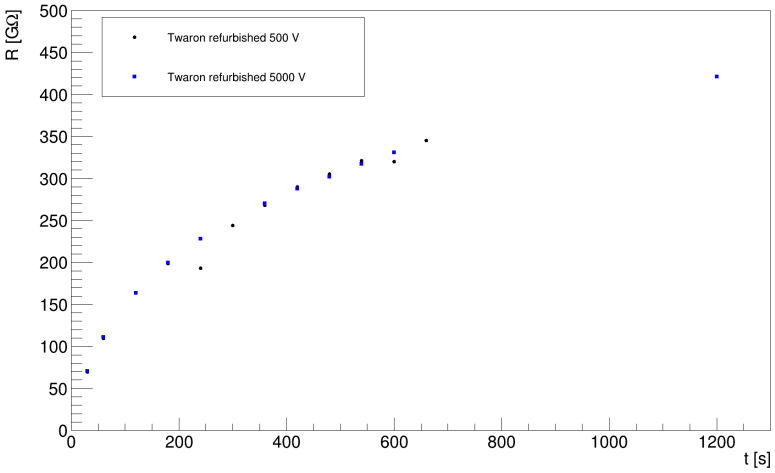


Figure 5.33: Resistance over time of refurbished internal Twaron layer for voltages of 500 V and 5000 V applied to the two glued copper rings parallel to the two flanges.

In conclusion, the work described in this chapter focus on the issues (electrical breakdown in the inner layer and not-uniform electric field) arising from the resistivity of field cages inner layers which was unexpectedly low in our first full scale cage FC0.

In general special care must be given to the resistivity of field cage layers adjacent to the copper strips, as these regions are particularly susceptible to failure. Over the long term, the impact of sustained high electric fields inside the field cage remains difficult to predict. However, as demonstrated in this chapter, even thin insulating layers, though nominally rated to withstand the design electric fields, are highly vulnerable to breakdown when small defects are present.

The resistivity is a potential failure point in any composite material field cage so that the measurements and the model described in this chapter may be a useful general tool for designing and building future field cages. In the literature, the leakage current flowing through the walls of the field cage toward the external shielding is a well-known phenomenon, commonly referred to as *mantel resistance*, as discussed in [101]. Here we included the effects of horizontal conductivity along the layers of field cage walls as additional component to be considered in order to achieve long-term electrical stability of field cages with compact, lightweight multilayer walls.

# Chapter 6

# Electric field in HA-TPCs

The field cages of the HA-TPCs are designed to ensure a uniform electric field within the active drift volume. The target performance is a field homogeneity better than $10^{-3}$ at a distance of 15 mm from the walls, corresponding to a ratio of the transverse field $E_{\perp}$ to the longitudinal field $E_{\parallel}$ of less than $10^{-3}$. The initial HA-TPC design met these criteria, as detailed in [96], which includes comprehensive electric field studies.

However, modifications were necessary to mitigate the risk of electrical breakdown and ensure long-term detector reliability. Two key changes were made to the Cathode region: (i) increasing the separation between the Cathode edges and the wall to more than 12 mm, and (ii) shifting the first field strip 8 mm toward the anode (along the $X$-axis in the ND280 coordinate system) to move it away from the flange plane. These changes resulted in a 12 mm gap between the Cathode and the wall in the transverse plane ($Y$-$Z$ plane), and the first strip was no longer aligned with the Cathode plane but positioned 8 mm away from the intersection of the Cathode plane with the wall surface.

These modifications were implemented to enhance insulation and minimize leakage currents from the Cathode and the last strip to the external shielding through the flange. Given the HA-TPCs' operational requirements-running for several months per year over multiple years-and the unpredictable nature of insulation degradation (e.g., due to charge accumulation or material aging), all high-voltage leakage paths were extended to maintain a safe path-length-to-voltage-drop ratio above the breakdown threshold.

As discussed in Chapter 4, additional measures were taken to further reduce leakage currents. Both field cages' Cathode flanges were equipped with a 30 mm groove, in addition to the two 8 mm thick O-ring grooves. This groove acts as a gas and surface charge labyrinth, increasing the length of potential leakage paths and improving insulation.

The studies presented in this thesis revealed that shifting the first strip relative to the Cathode while maintaining them at the same voltage introduced distortions in the nominal electric field. Unfortunately, the tight schedule for HA-TPCs installation at J-PARC limited the commissioning phase at CERN, preventing the detection of these distortions with sufficient statistics. Consequently, fine-tuning the voltage drop between the first strip and the Cathode to compensate for their geometric mismatch was not possible. The issue was identified during commissioning at J-PARC, where hardware intervention was infeasible. However, the problem was greatly improved by implementing a correction for track deformations in the reconstruction process, as described in this thesis.

This chapter presents a detailed investigation into electric field homogeneity, leading to the identification and resolution of the aforementioned issue. The chapter is structured as follows: straight tracks from cosmic ray data collected at J-PARC without a magnetic field exhibited significant distortions in the HA-TPC active volume, particularly near the Cathode. To investigate the source of

these distortions, straight tracks were generated using Monte Carlo simulations and reconstructed under various non-ideal electric field configurations, numerically simulated. Initial studies used simplified field cage geometry and boundary conditions with an electrostatic solver in Mathematica. Subsequently, a more detailed geometry model with accurate boundary conditions was implemented using the FEA DC Module Solver in COMSOL Multiphysics [128]. By comparing simulated tracks with real data, the source of inhomogeneities was identified, and the corresponding electric field map was incorporated into the track reconstruction algorithm to correct distortions. The effectiveness of this correction was evaluated using data collected with and without a magnetic field. Biases in reconstructed momentum and spatial resolution for both cosmic ray and beam data were assessed, demonstrating no residual effects from non-ideal electric field conditions.

## 6.1 Brief Introduction to Electrostatics

The electrostatic force, or Coulomb force, describes the interaction between two charges $q_1$ and $q_2$, varying inversely with the square of their distance $d$. Coulomb's law is expressed as $\mathbf{F} = k\frac{q_1 q_2}{d^3}\mathbf{d} = \frac{1}{4\pi\varepsilon_0}\frac{q_1 q_2}{d^3}\mathbf{d}$, where $\varepsilon_0$ is the vacuum permittivity ($8.854\times10^{-12}$ $\mathrm{N^{-1}m^{-2}C^2}$). This force is conservative and central. A charge $q_1$ generates an electric field $\mathbf{E}$, exerting a force $\mathbf{F} = q_0\mathbf{E}$ on another charge $q_0$. The field exists independently of $q_0$ and is measured in N/C or V/m. Since the Coulomb force is conservative, the work $W$ to move a charge along a path $C_1$ is $W_1 = q_0\int_{C_1}\mathbf{E}\cdot d\mathbf{r}$. This work is path-independent, allowing the definition of an electrostatic potential $\phi(\mathbf{r})$: $\phi(\mathbf{r}_A) - \phi(\mathbf{r}_B) = \int_{\mathbf{r}_A}^{\mathbf{r}_B}\mathbf{E}\cdot d\mathbf{r}$. The potential is determined up to an additive constant, typically set to zero at infinity. The electric field is derived from the potential as $\mathbf{E} = -\nabla\phi$. The curl of $\mathbf{E}$ is zero, $\nabla\times\mathbf{E} = 0$. The flux of $\mathbf{E}$ through a surface $\Sigma$ is $\Phi = \int_\Sigma \mathbf{E}\cdot\mathbf{n}\,d\Sigma$. Gauss' law states that the flux through a closed surface equals the enclosed charge $Q_{int}$ divided by $\varepsilon_0$: $\Phi = \frac{Q_{int}}{\varepsilon_0}$. For a charge density $\rho$, Gauss' law becomes $\nabla\cdot\mathbf{E} = \frac{\rho}{\varepsilon_0}$. Combining $\mathbf{E} = -\nabla\phi$ and $\nabla\cdot\mathbf{E} = \frac{\rho}{\varepsilon_0}$ yields Poisson's equation: $\nabla^2\phi = -\frac{\rho}{\varepsilon_0}$. In charge-free regions ($\rho = 0$), this reduces to Laplace's equation: $\nabla^2\phi = 0$. These equations allow the determination of the electric field and potential, essential for modeling complex systems like HA-TPCs.

A body is an electric conductor if it contains charge carriers free to move over macroscopic distances. In metals, these are electrons. Under static conditions, a conductor in equilibrium has: (i) zero charge density, (ii) an equipotential body, (iii) zero net charge density, and (iv) an electric field outside its surface with surface density $\sigma(r)$, given by $\mathbf{E} = \frac{\sigma(r)}{\varepsilon_0}\mathbf{n}$.

In contrast, insulators or dielectrics lack free charge carriers and do not conduct electricity. However, they respond to electric fields by rearranging charges on a sub-molecular scale. Dielectrics are classified based on whether their molecules have intrinsic dipole moments. Nonpolar molecules develop induced dipole moments $\mathbf{p} = q\boldsymbol{\delta}$ under an electric field, where $q$ is the charge and $\boldsymbol{\delta}$ is the displacement between charges. For polar molecules, the effect is stronger. In an isotropic medium, $\mathbf{p}$ aligns with $\mathbf{E}$, and for weak fields, $\mathbf{p} = \alpha\mathbf{E}$, where $\alpha$ is the atomic polarizability. The macroscopic polarization $\mathbf{P}$ is $\mathbf{P} = n_p q\boldsymbol{\delta} = n_p\alpha\mathbf{E} = \varepsilon_0\chi_e\mathbf{E}$, where $\chi_e$ is the electric susceptibility.

In dielectrics, Gauss' law includes polarization charges $\rho_p$: $\boldsymbol{\nabla}\cdot\mathbf{E} = \frac{\rho_f}{\varepsilon_0} + \frac{\rho_p}{\varepsilon_0}$. Introducing the electric displacement $\mathbf{D} = \varepsilon_0\mathbf{E} + \mathbf{P}$, Gauss' law becomes $\boldsymbol{\nabla}\cdot\mathbf{D} = \rho_f$. For normal dielectrics, $\mathbf{D} = \varepsilon_0\varepsilon_r\mathbf{E}$, where $\varepsilon_r = 1 + \chi_e$ is the relative dielectric constant. Thus, Gauss' law and the curl of $\mathbf{E}$ in dielectrics are:

$$\boldsymbol{\nabla}\cdot(\varepsilon_r\mathbf{E}) = \frac{\rho_f}{\varepsilon_0}, \quad \boldsymbol{\nabla}\times(\varepsilon_r\mathbf{E}) = 0.$$

In a normal dielectric, the field $\mathbf{E}$ is related to the vacuum field $\mathbf{E}_0$ by $\varepsilon_r\mathbf{E} = \mathbf{E}_0$, meaning the field

in the dielectric is weaker by a factor of $\varepsilon_r$.

## 6.2 Electric Field Distortions and Track Reconstruction in the HA-TPC

The electric field in the field cages is shaped by a planar Cathode, a series of 393 rectangular-shaped copper strips, and a planar Anode where ERAMs (Electron Readout Modules) are positioned. An electric potential gradient is established by high accuracy resistors connecting adjacent strips. The field cage design incorporates both conductive and insulating materials, with detailed descriptions provided in the previous Chapter dedicated to field cage production.

Understanding the electric field in HA-TPCs is critical for interpreting the detector's response. Field distortions can affect both track projected position and arrival time of drifting electrons, potentially degrading the the reconstructed momentum of particles and altering the matching with surrounding detectors. In the ND280 vertical TPCs (v-TPCs), the electric field was probed using a LASER source, which is aimed towards metallic strips placed on the cathode, and Cosmic Rays. However, in HA-TPCs, LASER-based characterization was not feasible at CERN during the initial phase and is impractical at J-PARC after installation. Optical access to the internal volume is limited to a 3 cm diameter quartz window on the module frame.

In the absence of LASER data, Cosmic Rays remain the primary tool for evaluating local electric field distortions in HA-TPCs. Without a magnetic field, charged particles in the gas undergo multiple scattering, but for high-energy muons, this effect is negligible for the study's purposes. By analyzing a large sample of cosmic ray events, distortions can be assessed statistically rather than on an event-by-event basis. Cosmic Rays predominantly traverse the detector vertically, providing limited insight into horizontal field distortions. Horizontal tracks, generated by accelerator Neutrino interactions in material upstream of ND280, offer additional information, but these are usually available when the accelerator and magnetic field are operational. Special data taking with Neutrino Beam and no magnetic field is not yet planned.

Cosmic ray data were collected in May and November 2024 using both HA-TPCs installed in ND280, with Time-of-Flight (TOF) panels providing triggers, both with and without the magnetic field. The initial reconstruction step involved applying the standard spatial reconstruction algorithm. At this stage, cluster-based track position estimates were extracted, and a linear fit was performed instead of the usual helical fit. The coordinate system was inverted, so positive residuals indicate downstream displacement, while negative residuals correspond to upstream displacement. For vertical tracks, the residual distribution primarily reflects the relative displacement $\Delta z$, as the vertical displacement $\Delta y$ is largely masked by the track direction.

Figure 6.1 shows two distributions of spatial residual for projections on End-Plate EP0 of tracks (i) next to the Cathode, with $x \leq 20$ cm), and of tracks (ii) far away from the Cathode and not close to the Anode, with 60 cm $\leq x \leq 80$. Residuals for tracks near the Cathode exhibit a clear "C-shaped" bending near the cage walls, with the central region displaced further away from the vertical walls. This behavior is absent in the second sample, suggesting localized electric field non-uniformities are affection the region close to the Cathode. Both samples show residual bending near the edges of each ERAM.

Such C-shaped distortion introduces an apparent curvature in the helical fit used in the reconstruction algorithm. The Larmor radius equation $p_T \propto \frac{1}{R}$ relates transverse momentum $p_T$ to curvature, defined as curv $= \frac{(q/e)}{R}$, where $q/e$ is typically $\pm 1$ for particles in HA-TPCs. Initial analysis of cosmic ray data revealed significant track distortions, particularly near the Cathode.

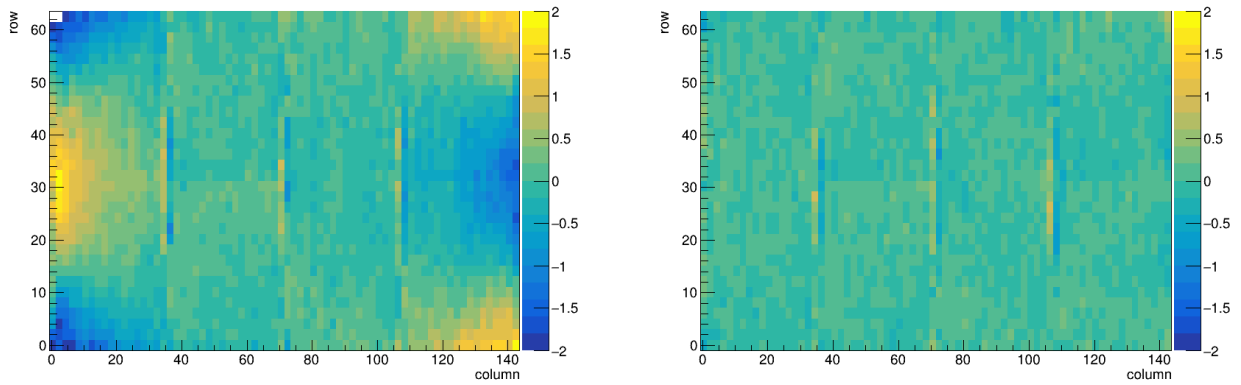


(a) (b)

Figure 6.1: Residuals distribution for vertical tracks, with system of reference rotated, such that residuals are evaluated as horizontal displacement $\Delta z$ in the usual ND280 coordinates. Figure 6.1a represents tracks less than 20 cm away from Cathode, while Figure 6.1b refers to tracks between 60 cm and 80 cm away from Cathode. Scale in mm.

Figures 6.2 show the reconstructed curvature for cosmic data without a magnetic field, divided by End-Plate and drift distance (in 100 mm bins). Figures 6.3 display the standard deviation of Gaussian fits to these distributions. Selected tracks have a y-axis direction $u_y > 0.9$ and at least 50 clusters ($n_{cl} > 50$).

The Cathode is positioned at $x = 0$ in all graphs. Each color represents 18 columns (half the width of an ERAM) for both vertically aligned ERAMs, numbered from 0 (upstream) to 3 (downstream). End-Plates (EPs) are labeled from 0 to 3, with EP0 and EP1 in the bottom HA-TPC and EP2 and EP3 in the top HA-TPC. Even-numbered EPs are on the negative x-axis of the ND280 standard geometry, while odd-numbered EPs are on the positive x-axis. The center of the HA-TPCs is at $x = 0$. The momentum sign in reconstruction assumes particles originate from the sFGD, resulting in mirrored curvature distortions between the top and bottom HA-TPCs.

The region near the Cathode exhibits significant bias in apparent curvature and increased variance in the distribution. This effect is more pronounced for tracks reconstructed by ERAMs near the vertical walls of the field cages. In the absence of a magnetic field, the apparent curvature indicates deviations in electron drift paths originating far from the Anode.

Two primary hypotheses about electric field distortions were formulated to explain this effect:

- Space charge effects in the active volume of the TPC
- Non ideal matching of electrical potential applied to the cage electrodes

## 6.3 Space charge effects in the HA-TPCs

Cosmic rays passing through the HA-TPC not only generate primary electron-ion ionization pairs but also produce ions that escape the amplification region past the mesh, a phenomenon known as ion backflow. Electrons take a very short time (less than 20 $\mu s$) to reach the anode, resulting in an evacuation rate from the TPC active volume that is significantly higher than the cosmic ray

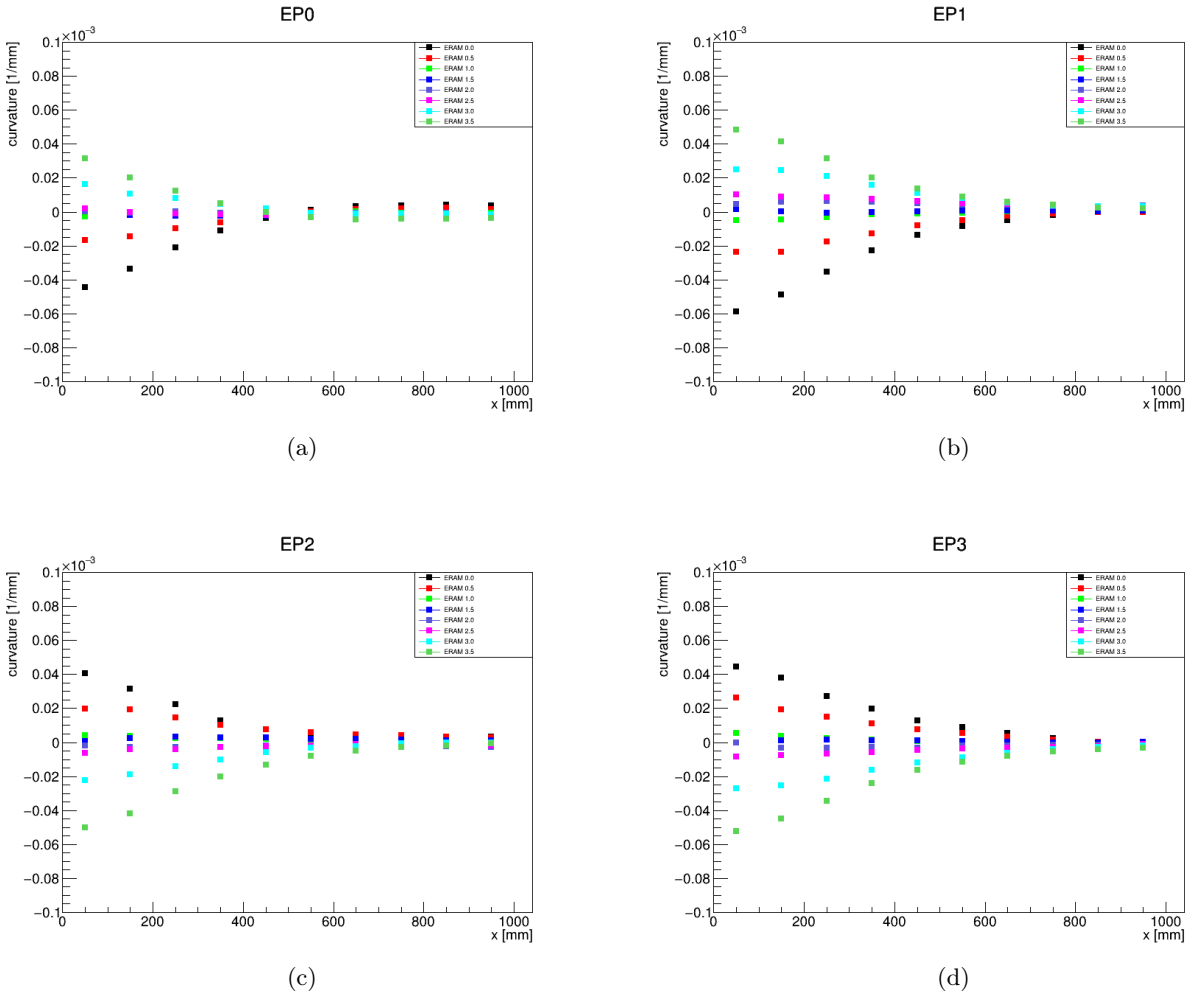


(a) (b)

(c) (d)

Figure 6.2: Centroid of a gaussian fit for apparent curvature for tracks passing in bottom HA-TPC EP0 (6.2a) and EP1 (6.2b) and top HA-TPC EP2 (6.2c) and EP3 (6.2d).

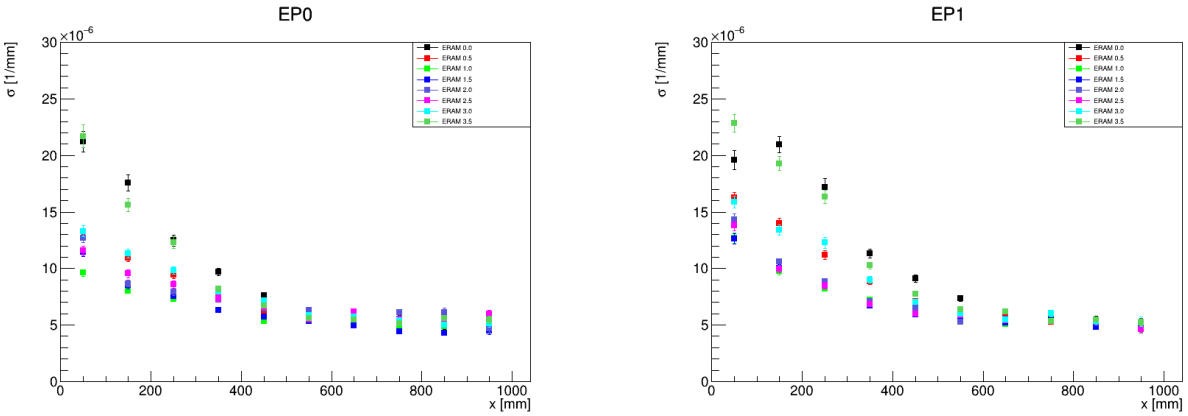


(a) (b)

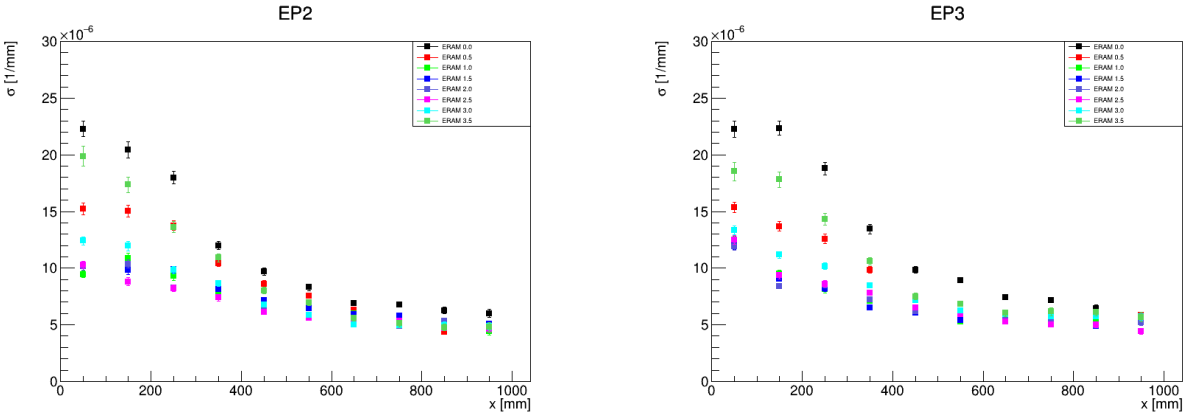


(c) (d)

Figure 6.3: Standard deviation of a Gaussian fit for apparent curvature distribution for tracks passing in bottom HA-TPC EP0 (6.2a) and EP1 (6.2b) and top HA-TPC EP2 (6.2c) and EP3 (6.2d).

ionization rate (a few hundred Hz). In contrast, ions drift at much larger velocities, leading to a much slower evacuation rate. As a result, ions can accumulate within the active volume, forming a steady space-charge that may alter the nominal electric field and distort the trajectories of primary electrons [101].

An estimate of the expected positive space-charge within the HA-TPCs due to ions is derived in the following.

Let $R$ [$\mathrm{m^{-3}s^{-1}}$] be the rate of electrons freed by Cosmic Rays in the active volume. When these electrons reach the amplification gap, the signal is amplified by a factor $G \sim 1000$. However, a significant fraction of the ions flowing backward toward the mesh are trapped, with only a small percentage (up to a few percent) escaping. Assuming a non-optimistic scenario where 10% of the ions escape into the active volume, approximately $G^{+}_{esc} \sim 100$ ions per primary electron enter the active volume. The accumulation of charge in the active volume depends on the ion drift velocity $v^{+}_{D} \sim 1$ m/s, which is much slower than that of electrons. For a drift region of length $L$, the ion charge density $\rho^{+}$ is given by:

$$\rho^{+} = \frac{eRG^{+}_{esc}L}{v^{+}_{D}},$$

where $e$ is the elementary charge. The goal is to determine the strength of the transverse electric field induced by this positive space charge.

Field cages are cuboidal in shape, so by geometric symmetry, an electron placed exactly at the center of the TPC experiences no net electric field contribution. For instance, the transverse component along the $z$-direction is maximized for an electron near one of the vertical walls. By treating the two halves of the TPC as independent, the electric field component $E^{+}_{z}$ due to the ion space charge can be expressed as:

$$E^{+}_{z} = \frac{1}{4\pi\varepsilon_0} \iiint \rho^{+} \frac{z - z_0}{r^3}\, dV.$$

Using the dimensions of the field cages from metrology data and the estimated values for $v^{+}_{D}$ and $R$ from [101], the charge density is:

$$\rho^{+} = \frac{1.6 \times 10^{-19} \times 2 \times 10^{6} \times 100 \times 0.994}{1.5} = 2.1 \times 10^{-11}\,\mathrm{C/m^3}.$$

Thus, the transverse electric field is:

$$E^{+}_{z} \sim \frac{0.7}{4\pi \times 8.85 \times 10^{-12}} \times 2.1 \times 10^{-11} = 0.13\,\mathrm{V/m}.$$

This value is more than five orders of magnitude smaller than the nominal electric field $E \sim -27.5\,\mathrm{kV/m}$. So that the space charge effect appears to be insufficient to explain the track distortions observed in cosmic ray data.

The overall ion-feedback current associated with space charge is estimated to be

$$I_{ifb} = \rho^{+} \times S_{\perp} \times v^{+}_{D} \sim 20pA$$

and might be measured by comparing the Cathode return current with and without primary ionization amplification in ERAMs. By averaging the Cathode current over an extended period to minimize the impact of electrical noise, no difference was detected at the level of 1 nA, confirming that the ion-feedback current is negligible.

## 6.4 Electric field model for HA-TPCs

A potential source of electric field inhomogeneity was anticipated due to the non-ideal geometry of the HA-TPC electrodes and imperfect matching of the electrical potentials applied to the cage electrodes. As outlined in the introduction to this chapter, two key modifications were implemented to mitigate the risk of electrical breakdown: (i) introducing a 12 mm gap in the transverse plane and (ii) displacing the first field strip from the Cathode plane.

This section analyzes the effects of these modifications on the resulting electric field distortions. Initial studies employed a simplified field cage geometry and boundary conditions, using an electrostatic solver in Mathematica. Subsequently, a more detailed model with accurate boundary conditions was developed using the FEA DC Module Solver in COMSOL Multiphysics. While the preliminary results were instrumental in identifying the origin of the issue, only the most accurate results obtained with COMSOL are presented here.

COMSOL is a versatile tool for numerical simulations across various branches of physics, including electrostatics via the AC/DC module. This module enables the design and analysis of electric and magnetic fields in static, low-frequency, and transient applications, even for 3D models. For the HA-TPCs, the electric field under static conditions is considered. The COMSOL AC/DC module solves the differential form of Maxwell's equations, along with the specified initial conditions, in both vacuum and dielectric media, as discussed earlier in this chapter. The most accurate simulations of the electric field in the HA-TPCs were conducted using COMSOL Multiphysics version 6.1 (referred to as COMSOL).

### 6.4.1 Electric field model for early HA-TPC design

Studies performed in TDR, also exploiting COMSOL, were crucial for choosing the final configuration with two layers of alternating copper strips, with a pitch of 5 mm. In such studies, a much larger degradation of electric field near the Cathode region was already predicted with respect to of other regions near the field cage walls. In Figure 6.4, the electric field simulation on a part of the field cage is reported. The geometry is reduced with respect to the actual size and only 221 strips are considered. In addition, the symmetry planes of the field cage are used to reduce the computation resources. The Cathode is set at -22.1 kV, while the Anode is at ground. In this way, the nominal longitudinal field is equal to -200 V/cm. Each plot uses a color scale for electric field magnitude in an interval between $\pm 1\%$ of the nominal value. Using such configuration, it was concluded that the field uniformity was better than $10^{-4}$ at more than 10 mm from the walls excluding Cathode and Anode proximity. Top right plot shows that the inhomogeneities in the electric field extend up to 3 cm away from the walls and the Cathode. However, the projection of this region on the Anode plane is not instrumented. Additionally, in the top right plot is shown that the Cathode is reaching the wall and the first strip is adjacent to the Cathode.

### 6.4.2 Electric field model for the real field cage

The geometry used for field cages simulation is based on the average measurements for width and length, defined as the distance between the two opposite walls, performed by the NEXUS metrology service and presented in the chapter regarding the field cage production.
The distance between the central flange and the first copper strip on the Cathode side is estimated to be 15 mm, while the Cathode dimension is 12 mm (6 mm per each side). So, the distance between the copper foil on Cathode and the first strip is 8 mm. In addition, the gap between the Cathode and both vertical and horizontal walls is set to 12 mm.

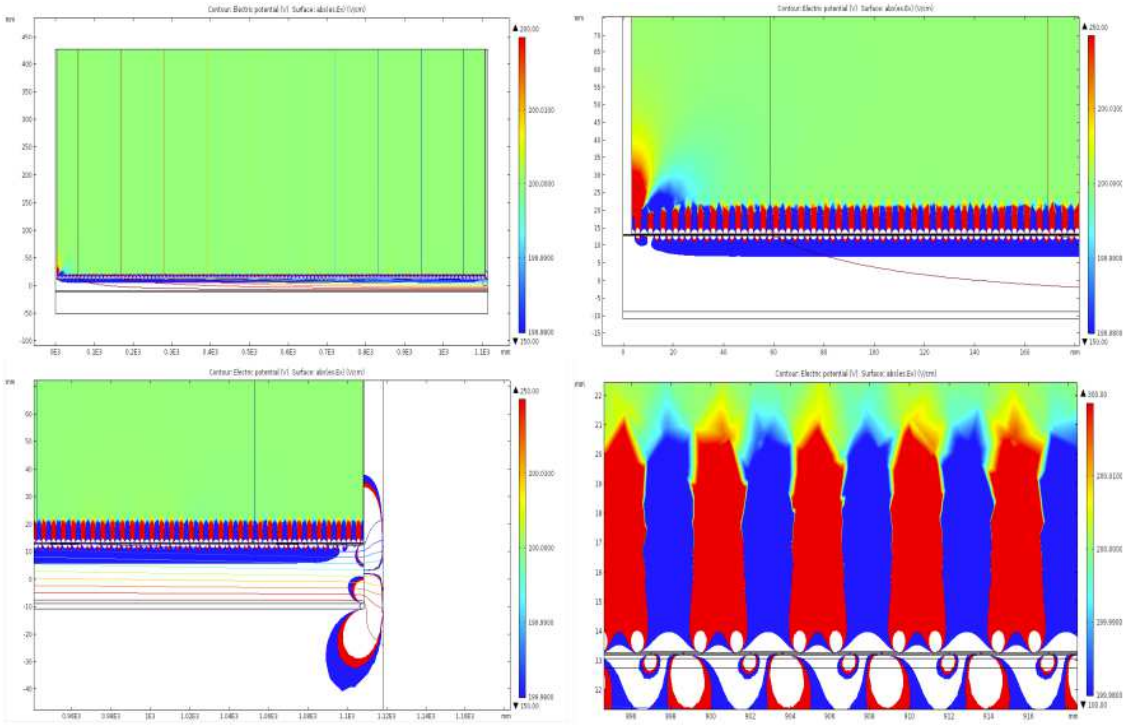

Figure 6.4: Electric field simulation in a part of field cage model as designed for TDR. Field and mirror strips are 3 mm wide and the pitch is 5 mm. The voltages at Cathode and at Anode are set to obtain an expected magnitude for longitudinal field of 200 V/m. Picture from [96].

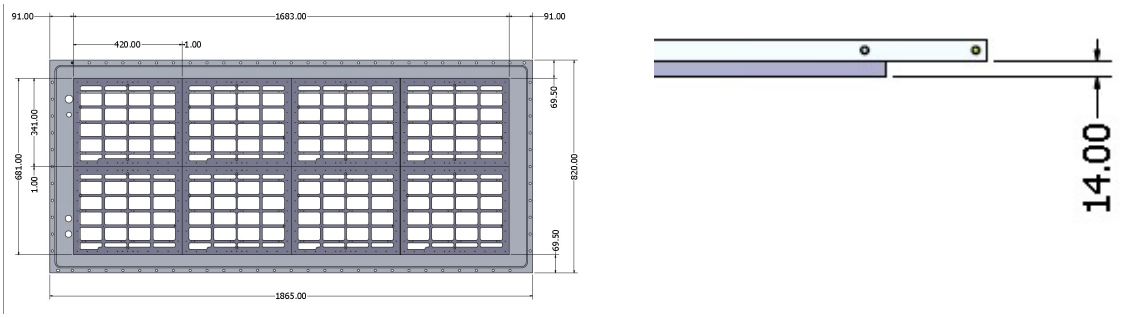


(a) (b)

Figure 6.5: Sketch of module frame 6.5a and thickness of stiffeners on module frame 6.5b, which extend inside the active volume. Dimensions in mm.

On the Anode side, the geometry is not a flat plane, but there are some protrusions on the module frame as shown in picture 6.5a and 6.5b. The distance between the flange on the Anode side and the closest copper strip is equal to the Cathode side (15 mm), hence the total protrusion of ERAMs ends on the projection of the space occupied by the last copper strip. The instrumented area is smaller than the total surface of the field cage aperture: in the vertical direction, ERAMs end about 12 mm away from the wall, while in the horizontal direction the distance between ERAMs and walls is about 35 mm. In this external area, there are no protrusions, therefore there is a step on the drift direction of about 15 mm which might alter locally the electric field. The ERAMs model is smeared at the angles, since the presence of orthogonal sides might create local strong fields due to limited performances on the numerical computation. The wall thickness is assumed 39 mm and for simplicity they are filled with Kapton, since many of the materials used present a similar relative permittivity. All 393 copper strips are designed at a distance of 50 $\mu$m between the field and mirror layers, but since their nominal thickness of 17 $\mu$m is much smaller the total dimension of the field cage and would introduce many mesh cells they are assumed as 2D conductors. The final configuration of field cages is such that the first copper strip near the Cathode is set at the same potential of the Cathode, since they are connected simply via a copper wire. This configuration was an oversight in the preparation phase. In fact, in the geometry presented in Figure 6.4, the first copper strip and the Cathode are adjacent, while in the final configuration there are 8 mm between them. Two hypotheses are tested as possible sources of electric field distortions:

- the Cathode dimensions not reaching the walls;
- the wrong potential applied to the first copper strip.

The potential at the Cathode is set in order to have a nominal longitudinal field of -1 V/m, since the important result are the ratio between the transversal and longitudinal field and the local field magnitude with respect to the nominal one. Three planes of symmetry are defined in order to exploit the properties of HA-TPCs geometry, therefore only one eighth of the total volume is simulated, which is the cuboid delimited by the central plane of the Cathode and the two half-planes from the external shielding to the central coordinates of the HA-TPC. The geometry used for the finite element method simulation by AC/DC module is reported in Figure 6.6.

In the results presented in the next section, the system of reference Origin is placed on the central point of the Cathode, while the drift direction is along the positive direction of $x$ axis. The electric field simulation is performed also on a geometry similar to the one presented in the TDR.

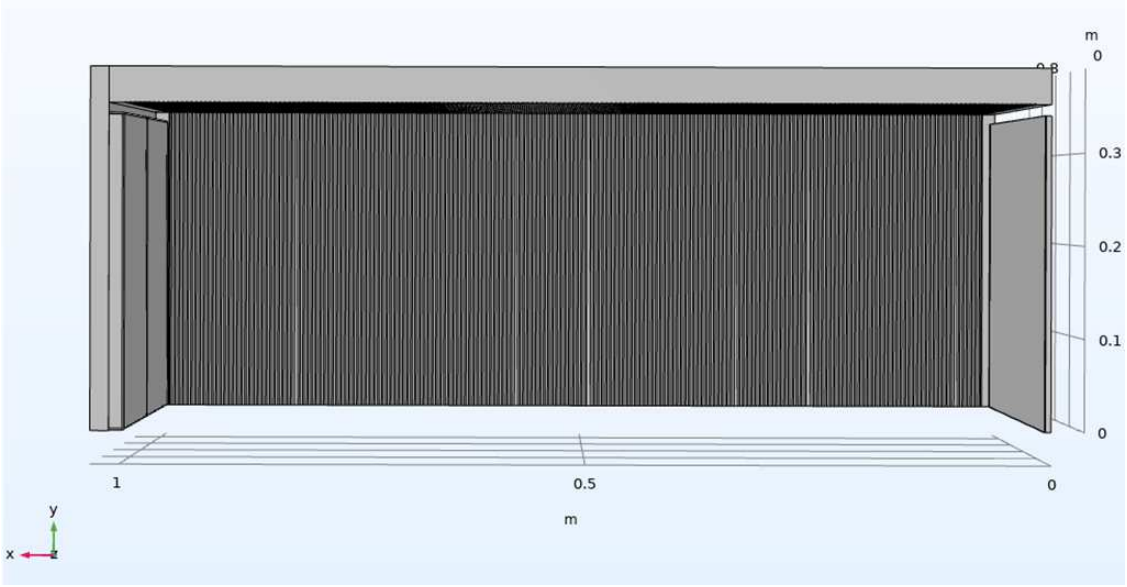


Figure 6.6: Side view of HA-TPC model used for COMSOL simulation. Only one eighth of the total volume is implemented, since three symmetry plane are used in (i) $x = 0$, (ii) $y = 0$ and (iii) $z = 0$. The Anode region is on the left, while the Cathode region on the right.

In such geometry, the Cathode is extended up to the field cage walls and 3 additional strips are placed in order to reach the same x position of the Cathode. A comparison between the Cathode regions in the two configurations is shown in Figures 6.9a and 6.9c.

### 6.4.3 Electric field simulation

After the geometry is created and the potentials are defined, a fine mesh is created to numerically solve the Laplace equation. From the computation of the potential, a map of the electric field is derived. The solution for the plane $y = \frac{y_{max}}{2}$ is shown in Figure 6.7. In the picture, the difference of the electric field shape with respect to 6.4 is very relevant, in particular close to the corners in the Cathode and Anode regions. The field lines in the central plane $z = 0$ are plotted in picture 6.8 for the mentioned regions where the effect is more intense. The field lines are curved for two different reasons: near the Cathode, there is a large potential difference between the Cathode and the first strip and the external shielding; near the Anode, the whole ERAM surface is at ground, as well as the module frame, therefore all the surfaces at the same potential are not placed in the same direction and at the same $x$ value.

In order to quantify the electric field distortion, an important estimator is the local ratio between its transversal and longitudinal components. The ratio $E_y/E_x$ is reported in Figure 6.10 as a function of x, for the plane $z = 0$ at several values of $y$. The same is performed for ratio $E_z/E_x$ at several $z$ values in the plane $y = 0$. In both series of graphs, the electric field simulation for three different configurations are compared: (i) actual HA-TPC setup; (ii) actual HA-TPC geometry but the first strip near the Cathode is placed at a calibrated voltage step which increases linearly with $x$; (iii) HA-TPC as if the Cathode length and first strip placement were in agreement with the TDR simulations. The transversal component of the field increases quickly when evaluating points close to the field cage walls. In plots 6.10, the last point is about 2 cm away from the horizontal field cage walls and 1 cm away from the top edge of the ERAMs. In Figure 6.12, the last point

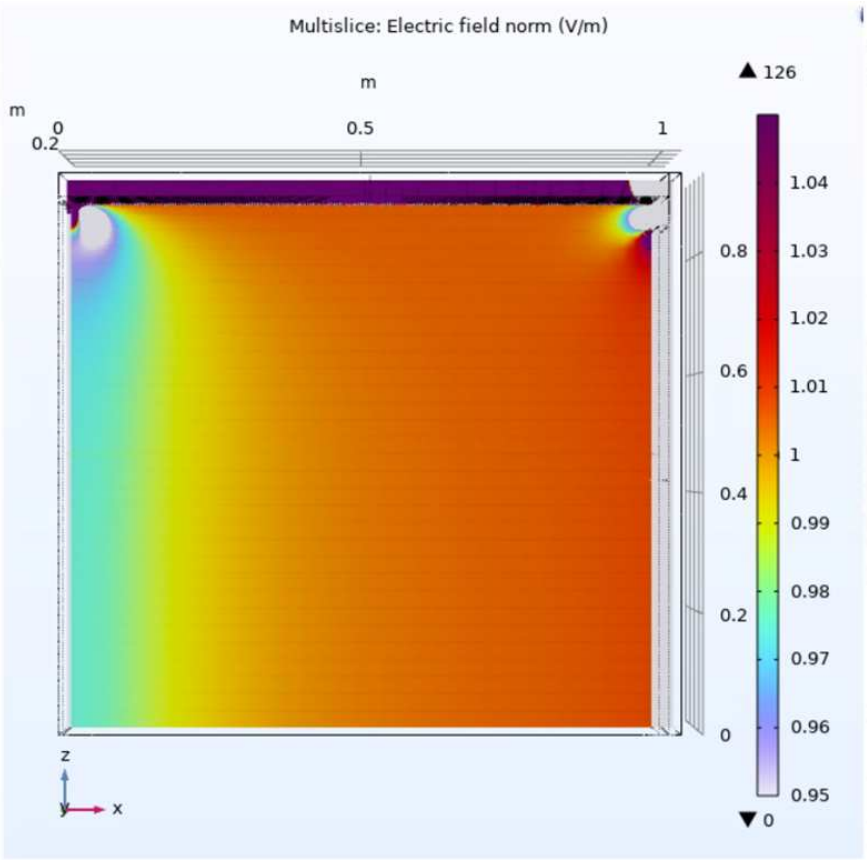


Figure 6.7: Electric field norm in a color scale of ±5% around the set value of 1 V/m.

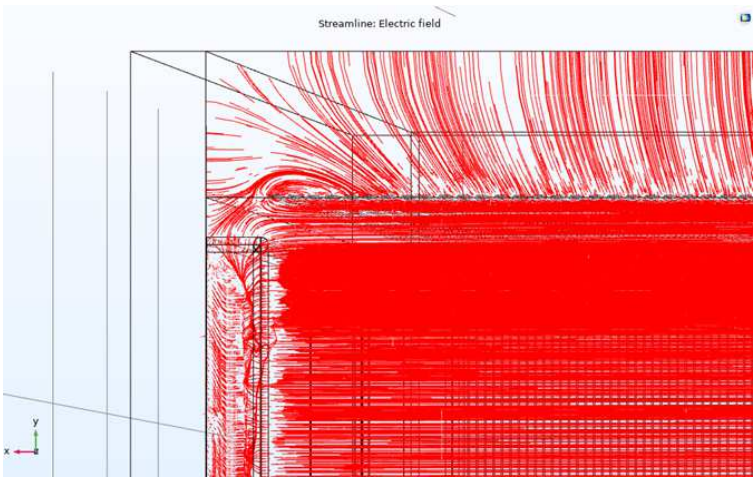


Figure 6.8: Electric field lines in the region near the Anode, which is similar for every geometry.

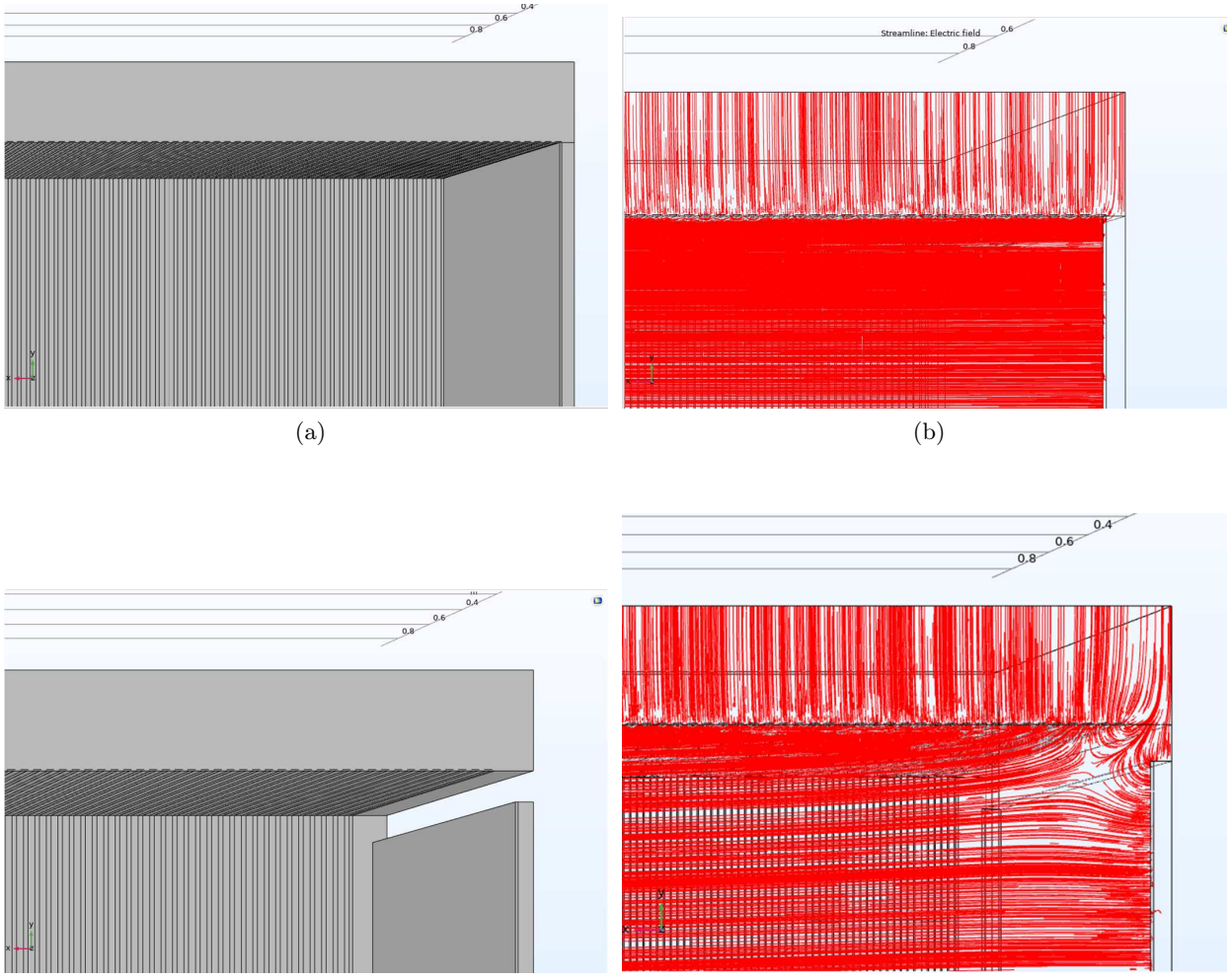


(a) (b)

(c) (d)

Figure 6.9: Comparison of the Cathode region in the two geometries: TDR-like on top and actual one on bottom. For each geometry, electric field lines are drawn in the central plane $z = 0$.

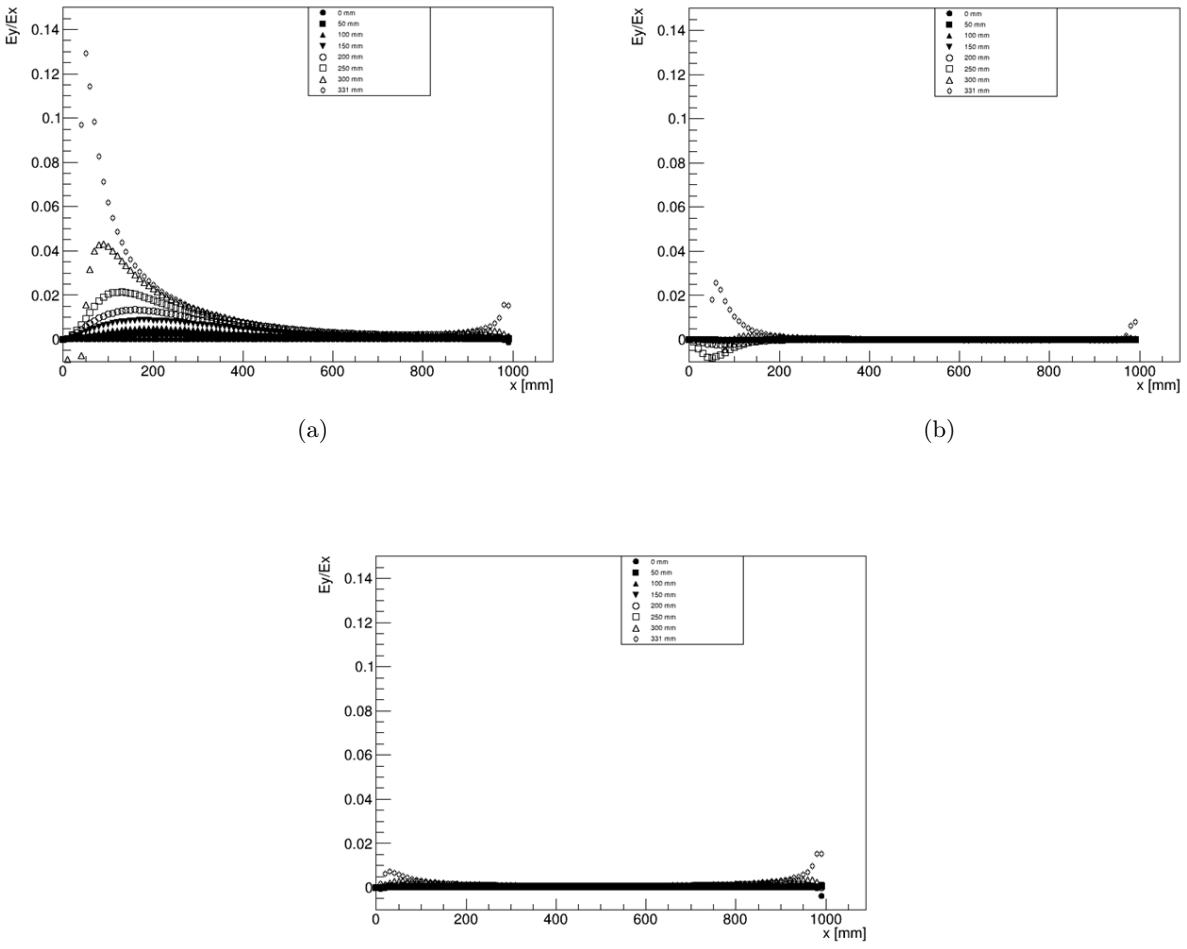


(a)

(b)

(c)

Figure 6.10: $E_y/E_x$ for three different configurations of HA-TPC: top left (6.10a) actual HA-TPC setup; top right (6.10b) actual HA-TPC geometry with the first strip at the correct potential according to its $x$ coordinate; bottom (6.10c) HA-TPC as simulated in TDR.

is 1 cm away from the lateral ERAMs edge, but about 4 cm away from the lateral walls. The transversal components of the fields are in the same verse near the Cathode and near the Anode, giving a cumulative effect over drift. According to the simulations, the transversal component near the Cathode is due to the wrong potential of the first strip: in fact, the component is much smaller in configuration (ii), which represents the best field shape achievable with the current field cage geometry. The transversal component is reduced below 1% if the TDR geometry is used, achieving a consistent result with the simulations performed at the time.
In the Anode side, the deformations are due to the shape of the module frame and the protrusions of the ERAMs, since all the three configurations yields the same level of the deformation. The direction of the transversal field is such that an electron subjected to it will drift to the inner side while moving towards the Anode. As shown in Figure 6.11a for $E_y$ and in Figure 6.11b for $E_z$, the transversal field is much larger close to a wall and on the central plane, so electrons for a straight track will be shifted differently according to their distance from field cage walls. In addition, at near the corners the transversal field component is close to zero.

The electric field map is then extracted from COMSOL and an implementation in the official ND280 Software has been performed, in order to evaluate the effect of the model-driven corrections on the track reconstruction.

### 6.4.4 Electric field map implementation in ND280 Software

The ND280 software is responsible for producing processed output from either data or Monte Carlo input related to the T2K Near Detector. The steps performed in ND280 Software in order to reconstruct data and simulated events are reported in Figures 6.13 and 6.14. The drift of electrons in gas is developed in oaUtility package, firstly implemented for vTPCs and later extended to include HA-TPCs. The drift of electrons in gas is realized using Runge-Kutta methods. For simulations, the deposition of charge along a track is simulated via GEANT4, while the drift is simulated by evaluating locally the Magnetic and electric field and by performing *small* steps until the Anode is reached. Successively, the simulation of the charge multiplication in the amplification gap, the charge spreading on DLC and the electronics response are simulated in the detResponseSim package as explained in the HA-TPC chapter. In both MIDAS and MC data, first a calibration on the electronics channel is applied. Then, the reconstruction of the original position of the primary ionization caused by the traversing particle is performed. Before the application of the log(Q) method, a drift from the Anode back into the drift region is performed to apply the corrections for E×B distortions. Prior to the work presented in this thesis, only magnetic field distortions were considered in the correction framework for HA-TPCs, while the electric field was assumed to be ideal.

To maintain a reasonable memory allocation for the electric field map, a step size of 1 cm in each direction was adopted. This results in a total of $100 \times 37 \times 88$ points in the $x \times y \times z$ directions, with symmetries applied to extend the map to the entire volume. To ensure smooth transitions between map entries, the field at each point is computed as a weighted average of the eight values at the vertices of the surrounding cube.

$$\mathbf{E}_w = \frac{\sum_{i=1}^{8} \frac{1}{d_i} \cdot \mathbf{E}_i}{\sum_{i=1}^{8} \frac{1}{d_i}}, \tag{6.1}$$

in which $d_i$ is the distance of the point to the vertex $i$.

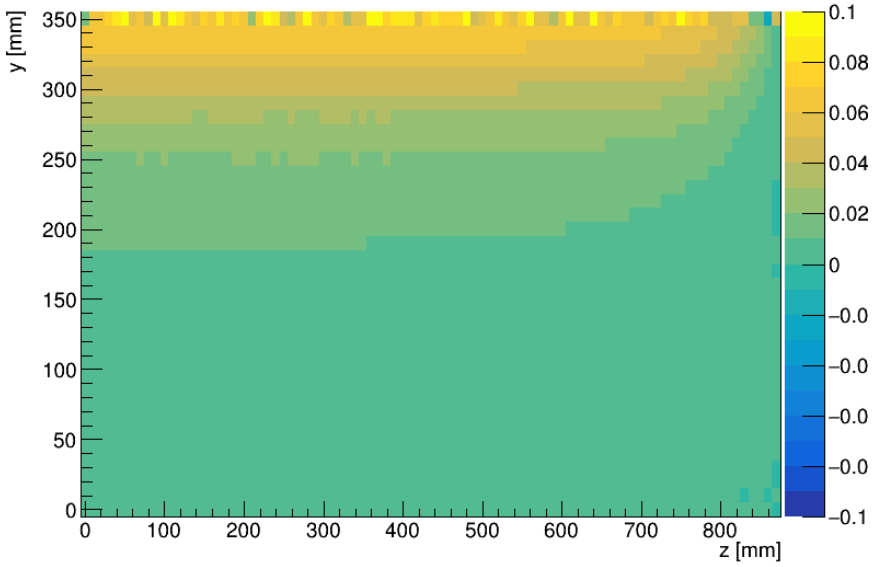


(a)

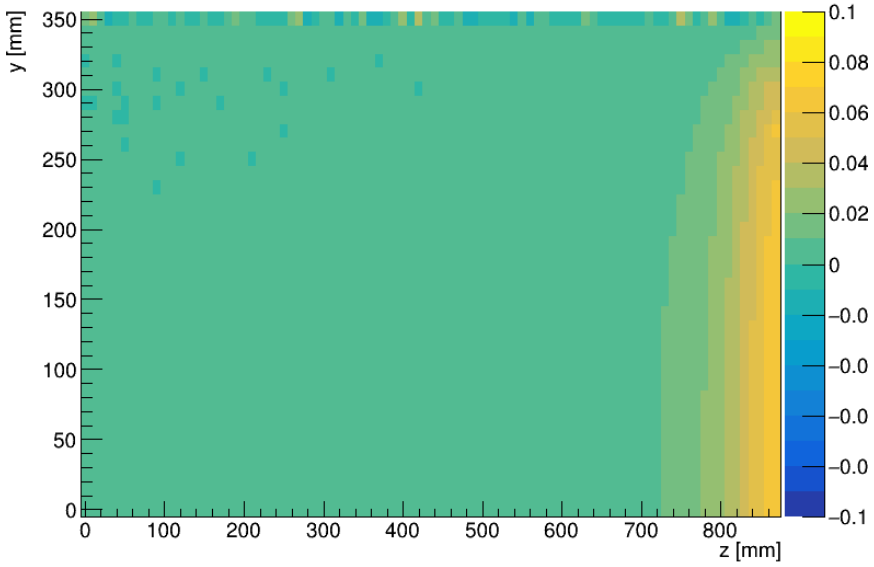


(b)

Figure 6.11: $E_y$ (6.11a) and $E_z$ in the first quadrant of a HA-TPC (6.11b) components at x=100 mm in COMSOL simulation of the actual HA-TPCs setup.

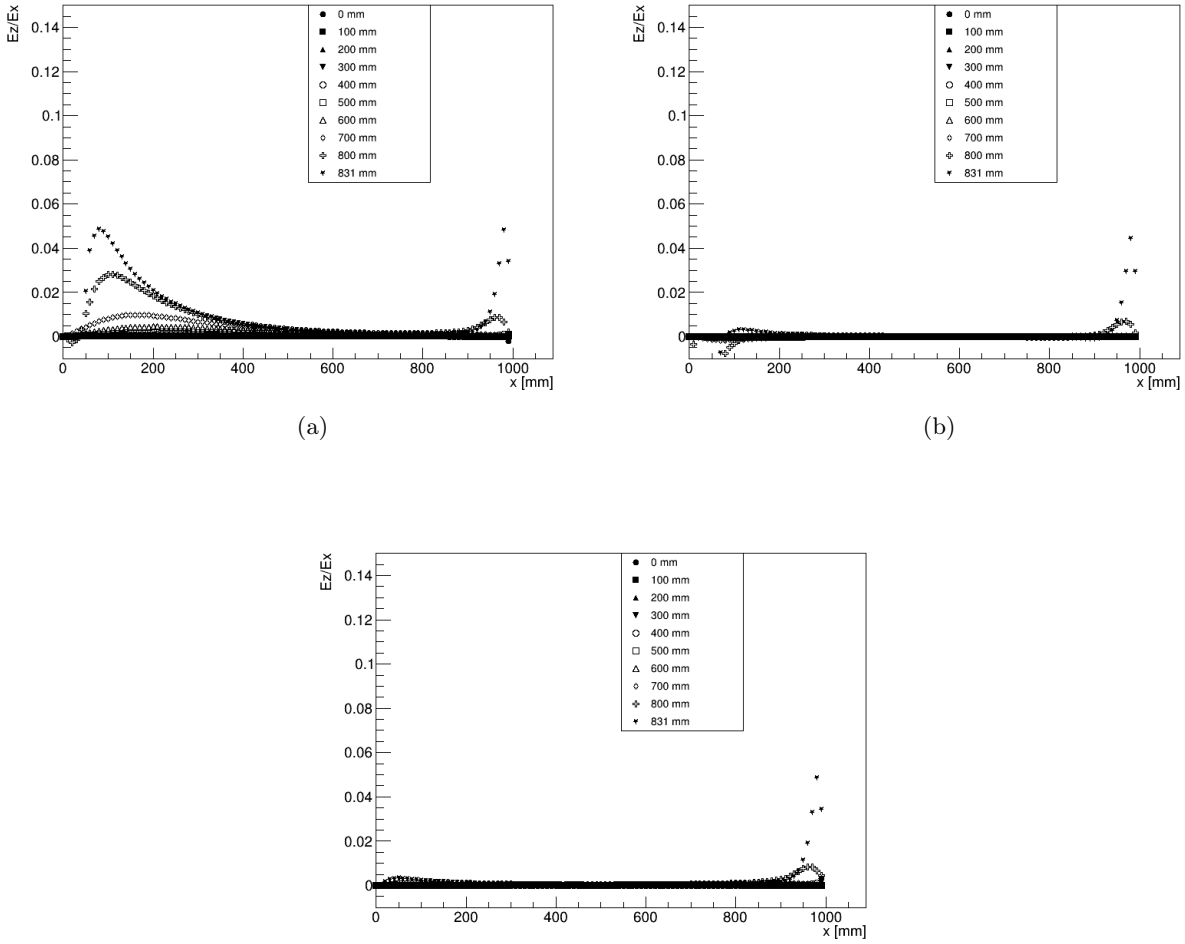


(a)

(b)

(c)

Figure 6.12: $E_z/E_x$ for three different configurations of HA-TPC: top left (6.12a) actual HA-TPC setup; top right (6.12b) actual HA-TPC geometry with the first strip at the correct potential according to its $x$ coordinate; bottom (6.12c) HA-TPC as simulated in TDR.

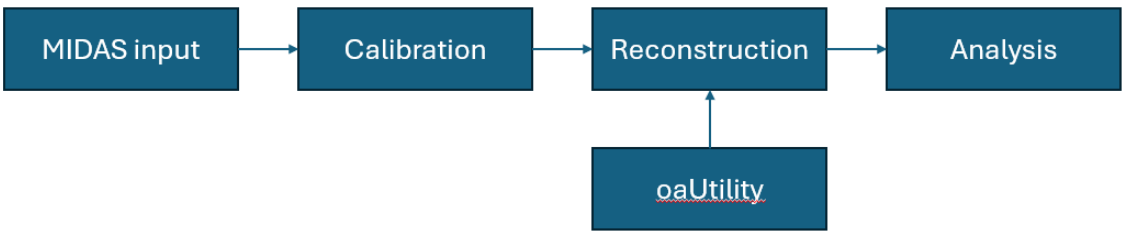


Figure 6.13: ND280 steps related to HA-TPCs data processing, with a focus on oaUtility usage for real data.

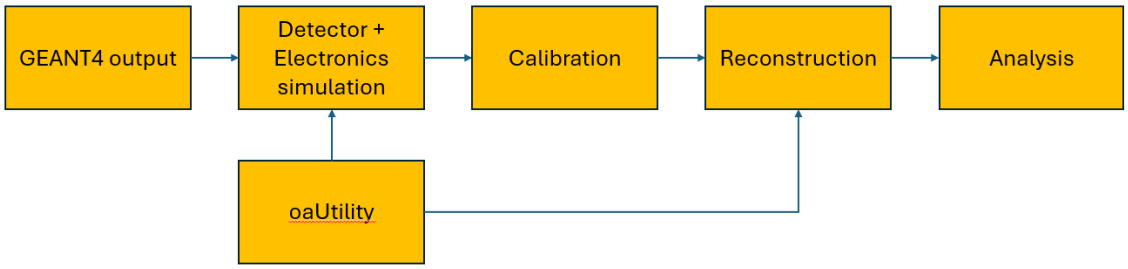


Figure 6.14: ND280 steps related to HA-TPCs Monte Carlo data simulation and processing, with a focus on oaUtility usage for simulated data.

## 6.5 Effect of electric field map on drift of a point-like charge

The information showed in Figures 6.10 and 6.12 can be used to evaluate the absolute displacement of drift electrons between the starting and arrival points on the ERAM plane projection. In fact, residuals distributions in Figure 6.1 show the relative displacement with respect to a fitted line, whose projection on ERAM plane might be rotated and translated from its original position. As a first evaluation, the application of the electric field map is evaluated on a simplified simulation which does not take into account the presence of gas in the active volume. Considering a point-like negative charge starting in the position $(x_0, y_0, z_0)$, the value of the electric field according to 6.1 is computed and a 1 mm long step is performed along the field direction. The process is repeated until the charge reaches the Anode. The process is repeated on a regular grid with a granularity of 1 mm and the results for $x = 10$ cm is reported, covering only the instrumented End-Plate surface corresponding to the two ERAMs in 6.6. Plots in Figure 6.15 show the absolute displacement for points in such grid, which are much larger than the relative displacement reported in Figure 6.1, reaching displacements up to 10 mm in horizontal or vertical direction alone. Then, the effect is compared to the best case scenario for the actual geometry, corresponding to plots 6.10b and 6.12b. In this case, the global displacement is sensibly smaller for the reported example of $x = 10$ cm. The results presented in these plots suggest that, in simulations, the field cage design would be able to satisfy the required levels of field homogeneity.

## 6.6 Application of electric field map to Cosmic Rays

After the implementation of the electric field map in oaUtility package, the next step is to apply the related correction to the Cosmic Rays data. The linear fit procedure presented in section 6.2 is repeated on the same run after the application of the electric field map correction. Residuals distributions in Figure 6.16 show that the electric field map is effective in the correction of the relative horizontal displacement near the Cathode and it does not affect tracks in the region 60 cm $\leq x \leq$ 80 cm.

The results for the apparent curvature are reported in Figure 6.17, while the $\sigma$ of the distributions are reported in Figure 6.18. Therefore, the applied electric field map is reducing globally the apparent curvature showed in Figure 6.2. The four End-Plates show small differences probably due to differences in the structure of the field cages, since their production and the assembly of HA-TPCs were performed manually. Therefore, a possible improvement would be to implement a field map for every field cage. The application of the electric field correction has a positive impact also on the variance of the curvature, with large improvements especially in the Cathode region.

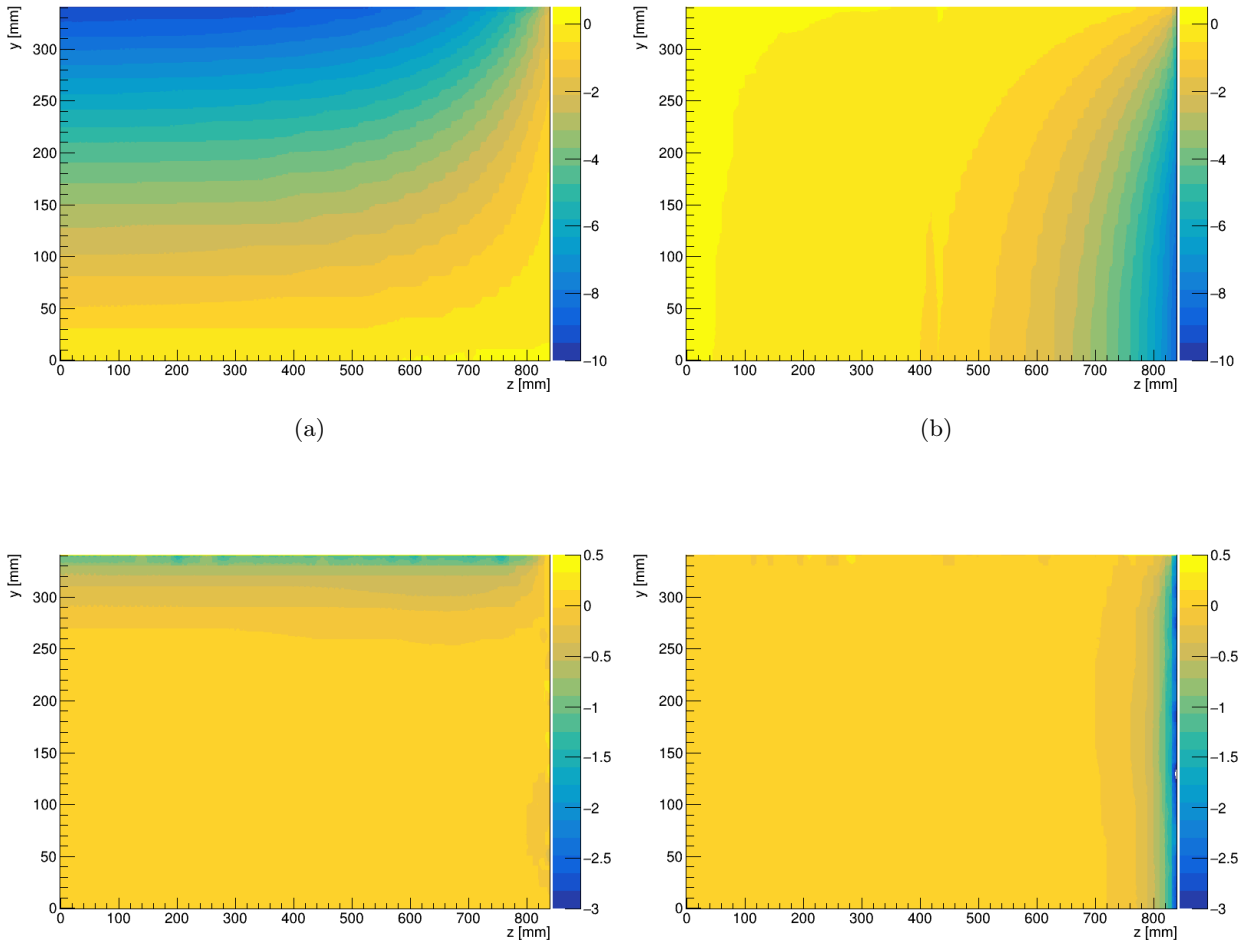


(a) (b)

(c) (d)

Figure 6.15: Global displacement for point-like charges starting at $x = 10$ cm on the two top right ERAMs being (0,0) the center of the module frame. The top row shows the absolute displacement in $\Delta y$ (left) and $\Delta z$ (right) coordinates between the starting and ending point of the drift trajectory in the actual HA-TPC setup. Bottom row shows the correspondent effects for the map in which the potential decrease in homogeneity is improved. The color range is reported in mm and it changes from top row to bottom row in order to visually enhance the effect.

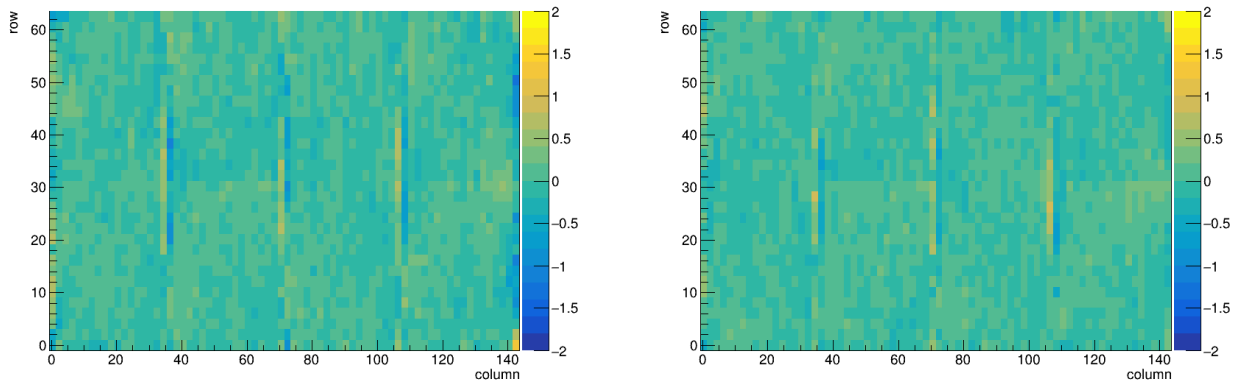


(a) (b)

Figure 6.16: Residuals distribution for vertical tracks, with system of reference rotated, such that residuals are evaluated as horizontal displacement $\Delta z$ in the usual ND280 coordinates. Figure 6.16a represents tracks less than 20 cm away from Cathode, while Figure 6.16b refers to tracks between 60 cm and 80 cm away from Cathode for tracks in which the electric field corrections are applied. Scale in mm.

The evaluation of the electric field correction performances might be estimated also by looking at the spatial resolution for local subsets of pads, grouped together for the lack of a reasonable amount of data. The spatial resolution is defined as the $\sigma$ of the Gaussian distribution which is used to fit the residuals distribution of the local cluster estimator with respect to the overall helix fit 2D projection on the ERAMs plane.

## 6.7 Impact of electric field inhomogeneity on timing

The homogeneity of electric field is fundamental also for the timing reconstruction in HA-TPCs. The inhomogeneity of electric field might act on drifting electrons for two different reasons: (i) presence of transverse field and (ii) change in the magnitude of the field. Considering only the transverse field action, drifting electrons might be reconstructed with delay due to the additional length travelled with respect to a straight line parallel to the drift direction. The change in the electric field magnitude modifies the drift velocity, which for a *small* deviation from the ideal value is a linear relation. An in depth study of the drift velocity in the T2K gas is reported in [129]. Plot 6.7 shows that the magnitude of the electric field changes near the Cathode from few percent up to at least 5% near the corners. The drift velocity and the diffusion coefficients in the T2K gas for NTP conditions (T=293.15 K and p = 1 atm) are simulated in the absence of magnetic field using the `Magboltz` library interfaced with Garfield++[130]. The nominal voltage has been set to E = 270V/cm and values down to 50% are simulated and are reported in Figure 6.19, with finer steps near the nominal values. Results show that the drift velocity changes relatively slower than the electric field, but the effect is not negligible for long drift distances. For example, a change of 1% in the drift velocity for a drift distance of 90 cm corresponds to a change in the time of arrival of about 100 ns, for a displacement in the reconstruction of $\Delta x \sim 8$ mm from its true position. Such differences might be reached close to the Cathode or near the walls.

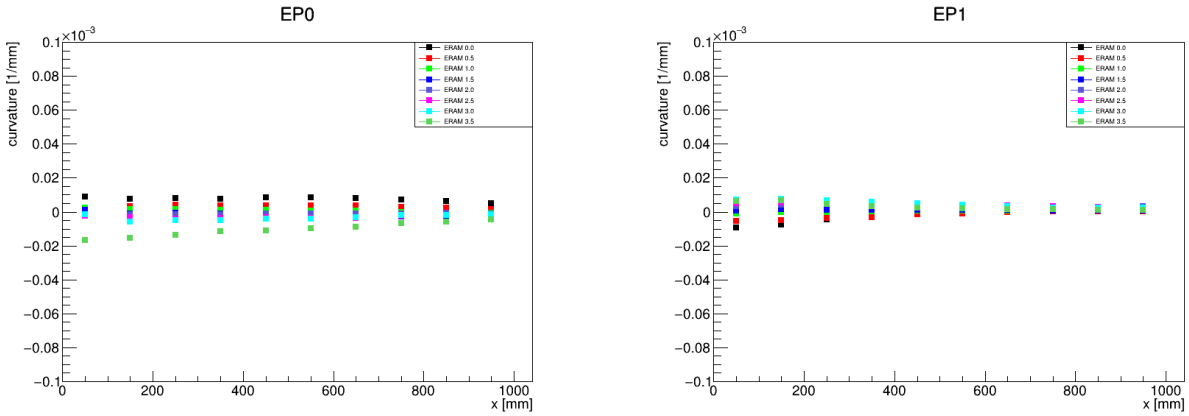


(a)




(b)

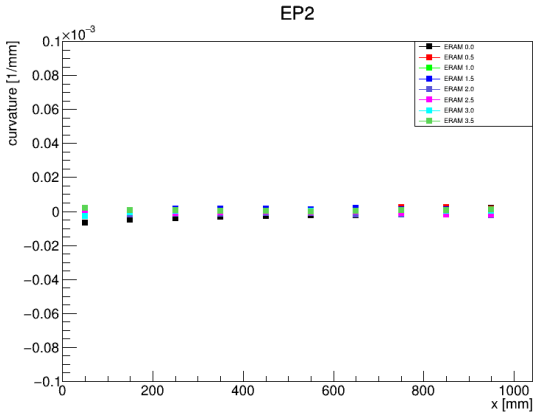


(c)

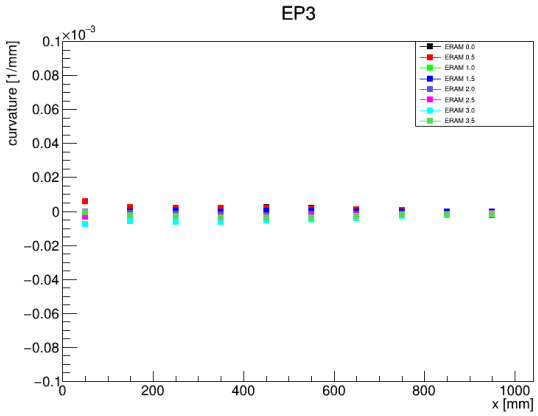


(d)

Figure 6.17: Centroid of a gaussian fit for apparent curvature distribution after the application of electric field correction for tracks passing in bottom HA-TPC EP0 (6.17a) and EP1 (6.17b) and top HA-TPC EP2 (6.17c) and EP3 (6.17d).

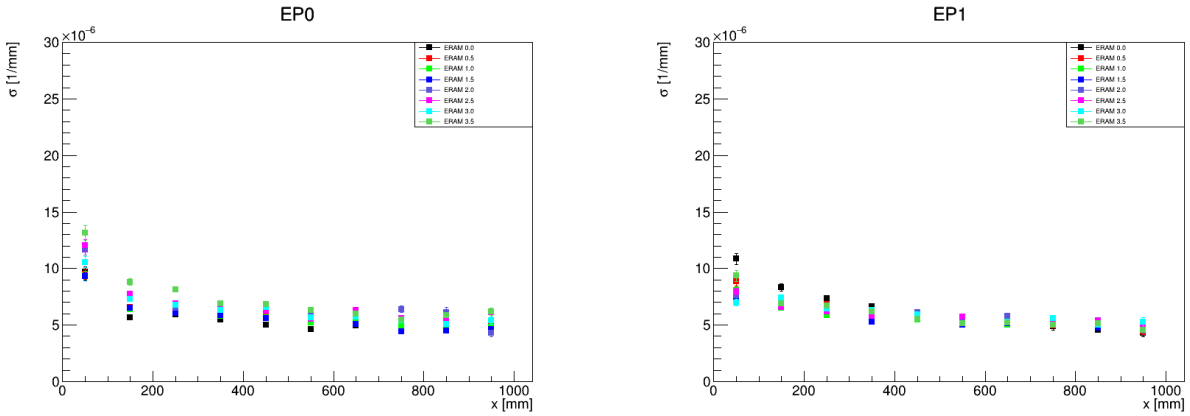


(a) (b)

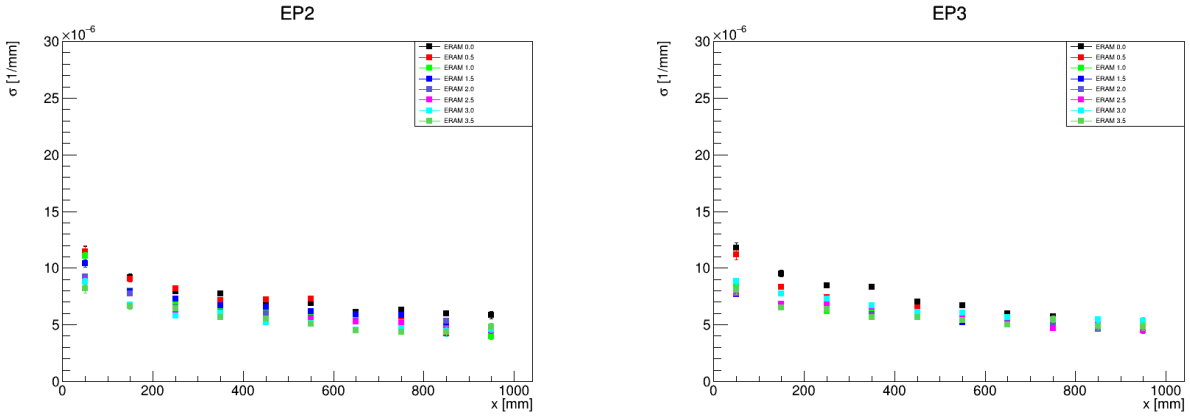


(c) (d)

Figure 6.18: Sigma of a gaussian fit for apparent curvature distribution after the application of electric field correction for tracks passing in bottom HA-TPC EP0 (6.17a) and EP1 (6.17b) and top HA-TPC EP2 (6.17c) and EP3 (6.17d).

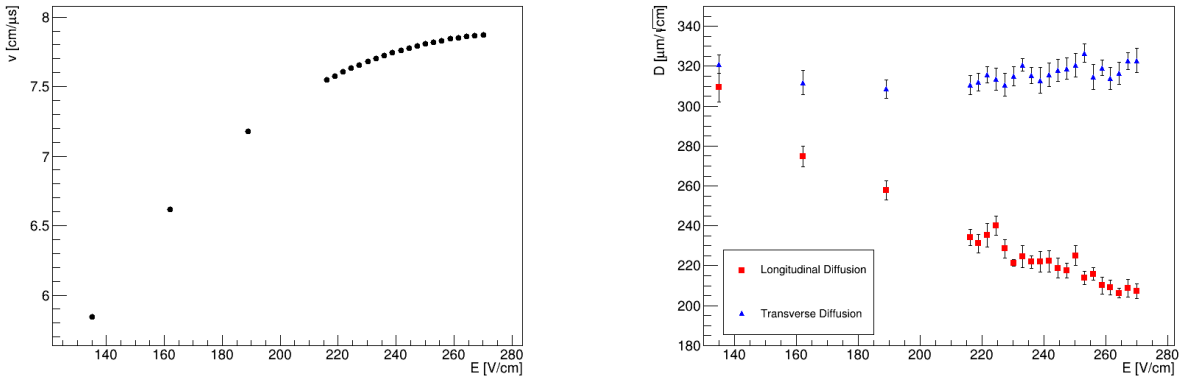


(a) (b)

Figure 6.19: Simulated drift velocity (left) and diffusion coefficients (right) in T2K gas for NTP conditions and no magnetic field.

### 6.7.1 Effects on a point-like charge

Using the same numerical simulation implemented for evaluating the transversal displacement, a similar procedure can be repeated for evaluating timing displacements in several points of the TPC using a much finer step of 10 $\mu$m. In plots 6.20, the difference in drift time for a point-like source in distorted and ideal electric field are reported for starting planes $x = 5$ cm and $x = 10$ cm, which are in the region where the electric field magnitude is visibly changing in 6.7. The plots suggest that the difference between the first and last arriving electrons might reach few nanoseconds, much smaller than the sampling time of 40 ns. Considering tracks in the yx plane, the discretization due to time binning is quite large with respect to the yz plane: 1 time bin $\sim$ 3 mm, therefore the resolution is expected to be worse than in the ERAM plane. Additionally, the region up to 10 cm from the Cathode shows a great change in the residual distribution as reported in 6.20, so it would be possible that space regions in which electrons might be delayed (e.g. x=5 cm) and regions where electrons might arrive early (e.g. x=10 cm) level the residual distribution hiding local biases in an apparent unbiased distribution.

## 6.8 Future investigation of electric field with FC0

The refurbishment of FC0 was an important milestone to give the possibility of creating an additional TPC, with geometry very similar to the ones installed at J-PARC. There are three main differences: (i) the installation of a G10 panel over the Twaron layer, (ii) the gluing procedure for the strip foil and (iii) the fact that the TPC will have a single field cage instead of two.
Currently, the idea of probing the electric field map with FC0 is under examination. With the help of a LASER source, it would be possible to ionize the gas with extreme accuracy and precision using UV light, installing a quartz window in place of one of the eight ERAMs in the module frame as entrance point. The LASER source might be redirected internally using carefully placed mirrors. A schematic view of the setup is shown in picture 6.21a. The TPC is closed using a G10 cover as reported in Figure 6.21b.

The main challenge consists in recreating the same electric field configuration with a single field cage instead of two. A COMSOL based simulation was performed to illustrate the main difference

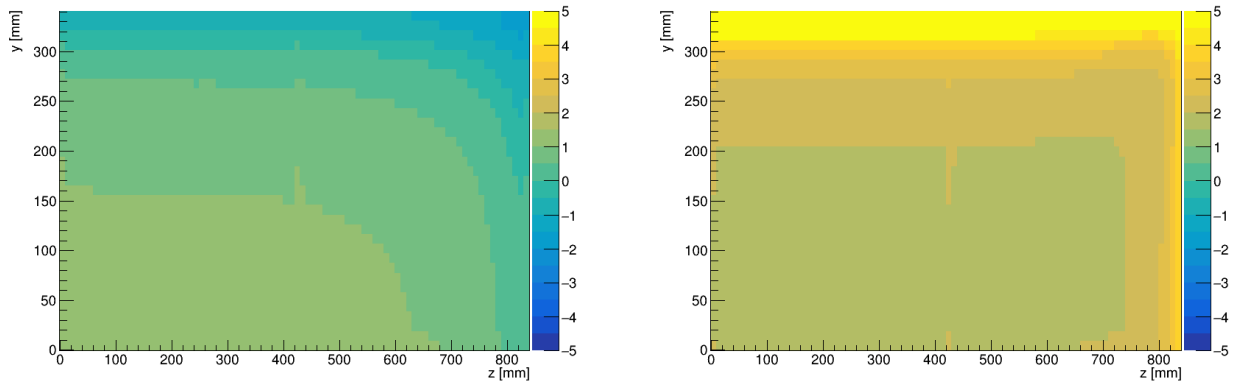


(a) (b)

Figure 6.20: Difference in time of arrival for a point-like source moving in the simulated electric field map and in an ideal electric field, starting at $x = 10$ cm (left) and $x = 5$ cm (right). Color scale is expressed in nanoseconds.

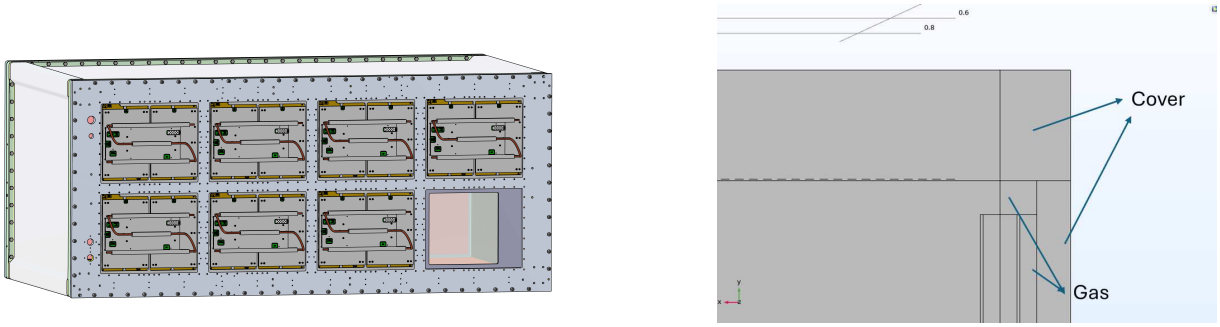


(a) (b)

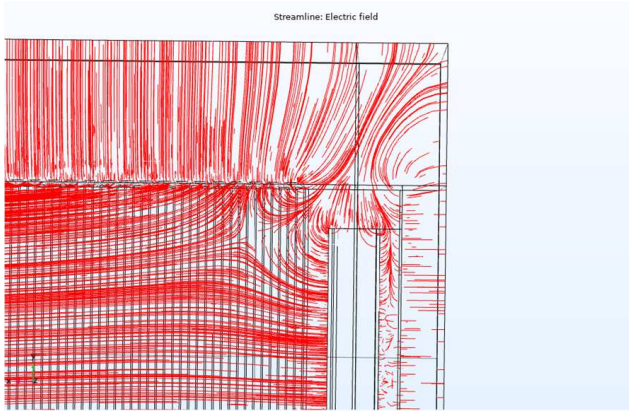


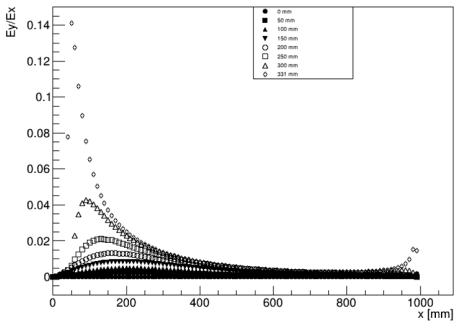


(c) (d)

Figure 6.21: On the left, drawing of a possible configuration of a TPC based on FC0 for the study of electric field distortions is shown, in which a quartz window is installed in place of an ERAM. On the right, the field lines for plane z=0 on the Cathode region for FC0 and a G10 cover are reported.

between the two setups. The first attempt to recover the symmetry condition was to simulate the presence of a conductive layer on the inner side of the cover 5 mm away from the copper layer of the Cathode. This additional electrode is introduced in such a position since the first strip on the other side is at the same potential of the Cathode 8 mm away from the correspondent copper layer. A visual representation of the electric field lines from the central plane z=0 is reported in Figure 6.21c, in which the geometry near the Cathode region is visible. As in previous simulations for the actual geometry of HA-TPCs, the Cathode is 12 mm away from walls and it is 7 mm long in both sides in x direction. In the simulation, the ground condition was place all along the external surface as a safety measure during the data taking. Differently from the results shown in 6.8, the field lines are not following the flange direction for x=0, but are moving partly on the negative direction of x-axis. This effect is believed to arise from the loss of symmetry condition and improvements on such conditions are under examination. Nevertheless, the evaluation of the transversal component of the electric field has shown that a clear difference with respect to the HA-TPCs electric field is visible only up to few centimeters from the walls and near the Cathode as reported in Figure 6.21d. The comparison of the actual configuration (left) and single FC0 (right) shows that just with the addition of an electrode on the inner part of FC0 cover the transversal components are compatible already after 5 cm from the walls.

## 6.9 Impact of electric field map correction with magnetic field

The ultimate goal of the electric field study and correction is to minimize any bias in the momentum reconstruction due to the known features of the field cages presented in the previous sections.As a test for evaluating the effect of the newly implemented map, the bias on momentum reconstruction for simulated data in which both electric and magnetic fields distortions are applied to detResponseSim and corrected in hatRecon is reconstructed. A comparison is performed with the application of only magnetic field distortion in oaUtility to the same output of GEANT4, while E is assumed ideal. The MC data consists of muons or anti-muons in a momentum range between 200 MeV/c up to 3000 MeV/c with a uniform distributions. Selected events are required to have at least 50 clusters and are divided into two groups based on their $z$ coordinates, separated by the central symmetry plane: positive and negative coordinates, depending if their $z$ coordinate is larger or smaller than the $z$ of the symmetry plane. In order to accentuate the effect of deformation, only tracks detected by the four ERAMs close to the vertical walls are selected. The momentum bias is defined as the centroid of the relative difference distribution between the reconstructed $p_{reco}$ and $p_{true}$ momenta:

$$\Delta p = \frac{p_{reco} - p_{true}}{p_{true}}. \tag{6.2}$$

The distributions are divided in 5 subsets in step of 200 mm in the $x$ axis, starting from 0. The events are divided according to their true momenta. In the range 200 MeV/c $\leq p_{true} \leq$ 1000 MeV/c, particles have a momentum similar to the expected events from Neutrino Beam, however their curvature due to the B field are comparable with the apparent curvature seen in Figure 6.2. In the range 1000 MeV/c $\leq p_{true} \leq$ 3000 MeV/c, the apparent curvature should be the dominant effect, but such events are more rare in ND280. In every case reported in Figures 6.22, 6.23 the momentum bias is negative near the Cathode. The effect is not yet understood, but it is in agreement with the results where E field is assumed ideal (Figures 6.22b and 6.23b).

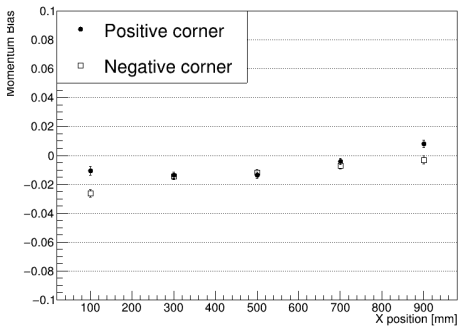


(a)

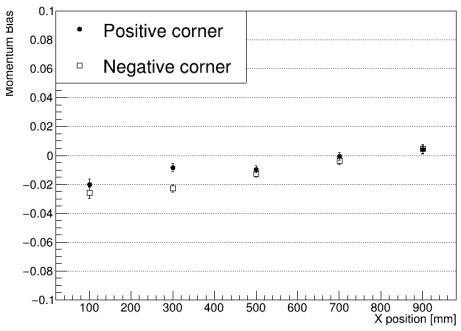


(b)

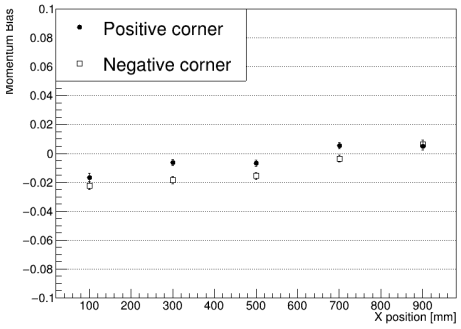


(c)

Figure 6.22: Momentum bias for MC data in which 200 MeV/c $\leq p_{true} \leq$ 1000 MeV/c for muons using the E field map (6.22a) or ideal E field (6.23b. The bottom plot (6.22c) refers to anti-muons using E field map. Positive corner refers to the downstream corner, while negative one is the upstream corner.

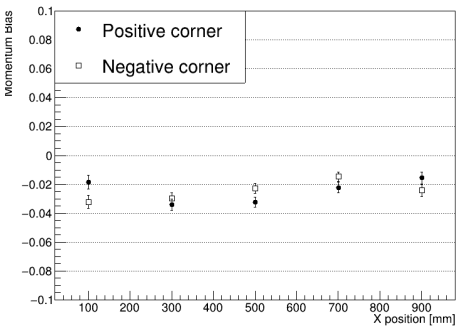


(a)

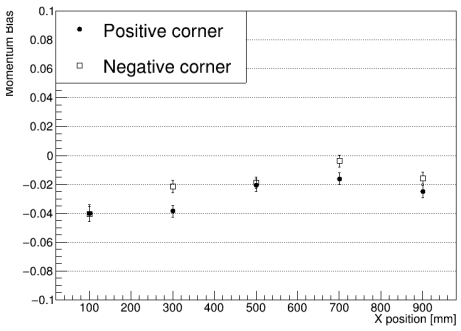


(b)

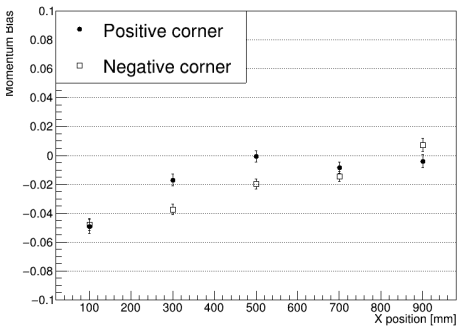


(c)

Figure 6.23: Momentum bias for MC data in which 1000 MeV/c $\leq p_{true} \leq$ 3000 MeV/c for muons using the E field map (6.23a) or ideal E field (6.23b. The bottom plot (6.23c) refers to anti-muons using E field map. Positive corner refers to the downstream corner, while negative one is the upstream corner.

## 6.10 Summary

The reconstruction of cosmic rays in the HA-TPCs revealed unexpected deformations near the cathode. To investigate the cause, two hypotheses were considered: (i) space charge effects, which were ruled out based on a rough estimation of their expected magnitude, and (ii) electric field distortions, resulting from the field cage design changes required to cancel the risk of electrical breakdown in the flange region around the central Cathode of the HA-TPC.

A COMSOL-based simulation of the field cages was performed implementing the actual electric potential configuration and the most accurate field-cage geometry description derived from metrology measurements, and a precise electric field map was generated. Applying a correction based on this map during the track reconstruction stage significantly improved track measurements and in particular canceled the distortions.

These studies revealed that the distortions observed in straight tracks were caused by an imperfect matching of the electrical potentials applied to the cage electrodes. Specifically, maintaining the first strip at the same potential as the Cathode, despite its slight displacement along the nominal direction of the electric field, introduced these distortions. This aspect was clearly overseen and unfortunately, the tight schedule for HA-TPCs installation at J-PARC limited the commissioning phase at CERN, preventing the detection of these distortions with sufficient statistics. The issue was identified during commissioning at J-PARC, where hardware intervention, namely soldering a properly defined resistor in order to match the voltage drop between the first strip and the Cathode, was infeasible.

However, the issue was greatly improved by implementing a correction for track deformations in the reconstruction stage, as detailed in this thesis. Ongoing studies aim to accurately evaluate residual effects and potential systematic biases introduced by the correction method, such as those arising from the reconstruction algorithm. These studies include measurements on a TPC equipped with the repaired field cage FC0, using straight tracks generated both at CERN test beams and by a Q-switched UV laser source, which provides highly accurate and reproducible track impact and pointing precision. Hence, they offer a robust basis for direct comparison between experimental data and simulation results.

Despite the application of electric field corrections, some anomalous behaviors persist especially as timing deviations from the expected trajectory. At the time of this thesis submission, potential causes of these deviations are still under investigation. One possibility is local variations in electric field intensity, which could lead to significant changes in the magnitude of the electrons drift velocity.

As illustrated in Figure 6.19a, the relationship between drift velocity and electric field intensity in a gaseous medium is nonlinear. As a consequence, while at different electric field intensities the ratio between transverse and longitudinal components remains constant, so that transverse track distortions should not change, on the contrary longitudinal distortions may vary at different electric field intensities.

Datasets at several electric field intensity have been recently collected, and will be analyzed in order to evaluate the impact of not-uniform electric field at nominal potential. In addition the effects of drift velocity as a function of electric field will be included in both reconstruction and simulation in order to cope with such distortions.

Another possible source of error could arise from the interplay between electric and magnetic field corrections, particularly in how *ExB* effects are handled. Even minor discrepancies between simulated and actual field configurations can introduce biases, especially in regions with strong local electric field variations, such as near the cathode or detector walls.

# Chapter 7

# Track reconstruction with Multi-Layer Perceptron

The track reconstruction for HA-TPCs, as discussed in Chapter 3, is based on grouping pads into clusters to estimate the local trajectory points of tracks. Each pad's signal is recorded as a waveform over several microseconds; however, the current reconstruction approach utilizes only limited information – specifically, the waveform's maximum value and its corresponding sampling time. Two validated reconstruction algorithms are currently employed for HA-TPCs: (i) the Pad Response Function (PRF) method[117][98] and (ii) the so called *log(Q) method*, described in Chapter 3. Both techniques rely on an empirical relationship between a pad's signal and the track position relative to a cluster, with parameters finely tuned using test beam and cosmic ray datasets.

The primary goal of the work described in this chapter is to develop an improved reconstruction method based on two key aspects:

- A simplified clustering approach
- The utilization of additional information from each pad's waveform

This new method, referred to as the *3×3 method*, seeks to maintain the approach of leveraging the relationship between pad signals and track positions, derived either from data or a simplified model. This work aims to assess the potential impact of implementing a Machine Learning (ML) algorithm on the spatial and momentum resolution of HA-TPCs. Rather than depending on an empirical function, the ML approach is expected to quantitatively determine the relationship between waveform amplitude and timing and the track position.

The new clustering method and algorithm are outlined in Section 7.1 and discussion about the core of the method – i.e. the Machine Learning component of the algorithm – is presented in dedicated Sections 7.2 to 7.6.

Results concerning the overall performance of the new algorithm on simulated tracks are discussed in Sections 7.7 and 7.8, and eventually preliminary results on real track data are discussed in Section 7.9.

## 7.1 Outline of the Method

The track reconstruction developed within the present thesis work is performed according to the following steps, where track preparation procedures are retained from basic pre-reconstruction phase,

as described in Chapter 3, including preliminary primary pads finding, while the new method diverges from the log(Q) method from the subsequent first clustering step.

In the first step, clusters of interest are defined around the primary pads using a simple pre-reconstruction algorithm. Clustering stage is described in Section 7.1.1. Second step, for each cluster, parameters are estimated to provide input to the machine learning algorithm, which in turn yields the local *slope-intercept* line parameters for each cluster. Input parameters are discussed in Section 7.1.2. The Machine Learning method implementation and performance evaluation are discussed in detail in Sections from 7.2 to 7.6. Third step, for each leading pad, the best segment representing the track crossing the pad is estimated by considering all clusters containing that pad and averaging the local points (to obtain the best point for that pad) along the local line that is closest to the center of the pad. Finally, the track is reconstructed by combining the best segments corresponding to the primary pads and fitting the best points with a helix. This step is outlined in Section 7.1.3

### 7.1.1 Clustering

In the log(Q) reconstruction method, pad clustering follows different patterns based on the local track direction: horizontal, vertical, diagonal up, and diagonal down. This clustering method leverages information from the two "secondary" pads located in the transverse direction with respect to the track, which are adjacent to the "primary" pad crossed by the track. In other words, the cluster extends the pad information along the transverse direction to improve the track's transverse position. This approach is inherited from the early applications of resistive MicroMegas in collider detectors, where due to track topology and bending in the (r,$\phi$) transverse plane, pads are smaller in the azimuthal direction than in the radial direction. This difference in granularity is necessary because the azimuthal direction is typically transverse to the track and requires finer spatial resolution. In the case of the HA-TPC, however, there is no such difference between the two directions of the bending plane (the (Y,Z) transverse plane), and pads are accordingly square in shape.

In order to simplify clustering, improve the approach, and adapt it to the HA-TPC square-shaped pads, an alternative clustering method was developed. Instead of predefined patterns, each pad is grouped with its eight neighboring pads, forming a 3×3 matrix. This matrix incorporates all adjacent pads, including those that did not register a signal above the threshold, ensuring a simpler and uniform clustering pattern. The labeling of each pad within a cluster is illustrated in 7.1a, providing a standardized reference framework. With this approach, clusters consistently maintain always the same shape, regardless of the local track direction, and partially overlap with one another. An example of clustering applied to a 4×4 grid is shown in Figure 7.2, where four clusters are identified.

Since the new clustering method constructs a grid extending equally in both dimensions, the reconstruction goal shifts from estimating a single point along the track transverse direction, to identifying the line that best approximates the local segment of the track trajectory. Because a line is defined by two parameters, the algorithm must establish a relationship between these parameters and the signals recorded by the nine pads within each cluster.

A line can be mathematically represented in various forms, with the commonly used *slope-intercept* form being one of them:

$$y = mz + q. \tag{7.1}$$

By introducing a local coordinate system where the center of the middle pad (pad 4 in figure 7.1a) is taken as the origin, this representation offers the advantage of directly capturing the local trend of the line and its position relative to the cluster center. However, the slope value becomes prob-

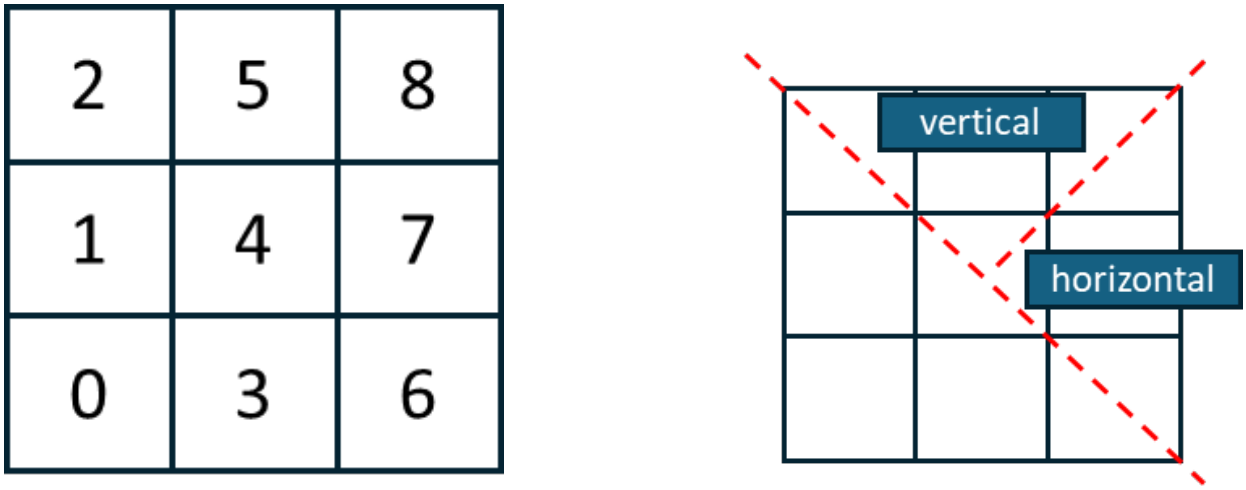


(a) (b)

Figure 7.1: On the left, pads labeling in a cluster is reported. On the right, the two types of clustering are reported: if in the standard ND280 system of reference the slope of the local line approximation is such that $-1 \leq m_{yz} \leq 1$ the cluster is *horizontal*, otherwise it is *vertical*.

lematic for vertical tracks, where $m \to \pm\infty$. To constrain the range of possible values for $m$ and $q$, a rotation of the local coordinate system is applied when $|m| > 1$, thereby distinguishing between *horizontal* and *vertical* orientations for the clusters, as shown in figure 7.1b. This distinction requires additional input, which can be computed in the same manner as in the log(Q) method. Since standard clustering is necessary for the $WF_{sum}$ method for estimating the track energy loss density ($dE/dx$), the local orientation is determined from the output parameters of the helix derived from the log(Q) algorithm.

Other possible representations of a line may not require this additional step. For example, the $(d, \phi)$ representation, where $d$ is the perpendicular distance of the line from the center of the cluster and $\phi$ is the angle of the track relative to the local horizontal axis ($\phi \in [0, 2\pi]$). However, in this representation, if $d \to 0$, a small shift in position results in a large change in the angle, with $\phi \to \phi \pm \pi$, depending on the sign of the *intercept*. Given these considerations, the *slope-intercept* form is chosen for the representation.

Including the change of system of reference, the slope is in the interval $m \in [-1, 1]$ and the intercept does not have a clear cut, but rarely exceeds 20 mm considering the local system of reference.

### 7.1.2 Input parameters to ML algorithm

The signal recorded by each pad within a cluster is considered, and as for other algorithms, the maximum of the waveform is included as one of the parameters used in the reconstruction. The shape of the waveform is taken into account by computing the Full Width at Half Maximum (FWHM). To minimize the effect of noise on the FWHM estimation, the rising and falling sides of the waveform are fitted with a linear function. The timing corresponding to $Q_{max}/2$ is then extracted, and the FWHM is estimated as shown in figure 7.3. Furthermore, since the fit is sometimes unreliable at low amplitudes, FWHM information is rejected when $Q_{max} < 80$ ADC FWHM is typically larger for secondary pads, where they are not directly hit by electrons from the avalanche, and the induced

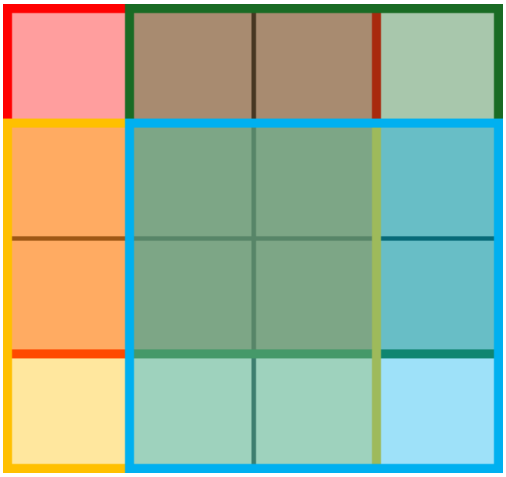

Figure 7.2: Examples of clustering of a 4×4 grid. Four clusters are found and drawn in different colors, with regions of partial overlap between them.

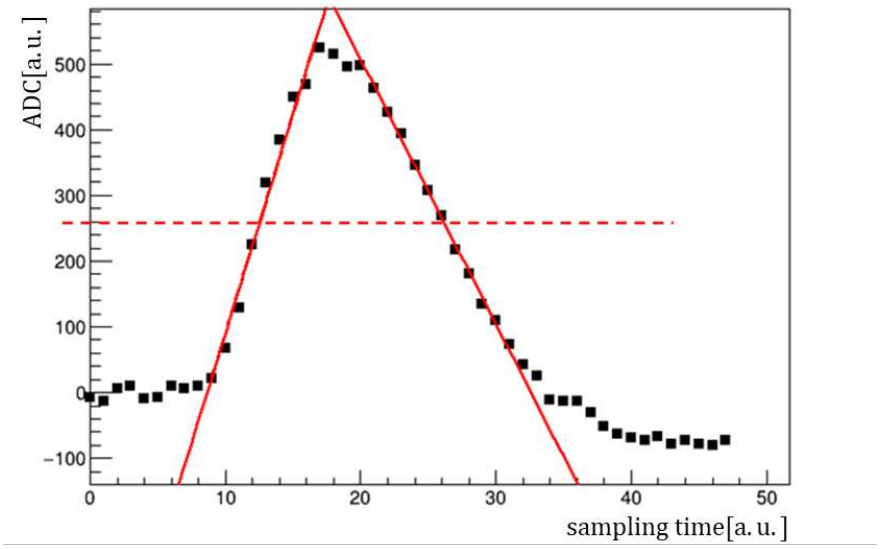


Figure 7.3: Example of FWHM estimation for a waveform in a pad. The FWHM is computed as the time interval between the instersection points of the dashed line with the solid lines.

signal is instead generated by charge spreading. In contrast, for primary pads, where the induced signal is generated directly by the avalanche, FWHM is generally smaller. The minimum value of FWHM is determined by the response shape of the analog electronics chain used to read out the pad. Since FWHM has a minimum possible value, it is less sensitive to fluctuations in ionization within the gas.
Pads with no signal above the threshold are also included in clusters and are assigned values of $Q$ and $FWHM$ equal to 0. For pads with recorded signals, the reciprocal of the FWHM is used, to maintain a consistent trend across all pads. This ensures that for $Q \to 0$ the shape parameter $1/FWHM \to 0$, mirroring the behavior of pads with no signal. This approach improves the pattern recognition capabilities of the Machine Learning algorithms.
In summary, for track reconstruction on the transverse plane, a total of 18 parameters are collected for the reconstruction algorithm. These include 9 waveform maxima, denoted as $q_0, q_1, ..., q_8$, based on the pad labeling in Figure 7.1a, and 9 reciprocals of the FWHM, referred to as $f_0, f_1, ..., f_8 = 1/FWHM_0, 1/FWHM_1, ..., 1/FWHM_8$.
For the reconstruction of the track along the drift distance, the third coordinate is determined by taking the time of the maximum in specific pads, as will be explained later in the chapter.

### 7.1.3 ML algorithm output parameters processing and track fitting

Once the local line parameters are obtained for each cluster, it is necessary to determine space points to perform the helix fit. As discussed about the log(Q) method, the leading pads provide most relevant and always reliable timing information. At this stage, for the present method, with respect to preliminary track preparation definition, the leading pads are re-defined by retaining only pads with amplitude above a threshold. This new definition being consistent with the new clustering method.

Then, For each newly defined leading pad, the closest point from the center of the pad to the estimated local line is found. Since a leading pad may belong to multiple clusters, the estimated points are averaged using a weighted $w$ scheme: $w = 8$ if the pad is at the center; $w = 4$ if the pad is at position 1, 3, 5, or 7; and $w = 3$ if the pad is at position 0, 2, 6, or 8 (corner positions). A visual representation of these operations is shown in figure7.4. Successively, a second cut is performed to exclude wrongfully identified leading by requiring that the related local point estimator lies on the pad surface less than 5 mm away from the pad center.
The information on the ERAM plane is combined with the timing of the maximum for the leading pad and the three dimensional helix fit is performed. The next section is dedicated on method used for the estimation of the local line parameters for each cluster.

## 7.2 The Multi Layer Perceptron (MLP)

As already anticipated, the estimation of local track parameters is performed by considering the expected circular track as a line in the surface of a cluster. Therefore, the algorithm is required to use the 18 input parameters to extract the 2 output parameters

$$\{q0, ..., q8, f0, ..., f8\} \to \{q, m\}. \tag{7.2}$$

Instead of using a user defined empirical formula such as in PRF and log(Q) methods, the new approach considered in this chapter consists in using a Machine Learning algorithm which should be able to identify a relation between the input and output parameters.

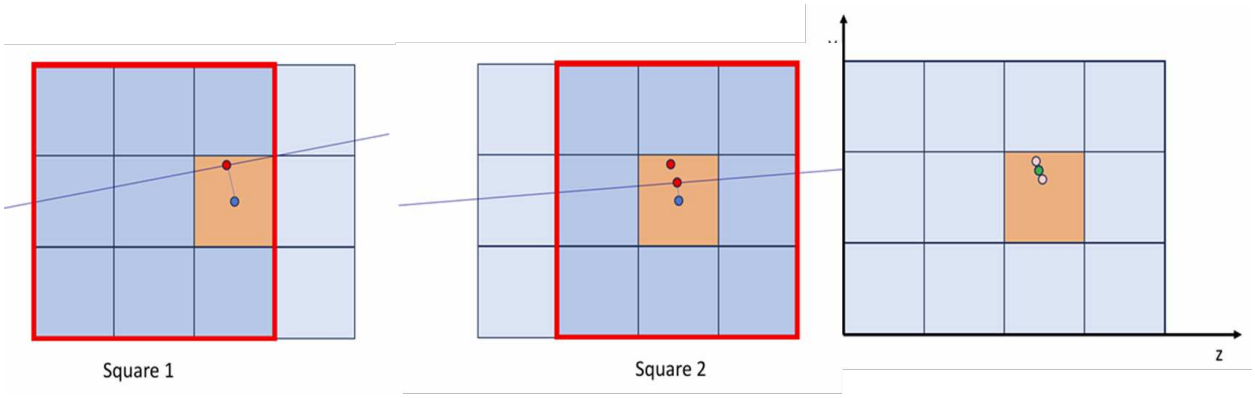


Figure 7.4: Schematic view on how a point-like estimator of the track is computed for each single leading pad (orange). Top left plot shows the closest point on the estimated line for the first cluster where the leading pad appears, while the middle plot shows the same estimator for a different cluster. Notice how the same leading pad is placed differently in the two clusters. The average of such positions is the final estimator for the leading pad.

The problem falls in the *regression* category and uses a rather limited amount of parameters, for this reason a basic algorithm is chosen: the Multi Layer Perceptron. In addition, MLP method is supported by the Toolkit for MultiVariate data Analysis (TMVA) [131] developed for CERN ROOT. Since ND280 Software extensively uses CERN ROOT framework, the advantage of developing a ML algorithm using TMVA is due to the fact that no additional libraries are required and it can be easily implemented in HA-TPC reconstruction project.
The Multi Layer Perceptron algorithm is formed by a series of interconnected neurons, which are entities that produce a certain scalar response to a given set of input signals. Therefore, it is a mapping from the space of the input parameters $x_i$ to the space of the output parameters $y_j$. The mapping is defined as *non-linear*, since the neurons have a *non-linear* response to their inputs. The behavior of a neural network (NN) is determined by the layout of the neurons, their interconnections and their response to the input which depends on the *neuron response function* $\rho$.
A network with $n$ neurons might present up to $n^2$ connections, but in MLP case the neurons are organized in series of layers and each neuron in a layer is allowed to communicate with each neuron in the previous and successive layer, thus reducing the *complexity*. In MLP, the first layer is the *input layer*, the last layer is the *output layer* and the layers in the middle are named *hidden layers*. An example of a MLP network with 4 input variables, 1 hidden layer and 1 output variable is reported in figure 7.5.

### Neuron response function

The neuron response function $\rho$ maps the neuron inputs onto the neuron output. Often, it can be separated in a *synapse function* $\kappa\ \mathscr{R} \to \mathscr{R}$ and a *neuron activation function* $\alpha$, such as $\rho = \alpha \circ \kappa$. Considering a single neuron $j$ in layer  with $n$ input connections, to each connection a weight $w$ is

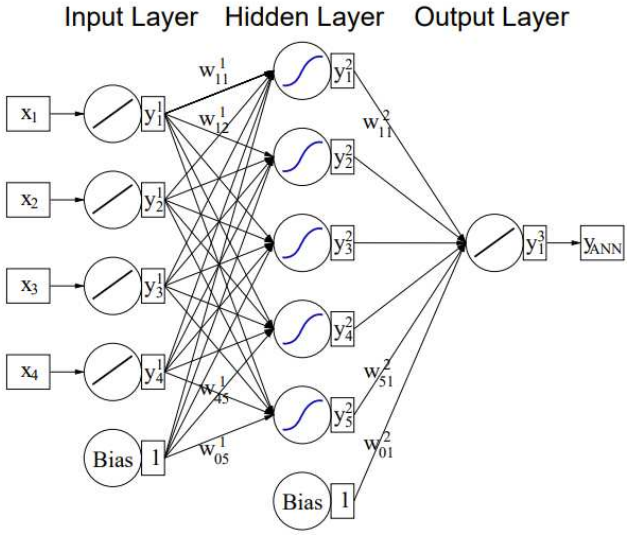


Figure 7.5: Example of a MLP network with 4 input parameters and 1 output. Picture from [131].

assigned, hence the $\kappa$ function might assume one of the following forms:

$$\kappa : \left(y_1^{(\ell)}, .., y_n^{(\ell)} \mid w_{0j}^{(\ell)}, .., w_{nj}^{(\ell)}\right) \rightarrow \begin{cases} w_{0j}^{(\ell)} + \sum_{i=1}^{n} y_i^{(\ell)} w_{ij}^{(\ell)} & \text{Sum} \\ w_{0j}^{(\ell)} + \sum_{i=1}^{n} \left(y_i^{(\ell)} w_{ij}^{(\ell)}\right)^2 & \text{Sum of squares} \\ w_{0j}^{(\ell)} + \sum_{i=1}^{n} \left|y_i^{(\ell)} w_{ij}^{(\ell)}\right| & \text{Sum of absolutes.} \end{cases} \tag{7.3}$$

On the other hand, $\alpha$ might assume on of the following forms:

$$\alpha : x \rightarrow \begin{cases} x & \text{Linear ,} \\ \frac{1}{1+e^{-kx}} & \text{Sigmoid ,} \\ \frac{e^x - e^{-x}}{e^x + e^{-x}} & \text{Tanh ,} \\ e^{-x^2/2} & \text{Radial. .} \end{cases} \tag{7.4}$$

### Network architecture

The number of hidden layers and of neurons can be modified, keeping in mind two rules: (i) the Weierstrass theorem applied to NN ascertains that in a MLP a single layer is sufficient to approximate a given continuous correlation function to any precision with a large enough number of neurons. However, if the dataset for training the NN is large enough, using more layers might achieve an optimal result with potentially less neurons and training time.

### Network training

The most common algorithm for adjusting the weights in a NN is called back-propagation (BP). Considering a NN with a single hidden layer with a Tanh activation and a linear activation in the

output function, its output is given by:

$$y_{\mathrm{ANN}} = \sum_{j=1}^{n_{\mathrm{h}}} y_j^{(2)} w_{j1}^{(2)} = \sum_{j=1}^{n_{\mathrm{h}}} \tanh\left(\sum_{i=1}^{n_{\mathrm{var}}} x_i w_{ij}^{(1)}\right) \cdot w_{j1}^{(2)}, \tag{7.5}$$

where: $n_{var}$ and $n_h$ are the number of neurons in the input layer and in the hidden layer; $w_{ij}^{(1)}$ are the weights between the input layer and the hidden layer; $w_{j1}^{(2)}$ are the weights between the neurons in hidden layer and the one in the output layer. For $\kappa$, a sum is used between the options available in 7.3.
In the *training phase*, $a = 1, ..., N$ training events are given and for each one of them the output value $\hat{y}_{ANN,a}$ is known. An *error function* $E$ is used for introduced for measuring the agreement between the network response with the desired one. One example of error function is given by the squared sum of all residuals:

$$E\left(\mathbf{x}_1, \ldots, \mathbf{x}_N \mid \mathbf{w}\right) = \sum_{a=1}^{N} E_a\left(\mathbf{x}_a \mid \mathbf{w}\right) = \sum_{a=1}^{N} \frac{1}{2}\left(y_{\mathrm{ANN},a} - \hat{y}_a\right)^2 \tag{7.6}$$

where $\mathbf{w}$ is the vector of weights in the NN. The search for the optimal set of weights that minimize the error function is estimated using the Broyden-Fletcher-Goldfarb-Shannon (BFGS) method. BFGS uses second order derivatives of the error function for adapting the synapse weights using an algorithm of four steps:

- the vector $D$ that represents the evolution between one iteration of the algorithm *(k-1)* to the next *(k)* is computed. Each synapse weight is an element of such vector. Meanwhile, the vector $Y$ that represents the vector of gradient errors is also computed:

$$\begin{aligned} D_i^{(k)} &= w_i^{(k)} - w_i^{(k-1)} \\ Y_i^{(k)} &= g_i^{(k)} - g_i^{(k-1)}, \end{aligned} \tag{7.7}$$

  where: $i$ is the synapse index, $g_i$ is the $i$-th synapse gradient, $w_i$ is the weight of the $i-$th synapse and $k$ is the iteration counter.

- The inverse of the hessian matrix $H^{-1}$ is approximated at the iteration $k$ as

$$H^{-1(k)} = \frac{D \cdot D^T \cdot \left(1 + Y^T \cdot H^{-1(k-1)} \cdot Y\right)}{Y^T \cdot D} - D \cdot Y^T \cdot H + H \cdot Y \cdot D^T + H^{-1(k-1)}. \tag{7.8}$$

- The change of the weights vector is estimated

$$D^{(k)} = -H^{-1(k)} \cdot Y^{(k)}. \tag{7.9}$$

- A new vector of weights is computed by using the *line search* algorithm: the error function is locally approximated as a parabola and an evaluation of the second derivatives is performed to find where the local minimum is expected. From such point, through a line in the parameters space whose direction is determined by the gradient of the error function, the absolute minimum is searched. The weights at the minimum are used for the next iteration. The learning rate can be tuned.

The advantage of BFGS method with respect to back propagation (BP) is the smaller number of iterations, however the computing time for one iteration is proportional to the squared number of synapses, hence large networks are penalized.
This kind of training is called *supervised learning*, since for any event used for training, the desired output is known and used in the training phase.

#### Bayesian extension of MLP

A good performance using MLP algorithm is a trade-off between flexibility of the network that might adapt to model complex functions and the avoidance of overfitting, a key concept explained in the next section. The risk of overfitting might be overcome by using simple networks, however this approach generally does not allow to reach optimal performances. The Bayesian extension of MLP is introduced to use more complex NNs, but keeping under control the overfitting at the price of a large computational time. This extension adds a *penalty term* to the error function E:

$$\tilde{E}(\mathbf{w}) = E(\mathbf{w}) + \alpha|\mathbf{w}|^2, \tag{7.10}$$

which effectively penalizes large weights, resulting in a reduced model complexity. The term is tuned by a parameter $\alpha$. This term is referred to as *Bayesian extension* since it is equivalent to add a Gaussian prior for the network weights, whose width is controlled by parameter $\alpha$. $\alpha$ is directly tuned by TMVA without the action of the user.

## 7.3 Overfitting and Underfitting

The main goal of a Machine Learning (ML) algorithm is to properly perform on a previously *unseen* and independent dataset with respect of the dataset used for training. The ability to perform well on previously unseen inputs is called generalization[132].

When training an ML model, two datasets are available: (i) the training set, which is used to train the neural network (NN) by minimizing the *training error* through the loss function; and (ii) the test set, which is used to evaluate the NN's performance on data that was not used for training. In an NN problem, the goal is to minimize the error on the test set, known as the generalization error or *test error*. Therefore, a fundamental assumption is that the training and test datasets are independent and identically distributed. The performance of an ML algorithm depends on its ability to minimize the training error while keeping the gap between the training error and test error as small as possible. These two aspects are linked to the concepts of underfitting and overfitting.
Underfitting occurs when the model is not able to obtain a sufficiently low error value on the training set. Overfitting occurs when the gap between the training error and the test error is too large. The user is able to control the underfitting or overfitting of a model by altering the algorithm *capacity*, which is its ability to fit a wide range of functions as shown in picture 7.6b. Machine learning algorithms will generally perform best when their capacity is appropriate for the true complexity of the task they need to perform and the amount of training data they are provided with as visually represented in figure 7.6a. The common strategy for improving the generalization of a ML model dates back to the *Occam's razor principle*: among competing hypotheses that explain known observations equally well, we should choose the "simplest" one.

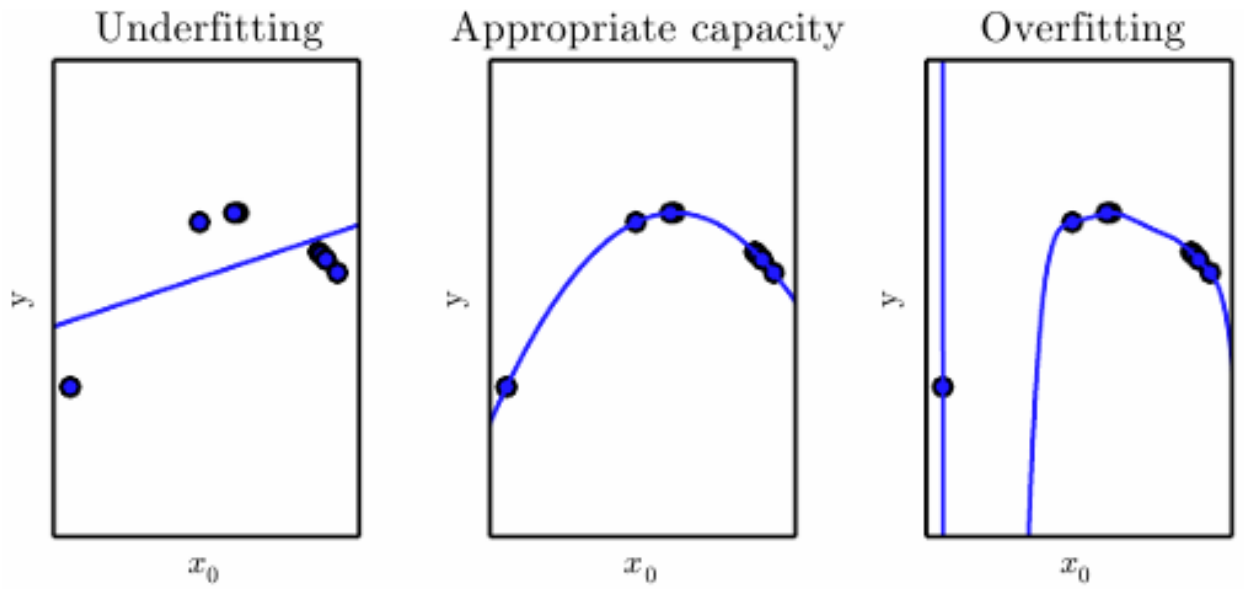


(a)

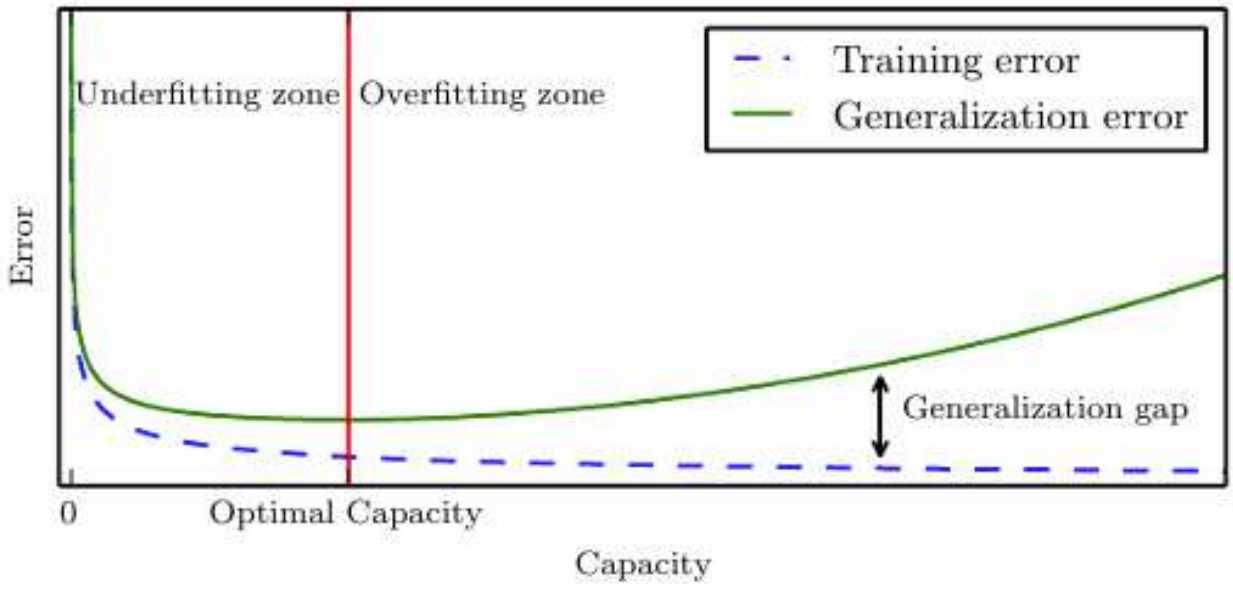


(b)

Figure 7.6: On top, three models are fitted to an example training set: (i) top left shows that a linear model suffers from underfitting; (ii) top central plot shows that a quadratic model is able to represent the curvature present in data; (iii) top right plot shows that a polynomial of a much larger degree ($9^{th}$ degree) suffers from overfitting. In the bottom plot, the typical trend of training and test errors as a function of capacity are reported is represented. For a model with small capacity both training and test errors are high, a typical property of the underfitting regime. At larger capacities the test errors firstly reduces but then it starts to increase again, meanwhile the training errors continue to slowly decrease. The increasing generalization gap for algorithm at high capacity represents the overfitting phenomenon. Pictures from [132].

## 7.4 Generation of training and test datasets

The generation of training and test datasets was performed using ND280 software packages presented in chapter 3. Since in clusters the circular trajectories are approximated as linear, the simulated data were performed with no Magnetic field. In this way, the true information can be fitted with a line and the true position of the tracks are known with high precision and accuracy. Muons in the momentum range between 300 MeV to 3000 MeV were simulated parallel to the ERAMs plane starting at a drift distance of about $x = 50$ cm. Considering a possible parameters range equal to $m \in [-1.2, 1.2]$ and $q \in [-20, 20]$ mm, the numbers of simulated events was adjusted until the population of clusters was large enough to have a uniform distribution in the output parameter space. Considering a binning with a width of 0.02 in $m$ and 0.08 mm in $q$, the number of events in each bin was set to be 30.

#### Training for vertical and horizontal clustering

The introduction of two orientations is significative for the training procedure since the pad is not a perfect square: the horizontal side is about 11.18 mm, while the vertical side is about 10.09 mm. For this reason, a slightly different behavior for horizontal and vertical tracks is expected in terms of relation between input and output variables. For this reason, the training for clusters with different orientations are performed separately. Since for vertical clusters the system of reference is rotated, in both orientations $|m| < 1$, so in order to have a region of partial overlap between the two groups, $m$ for training is chosen in the mentioned interval $m \in [-1.2, 1.2]$, forcing a *wrong* classification of cluster orientation when required.

## 7.5 Training of the Neural Network for horizontal clustering

The successful training of NN greatly depends on the tuning of hyper-parameters that describe the network structure and its learning process. A comprehensive approach on how to handle such hyper-parameters is described in [133], where the author describes the concepts of *learning rate*, *batch size*, *momentum* and *weight decay*. *Learning rate* $\eta$ is a parameter that rules the size of the changes the model is permitted to make while training. *Momentum* is another term that acts in the training to reduce the local oscillations when updating the weights using the gradient descent algorithm. In order to understand the *batch size*, additional terms need to be introduced. A *epoch* is one entire passing of training data through the algorithm. A subset of events might be passed instead of the whole dataset: the size of such subset (or batch) is called *batch size*. A small batch size requires less computational memory and trains the network faster, but the estimator for the gradient descent will be less accurate. An *iteration* corresponds to an update of the NN parameters. Consider a dataset where the the size of the batch is 1/10 of the total training size: then, 10 iterations are needed to complete 1 epoch. To assess the effect of hyper-parameters, a good way is to train the network with a sufficient amount of epochs to reach the plateau region for the test loss. Then, the training is repeated by changing the hyper-parameters values scanning in a grid values to find the best performances.
As already mentioned in the section related to MLP introduction, a precise rule for determining the NN structure is not available, since in principle even a single hidden layer might be enough for approximating any kind of function given enough time for training. Two structures with 3 and 4 hidden layers and a progressively smaller amount of neurons per layers were studied and produced

similar results.
In [133], for a small depth NN like the one proposed in this work: a large LR is considered to be 0.01; while Batch Size depends on the hardware computational limitation. The MLP network developed in TMVA allows the user to decide the structure of the NN, the activation function, and the hyper-parameters introduced before among many others: unless explicitely stated, parameters are left at their standard value as stated in [131]. In addition, in TMVA guide it is suggested to transform the input variables to a Gaussian distribution, however due to the peculiar shapes of $q_i$ and $f_i$ a uniform scale transformation was chosen, in particular to highlight the bi-modal distributions for $f_i$ variables. A scan on 2 hyper-parameters was performed:

- LR= 0.001,0.01,0.1;
- Batch size= 20, 100, 500;

while the best parameters for MLP regulator (equation 7.10) is automatically estimated by TMVA on the given training dataset. The performance of the training is computed by evaluating the root mean square (RMS) of the output variables in the test dataset with respect to their true value. Each set of hyper-parameters yielded very similar results, probably due to the limited complexity of the posed problem. Hence, in the next sections the preferred network configurations is based on hyper-parameters LR=0.001, BS=20. The chosen network layout is formed by 3 hidden layers with respectively 37, 13, 9 neurons.

## 7.6 Network performance evaluation

The training dataset size was chosen to be equal to 20 000 randomly chosen clusters in a sample uniformly distributed in $(q, m)$. The distribution of input and output variables in the training dataset for the central pad (number 4) is reported in figure 7.7. The two variables show a clear correlation as reported also in figure 7.8, with an important feature: when the charge is over a given threshold, the $f$ reaches a plateau value around $f \sim 0.07\ s.t.^{-1}$, meaning that $f$ is much less susceptible to the charge fluctuation deriving from the primary ionization above a given charge threshold. The relation between the input variables is estimated by introducing the *correlation* between two variables X and Y as

$$\rho_{XY} = \frac{\mathrm{cov}(X, Y)}{\sigma_X \sigma_Y}, \tag{7.11}$$

where $\mathrm{cov}(X, Y)$ is the covariance between the two variables and $\sigma$ is the square root of their variance. The correlation value between all variables is summarized in the covariance matrix in figure 7.8. The covariance matrix shows that in addition to the correlation $(q_i, f_i)$ in the same pads, also the variables for neighbor pads are related.
The progression of the network performances is summarized in figure 7.9, where the error function is computed for training and test dataset as a function of epochs. A quick steep decline is observed for the first epochs, then a slower but steady decline is observed until a third regime is reached where performances improve for the training dataset but not for the test dataset. Once the optimal weights for the NN are selected, a more in depth evaluation of the network performances on the test dataset can be performed. In figure 7.10, the residual distributions for the output variables for each entry are summarized. Residuals are generally unbiased and with a similar variance for almost the entirety of the output variables domains, with the exception of the large values of $m$ and $q$. In such cases, when $|m| > 1$ or $|q| > 18$ mm, the reconstructed output tends to be underestimated. However, those cases refer to clusters whose orientation is wrongfully reconstructed

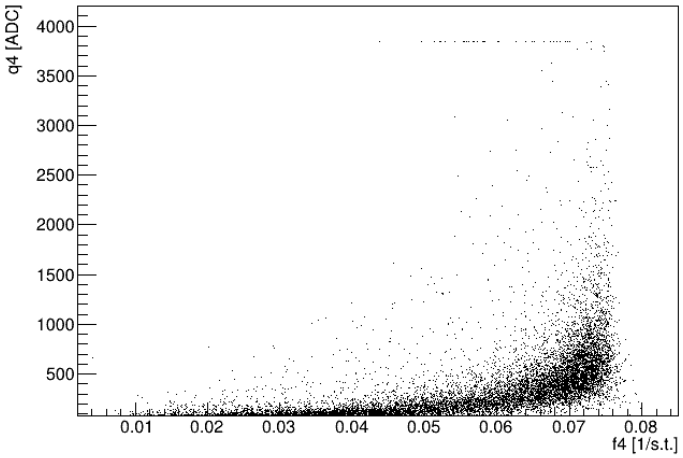


Figure 7.7: Distribution for charge and reciprocal of FWHM for the central pad in clusters in test dataset.

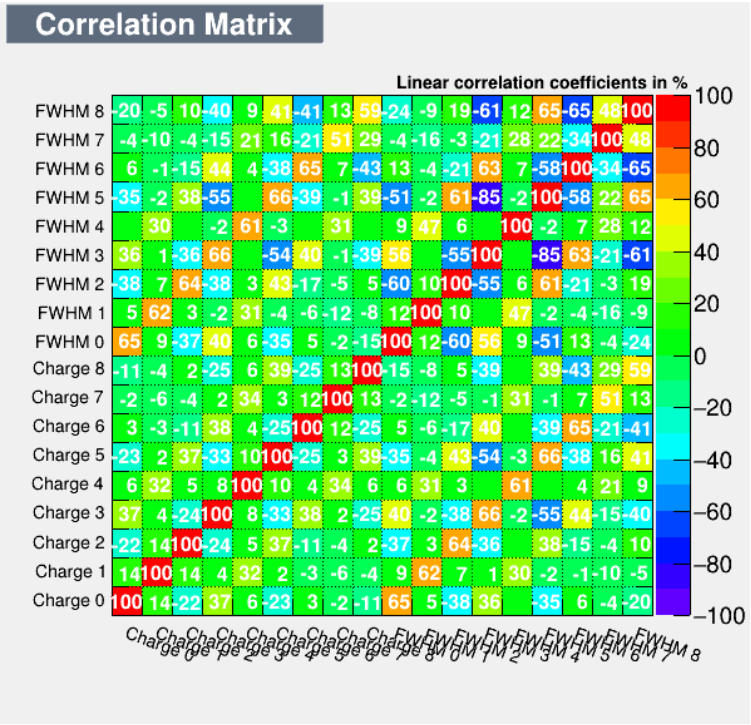


Figure 7.8: Covariance matrix for input variables expressed in percentage.

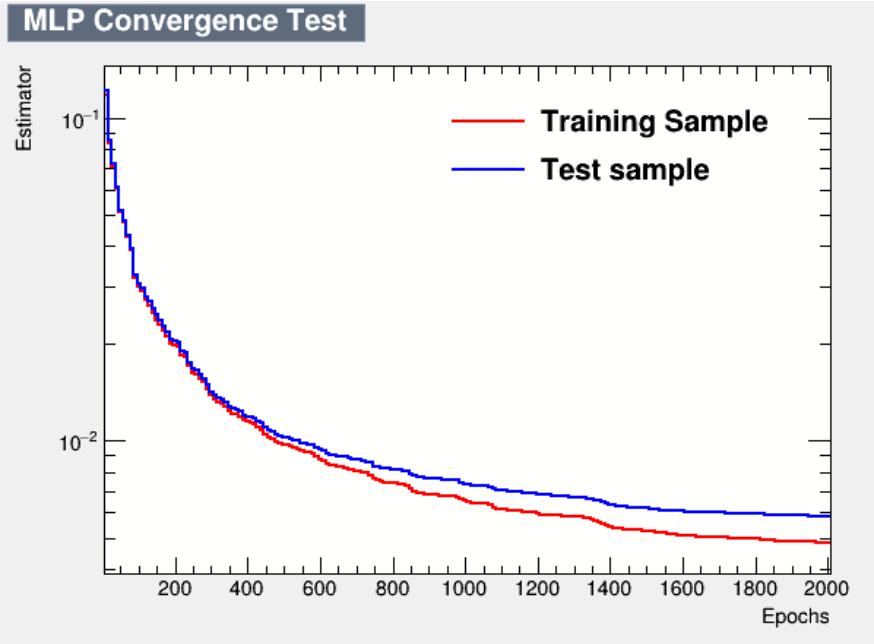


Figure 7.9: Error function for training and test datasets as a function of epochs.

and should not appear frequently in the reconstruction. The overall residual distribution for both horizontal and vertical clustering training is reported in figure 7.11 where they have been fitted with a Gaussian distribution. Since relative large tails are present, the fit is performed in the range $(m_{regression} - m_{true}) \in [-0.2, 0.2]$ and $(q_{regression} - q_{true}) \in [-2, 2]$ mm. The centroid and the $\sigma$ parameters from the fit are summarized in table 7.1, where $m$ and $q$ refer to the respective distribution of residuals. Horizontal and vertical trainings show similar results, with a slight improvement in the vertical case. In addition the correlation between $(m_{regression} - m_{true})$ and $(q_{regression} - q_{true})$ are computed, with no clear correlation between the two distributions for both horizontal and vertical training.

| Dataset | $\mu_m$ | $\sigma_m$ | $\mu_q$ [mm] | $\sigma_q$ [mm] | $\rho_{mq}$ |
|---|---|---|---|---|---|
| Horizontal | -0.0077±0.0008 | 0.0941 ± 0.0008 | 0.031 ± 0.008 | 0.942 ± 0.007 | 0.002 |
| Vertical | 0.0002 ± 0.0007 | 0.0900 ± 0.0007 | 0.008 ± 0.007 | 0.882± 0.006 | 0.006 |

Table 7.1

## 7.7 Spatial reconstruction performance on Montecarlo simulated data

Once the training performances are evaluated on single clusters, the reconstruction algorithm is tested on simulated tracks. For this purpose, 100 muons were simulated with no Magnetic field, at a drift distance of $x = 50$ cm and at several angles on the anode plane: 0°, 30 °, 45 °, 60 °, 90 °. Those particular angles are chosen since they contain:

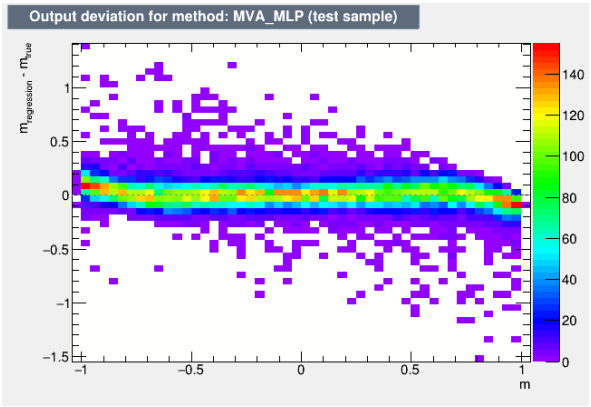


(a)

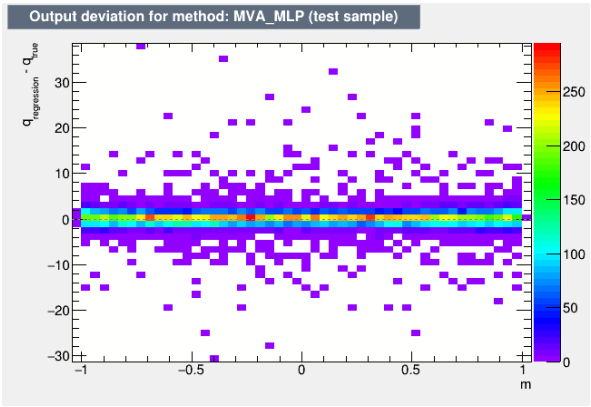


(b)

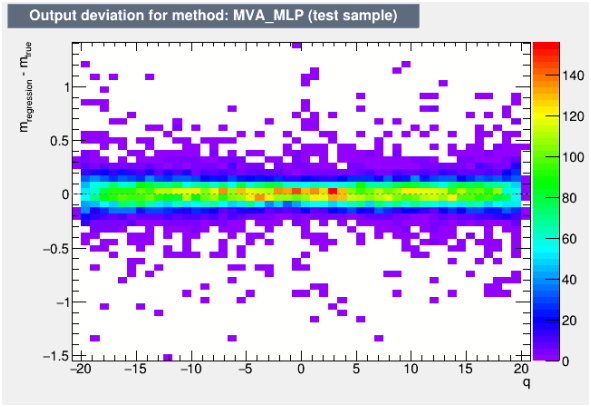


(c)

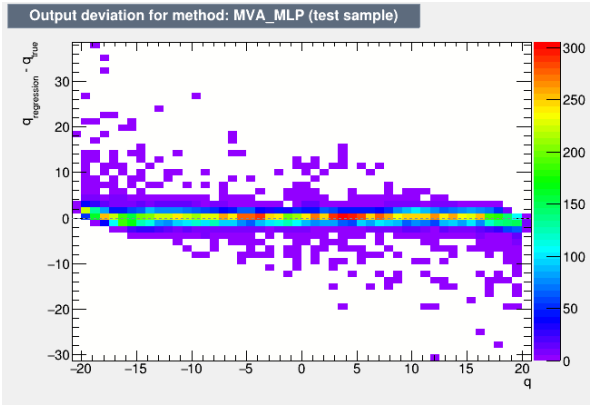


(d)

Figure 7.10: On top, the distribution of residuals for $(m_{regression} - m_{true})$ variable based on the true value of $m_{true}$ (left) or $q_{true}$ (right). On bottom, the same distributions for $(q_{regression} - q_{true})$ as a function of $m_{true}$ (left) and $q_{true}$ (right) are reported.

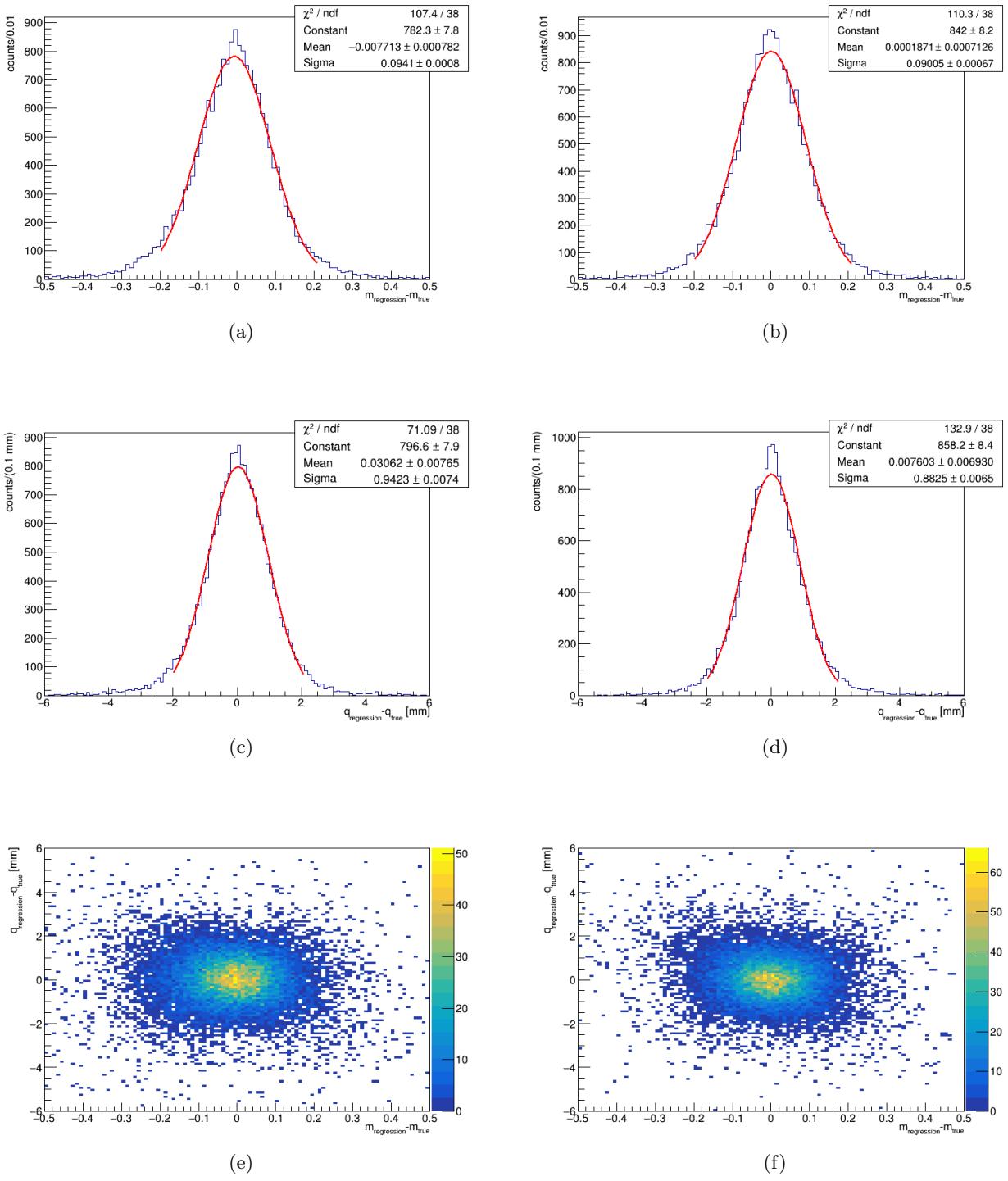


Figure 7.11: On top, the overall distribution of residuals for ($m_{regression} - m_{true}$) variable for horizontal (left) and vertical (right) test dataset. In the center, the same distributions for ($q_{regression} - q_{true}$) for horizontal (left) and vertical (right) test dataset is shown. Bottom plots report the 2D distribution of residuals ($m_{regression} - m_{true}$) and ($q_{regression} - q_{true}$) for horizontal (left) and vertical (right) test dataset.

- horizontal and vertical tracks at 0 ° and 90 °;
- tracks close to the change of clustering in the log(Q) method at 30° and 60°;
- tracks close to the change of orientation in the new method at 45°.

A fit with a line of the true points was performed and the residuals for the cluster points estimation for each method with respect to the true line were computed, adjusted for the orientation such that $residuals = (y_{cluster} - y_{true}) \cdot \cos\phi$, where $residuals$ are the signed distance to the line. For the vertical case, the fit is computed in a rotated system of reference. The distributions for the two methods were then fitted with a Gaussian distribution and the parameters are summarized in the plot 7.12 and in table 7.2.

Regarding the space resolution, as represented by the width of the residual distributions, the 3x3 method demonstrates excellent performance, regardless of the track angle. In contrast, the log(Q) method performs worse for non-vertical and non-horizontal tracks due to its different clustering approach. This improvement was expected and is the motivation behind the current work. On the contrary, in terms of the average of the residual distributions, a larger bias is observed with the 3x3 method compared to log(Q). This bias may be caused by the shifted average observed in the pull distribution of the local line slope parameter (see figure 7.10a) and calls for further careful investigation.

Regarding the evaluation of momentum resolution, this is not easily achievable through the Glückstern relation. In fact, this relation between spatial resolution and momentum resolution holds if the local estimations for the track position are independent. For the log(Q) method, this is approximately true, as each pad belongs to only one cluster, although charge spreading can introduce some correlation, especially for diagonal clusters. For the 3x3 method, however, the clusters are correlated, even in the first approximation, because adjacent clusters can share up to 6 pads. Therefore, a better spatial resolution may not necessarily correspond to a better momentum resolution. For this reason, a direct evaluation of the momentum reconstruction resolution is performed.

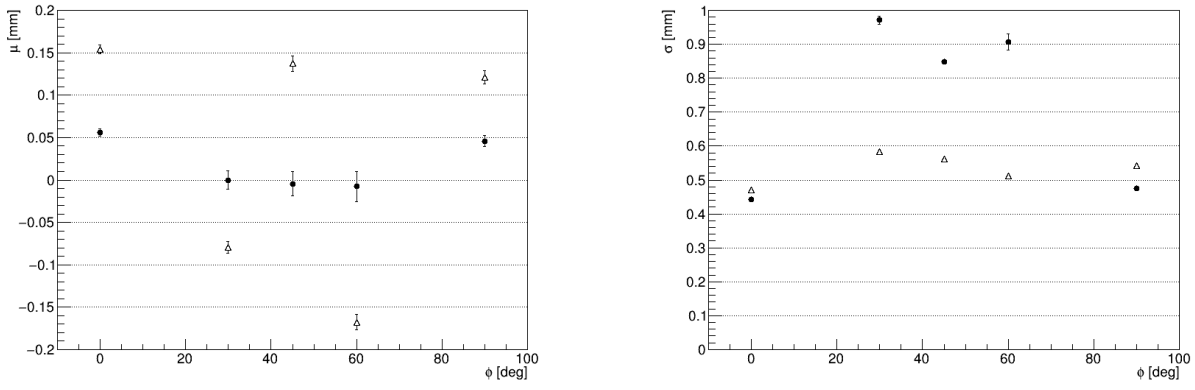


(a) (b)

Figure 7.12: Bias $\mu$ (left) and standard deviation $\sigma$ (right) for log(Q) method (square points) and 3x3 method (triangle points).

| | log(Q) | | 3x3 | |
|---|---|---|---|---|
| Angle [deg] | $\mu$ [mm] | $\sigma$ [mm] | $\mu$ [mm] | $\sigma$ [mm] |
| 0 | 0.056±0.004 | 0.443 ± 0.004 | 0.154 ± 0.005 | 0.470 ± 0.004 |
| 30 | 0.00 ± 0.01 | 0.97 ± 0.01 | -0.079 ± 0.007 | 0.583 ± 0.006 |
| 45 | 0.00 ± 0.01 | 0.848 ± 0.002 | 0.137 ± 0.009 | 0.563± 0.008 |
| 60 | 0.01 ± 0.02 | 0.91 ± 0.02 | -0.168 ± 0.009 | 0.511± 0.009 |
| 90 | 0.046 ± 0.007 | 0.476 ± 0.005 | 0.121 ± 0.008 | 0.543 ± 0.007 |

Table 7.2

## 7.8 Momentum resolution performance on simulation

Momentum resolution is estimated by simulating tracks using the same critical angles identified for the spatial resolution analysis: 0°, 30°, 45°, 60°, 90°. In this study, 8000 muons with a momentum range in [300,3000] MeV/c are simulated using the nominal Magnetic field equal to 0.2 T. The resolution with respect to the true information for the transverse momentum is computed for both algorithms. Due to the presence of Magnetic field, the local angle of the track is not uniform, therefore the division of the datasets per angle is less significative but still meaningful in order to identify the majority of the clusters orientation. The tracks are then divided in two categories: (i) $p_T \in [300, 1000]$ MeV and (ii) $p_T \in [1000, 3000]$ MeV.
Momentum resolution for tracks at different angles is not a fair comparison since tracks have different length depending on their trajectory. The main goal of the study is to compare the two methods performances on the same events. For each reconstructed track, the variable

$$\Delta p_T = \frac{p_{T,reco} - p_{T,true}}{p_{T,true}} \tag{7.12}$$

is computed for both methods. Then, the distributions are fitted with a Gaussian and the results are summarized in figure 7.13 and in table 7.3.

In both groups (i) and (ii), the bias distribution is similar for both reconstruction algorithm with the exclusion of vertical tracks, which are also the shortest ones. The global tendency to show a negative bias for momentum reconstruction was already observed in the Electric field chapter, and such unexpected behavior is not yet understood and calls for deeper investigation. Concerning the resolution, the two methods perform quite similarly for tracks up to 30°, Beyond that angle the log(Q) method shows a better standard deviation, which need also further understanding.

## 7.9 Preliminary Insights into the New Reconstruction of Real Tracks from Neutrino Beam Data

The results presented in the previous sections are obtained by applying the reconstruction algorithms to MonteCarlo simulated data, where the detector response is modeled based on our best, but possibly yet incomplete understanding of the new detector. In order to evaluate the possibility to apply the 3×3 method to real data, a preliminary test on a single run from June 2024 data taking with neutrino beam is performed. The reconstruction efficiency and the tracks reconstructed momentum spectrum are compared between the 3x3 and the log(Q) method on the same events

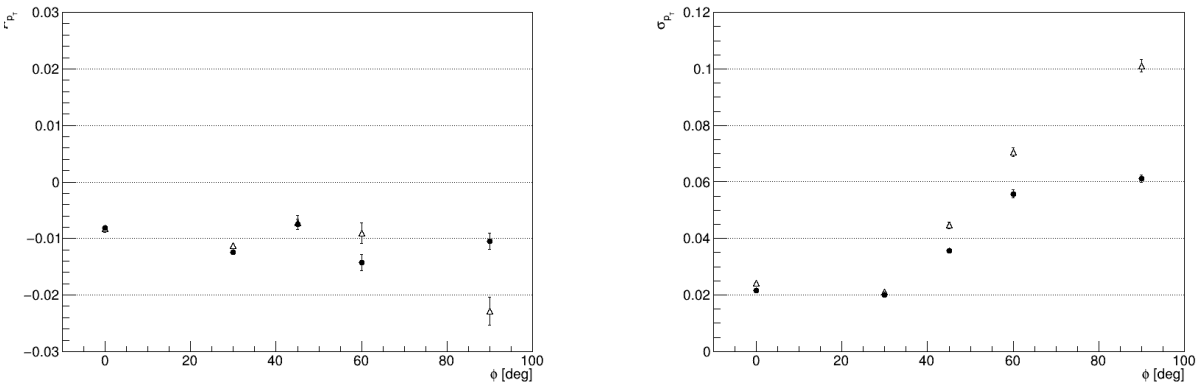


(a)




(b)

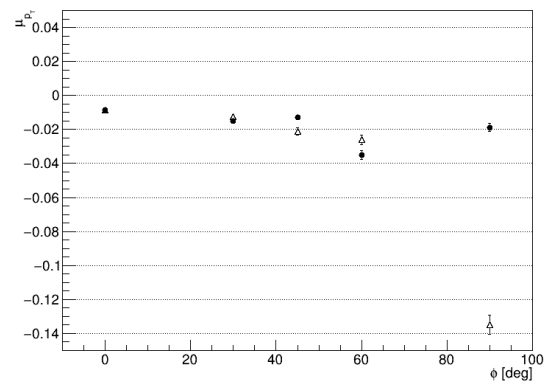


(c)

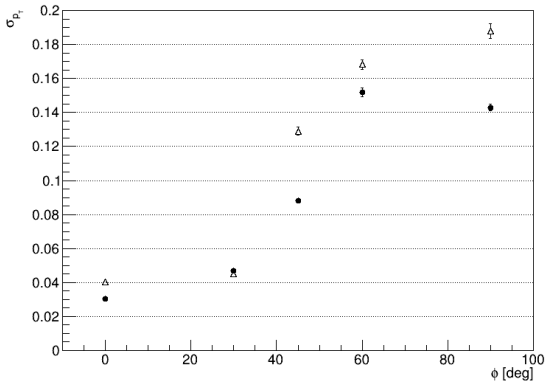


(d)

Figure 7.13: On top, bias $\mu$ (left) and standard deviation $\sigma$ (right) for log(Q) method (square points) and 3x3 method (triangle points) are reported for tracks with $p_{T,true} \in [300, 1000]$ MeV. Bottom plots are the equivalent estimators for tracks such that $p_{T,true} \in [1000, 3000]$ MeV.

| $p_T \in [300, 1000]$ MeV | | | | |
|---|---|---|---|---|
| | log(Q) | | 3x3 | |
| Angle [deg] | $\mu$ | $\sigma$ | $\mu$ | $\sigma$ |
| 0 | -0.0082±0.0005 | 0.0215 ± 0.0005 | -0.0082 ± 0.0006 | 0.0241 ± 0.0006 |
| 30 | -0.0124 ± 0.0005 | 0.0201 ± 0.0004 | -0.0113 ± 0.0005 | 0.0210 ± 0.0004 |
| 45 | -0.0075 ± 0.0009 | 0.0355 ± 0.0009 | -0.007 ± 0.001 | 0.045± 0.001 |
| 60 | -0.014 ± 0.001 | 0.056 ± 0.001 | -0.009 ± 0.002 | 0.070± 0.002 |
| 90 | -0.010 ± 0.001 | 0.061 ± 0.001 | -0.023 ± 0.002 | 0.101 ± 0.002 |
| $p_T \in [1000, 3000]$ MeV | | | | |
| | log(Q) | | 3x3 | |
| Angle [deg] | $\mu$ | $\sigma$ | $\mu$ | $\sigma$ |
| 0 | -0.0085±0.0004 | 0.0304 ± 0.0005 | -0.0085 ± 0.0006 | 0.0405 ± 0.0007 |
| 30 | -0.0152 ± 0.0006 | 0.0468 ± 0.0007 | -0.0124 ± 0.0007 | 0.0452 ± 0.0007 |
| 45 | -0.013 ± 0.001 | 0.088 ± 0.001 | -0.021 ± 0.002 | 0.129± 0.002 |
| 60 | -0.035 ± 0.002 | 0.152 ± 0.003 | -0.026 ± 0.003 | 0.168± 0.003 |
| 90 | -0.019 ± 0.002 | 0.143 ± 0.002 | -0.135 ± 0.006 | 0.188 ± 0.004 |

Table 7.3

sample.
For the evaluation of the momentum spectrum, with reconstructed transversal momentum $p_T \in ]0, 3000[$ where considered, with $n_{cl} > 30$ and $\chi^2/NDF < 5$ as additional constraints. The two distributions are shown in picture 7.14 where no clear discrepancy is visible. A quantitative comparison is performed by applying the Kolmogorov-Smirnov test to the two unbinned populations of reconstructed momenta by log(Q) and 3x3 methods. The result of the Kolmogorov-Smirnov test performed using CERN ROOT "TMath.h" library is about 0.496, which indicates good agreement between the distributions of the two datasets.

Regarding the reconstruction efficiency, the two histograms present a similar amount of data: $N_{log(Q)} = 1920 \pm 30$ and $N_{3x3} = 1930 \pm 30$ so that the two efficiencies are fairly compatible within the binomial error. As a very preliminary conclusion we notice that the 3x3 method can be applied successfully to data and further studies. Further evaluation of the novel reconstruction method discussed here will be conducted using dedicated data samples, where the reconstruction of well-defined and known physical constants, such as the invariant masses of unstable particles, will serve as an absolute reference for comparison.

## 7.10 Summary

The track reconstruction method introduced in this chapter represents an attempt first, to improve pad clustering and making it consistent with pad shape and track topology, and, second, to incorporate additional waveform information beyond the only maximum amplitude into algorithm. This new method has demonstrated the potential to achieve improved spatial resolution across all track angles, as expected by employing a uniform clustering approach. However, biases in the spatial reconstruction may result in degraded momentum resolution which requires to be addressed before including this algorithm as an alternative to the already present log(Q) method.

While exploring alternative neural network architectures may be worthwhile, the current algo-

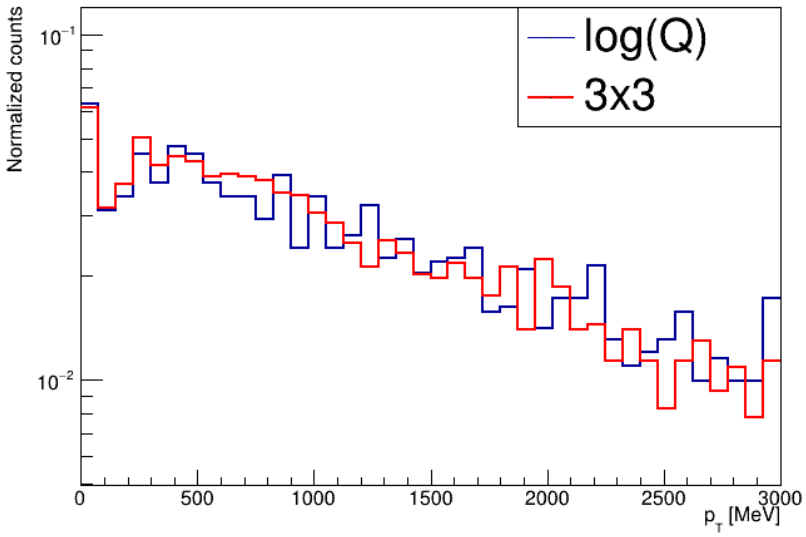


Figure 7.14: Spectrum comparison for the two reconstruction methods log(Q) in blue and 3x3 in red lines.

rithm's performance can be enhanced by implementing the following improvements:

- Optimizing the selection criteria for pad signals to minimize the impact of noise on input variables;
- Excluding pathological 3x3 clusters from training, such as those where pads are saturating or where the true track generates signals in only a few pads;
- Employing a more robust method to compute the FWHM of waveforms;
- Implement a method to consider the local estimation of the track's slope given by the MLP as an output parameter, in addition to the estimated local point of passage. Such information might be used while performing the helix fit step.

More generally, additional information can be extracted from waveforms to enlarge the input features for the Machine Learning algorithm and further enhance the algorithm accuracy.

Ultimately, to evaluate the reconstruction performance on real data, dedicated control samples will be analyzed. In these samples, the reconstruction of physical constants such as invariant masses, will serve as an absolute reference for comparison.

# Conclusions

The T2K experiment is a long-baseline neutrino experiment located in Japan, designed to measure neutrino oscillation parameters, including $\theta_{13}$, $\delta_{CP}$, $\theta_{23}$, and $\Delta m^2_{32}$. These parameters are determined by studying electron neutrino appearance probabilities and muon neutrino survival probabilities. In recent years, T2K has undergone significant upgrades to its beam-line and near detector (ND280) to increase the neutrino flux and reduce systematic uncertainties. These improvements are crucial not only for T2K but also for the next generation of neutrino oscillation experiments. The beamline and ND280 will play a key role in the long-baseline program of Hyper-Kamiokande, which is expected to be completed in 2027.

A key component of the ND280 upgrade is the installation of two High-Angle Time Projection Chambers (HA-TPCs), covering the acceptance for tracks at large angles relative to the neutrino beam direction. Both HA-TPCs were successfully installed at J-PARC by May 2024. This thesis focuses on three main aspects of the HA-TPCs: (i) the design, production and performance evaluation of field cages, (ii) the study of their electric field properties, and (iii) the development of a novel machine learning-based track reconstruction algorithm.

The first part of this thesis details the production and validation of the HA-TPC field cages, which are essential for maintaining a uniform electric field and providing robust mechanical support. The field cages are constructed from a composite material structure that combines low material budget with excellent electrical and mechanical properties. A significant challenge arose during this phase with the first full-scale field cage (FC0), which exhibited unexpected electrical behavior due to parasitic conductive paths within its layers. Through detailed electrical characterization, the development of a mathematical model, and subsequent design improvements, this issue was successfully resolved.

The second part of the thesis addresses the characterization of the electric field within the HA-TPCs. The uniformity of the electric drift field is critical for accurate track reconstruction, as deviations from ideal conditions can introduce systematic distortions in particle trajectories. A finite element method (FEM) simulation of the electric field was developed, and its results were validated using cosmic ray data. These studies identified distortions in the electric field near the cathode region, which were corrected using an electric field map derived from the FEM simulation.

The final part of the thesis introduces a novel track reconstruction method for the HA-TPCs based on a machine learning algorithm. The algorithm utilizes the amplitude and full width at half maximum of pad response signals as inputs to determine the parameters of a local linear approximation of the track trajectory. While the current method still features better momentum reconstruction but has limited potential for further improvement in this regard, preliminary comparisons with the novel method developed in this thesis indicate promising enhancements in spatial resolution, particularly for diagonal tracks. The novel method offers significant potential for further optimization, including refining input features and improving the machine learning model.

# Acknowledgement

I would like to express my sincere gratitude to all the friends and colleagues I met throughout my Ph.D. journey. From the very beginning, the HA-TPC group has been a place of stimulating discussions and a source of diverse expertise from which I've learned immensely.

In primo luogo, vorrei ringraziare Gianmaria per il supporto dimostrato durante tutto il dottorato. I capitoli contenuti in questa tesi presentano soluzioni a problemi che inizialmente sembravano insormontabili. Tuttavia, grazie alla sua costante determinazione e profonda conoscenza, in questi anni ho potuto imparare molto.

I would also like to thank my office colleagues Camilla, Daniele, David, Leo, Marco, Stefano for the time we spent together and for the environment we shared as a group.

Vorrei ringraziare Lorenzo per la disponibilitá e l'aiuto dimostrato in questi anni.

Un ringraziamento speciale va alle persone che hanno dedicato molto del loro tempo alla revisione di questa tesi. In particolare, desidero ringraziare Mauro per il sostanziale aiuto e per gli spunti molto interessanti forniti per dare forma e contenuto all'introduzione.

Next, I would like to express my gratitude to my Siena friends Andrea, Matteo, and Mina for all the memories we built together during my time there.

Vorrei estendere i miei ringraziamenti a tutti i miei amici, che sono sicuro siano arrivati fino a questa sezione dopo aver letto tutta la tesi, dimostrando cosí il loro sostegno al mio lavoro.

Concludo ringraziando i miei familiari per il sostegno durante tutti questi anni che mi ha permesso di arrivare a questo punto.

# List of Figures


1.1 The picture summarizes the fundamental particles, grouped according to their properties. Each particle is presented along with its electric charge, color charge and mass. In particular, the mass scale for massive particles span up to 12 orders of magnitude, from the top quark to the very light neutrinos. Adapted from [1]. . . . . 1

1.2 Measurements of the hadron production cross-section around the Z resonance and the predicted curves in the case of 2, 3 or 4 neutrino species with SM couplings and negligible mass. SM couplings and negligible mass[14]. . . . . 5

1.3 The plot shows the electrons emission directions for the two different verses of Magnetic fields. The asymmetry is due to P violation. Graphs from [15]. . . . . 5

1.4 Electroweak Lagrangian density for one generation of fermions, in which the terms are arranged by interaction. . . . . 8

1.5 Neutrinos mass eigenstates and their composition in neutrino flavor eigenstates (red $\nu_e$, blue $\nu_\mu$, green $\nu_\tau$) for normal (NO) and inverted ordering (IO). . . . . 16

1.6 Schematic view of the pp and CNO nuclear fusion sequences. The solarneutrino energy spectrum is obtained from http://www.sns.ias.edu/ jnb/, using the updated fluxes taken from [36]. The flux (vertical scale) is given in units of $cm^{-2}s^{-1}MeV^{-1}$ for continuum sources and in $cm^{-2}s^{fl1}$ for monoenergetic sources. Picture from [37]. . 21

1.7 Flux of $\nu + \tau$ neutrinos versus flux of electron neutrinos. CC, NC and ES flux measurements are indicated by the filled bands. The total $^8$B solar neutrino flux predicted by the Standard Solar Model[30] is shown as dashed lines, and that measured with the NC channel is shown as the solid band parallel to the model prediction. The narrow band parallel to the SNO ES result correponds to the Super-Kamiokande result in [43]. The intercepts of these bands with the axes represent the $\pm 1\sigma$ uncertainties. The non-zero value of $\phi_{\mu\tau}$ provides strong evidence for neutrino flavor transformation. The point represents $\phi_e$ from the CC flux and $\phi_{\mu\tau}$ from the NC-CC difference with 68%, 95%, and 99% C.L. contours included. Picture from [42]. . . . . 22

1.8 The pink band is the $\pm 1\sigma$ prediction of MSW-LMA with oscillation parameters determined from [48]. The grey band is the vacuum-LMA case with oscillation parameters determined from [49][50]. Data points represent the Borexino results for pp (red), $^7$Be (blue), pep (cyan) and $^8$B (green for the HER range, and grey for the separate HER-I and HER-II sub-ranges), assuming HZ-SSM. $^8$B and pp data points are set at the mean energy of neutrinos that produce scattered electrons above the detection threshold. The error bars include experimental and theoretical uncertainties. Picture from [37]. . . . . 23

1.9 Correlation between direction and path length of neutrinos. Picture from [2]. . . . . 24

1.10 Distribution of e-like and $\mu$-like events in Super-Kamiokande as a function of zenith angle. The top two figures refer to events with neutrino energy below 1.33 GeV, while the bottom two represent the case above that energy. Cyan boxes show the expected result in the case of no oscillation, while full drawn lines are the best fit to data in the oscillation hypothesis. Picture from [28], in which it was provided by Super-Kamiokande collaboration. . . . . 25
1.11 Survival probability of $\bar{\nu}_e$ as a function of the ratio $\frac{L_0}{E_{\bar{\nu}_e}}$. The blue histogram is the best $3\nu$ fit from the three-flavor unbinned maximum likelihood with KamLAND data. Picture from [50]. . . . . 27
1.12 Comparison of $2\sigma$ allowed region for T2K (red), NOvA (purple) and MINOS (green) disappearance data assuming Normal Ordering for $\Delta m^2_{32}$ and $\theta_{13}$. The dotted (dashed) lines correspond to neutrino (antineutrino) data. In the left panels a prior on $\theta_{13}$ has been imposed to account for reactor bounds, while in the right panels LBL and reactor data are consistently combined together. In all panels solar and KamLAND data are included to constrain $\Delta m^2_{21}$ and $\theta_{12}$. Picture adapted from [70]. . . . . 30
1.13 JUNO reactor anti-neutrino energy spectrum after 6 years of data taking under the assumption of no oscillations (black line) or oscillations: (i) modulation depending only on $\sin^2 2\theta_{12}$ (gray dashed line), (ii) full oscillation in vacuum for NO (blue line) and (iii) full oscillation in vacuum for IO (red line). The lines are drawn under the assumption of perfect energy resolution. Picture from [83]. . . . . 34

2.1 Sketch of T2K the Experiment, in which the accelerator, the near detector complex and the far detector are highlighted. . . . . 35
2.2 Sketch of T2K the Experiment main facilities, with a focus on the tilt angle between the beam direction and Super-Kamiokande. . . . . 35
2.3 The muon neutrino survival probability (top) and electron neutrino appearance probability (middle) at 295 km as a function of neutrino energy. The bottom plot shows the unoscillated spectrum at the far detector for three off-axis angles. The appearance probability is shown for two values of the phase $\delta_{CP}$, and for normal (NH) and inverted (IH) mass hierarchies. . . . . 36
2.4 The neutrino beamline at J-PARC facility. Picture from [67]. . . . . 38
2.5 A scheme of the hall housing the detectors in the ND280 facility at J-PARC. On the right, an exploded view of ND280 detector configuration as it was until 2023 is visible. 39
2.6 A scheme of the front view of INGRID detector. Picture from [67]. . . . . 40
2.7 Magnetic field map for the central plane (x=0) of the magnet. Magnetic field values are expressed in Gauss. Picture from [67]. . . . . 41
2.8 SMRD components before assembling. Picture from [67]. . . . . 42
2.9 Schematic view of P0D structure. Four macro-regions are highlighted by labels and are characterized by the presence of layers with different materials. Picture from [67]. 43
2.10 Schematic view of a FGD, in which the cover was removed. The modules (in green) are arranged in XY planes perpendicular to the beam direction. On the top, six mini-crates with electronics and their cooling lines are visible. Picture from [67]. . . . 44
2.11 View of one inner vessel of vertical TPCs and its components: (A) vessel walls, (B) module frame stiffening plate, (C) module frame, (D) inner box endplate, (E) field reducing corners and (F) central cathode location. Picture from [88]. . . . . 45
2.12 Energy loss *pull* for electron hypothesis on a sample of traversing muons as a function of particle momentum. Picture from [88]. . . . . 46

2.13 Schematic view of Super-Kamiokande and its location under the mount Ikenoyama. . 46
2.14 Examples of a muon-like ring (left) and a electron-like ring (right), which are recognizable by the sharpness of the light ring. . . . . 47
2.15 Top left plot shows the comparison of measured $\nu_e$ and $\bar{\nu_e}$ appearance at Super-K with the expected values from models with several $\delta_{CP}$ and $\sin^2(\theta_{23})$ values. Top right plot shows a data/models comparison dividing the events based on neutrino energy. Bottom left plot highlights the excluded regions at several values of $\sigma$ for both NO and IO, while the bottom right highlights the importance of reactor constraint: it represents the 68% and 90% credible intervals from the marginalised $\sin^2(\theta_{13} - \delta_{CP}$ posterior distribution with (red) and without (blue) the reactor constraint (green band) applied, marginalised over both mass orderings. Picture from [69]. . . . . 49
2.16 Left plot shows the confidence regions in $\sin^2(\theta_{23}) - \Delta m^2_{32}$ ($|\Delta m^2_{31}|$ in IO) for the data fit with the reactor constraint applied, obtained with the constant $\Delta\chi^2$ method, where in each mass ordering hypothesis a fixed mass ordering is assumed. On the right plot, The $\Delta\chi^2$ distribution in $\sin^2(\theta_{23})$ for fitting to the data with the reactor constraint applied. Pictures from [69]. . . . . 50
2.17 Reconstructed momentum and angle for muons selected at ND280 (a) and electrons selected at Super-K (b). Picture from [94]. . . . . 52
2.18 ND280 upgrade efficiency in reconstructing muons (a) and protons (b) where FGDXZ are the current FGDs of ND280. Picture from [94]. . . . . 52
2.19 Comparison of previous (left) and upgraded (right) designs for ND280 detector. . . . 52
2.20 Scheme of Super Fine Grained Detector. On the right, a focus on a single cube is visible, with the holes for WLS fibers insertions on three directions. . . . . 53
2.21 Comparison of dE/dx for protons, muons and electrons at a momentum of 0.8 GeV/c. Picture from [95]. . . . . 53
2.22 Placement of TOF panels around the new tracker of ND280. . . . . 54
2.23 Event display of an event with the upgraded ND280 detector (beam coming from left). On the left side, the primary interaction vertex is within the Super-FGD. Most of the particles move in the forward region towards FGDs and vTPCs, while few of them are directed at large angles to HA-TPCs on both sides of Super-FGD. . . . . 55
2.24 Left plot refers to the significance level to exclude CP conservation at Hyper-K after 10-year assuming the reported oscillation parameters. Right plot shows sensitivity to CPV as a function of data-taking time for two values of $\delta_{CP}$. "Physics Official Plots" from Hyper-K Collaboration. . . . . 56
2.25 Sketch of IWCD experiment. . . . . 57

3.1 Differential energy loss for a positive muon in a copper medium as a function of its momentum. Picture from [28]. . . . . 59
3.2 Comparison between experimental data and Landau theory calculation (solid line) of energy loss in thin sample of gas. The dashed line shows the Gaussian expectation for the same average energy loss. Picture from [100]. . . . . 60
3.3 Most probable values of the ionization (normalized to the minimum value) in argon at ordinary density as function of the momenta of the known stable charged particles. Picture from [101]. . . . . 63
3.4 Drawing of ALEPH TPC structure. Picture from [105]. . . . . 64

3.5 Sketch of a HA-TPC, in which one of the two instrumented anodes is visible, while the other is on the back. The cathode is placed in the middle of the active volume, corresponding with the visible flange. Picture from [96]. . . . . 65
3.6 Sketch of a bulk Micromegas (left) and a resistive Micromegas (right). . . . . 66
3.7 Mean and variance of the main $^{55}$Fe peak for each pad in ERAM-30. Pictures adapted from [107]. . . . . 68
3.8 Schematic view of an ERAM module and the related electronics. . . . . 69
3.9 Picture from inside the TPC in which the mesh is visible (left). . . . . 70
3.10 Picture of the first HA-TPC at CERN. On the right, one endplate is visible, in which FECs and FEMs are mounted on ERAMs. . . . . 71
3.11 Picture of the SFGD (middle) and the two HA-TPCs on top and bottom installed in the ND280 basket in April 2024. . . . . 71
3.12 On the right a vertical cluster with a leading pad and two secondary pads is shown, with an horizontal track crossing the leading pad. On the left, the corresponding waveforms are visible with a clear difference between the leading and secondary pads. Picture from [97]. . . . . 72
3.13 Shapes of cluster used for spatial reconstruction with horizontal (a), vertical (b) and diagonal (c) orientations. Red line represents the typical inclination of tracks for which each cluster is used. An additional cluster direction similar to (c) is used for diagonal tracks moving with negative slope in ERAMs plane. Picture from [111]. . . 72
3.14 Example of waveform segmentation for several maxima in a channel. Picture from T2K-TN-466. . . . . 73
3.15 Example of a residual (red line) for a single cluster once helix fit is performed (green line). The typical radius R of the helix is greatly reduced for an improved visualization. 75
3.16 Spatial resolution as a function of MMs column (left) and row (right). Pictures from T2K-TN-466. . . . . 75
3.17 Spatial resolution in data (blue) and MC simulations (green) for HA-TPCs as a function of drift distance. Pictures from T2K-TN-466. . . . . 76
3.18 dE/dx resolution as a function of drift distance for HA-TPC prototypes in 2019 (black) and 2021 (orange) compared with simulated data (light blue). Picture from [111]. . . . . 77
3.19 Estimator of dE/dx for electrons and muons in simulations as a function of particle momenta on the left. On the right, the resolution for dE/dx estimation related to the same population is reported. Pictures from [111]. . . . . 78
3.20 Pulls distributions for muon and electron hypotheses applied to a muon (left) and electron (right) simulated samples. Pictures from [111]. . . . . 78
3.21 Perfomances of HA-TPCs prototype at 2021 DESY test beam[98]. Left picture shows spatial resolution as a function of drift distance, while right picture shows the energy loss resolution as a function of number of clusters in a track as defined in 3.13 (vertical or horizontal option). . . . . 80
3.22 On top, a picture of CERN 2022 test beam setup is reported. In the center, the HA-TPC prototype with a single full scale field cage instrumented with 8 ERAMs is placed near to the small prototype used for DESY 2021 and CERN 2021 test beams. On the left of the picture, the gas rack containing the gas analysis branch is visible. The bottom picture is a schematic view of the detectors involved in the test beam and included in the trigger logic development. . . . . 81

3.23 Perfomances of HA-TPC full scale prototype at 2022 CERN test beam. Top picture shows dE/dx resolution as a function of particle energy for $e, \mu, \pi, p$, while top right picture shows the spatial resolution. Bottom left and right pictures show the dE/dx and spatial resolutions for electrons sample as a function of drift length Z. Pictures from [111]. . . . . 82

4.1 Schematic view of a cross section of the field cage, with focus on the strips. Two voltage dividers connect all the strips from cathode to anode. . . . . 84
4.2 Schematic view of a cross section of the field cage on scale, with the side facing the inner volume on top. Quotations are reported in mm. . . . . 86
4.3 On top, a detailed view of the field cage wall is shown. Due to the large intensity of electric field in this region, several Kapton layers are glued together as insulation. On the other side, an aluminum layer is applied to shield the system from possible charge accumulation and field distortions. . . . . 87
4.4 Picture of a strip foil with field strips side facing the observer. The strip foil is 5 m long and 1 m wide and it covers the whole internal perimeter of the field cage. In the center of the strip foil, the junction line of the two parts composing the strip foil is visible parallel to the long sides. . . . . 88
4.5 Comparison of HA-TPC prototype on left 4.5a with the old ARC electronics installed and full scale HA-TPC on right 4.5b. Each HA-TPC endplate houses 8 ERAMs module. The total lateral surface covered by the HA-TPC is 5 times larger than the prototype, which is designed for only 1 ERAM. . . . . 89
4.6 Strip foil placement on mold before 4.6a and after 4.6b vacuum bag is applied. Vacuum is obtained by pumping out the air in between strip foil and mold with the aid of holes in the mold surface. The system is sealed by means of vacuum bags attached to the strip foil extremities as shown in figure 4.6b. Strip foil is kept in place with the aid of tape which will be removed in the next stages. In figure 4.6b the tape on coverlay is temporarily placed to stretch the strip foil and avoid the formation of wriggles. . . . . 91
4.7 In figure 4.7a the two extremities on the short side of the strip foil are aligned with the accuracy of few hundreds of micrometers before the application of vacuum. Once the vacuum is applied, bubbles might form inside the strip foil, which are removed as shown in figure 4.7b. . . . . 92
4.8 Once the mold and the applied layers are placed in the clean room after curing in autoclave, the vacuum bag and the Peel-Ply layer in figure 4.8a are removed. The large pressure applied to the system forces the glued layers against the rigid mold and the strip foil. Few defects are still possible, such as trapped bubbles or inhomogeneity in the resin placement as reported in figure 4.8b. . . . . 93
4.9 Set of electrodes used for resin surface resistance 4.9a and volumetric resistance 4.9b. 93
4.10 Current over time for volumetric resistivity measurements for resin samples realized with resin from Kapton (red) and Twaron (blue) lamination. The other two samples are made with the same resin but with room temperature (magenta) and 40°C (black) curing temperatures. . . . . 94
4.11 Current over time for surface resistivity measurements for resin samples, realized with resin from Kapton (red) and Twaron (blue) lamination. The other two samples are made with the same resin but with room temperature (magenta) and 40°C (black) curing temperatures. . . . . 95

4.12 Picture of setups for volumetric resistivity measurement of proto-FC layers. Picture 4.12a shows the large 40×50 $cm^2$ electrode applied on the coverlay and pushed against it thanks to vacuum. One end of the insulator tester is connected to the electrode, while the other is applied to the support. Analogously, picture 4.12b shows the two long electrodes in separated vacuum bags. The two cables are connected to the insulator tester. . . . . 96
4.13 Sketch of strip foil section (not on scale) with the expected path for current from the electrode to the mold. . . . . 97
4.14 Electrode for surface resistivity estimation of proto-FC layers. Picture 4.14a shows the electrode held in place on the inner Twaron layer by Kapton tape. Picture 4.14b shows the sealing with vacuum bag. Two pieces of copper tape connect the electrode with the insulator tester through two small openings. . . . . 98
4.15 Current as a function of time for volumetric resistivity estimation of strip foil at 1 kV for square electrode configuration on 4.15a and long electrodes configuration on 4.15b. Both plots reach a plateau value that is given by the tester. . . . . 99
4.16 Current as a function of time for volumetric resistivity estimation for the proto-FC formed by strip foil and laminated Kapton layers at 1 kV and 2 kV for square electrode configuration on 4.16a and long electrodes configuration on 4.16b. At 1 kV, both plots reach a plateau value that is given by the tester, while at 2 kV the configuration 4.16b appears to stay at a larger value. The resistance is estimated by fitting the tail of the curves with a horizontal line. . . . . 100
4.17 Surface resistance of laminated Kapton layers on strip foil, measured with concentric circular electrodes at a voltage of 1 kV. . . . . 101
4.18 View of the G-10 bars installed on the sides of the proto-field cage on top of the inner Twaron layers. The faces are sanded in preparation for the installation of the HoneyComb. . . . . 103
4.19 View of the proto-FC with HoneyComb installed on the four faces. On top of it, the external Twaron layers will be laminated. . . . . 104
4.20 Left image 4.20a is a view of one of the two Copper-plated faces of the cathode. In this picture, the protective film is still applied. The cathode is secured to the field cages with six supports placed on the perimeters, as shown in picture 4.20b. . . . . 106
4.21 The picture is a sketch of the junction section. Starting from bottom, the cathode is visible, which expands symmetrically in both field cages inner volume. Between the cathode and the wall there is a small gap for gas passage. In the flange, three groves are present. The innermost one is used for insulating purposes, while the other two host an O-ring each. Eventually, on the external part G10 bolts hold the field cages in place. . . . . 107
4.22 The picture is a sketch of the HV connector. High voltage is fed from the wire on the right to the standard socket, which extends for about 10 cm inside the connector case. Then, from the hot end, a copper wire is soldered and connected to the cathode thanks to a feed-through. The case is then closed by plastic screws. . . . . 107
4.23 Measurement of field cages planarity performed at NEXUS. Color scheme represents the deviation from ideal planar surface in millimeters. . . . . 109
4.24 Measurement of distances between series of two points on the two opposite large area sides of the field cage. Colour scheme represents the deviation from ideal planar surface in millimiters. . . . . 110

4.25 Measurement of distances between series of two points on the two opposite small area sides of the field cage. Colour scheme represents the deviation from ideal planar surface in millimiters. . . . . 110
4.26 Measurement of cathode and flanges planarity performed by CERN metrology service. Colour scheme represents the deviation from ideal planar surface in millimeters. . . . 111
4.27 Measurement of the distance between the last field strip and the anode flange for a side of a field cage.Colour scheme represents the deviation from ideal planar surface in millimeters for the visible part of field cage walls. . . . . 112
4.28 Load test for setups *FC0+FC1* (red) and *FC1+FC2* (blue). The two setups show similar deflection rates and have been tested up to 200 kg. . . . . 113
4.29 Displacement as a function of the internal pressure is reported. The outer pressure was measured to be around 970 mbar, however its accuracy is not relevant, since the important parameter is the structural deflection rate. Central position for field cages walls on one of the large faces 4.29a and on one of the short faces 4.29b. Figure 4.29c reports the displacement for flanges on the cathode side, which are jointed by fiberglass screws. . . . . 114
4.30 Simulation of field cages response to overpressure of 10 mbar in the hypothesis of free (left) and constrained (right) middle flange by the action of cathode. Picture from [96]. 115
4.31 Distribution of measured resistance values for a single voltage divider in FC4 at 70 V. 116
4.32 Measurement of current flowing through the voltage divider resistances for FC1 and FC2 at a voltage of 10 kV in figure 4.32a. On the right in figure 4.32b, the leakage current at 10 kV from the feed-thorugh to the shielding of FC1 is reported. The two plots estimate the alternative paths from cathode to ground, in which the leakage to the shielding is negligible as intended. . . . . 117

5.1 Measured total current (star points) compared to the simple ohmic model which consider only the voltage divider (red dashed line) of 1 GΩ. . . . . 119
5.2 Measured total current over time using a voltage of 15 kV over a nominal total resistance equal to 1 GΩ. . . . . 120
5.3 Comparison of measured value of resistances for two different field cages. Picture on left 5.3a represents the total resistance between two consecutive field strips on FC0 at 140 V, while picture on right 5.3b shows the resistance between two adjacent strips (mirror-field) at 70 V with only one voltage divider soldered for FC4. The number of measurements for 5.3a is half 5.3b, but both plots cover the whole drift length. . 121
5.4 Plot of difference of potential between two successive strips on different points along the Field Cage with a tension of 5 kV applied to the voltage divider, normalized to the variation at the edge for each dataset j = 1,2,3,4. . . . . 122
5.5 Sketch of the Field Cage walls from inner part on top to the external Aluminum shielding. Not on scale. . . . . 123
5.6 Sketch of possible paths for current on Field Cage walls. . . . . 123
5.7 Sketch of the possible paths for current for a voltage applied at two successive field strips. The resistance between field-mirror strips is called R≃2.5 MΩ, while K and T are the respective Kapton and Twaron resistivity for a single cell. The additional loops represent the n-term correction due to the presence of additional cells on the two side of the voltage divider. . . . . 125
5.8 Relative difference for $K_{eff}$ at the $n^{th}$ and $(n-1)^{th}$ orders for different values of Kapton coverlay resistance and same Twaron resistance value. . . . . 126

5.9 Relative difference for $K_{eff}$ at the $n^{th}$ and $(n-1)^{th}$ orders for same values of Kapton coverlay resistance and different Twaron resistance values. . . . . 126
5.10 Estimated value for K at for a given value of $R_{eff}$ as a function of parameter $\lambda$. . . . 127
5.11 Estimated value for K and T with $10^{-4} \leq \lambda \leq 1$ using as $R_{eff}$ the fitted value in the middle of FC0. . . . . 128
5.12 Picture of internal Twaron layer 5.12a that is visible after removing the Strip Foil still partly present. Few copper tape electrodes are already applied to measure the surface resistance. On the right side, a picture of the external Twaron layer is present 5.12b, in which the external shielding and Kapton layers were removed from the Field Cage 0. . . . . 130
5.13 Total current measured on the internal (blue) and external (red) Twaron layers on surfaces with the same width and length. . . . . 131
5.14 Current per square measured as a function of Electric field applied across the two electrodes and as a function of time. Each vertical series of points belong to the same dataset, in which the current is sampled over time. In order to facilitate the comparison among different datasets, points of the same style are taken at the same instant. . . . . 132
5.15 Current per square measured as a function of Electric field applied across the two electrodes and as a function of time. Each vertical series of points belongs to the same dataset, in which the current is sampled over time. In order to facilitate the comparison among different datasets, points of the same style are taken at the same instant. . . . . 133
5.16 Measured current through a Kapton foil of thickness 25 $\mu$m in picture 5.16a and 50 $\mu$m in picture 5.16b as a function of Electric field. Points with the same style are taken after the same time interval from the start of the measurement. . . . . 135
5.17 Current over time for each strip foil across the coverlay. . . . . 136
5.18 Current over time for strip foil 3 in figure 5.18a and for strip foil 4 in figure 5.18b, as a function of Electric field applied through the coverlay. A particular attention has to be given to the x-axis range. . . . . 137
5.19 Predicted value of K and T for each resistance measurement in FC0. . . . . 138
5.20 Schematic representation of hypothesized circuit. . . . . 139
5.21 Current on the voltage divider $I_1(x)$ for different order of magnitudes of k and t. . . 141
5.22 Current on the voltage divider for different values of k and t. On the left picture 5.22a, four different hypotheses for t at different order of magnitudes are reported at the same k. On the right 5.22b, the same exercise is reported but for different k and same t. The two parameters act differently on $I_1(x)$. . . . . 142
5.23 Comparison of datasets with the best fit from the model. Each figure contains a fit for all data points (blue), only first half (orange) and only second half (green). Datasets 5.23a,5.23b,5.23c present a much different behaviour with respect to 5.23d probably due to the modification of the Field Cage electrical properties once 20 kV of high voltage were reached. . . . . 143
5.24 Plot of residuals referring to fits in figure 5.23 . Each figure contains residuals for all data points (blue), only first half (orange) and only second half (green). . . . . 144
5.25 K as a function of $\lambda$ for data point i=13 in figure 5.3a. In red the fit for the empiric formula 5.30 is shown. . . . . 146
5.26 Total current output as a function of $\lambda$ in LTspice simulation of field cage model over the nominal current expected from the field cage voltage divider. . . . . 147

5.27 Predicted value of K and T for each resistance measurement in FC0 using parameter $\lambda$ obtained from the LTspice simulation of the field cage. . . . . 148
5.28 Predicted current on the voltage divider and on the Twaron layer according to LTspice simulation for $\lambda = 3.97 \times 10^{-3}$. . . . . 148
5.29 Predicted current on the voltage divider and on the Twaron layer for the best fit in the case of K,T homogeneous. . . . . 149
5.30 Comparison between FC0 before (left) and after(right) the installation of a fiberglass panel to cover the internal Twaron layer and prepare strip foil installation. The Twaron layer was levigated and cleaned of visible impurities in order to facilitate the panels gluing. . . . . 150
5.31 Details of the corner (left) of FC0, in which resin was added to increase the radius of curvature for proper gluing of the strip foil. On the right, a picture of the inner side of FC0 after the strip foil was glued. . . . . 150
5.32 Values of resistance between two neighboring strips along the drift length in the picture (left) and their fit with a gaussian distribution (right). . . . . 151
5.33 Resistance over time of refurbished internal Twaron layer for voltages of 500 V and 5000 V applied to the two glued copper rings parallel to the two flanges. . . . . 152

6.1 Residuals distribution for vertical tracks, with system of reference rotated, such that residuals are evaluated as horizontal displacement $\Delta z$ in the usual ND280 coordinates. Figure 6.1a represents tracks less than 20 cm away from Cathode, while Figure 6.1b refers to tracks between 60 cm and 80 cm away from Cathode. Scale in mm. . . . . 156
6.2 Centroid of a gaussian fit for apparent curvature for tracks passing in bottom HA-TPC EP0 (6.2a) and EP1 (6.2b) and top HA-TPC EP2 (6.2c) and EP3 (6.2d). . . . 157
6.3 Standard deviation of a Gaussian fit for apparent curvature distribution for tracks passing in bottom HA-TPC EP0 (6.2a) and EP1 (6.2b) and top HA-TPC EP2 (6.2c) and EP3 (6.2d). . . . . 158
6.4 Electric field simulation in a part of field cage model as designed for TDR. Field and mirror strips are 3 mm wide and the pitch is 5 mm. The voltages at Cathode and at Anode are set to obtain an expected magnitude for longitudinal field of 200 V/m. Picture from [96]. . . . . 161
6.5 Sketch of module frame 6.5a and thickness of stiffeners on module frame 6.5b, which extend inside the active volume. Dimensions in mm. . . . . 162
6.6 Side view of HA-TPC model used for COMSOL simulation. Only one eighth of the total volume is implemented, since three symmetry plane are used in (i) $x = 0$, (ii) $y = 0$ and (iii) $z = 0$. The Anode region is on the left, while the Cathode region on the right. . . . . 163
6.7 Electric field norm in a color scale of $\pm 5\%$ around the set value of 1 V/m. . . . . 164
6.8 Electric field lines in the region near the Anode, which is similar for every geometry. 164
6.9 Comparison of the Cathode region in the two geometries: TDR-like on top and actual one on bottom. For each geometry, electric field lines are drawn in the central plane $z = 0$. . . . . 165
6.10 $E_y/E_x$ for three different configurations of HA-TPC: top left (6.10a) actual HA-TPC setup; top right (6.10b) actual HA-TPC geometry with the first strip at the correct potential according to its $x$ coordinate; bottom (6.10c) HA-TPC as simulated in TDR. 166
6.11 $E_y$ (6.11a) and $E_z$ in the first quadrant of a HA-TPC (6.11b) components at x=100 mm in COMSOL simulation of the actual HA-TPCs setup. . . . . 168

6.12 $E_z/E_x$ for three different configurations of HA-TPC: top left (6.12a) actual HA-TPC setup; top right (6.12b) actual HA-TPC geometry with the first strip at the correct potential according to its $x$ coordinate; bottom (6.12c) HA-TPC as simulated in TDR. 169
6.13 ND280 steps related to HA-TPCs data processing, with a focus on oaUtility usage for real data. . . . . 169
6.14 ND280 steps related to HA-TPCs Monte Carlo data simulation and processing, with a focus on oaUtility usage for simulated data. . . . . 170
6.15 Global displacement for point-like charges starting at $x = 10$ cm on the two top right ERAMs being (0,0) the center of the module frame. The top row shows the absolute displacement in $\Delta y$ (left) and $\Delta z$ (right) coordinates between the starting and ending point of the drift trajectory in the actual HA-TPC setup. Bottom row shows the correspondent effects for the map in which the potential decrease in homogeneity is improved. The color range is reported in mm and it changes from top row to bottom row in order to visually enhance the effect. . . . . 171
6.16 Residuals distribution for vertical tracks, with system of reference rotated, such that residuals are evaluated as horizontal displacement $\Delta z$ in the usual ND280 coordinates. Figure 6.16a represents tracks less than 20 cm away from Cathode, while Figure 6.16b refers to tracks between 60 cm and 80 cm away from Cathode for tracks in which the electric field corrections are applied. Scale in mm. . . . . 172
6.17 Centroid of a gaussian fit for apparent curvature distribution after the application of electric field correction for tracks passing in bottom HA-TPC EP0 (6.17a) and EP1 (6.17b) and top HA-TPC EP2 (6.17c) and EP3 (6.17d). . . . . 173
6.18 Sigma of a gaussian fit for apparent curvature distribution after the application of electric field correction for tracks passing in bottom HA-TPC EP0 (6.17a) and EP1 (6.17b) and top HA-TPC EP2 (6.17c) and EP3 (6.17d). . . . . 174
6.19 Simulated drift velocity (left) and diffusion coefficients (right) in T2K gas for NTP conditions and no magnetic field. . . . . 175
6.20 Difference in time of arrival for a point-like source moving in the simulated electric field map and in an ideal electric field, starting at $x = 10$ cm (left) and $x = 5$ cm (right). Color scale is expressed in nanoseconds. . . . . 176
6.21 On the left, drawing of a possible configuration of a TPC based on FC0 for the study of electric field distortions is shown, in which a quartz window is installed in place of an ERAM. On the right, the field lines for plane z=0 on the Cathode region for FC0 and a G10 cover are reported. . . . . 176
6.22 Momentum bias for MC data in which 200 MeV/c $\leq p_{true} \leq$ 1000 MeV/c for muons using the E field map (6.22a) or ideal E field (6.23b. The bottom plot (6.22c) refers to anti-muons using E field map. Positive corner refers to the downstream corner, while negative one is the upstream corner. . . . . 178
6.23 Momentum bias for MC data in which 1000 MeV/c $\leq p_{true} \leq$ 3000 MeV/c for muons using the E field map (6.23a) or ideal E field (6.23b. The bottom plot (6.23c) refers to anti-muons using E field map. Positive corner refers to the downstream corner, while negative one is the upstream corner. . . . . 179

7.1 On the left, pads labeling in a cluster is reported. On the right, the two types of clustering are reported: if in the standard ND280 system of reference the slope of the local line approximation is such that $-1 \leq m_{yz} \leq 1$ the cluster is *horizontal*, otherwise it is *vertical*. . . . . 183

7.2 Examples of clustering of a 4×4 grid. Four clusters are found and drawn in different colors, with regions of partial overlap between them. . . . . 184
7.3 Example of FWHM estimation for a waveform in a pad. The FWHM is computed as the time interval between the instersection points of the dashed line with the solid lines. . . . . 184
7.4 Schematic view on how a point-like estimator of the track is computed for each single leading pad (orange). Top left plot shows the closest point on the estimated line for the first cluster where the leading pad appears, while the middle plot shows the same estimator for a different cluster. Notice how the same leading pad is placed differently in the two clusters. The average of such positions is the final estimator for the leading pad. . . . . 186
7.5 Example of a MLP network with 4 input parameters and 1 output. Picture from [131]. 187
7.6 On top, three models are fitted to an example training set: (i) top left shows that a linear model suffers from underfitting; (ii) top central plot shows that a quadratic model is able to represent the curvature present in data; (iii) top right plot shows that a polynomial of a much larger degree ($9^{th}$ degree) suffers from overfitting. In the bottom plot, the typical trend of training and test errors as a function of capacity are reported is represented. For a model with small capacity both training and test errors are high, a typical property of the underfitting regime. At larger capacities the test errors firstly reduces but then it starts to increase again, meanwhile the training errors continue to slowly decrease. The increasing generalization gap for algorithm at high capacity represents the overfitting phenomenon. Pictures from [132]. . . . . 190
7.7 Distribution for charge and reciprocal of FWHM for the central pad in clusters in test dataset. . . . . 193
7.8 Covariance matrix for input variables expressed in percentage. . . . . 193
7.9 Error function for training and test datasets as a function of epochs. . . . . 194
7.10 On top, the distribution of residuals for ($m_{regression} - m_{true}$) variable based on the true value of $m_{true}$ (left) or $q_{true}$ (right). On bottom, the same distributions for ($q_{regression} - q_{true}$) as a function of $m_{true}$ (left) and $q_{true}$ (right) are reported. . . . . 195
7.11 On top, the overall distribution of residuals for ($m_{regression} - m_{true}$) variable for horizontal (left) and vertical (right) test dataset. In the center, the same distributions for ($q_{regression} - q_{true}$) for horizontal (left) and vertical (right) test dataset is shown. Bottom plots report the 2D distribution of residuals ($m_{regression} - m_{true}$) and ($q_{regression} - q_{true}$) for horizontal (left) and vertical (right) test dataset. . . . . 196
7.12 Bias $\mu$ (left) and standard deviation $\sigma$ (right) for log(Q) method (square points) and 3x3 method (triangle points). . . . . 197
7.13 On top, bias $\mu$ (left) and standard deviation $\sigma$ (right) for log(Q) method (square points) and 3x3 method (triangle points) are reported for tracks with $p_{T,true} \in [300, 1000]$ MeV. Bottom plots are the equivalent estimators for tracks such that $p_{T,true} \in [1000, 3000]$ MeV. . . . . 199
7.14 Spectrum comparison for the two reconstruction methods log(Q) in blue and 3x3 in red lines. . . . . 201

# List of Tables


1.1 Results of the global $3\nu$ oscillation analysis, in terms of best-fit values and allowed 1 and $3\sigma$ ranges for the $3\nu$ mass-mixing parameters. The CP violating phase is taken in the (cyclic) interval $\delta_{CP} \in [0, 360]^\circ$, while the mixing angles are defined in the interval $\theta_{ij} \in [0, 90]^\circ$. Estimations are shown for both normal ordering (NO) and inverted ordering (IO). Note that $\Delta m^2_3 = \Delta m^2_{31} > 0$ for NO and $\Delta m^2_3 = \Delta m^2_{32} < 0$ for IO as visible also in 1.5. Table adapted from [28]. . . . . 32

2.1 Results for the oscillation parameters from the fit to data with and without the reactor constraint in the frequentist analysis, with the confidence intervals estimated using the constant $\Delta\chi^2$ method. . . . . 50

4.1 Summary of materials thickness which compose the field cage walls. Values for radiation length are reported in [120] and computed starting from single nuclei values when not available for a specific material. . . . . 85
4.2 . . . . . 94
4.3 . . . . . 95
4.4 . . . . . 99
4.5 . . . . . 100
4.6 . . . . . 101
4.7 . . . . . 101
4.8 . . . . . 113
4.9 . . . . . 114

5.1 . . . . . 133
5.2 . . . . . 137
5.3 Summary of model fit to datasets as shown in figure 5.23. . . . . 143
5.4 . . . . . 143
5.5 . . . . . 145
5.6 . . . . . 145
5.7 . . . . . 145

7.1 . . . . . 194
7.2 . . . . . 198
7.3 . . . . . 200

# Bibliography


[1] https://texample.net/tikz/examples/model-physics/.

[2] A Bettini. A brief history of neutrino. In *The State of the Art of Neutrino Physics: A Tutorial for Graduate Students and Young Researchers*, pages 1–36. World Scientific, 2018.

[3] James Chadwick. Intensitätsverteilung im magnetischen spectrum der $\beta$-strahlen von radium b+ c. *Verhandl. Dtsc. Phys. Ges.*, 16:383, 1914.

[4] J Chadwick. 10.1038/129312a0. *Nature*, 129(312):1932, 1932.

[5] Enrico Fermi. Tentativo di una teoria dei raggi $\beta$. *Il Nuovo Cimento (1924-1942)*, 11(1):1–19, 1934.

[6] Hans Bethe and Rudolph Peierls. The "neutrino". *Nature*, 133(3362):532–532, 1934.

[7] Frederick Reines and CLYDE L COWANjun. The neutrino. *Nature*, 178(4531):446–449, 1956.

[8] Frederick Reines and CL Cowan Jr. Detection of the free neutrino. *Physical Review*, 92(3):830, 1953.

[9] Bruno Pontecorvo. Neutrino experiments and the problem of conservation of leptonic charge. *Sov. Phys. JETP*, 26(984-988):165, 1968.

[10] Melvin Schwartz. Feasibility of using high-energy neutrinos to study the weak interactions. *Physical Review Letters*, 4(6):306, 1960.

[11] Gaillard Danby, Jean Maurice Gaillard, Konstantin Goulianos, Leon M Lederman, Nariman Mistry, Melvin Schwartz, and Jack Steinberger. Observation of high-energy neutrino reactions and the existence of two kinds of neutrinos. *Physical Review Letters*, 9(1):36, 1962.

[12] Martin L Perl, GS Abrams, AM Boyarski, Martin Breidenbach, DD Briggs, F Bulos, William Chinowsky, JT Dakin, GJ Feldman, CE Friedberg, et al. Evidence for anomalous lepton production in e+- e- annihilation. *Physical Review Letters*, 35(22):1489, 1975.

[13] K Kodama, N Ushida, C Andreopoulos, N Saoulidou, G Tzanakos, P Yager, B Baller, D Boehnlein, Walter Freeman, B Lundberg, et al. Observation of tau neutrino interactions. *Physics Letters B*, 504(3):218–224, 2001.

[14] The SLD Electroweak, Heavy Flavour Groups, ALEPH Collaboration, DELPHI Collaboration, L3 Collaboration, OPAL Collaboration, SLD Collaboration, LEP Electroweak Working Group, et al. Precision electroweak measurements on the z resonance. *Physics Reports*, 427(5-6):257–454, 2006.

[15] Chien-Shiung Wu, Ernest Ambler, Raymond W Hayward, Dale D Hoppes, and Ralph Percy Hudson. Experimental test of parity conservation in beta decay. *Physical review*, 105(4):1413, 1957.

[16] Richard L Garwin, Leon M Lederman, and Marcel Weinrich. Observations of the failure of conservation of parity and charge conjugation in meson decays: the magnetic moment of the free muon. *Physical Review*, 105(4):1415, 1957.

[17] John F Donoghue, Eugene Golowich, and Barry R Holstein. *Dynamics of the standard model*. Cambridge university press, 2014.

[18] Carlo Giunti and Chung W Kim. *Fundamentals of neutrino physics and astrophysics*. Oxford university press, 2007.

[19] Peter W Higgs. Broken symmetries and the masses of gauge bosons. *Physical review letters*, 13(16):508, 1964.

[20] Ettore Majorana. Teoria simmetrica dell,Äôelettrone e del positrone. *Il Nuovo Cimento (1924-1942)*, 14(4):171–184, 1937.

[21] Bruno Pontecorvo. Mesonium and antimesonium. *Zhur. Eksptl'. i Teoret. Fiz.*, 33, 1957.

[22] Ziro Maki, Masami Nakagawa, and Shoichi Sakata. Remarks on the unified model of elementary particles. *Progress of Theoretical Physics*, 28(5):870–880, 1962.

[23] Samoil M Bilenky and B Pontecorvo. Lepton mixing and neutrino oscillations. *Physics Reports*, 41(4):225–261, 1978.

[24] A. Y. Smirnov. Solar Neutrinos and Matter Effects. *Adv. Ser. Direct. High Energy Phys.*, 28:149–209, 2018.

[25] C. Jarlskog. Commutator of the Quark Mass Matrices in the Standard Electroweak Model and a Measure of Maximal CP Nonconservation. *Phys. Rev. Lett.*, 55:1039, 1985.

[26] SP Mikheev and A Yu Smirnov. Resonance amplification of oscillations in matter and spectroscopy of solar neutrinos. *Yadernaya Fizika*, 42(6):1441–1448, 1985.

[27] Lincoln Wolfenstein. Neutrino oscillations in matter. In *Solar neutrinos*, pages 294–299. CRC Press, 2018.

[28] S Navas, C Amsler, T Gutsche, C Hanhart, JJ Hernández-Rey, C Lourenço, A Masoni, M Mikhasenko, RE Mitchell, C Patrignani, et al. Review of particle physics. *Physical Review D*, 110(3):030001, 2024.

[29] John N Bahcall, Walter F Huebner, Stephen H Lubow, Peter D Parker, and Roger K Ulrich. Standard solar models and the uncertainties in predicted capture rates of solar neutrinos. *Reviews of Modern Physics*, 54(3):767, 1982.

[30] John N Bahcall, Aldo M Serenelli, and Sarbani Basu. New solar opacities, abundances, helioseismology, and neutrino fluxes. *The Astrophysical Journal*, 621(1):L85, 2005.

[31] Raymond Davis Jr, Don S Harmer, and Kenneth C Hoffman. Search for neutrinos from the sun. *Physical Review Letters*, 20(21):1205, 1968.

[32] Bruce T Cleveland, Timothy Daily, Raymond Davis Jr, James R Distel, Kenneth Lande, CK Lee, Paul S Wildenhain, and Jack Ullman. Measurement of the solar electron neutrino flux with the homestake chlorine detector. *The Astrophysical Journal*, 496(1):505, 1998.

[33] Carlos Pena-Garay and Aldo Serenelli. Solar neutrinos and the solar composition problem. *arXiv preprint arXiv:0811.2424*, 2008.

[34] Michael Altmann, M Balata, P Belli, E Bellotti, R Bernabei, E Burkert, C Cattadori, R Cerulli, Marco Chiarini, M Cribier, et al. Complete results for five years of gno solar neutrino observations. *Physics Letters B*, 616(3-4):174–190, 2005.

[35] JN Abdurashitov, VN Gavrin, VV Gorbachev, PP Gurkina, TV Ibragimova, AV Kalikhov, NG Khairnasov, TV Knodel, IN Mirmov, AA Shikhin, et al. Measurement of the solar neutrino capture rate with gallium metal. iii. results for the 2002–2007 data-taking period. *Physical Review C,ÄîNuclear Physics*, 80(1):015807, 2009.

[36] Núria Vinyoles, Aldo M Serenelli, Francesco L Villante, Sarbani Basu, Johannes Bergström, MC Gonzalez-Garcia, Michele Maltoni, Carlos Peña-Garay, and Ningqiang Song. A new generation of standard solar models. *The Astrophysical Journal*, 835(2):202, 2017.

[37] Comprehensive measurement of pp-chain solar neutrinos. *Nature*, 562(7728):505–510, 2018.

[38] Kohji S Hirata, Takaaki Kajita, T Kifune, K Kihara, Masayuki Nakahata, K Nakamura, S Ohara, Y Oyama, N Sato, M Takita, et al. Observation of b 8 solar neutrinos in the kamiokande-ii detector. *Physical review letters*, 63(1):16, 1989.

[39] J Hosaka, K Ishihara, J Kameda, Yusuke Koshio, A Minamino, C Mitsuda, M Miura, S Moriyama, M Nakahata, T Namba, et al. Solar neutrino measurements in super-kamiokande-i. *Physical Review D,ÄîParticles, Fields, Gravitation, and Cosmology*, 73(11):112001, 2006.

[40] P Anselmann, W Hampel, G Heusser, J Kiko, T Kirsten, M Laubenstein, E Pernicka, S Pezzoni, U Rönn, M Sann, et al. Gallex solar neutrino observations: complete results for gallex ii. *Physics Letters B*, 357(1-2):237–247, 1995.

[41] M Junker, A D,Äôalessandro, S Zavatarelli, C Arpesella, E Bellotti, C Broggini, P Corvisiero, Giovanni Fiorentini, A Fubini, Gianpiero Gervino, et al. Cross section of 3 h e (3 he, 2 p) 4 he measured at solar energies. *Physical Review C*, 57(5):2700, 1998.

[42] B Aharmim, SN Ahmed, AE Anthony, EW Beier, A Bellerive, M Bergevin, SD Biller, J Boger, MG Boulay, and MG Bowler. Electron energy spectra, fluxes, and day-night asymmetries of b-8 solar neutrinos from measurements with nacl dissolved in the heavy-water detector at the sudbury neutrino observatory. *Phys. Rev. C*, 72(arXiv: nucl-ex/0502021), 2005.

[43] S Fukuda, Y Fukuda, M Ishitsuka, Y Itow, T Kajita, J Kameda, K Kaneyuki, K Kobayashi, Y Koshio, M Miura, et al. Constraints on neutrino oscillations using 1258 days of super-kamiokande solar neutrino data. *Physical review letters*, 86(25):5656, 2001.

[44] C Arpesella, G Bellini, J Benziger, S Bonetti, B Caccianiga, Frank Calaprice, F Dalnoki-Veress, D d'Angelo, H de Kerret, A Derbin, et al. First real time detection of 7be solar neutrinos by borexino. *Physics Letters B*, 658(4):101–108, 2008.

[45] Experimental evidence of neutrinos produced in the cno fusion cycle in the sun. *Nature*, 587(7835):577–582, 2020.

[46] G Bellini, J Benziger, S Bonetti, M Buizza Avanzini, B Caccianiga, L Cadonati, Frank Calaprice, C Carraro, A Chavarria, A Chepurnov, et al. Measurement of the solar b 8 neutrino rate with a liquid scintillator target<? format?> and 3 mev energy threshold in the borexino detector. *Physical Review D,ÄîParticles, Fields, Gravitation, and Cosmology*, 82(3):033006, 2010.

[47] Gianpaolo Bellini, J Benziger, D Bick, S Bonetti, G Bonfini, D Bravo, M Buizza Avanzini, B Caccianiga, L Cadonati, F Calaprice, et al. First evidence of pep solar neutrinos by direct detection in borexino. *Physical Review Letters*, 108(5):051302, 2012.

[48] Ivan Esteban, MC Gonzalez-Garcia, Michele Maltoni, Ivan Martinez-Soler, and Thomas Schwetz. Updated fit to three neutrino mixing: exploring the accelerator-reactor complementarity. *Journal of High Energy Physics*, 2017(1):1–31, 2017.

[49] Feng Peng An, Akif Baha Balantekin, Henry Reyer Band, M Bishai, Simon Blyth, D Cao, Guo Fu Cao, Jun Cao, WR Cen, Yat Long Chan, et al. Measurement of electron antineutrino oscillation based on 1230 days of operation of the daya bay experiment. *Physical Review D*, 95(7):072006, 2017.

[50] Azusa Gando, Y Gando, H Hanakago, Hirokazu Ikeda, K Inoue, K Ishidoshiro, H Ishikawa, M Koga, R Matsuda, S Matsuda, et al. Reactor on-off antineutrino measurement with kamland. *Physical Review D,ÄîParticles, Fields, Gravitation, and Cosmology*, 88(3):033001, 2013.

[51] KS Hirata, T Kajita, M Koshiba, M Nakahata, S Ohara, Y Oyama, N Sato, A Suzuki, M Takita, Y Totsuka, et al. Experimental study of the atmospheric neutrino flux. *Physics Letters B*, 205(2-3):416–420, 1988.

[52] D Casper, R Becker-Szendy, CB Bratton, DR Cady, R Claus, ST Dye, W Gajewski, M Goldhaber, TJ Haines, PG Halverson, et al. Measurement of atmospheric neutrino composition with the imb-3 detector. *Physical Review Letters*, 66(20):2561, 1991.

[53] M Aglietta, G Battistoni, E Bellotti, C Bloise, G Bologna, C Broggini, P Campana, C Castagnoli, A Castellina, V Chiarella, et al. Experimental study of atmospheric neutrino flux in the nusex experiment. *Europhysics Letters*, 8(7):611, 1989.

[54] Fréjus Collaboration, K Daum, W Rhode, P Bareyre, R Barloutaud, G Chardin, B Degrange, J Ernwein, B Kuznik, H Meyer, et al. Determination of the atmospheric neutrino spectra with the frejus detector. *Zeitschrift für Physik C Particles and Fields*, 66(3):417–428, 1995.

[55] Yoshiyuki Fukuda, T Hayakawa, E Ichihara, K Inoue, K Ishihara, Hirokazu Ishino, Y Itow, T Kajita, J Kameda, S Kasuga, et al. Evidence for oscillation of atmospheric neutrinos. *Physical review letters*, 81(8):1562, 1998.

[56] Michelangelo Ambrosio, R Antolini, Giulio Auriemma, D Bakari, A Baldini, GC Barbarino, BC Barish, G Battistoni, Yvonne Becherini, Roberto Bellotti, et al. Matter effects in upward-going muons and sterile neutrino oscillations. *Physics Letters B*, 517(1-2):59–66, 2001.

[57] Me Sanchez, W WM Allison, GJ Alner, DS Ayres, WL Barrett, MC Goodman, T Joffe-Minor, and JL Thron. Observation of atmospheric neutrino oscillations in soudan 2. Technical report, Argonne National Lab., IL (US), 2003.

[58] Z Li, K Abe, C Bronner, Y Hayato, M Ikeda, K Iyogi, J Kameda, Y Kato, Y Kishimoto, Ll Marti, et al. Measurement of the tau neutrino cross section in atmospheric neutrino oscillations with super-kamiokande. *Physical Review D*, 98(5):052006, 2018.

[59] N Agafonova, A Alexandrov, A Anokhina, S Aoki, A Ariga, T Ariga, A Bertolin, C Bozza, R Brugnera, A Buonaura, et al. Final results of the opera experiment on $\nu$ $\tau$ appearance in the cngs neutrino beam. *Physical review letters*, 120(21):211801, 2018.

[60] MG Aartsen, M Ackermann, J Adams, JA Aguilar, M Ahlers, M Ahrens, D Altmann, K Andeen, T Anderson, I Ansseau, et al. Measurement of atmospheric tau neutrino appearance with icecube deepcore. *Physical Review D*, 99(3):032007, 2019.

[61] KamLAND& Eguchi, S Enomoto, K Furuno, J Goldman, H Hanada, H Ikeda, K Ikeda, K Inoue, K Ishihara, W Itoh, et al. First results from kamland: evidence for reactor antineutrino disappearance. *Physical review letters*, 90(2):021802, 2003.

[62] Takeshi Araki, K Eguchi, S Enomoto, K Furuno, K Ichimura, H Ikeda, K Inoue, K Ishihara, T Iwamoto, T Kawashima, et al. Measurement of neutrino oscillation with kamland: Evidence of spectral distortion. *Physical review letters*, 94(8):081801, 2005.

[63] FP An, JZ Bai, AB Balantekin, HR Band, D Beavis, W Beriguete, M Bishai, S Blyth, K Boddy, RL Brown, et al. Observation of electron-antineutrino disappearance at daya bay. *Physical Review Letters*, 108(17):171803, 2012.

[64] Jung Keun Ahn, S Chebotaryov, JH Choi, S Choi, W Choi, Y Choi, HI Jang, JS Jang, EJ Jeon, IS Jeong, et al. Observation of reactor electron antineutrinos disappearance in the reno experiment. *Physical Review Letters*, 108(19):191802, 2012.

[65] MH Ahn, E Aliu, S Andringa, S Aoki, Y Aoyama, J Argyriades, K Asakura, R Ashie, F Berghaus, HG Berns, et al. Measurement of neutrino oscillation by the k2k experiment. *Physical Review D,ÄîParticles, Fields, Gravitation, and Cosmology*, 74(7):072003, 2006.

[66] RB Patterson. The nova experiment: status and outlook. *Nuclear Physics B-Proceedings Supplements*, 235:151–157, 2013.

[67] K Abe, N Abgrall, H Aihara, Y Ajima, JB Albert, D Allan, P-A Amaudruz, C Andreopoulos, B Andrieu, MD Anerella, et al. The t2k experiment. *Nuclear Instruments and Methods in Physics Research Section A: Accelerators, Spectrometers, Detectors and Associated Equipment*, 659(1):106–135, 2011.

[68] Kou Abe, N Abgrall, H Aihara, T Akiri, JB Albert, C Andreopoulos, S Aoki, A Ariga, T Ariga, S Assylbekov, et al. Evidence of electron neutrino appearance in a muon neutrino beam. *Physical Review D,ÄîParticles, Fields, Gravitation, and Cosmology*, 88(3):032002, 2013.

[69] K Abe, N Akhlaq, R Akutsu, A Ali, S Alonso Monsalve, C Alt, C Andreopoulos, M Antonova, S Aoki, T Arihara, et al. Measurements of neutrino oscillation parameters from the t2k experiment using 3.6× 10 21 protons on target. *The European Physical Journal C*, 83(9):782, 2023.

[70] Ivan Esteban, MC Gonzalez-Garcia, Michele Maltoni, Ivan Martinez-Soler, João Paulo Pinheiro, and Thomas Schwetz. Nufit-6.0: Updated global analysis of three-flavor neutrino oscillations. *Journal of High Energy Physics*, 2024(12):1–33, 2025.

[71] Patrick Huber, Mauro Mezzetto, and Thomas Schwetz. On the impact of systematical uncertainties for the CP violation measurement in superbeam experiments. *JHEP*, 03:021, 2008.

[72] Tsuyoshi Nakaya. Near detectors for long baseline neutrino experiments. *J. Phys. Conf. Ser.*, 308:012004, 2011.

[73] Ke Abe, Ke Abe, H Aihara, A Aimi, R Akutsu, C Andreopoulos, I Anghel, LHV Anthony, M Antonova, Y Ashida, et al. Hyper-kamiokande design report. *arXiv preprint arXiv:1805.04163*, 2018.

[74] M Aker, D Batzler, A Beglarian, J Behrens, J Beisenkötter, M Biassoni, B Bieringer, Y Biondi, F Block, S Bobien, et al. Direct neutrino-mass measurement based on 259 days of katrin data. *arXiv preprint arXiv:2406.13516*, 2024.

[75] Andrei D Sakharov. Violation of cp-invariance, c-asymmetry, and baryon asymmetry of the universe. In *In The Intermissions,Ä¶ Collected Works on Research into the Essentials of Theoretical Physics in Russian Federal Nuclear Center, Arzamas-16*, pages 84–87. World Scientific, 1998.

[76] Peter AR Ade, Nabila Aghanim, M Arnaud, Mark Ashdown, Jea Aumont, Carlo Baccigalupi, AJ Banday, RB Barreiro, JG Bartlett, Nicola Bartolo, et al. Planck 2015 results-xiii. cosmological parameters. *Astronomy & Astrophysics*, 594:A13, 2016.

[77] María Belén Gavela, P Hernandez, Jean Orloff, and Olivier Pène. Standard model cp-violation and baryon asymmetry. *Modern Physics Letters A*, 9(09):795–809, 1994.

[78] Masataka Fukugita and Tsutomu Yanagida. Barygenesis without grand unification. *Physics Letters B*, 174(1):45–47, 1986.

[79] Silvia Pascoli and Jessica Turner. Matter–antimatter symmetry violated, 2020.

[80] Babak Abi, Roberto Acciarri, Mario A Acero, Giorge Adamov, David Adams, Marco Adinolfi, Zubayer Ahmad, Jhanzeb Ahmed, Tyler Alion, S Alonso Monsalve, et al. Volume i. introduction to dune. *Journal of instrumentation*, 15(08):T08008, 2020.

[81] Mauro Mezzetto and Francesco Terranova. Three-flavor oscillations with accelerator neutrino beams. *Universe*, 6(2):32, 2020.

[82] Francesco Terranova. Future long-baseline neutrino experiments. *Universe*, 10(5):221, 2024.

[83] JUNO collaboration et al. Juno physics and detector. *Progress in Particle and Nuclear Physics*, 123:103927, 2022.

[84] Y Itow, T Kajita, K Kaneyuki, M Shiozawa, Y Totsuka, Y Hayato, T Ishida, T Ishii, T Kobayashi, T Maruyama, et al. The jhf-kamioka neutrino project. *arXiv preprint hep-ex/0106019*, 2001.

[85] Constraint on the matter–antimatter symmetry-violating phase in neutrino oscillations. *Nature*, 580(7803):339–344, 2020.

[86] Kou Abe, N Abgrall, H Aihara, T Akiri, JB Albert, C Andreopoulos, S Aoki, A Ariga, T Ariga, S Assylbekov, et al. T2k neutrino flux prediction. *Physical Review D,ÄîParticles, Fields, Gravitation, and Cosmology*, 87(1):012001, 2013.

[87] K Abe, N Abgrall, Y Ajima, H Aihara, JB Albert, C Andreopoulos, B Andrieu, MD Anerella, S Aoki, O Araoka, et al. Measurements of the t2k neutrino beam properties using the ingrid on-axis near detector. *Nuclear Instruments and Methods in Physics Research Section A: Accelerators, Spectrometers, Detectors and Associated Equipment*, 694:211–223, 2012.

[88] Nicolas Abgrall, B Andrieu, P Baron, P Bene, V Berardi, J Beucher, P Birney, F Blaszczyk, Alain Blondel, C Bojechko, et al. Time projection chambers for the t2k near detectors. *Nuclear Instruments and Methods in Physics Research Section A: Accelerators, Spectrometers, Detectors and Associated Equipment*, 637(1):25–46, 2011.

[89] M Jiang, K Abe, C Bronner, Y Hayato, M Ikeda, K Iyogi, J Kameda, Y Kato, Y Kishimoto, L l Marti, et al. Atmospheric neutrino oscillation analysis with improved event reconstruction in super-kamiokande iv. *Progress of Theoretical and Experimental Physics*, 2019(5):053F01, 2019.

[90] K Abe, C Bronner, Y Hayato, K Hiraide, M Ikeda, S Imaizumi, J Kameda, Y Kanemura, Y Kataoka, S Miki, et al. First gadolinium loading to super-kamiokande. *Nuclear Instruments and Methods in Physics Research Section A: Accelerators, Spectrometers, Detectors and Associated Equipment*, 1027:166248, 2022.

[91] K Abe, C Bronner, Y Hayato, K Hiraide, K Hosokawa, K Ieki, M Ikeda, J Kameda, Y Kanemura, R Kaneshima, et al. Second gadolinium loading to super-kamiokande. *Nuclear Instruments and Methods in Physics Research Section A: Accelerators, Spectrometers, Detectors and Associated Equipment*, page 169480, 2024.

[92] K Abe, J Adam, H Aihara, T Akiri, C Andreopoulos, S Aoki, Akitaka Ariga, Tomoko Ariga, S Assylbekov, D Autiero, et al. Observation of electron neutrino appearance in a muon neutrino beam. *Physical review letters*, 112(6):061802, 2014.

[93] K Abe, H Aihara, A Ajmi, C Alt, C Andreopoulos, M Antonova, S Aoki, Y Asada, Y Ashida, A Atherton, et al. J-parc neutrino beamline upgrade technical design report. *arXiv preprint arXiv:1908.05141*, 2019.

[94] Adrien Blanchet. Physics and performance of the upgraded t2k,Äôs near detector. *Physics of Atomic Nuclei*, 84:519–523, 2021.

[95] Alain Blondel, M Bogomilov, S Bordoni, F Cadoux, D Douqa, K Dugas, T Ekelof, Y Favre, S Fedotov, Kjell Fransson, et al. The superfgd prototype charged particle beam tests. *Journal of Instrumentation*, 15(12):P12003, 2020.

[96] K Abe, H Aihara, A Ajmi, C Andreopoulos, M Antonova, S Aoki, Y Asada, Y Ashida, A Atherton, E Atkin, et al. T2k nd280 upgrade–technical design report. *arXiv preprint arXiv:1901.03750*, 2019.

[97] D Attié, M Batkiewicz-Kwasniak, P Billoir, A Blanchet, A Blondel, S Bolognesi, D Calvet, MG Catanesi, M Cicerchia, G Cogo, et al. Characterization of resistive micromegas detectors for the upgrade of the t2k near detector time projection chambers. *Nuclear Instruments and*

*Methods in Physics Research Section A: Accelerators, Spectrometers, Detectors and Associated Equipment*, 1025:166109, 2022.

[98] D Attié, O Ballester, M Batkiewicz-Kwasniak, P Billoir, A Blanchet, A Blondel, S Bolognesi, R Boullon, D Calvet, MP Casado, et al. Analysis of test beam data taken with a prototype of tpc with resistive micromegas for the t2k near detector upgrade. *Nuclear Instruments and Methods in Physics Research Section A: Accelerators, Spectrometers, Detectors and Associated Equipment*, 1052:168248, 2023.

[99] Lev Davidovich Landau. On the energy loss of fast particles by ionization. *J. Phys.*, 8:201–205, 1944.

[100] GJ Igo, DD Clark, and Robert Martin Eisberg. Statistical fluctuations in ionization by 31.5-mev protons. *Physical Review*, 89(4):879, 1953.

[101] Werner Riegler Blum, Walter and Luigi Rolandi. *Particle detection with drift chambers*. Springer Science Business Media, 2008.

[102] DR Nygren. Pep 198 (1975); ar clark, et al., proposal for a pep facility based on the time projection chamber. Technical report, PEP-PROPOSAL-004, 1976.

[103] AR Clark et al. Proposal for a pep facility based on the tpc. *PEP exp. 4*, 1976.

[104] Hans Jurgen Hilke. Time projection chambers. *Reports on Progress in Physics*, 73(11):116201, 2010.

[105] Fabio Sauli. *Gaseous radiation detectors: fundamentals and applications*. Cambridge University Press, 2015.

[106] Yannis Giomataris, Ph Rebourgeard, Jean Pierre Robert, and Georges Charpak. Micromegas: a high-granularity position-sensitive gaseous detector for high particle-flux environments. *Nuclear Instruments and Methods in Physics Research Section A: Accelerators, Spectrometers, Detectors and Associated Equipment*, 376(1):29–35, 1996.

[107] Joshi Shivam. *Characterization of resistive Micromegas for High Angle-Time Projection Chambers readout and preparation of neutrino physics analysis with upgraded near detector of T2K experiment.* PhD thesis, High Energy Physics - Experiment [hep-ex]. Université Paris-Saclay, 2024. English. <NNT : 2024UPASP123>. <tel-04836929>, 2024.

[108] L Ambrosi, D Attié, O Ballester, M Batkiewicz-Kwasniak, P Billoir, A Blanchet, A Blondel, S Bolognesi, R Boullon, D Calvet, et al. Characterization of charge spreading and gain of encapsulated resistive micromegas detectors for the upgrade of the t2k near detector time projection chambers. *Nuclear Instruments and Methods in Physics Research Section A: Accelerators, Spectrometers, Detectors and Associated Equipment*, 1056:168534, 2023.

[109] Madhu S Dixit, Jacques Dubeau, J-P Martin, and Kirsten Sachs. Position sensing from charge dispersion in micro-pattern gas detectors with a resistive anode. *Nuclear Instruments and Methods in Physics Research Section A: Accelerators, Spectrometers, Detectors and Associated Equipment*, 518(3):721–727, 2004.

[110] P Baron, E Delagnes, D Calvet, X de la Broise, A Delbart, F Druillole, JL Fallou, E Mazzucato, E Monmarthe, F Pierre, et al. After, an asic for the readout of the large t2k time projection chambers. In *2007 IEEE Nuclear Science Symposium Conference Record*, volume 3, pages 1865–1872. IEEE, 2007.

[111] Uladzislava Yevarouskaya. *Preparation for the ND280 near detector upgrade of the T2K experiment: development of the analysis and reconstruction for High-Angle TPCs and validation of GUNDAM, a new near detector fitting framework*. PhD thesis, Sorbonne université, 2023.

[112] RL Gluckstern. Uncertainties in track momentum and direction, due to multiple scattering and measurement errors. *Nuclear Instruments and Methods*, 24:381–389, 1963.

[113] Paul Colas. First test results from a micromegas large tpc prototype. *Nuclear Instruments and Methods in Physics Research Section A: Accelerators, Spectrometers, Detectors and Associated Equipment*, 623(1):100–101, 2010.

[114] Sea Agostinelli, John Allison, K al Amako, John Apostolakis, Henrique Araujo, Pedro Arce, Makoto Asai, D Axen, Swagato Banerjee, GJNI Barrand, et al. Geant4,Äîa simulation toolkit. *Nuclear instruments and methods in physics research section A: Accelerators, Spectrometers, Detectors and Associated Equipment*, 506(3):250–303, 2003.

[115] John Apostolakis, S Giani, L Urban, M Maire, AV Bagulya, and VM Grichine. An implementation of ionisation energy loss in very thin absorbers for the geant4 simulation package. *Nuclear Instruments and Methods in Physics Research Section A: Accelerators, Spectrometers, Detectors and Associated Equipment*, 453(3):597–605, 2000.

[116] Sergey Suvorov. *Search for heavy neutrinos in the T2K experiment and upgrade of the near detector ND280*. PhD thesis, Université Paris-Saclay; Académie des sciences de Russie (1992-....), 2020.

[117] David Attié, M Batkiewicz-Kwasniak, J Boix, S Bolognesi, S Bordoni, D Calvet, MG Catanesi, M Cicerchia, G Cogo, P Colas, et al. Performances of a resistive micromegas module for the time projection chambers of the t2k near detector upgrade. *Nuclear Instruments and Methods in Physics Research Section A: Accelerators, Spectrometers, Detectors and Associated Equipment*, 957:163286, 2020.

[118] Matteo Feltre. The reconstruction of charged tracks within the new time projection chambers of the t2k upgraded experiment at j-parc. Master's thesis, Universita degli Studi di Padova, https://hdl.handle.net/20.500.12608/4093, 2020.

[119] Camilla Forza. Characterization and commissioning of two large volume gaseous time projection chambers at cern and j-parc laboratories. Master's thesis, Universita degli Studi di Padova, https://hdl.handle.net/20.500.12608/4093, 2023.

[120] PDG. https://pdg.lbl.gov/2024/atomicnuclearproperties/index.html.

[121] Resoltech. https://www.resoltech.com/en/markets/1050t-detail.html.

[122] DuPont. https://www.dupont.it/fabrics-fibers-andnonwovens/honeycomb-composites.html.

[123] Resoltech. https://www.resoltech.com/en/markets/3350-detail.html.

[124] EVONIK. https://composites.evonik.com/en/products-services/foams/rohacell.

[125] Tektronix. *Series 2400 SourceMeter¬SMUInstrumentsDatasheet.*

[126] FibrXL. Twaron®.

[127] LTspice. Ltspice.

[128] COMSOL Multiphysics. Introduction to comsol multiphysics®. *COMSOL Multiphysics, Burlington, MA, accessed Feb*, 9(2018):32, 1998.

[129] Thomas Radermacher. *Measurements and simulation of drift gas properties for the time projection chambers of the T2K experiment and for future neutrino experiments.* PhD thesis, Dissertation, RWTH Aachen University, 2019, 2019.

[130] Garfield++. `https://garfieldpp.web.cern.ch/garfieldpp/documentation/UserGuide.pdf`. Accessed: 2025-01-17.

[131] Andreas Hoecker, Peter Speckmayer, Joerg Stelzer, Jan Therhaag, Eckhard von Toerne, Helge Voss, M Backes, T Carli, O Cohen, A Christov, et al. Tmva-toolkit for multivariate data analysis. *arXiv preprint physics/0703039*, 2007.

[132] Ian Goodfellow, Yoshua Bengio, and Aaron Courville. *Deep Learning.* MIT Press, 2016. `http://www.deeplearningbook.org`.

[133] Leslie N Smith. A disciplined approach to neural network hyper-parameters: Part 1–learning rate, batch size, momentum, and weight decay. *arXiv preprint arXiv:1803.09820*, 2018.